Study on low-temperature chemical vapor deposition growth of 2D $PdSe_2$ for applications in surface enhanced Raman scattering and cancer biology

A Thesis Submitted to

Indian Institute of Technology Guwahati

For the degree of

Doctor of Philosophy

By

Tadasha Jena

Centre for Nanotechnology,

Indian Institute of Technology Guwahati

Guwahati-781039, India

January 2025

Dedicated to my father Dr. Madhab Chandra Jena and mother Mrs. Tapaswini Senapati for providing me unwavering guidance and continuous encouragement.

Centre for Nanotechnology
Indian Institute of Technology Guwahati
Guwahati-781039, India

STATEMENT

The work contained in the thesis entitled "**Study on low-temperature chemical vapor deposition growth of 2D $PdSe_2$ for applications in surface enhanced Raman scattering and cancer biology**" has been carried out by me at the Indian Institute of Technology Guwahati under the supervision of **Prof. P. K. Giri**, Professor, Department of Physics and Centre for Nanotechnology, Indian Institute of Technology Guwahati. This work has not been submitted elsewhere for the award of any degree.

Tadasha Jena

Roll No. - 196153010

Senior Research Fellow
Centre for Nanotechnology
Indian Institute of Technology Guwahati
Guwahati-781039, India

Prof. P. K. Giri
Professor
Department of Physics
and Centre for Nanotechnology
Indian Institute of Technology Guwahati
Guwahati-781039, India
Phone: ***+91 361 2582703****, Fax:* ***+91 361 2690762***
Email: giri@iitg.ac.in

CERTIFICATE

This is to certify that the work contained in the thesis entitled "**Study on low-temperature chemical vapor deposition growth of 2D $PdSe_2$ for applications in surface enhanced Raman scattering and cancer biology**" has been carried out by **Ms. Tadasha Jena** at Indian Institute of Technology Guwahati under my supervision. This work has not been submitted elsewhere for the award of any degree.

Prof. P. K. Giri

Thesis supervisor

ACKNOWLEDGEMENT

Here I am closing my PhD journey; it was a tremendous journey! It started with an audacious dream of being a student of learning and of reliving a part of my life I had left way behind. It is nothing short of a miracle that I have somehow managed to complete the race. There have been some obstacles, but they made the race more entertaining. Now, I am standing at the edge of the precipice; I must look back to those persons for their assistance, support, and inspiration.

First and foremost, I would like to express my sincere gratitude to my thesis supervisor, Prof. P. K. Giri, for his inspiring guidance, valuable discussion, constant support, and helpful suggestions. His support and advice have carried me through my research journey, and I will be forever grateful to him for everything he has taught me. He is my guiding light, whose unstinting confidence in my abilities encouraged me to keep going when times get tough. I am genuinely thankful for the freedom to explore my ideas and the insight you provided, which profoundly shaped this thesis.

I am also thankful to my doctoral committee members, Dr. Partho Sarathi Gooh Pattader, Prof. Nageswara Rao Peela, and Prof. D. Pamu, for their valuable suggestions and patience during all my seminars. Your expertise and time have been crucial in assuring my progress throughout my research period.

I am grateful to our collaborators, Prof. Manabendra Sarma and Upasana Nath from the chemistry department at IITG, for helping with the theoretical calculations whenever needed. I must thank my collaborators, Prof. Minoru Fujii and Dr. Sugimoto from Kobe University, Japan, for the XPS and NIR photoluminescence measurements.

I want to thank the Head of the Centre for Nanotechnology, other faculty members of the Centre for Nanotechnology, members of the Central Instruments Facilities, and the Centre for Nanotechnology for providing me with the much-needed instrumental facilities. I am thankful to all the staff members of the Centre for Nanotechnology, especially Gobinda Chhetry, Gautam Barman, Kaustubh Acharyya, Dr. Pranjoli Das, Emlin Elsa Abraham, and Ayon Kumar Paul, for their help and cooperation throughout my Ph.D. journey. I must thank Dr. Md Tarik Hossain, my lab mate and collaborator. I am deeply grateful for his practical help in the lab, insightful feedback for my research work, solving problems together, and engaging in stimulating discussions, which

significantly enriched my research experience. I am thankful to lab mates Dr. Somorjit Singh, Dr. Abhilasha Bora, Ravinder Chahal, Abdul Kaium Mia, Koushik Ghosh, Sirsendu Ghosal, Sanju Nandi, Subhankar Debnath, Debabrata Sahu, Shipra Aswal, Sanjoy Sur Roy, Sourav Dey, Garima Choudhary, and Santanu Dhara for providing me a healthy work environment. I want to thank my close friends Bhagyashree, Aparna, Sruti, Arpita, Pujarini, and Upasana for their constant source of strength throughout my Ph.D. journey.

I am also thankful to the Central Workshop, Department of Mechanical Engineering, for fabricating essential components in my experimental setup. I immensely admire the Indian Institute of Technology Guwahati for offering me a fellowship, suitable accommodation on this beautiful campus, and a pleasant working environment.

To my mother, Tapaswini Senapati, and father, Madhab Chandra Jena, thank you for your endless encouragement and belief in me and for constantly reminding me of the importance of perseverance and hard work. It would be a grave injustice if I forgot to extend my special thanks to my sister, Maneesha Jena, and brother, Tarini Prasad. Thank you for being my pillar of strength and always being there to listen and understand. Last but not the least, I am deeply indebted to my husband, Rohan Chinchkar, for his unflagging support and sacrifice in all the difficult times. Your support means the world to me.

Tadasha Jena
IIT Guwahati

भारतीय प्रौद्योगिकी संस्थान गुवाहाटी
Indian Institute of Technology Guwahati

Table of Contents

SYNOPSIS

Many researchers have been drawn to the world of two-dimensional materials due to the ground-breaking applications of graphene in various fields, such as optoelectronic devices, energy-conversion devices, chemical and biological sensors, and high-frequency electronic and optical devices. As a very stable material, graphene exhibits an immensely high thermal conductivity of about 5300 W m^{-1} K^{-1}. This value strongly limits its electronic packaging applications and has led to a search for alternative 2D materials, such as hBN, black phosphorus, group 6, and group 10 TMDs. The commonality between graphene and most 2D materials is that they are highly symmetric due to their isotropic lattice structure. Over the past decade, some experimentally reachable 2D materials have exhibited in-plane isotropic behavior. However, the evolution of black phosphorus (BP) in 2014 as an anisotropic material has pinned scientists to search for alternative materials that exhibit anisotropic behavior. Over and above the most investigated TMDs, some of the materials in the group 10 TMDs have been attracting increasing attention in the last few years because of their anisotropic behavior, which provides fertile ground for many applications. Due to many noble applications in various fields, group 10 TMDs ($PdSe_2$, Pd_2Se_3, $PdTe_2$, PdS_2, $PtSe_2$, etc.) are named noble TMDs (NTMDs).

2D $PdSe_2$ has sparked as the star NTMD due to its low symmetry puckered pentagonal structure, easily exfoliated, thickness tunable bandgap (0 eV to 1.43 eV), in-plane anisotropy similar to 2D black phosphorous, high carrier mobility, high air stability, direction-dependent physical properties, etc. Although 2D $PdSe_2$ holds great promise for several applications, the controlled synthesis of monolayer and bilayer $PdSe_2$ remains challenging. Various methods have been used to prepare layered $PdSe_2$, although many thin-film deposition techniques have proved complicated when the coating of a large surface area is required. $PdSe_2$ few layers have been obtained via mechanical exfoliation, self-flux, magnetron sputtering, direct selenization, molecular beam epitaxy, etc.

Chemical vapor deposition (CVD) is commonly used to obtain high-quality 2D materials. It enables precise control of the samples' composition, thickness, and morphology and has been widely used in the synthesis of TMDs, NTMDs, graphene, etc. The CVD technique is a versatile tool that provides large-area, single-domain sizes, chemical and structural uniformity, a protective surface coating, etc. In recent years, CVD has had a dramatic shift towards the manufacturing

industry. $PdSe_2$ films using the CVD technique were grown with high growth temperatures (~480-900 °C). Thus, when implementing flexible optoelectronic devices, growing 2D $PdSe_2$ at lower temperatures remains challenging.

Catalytic CVD growth with a pre-determined morphology is a promising way to control the layer number and the kinetics of nanostructures. Recently, catalysts such as reduced graphene oxide, nickel (Ni), sodium chloride (NaCl), and potassium chloride (KCl) salts have been employed for the controlled growth of TMDs. Among the catalysts, salts are efficient candidates for constructing an in-situ patterned structure and controlling the number of layers during CVD growth. NaCl salt has been widely used to catalyze the synthesis of TMDs due to the following unique features: (1) NaCl reduces reaction temperature significantly from very high (>1200 °C) to much lower (~700 °C) value, (2) NaCl is highly water soluble, making them easily removable without any residue after the growth, (3) NaCl can assist an H_2O-assisted polymer-free transfer technique. In the growth of $PdSe_2$, the role of the NaCl catalyst in the CVD growth needs a thorough investigation. To the best of our knowledge, to date to transfer 2D $PdSe_2$, poly methyl methacrylate (PMMA), polystyrene (PS), poly dimethyl siloxane (PDMS), and reactive etchants, such as KOH, and HF solutions have been used during the transfer process. However, due to the polymer residue, the polymer-assisted transfer techniques significantly degrade the properties and performance of ultrathin CVD-grown 2D $PdSe_2$. Therefore, developing a polymer-free transfer strategy is highly desirable for CVD-grown 2D materials besides the limitations of using hazardous chemicals.

This thesis presents a systematic study on the controlled synthesis of bilayer to multilayer $PdSe_2$, dendritic $PdSe_2$, and an in-depth understanding of NaCl and Pd catalytic growth mechanisms. A unique growth method is presented using a chemical vapor deposition (CVD) method to grow monolayer to multilayer $PdSe_2$ as well as other NTMDs (2D PdS_2, 2D $PdTe_2$) on various substrates such as mica, quartz, Si, SiO_2, glass, and on flexible substrate. Then, a systematic low-temperature Raman study was conducted to understand the phonon dynamics of the $PdSe_2$ in the temperature range of 83–295 K, which revealed the anisotropic ratios to be 1.42 and 1.28 for bilayer and few-layer $PdSe_2$, respectively. We discover the phase evolution of Pd_2Se_3 from the $PdSe_2$ under the uniaxial tensile strain. This unique strain-induced phase modulation property enables the application of ultrathin $PdSe_2$ as a future strain sensor. Two unique chemical etchant-free transfer techniques are also presented to transfer $PdSe_2$ and various 2D materials. As

a new material in the TMD family, we then focused on $PdSe_2$ applications in multiple fields. Surprisingly, $PdSe_2$ revealed its great potential in SERS and Biosensing. We have investigated a benign thermally responsive method of scrolling bilayer $PdSe_2$ into nanoribbons and unscrolling to form a sheet. We highlight the applicability of $PdSe_2$ scrolls by encapsulating live cancer cells into the nanoscrolls, where Pd nanoparticles attack the cancer cells, leading to nuclear arrest and death.

We believe these studies are significant in understanding the synthesis of NTMD materials, catalytic growth, scrolling and unscrolling of bilayer $PdSe_2$, chemical reactive etchant free transfer method, and applications in the field of strain sensor, SERS, Cancer biology, foldable electronics, biosensing, and thermally active robots. The complete thesis work has been organized into seven chapters, as detailed below:

Chapter 1:

This chapter briefly introduces NTMDs and 2D $PdSe_2$ with reported research on crystal structure, unique, extraordinary properties, different synthesis routes, and applications in various areas. It ends with stating the challenges in the research on 2D $PdSe_2$ and the focus of the present thesis.

Chapter 2:

This chapter briefly introduces CVD synthesis techniques to synthesize 2D PdX_2 (X: S, Se, Te) on various substrates. Using a chemical vapor deposition (CVD) method in a tube furnace system, monolayer to multilayer $PdSe_2$ was grown on numerous substrates with and without pre-treatment of NaCl under a moisture-controlled gas flow. The growth results with different conditions were compared.

1. **Without NaCl pre-treatment:** The CVD-grown samples with no NaCl pre-treatment show the conventional, irregular 2D $PdSe_2$ flakes on different substrates such as mica, Si, quartz, and sapphire substrates with thicknesses ranging from 3 -13 nm.
2. **With NaCl pre-treatment:** It results in dendritic $PdSe_2$, b- directional growth. We have conducted salt solution-assisted CVD growth of bilayer (2L) $PdSe_2$ on a freshly cleaved

mica surface, which involved two steps: (1) pre-CVD patterning and (2) post-CVD growth of 2L $PdSe_2$ from the edge of the dendrite.

3. **Growth of NTMDs:** Furthermore, we have tested the general applicability of this growth method by conducting the growth of other NTMDs (2D PdS_2, 2D $PdTe_2$). In 2D PdS_2 and 2D $PdTe_2$, desired patterned dendrites could be grown, indicating the versatility of this technique.

Additionally, we described the formation of the 2D $PdSe_2$-Pd_2Se_3 atomic junction, which is responsible for very high SERS activity compared to the 2D $PdSe_2$. Density functional theory calculation shows that the $PdSe_2$-Pd_2Se_3 junction has a metallic property accountable for the high SERS sensitivity. The SERS spectrum of MB molecules at the $PdSe_2$-Pd_2Se_3 region decorated with Pd NPs shows the highest enhancement factor. The mechanism of SERS enhancement is further explained through Finite element method (FEM) simulation and Raman mapping.

We also studied different transfer techniques, including a method to fabricate $PdSe_2$ with a water-soluble NaCl sacrificial layer below. Then, $PdSe_2$ can be transferred from the mica substrate to any other substrate by immersing the sample in a water bath and dissolving the NaCl sacrificial layer. The NaCl sacrificial layer effectively prevents cross-contamination between the substrates and maintains chemically clean surfaces after the transfer. Here, we have successfully transferred the as-grown $PdSe_2$ from the parent substrate mica to any arbitrary substrate with the help of two transfer techniques: (1) H_2O-assisted transfer and (2) Scotch-tape transfer.

1. **H_2O-assisted transfer:** The H_2O-assisted transfer technique is much more convenient than the usual polymer-assisted transfer process. In this work, we took advantage of the presence of NaCl-salt and consequently adopted a water (H_2O) assisted transfer technique that didn't involve any polymer throughout the delamination process. A critical delamination process has been recorded for a clear demonstration of the efficacy of the transfer process, and it is indeed speedy (within a few seconds) and a facile technique. During this process, an H_2O film bridges the $PdSe_2$ layer to the inner edges of the mica and pulls it away from the mica surface. At the H_2O/$PdSe_2$ interface, the driving force originates from the out-of-plane shear, where the shear stress is normal to the $PdSe_2$ surface. Due to the high surface tension of H_2O (72 mNm^{-1}), the thin $PdSe_2$ film is successfully isolated and floated freely on the water surface. The H_2O membrane stretches until the whole $PdSe_2$ layer is lifted from the

mica surface. We have not used any polymer throughout the delamination process; thus, our process is contamination-free. The structural integrities of $PdSe_2$ dendrite detached from the growth substrates were characterized and confirmed by Raman spectroscopy. Raman spectra of $PdSe_2$ transferred on SiO_2 show all the characteristic Raman modes that exhibit higher intensity than mica, indicating a high-quality transfer of $PdSe_2$ and its adhesion with the SiO_2 substrate. After transfer, the remaining $PdSe_2$ is confirmed from the corresponding Raman spectra.

2. **Scotch-tape transfer:** A piece of thermal release tape (TRT) was gently pressed onto the $PdSe_2$/ substrate stack and mechanically peeled, delaminating the TRT/ $PdSe_2$ stack from the growth substrate, causing the $PdSe_2$ film to delaminate from the underlying growth substrate (mica). As the growth substrate has a NaCl sacrificial layer, during the transfer process, the NaCl layer below $PdSe_2$ helps detach $PdSe_2$ from the mica substrate and pull it away from the mica surface. The stack is then pressed onto the target substrate. Subsequently, 70 °C heat is applied, allowing for easy TRT removal and leaving behind the $PdSe_2$ film on the target substrate.

These two transfer techniques are significant for transferring various 2D materials without chemical residues.

Chapter 3:

This chapter presents a temperature-dependent Raman study, determination of the thermal conductivity and in-plane anisotropic ratio of low-temperature CVD-grown $PdSe_2$ using unpolarized laser excitation. Herein, we present the low-temperature (250–290 °C) chemical vapor deposition (CVD) growth of an air-stable atomically thin $PdSe_2$ layer and study its Raman temperature coefficients, anisotropy ratio, and thermal conductivity as a function of the layer thickness. Optical microscopy (OM), atomic force microscopy (AFM), and micro-Raman analyses confirm the growth of ultrathin sheet-like bilayer and ribbon-like few-layer $PdSe_2$ on a mica substrate. A low-temperature Raman study has been conducted to understand the phonon dynamics of the as-grown $PdSe_2$ in the temperature range of 83–295 K. This work opens up a new avenue for calculation of the anisotropic ratio without using a polarized laser, which is significant for

designing new functional materials. The temperature-dependent Raman data analysis revealed the anisotropic ratios to be 1.42 and 1.28 for bilayer and few-layer $PdSe_2$, respectively.

Chapter 4:

This chapter presents a novel surface-enhanced Raman spectroscopy (SERS) application of dendritic defective $PdSe_2$. SERS is a potent tool for identifying molecular species and has relied mostly on noble metal-based substrates to obtain a high enhancement factor. Here, we demonstrate that intrinsic defects in 2D $PdSe_2$ dendrites grown at low temperatures (280 °C) act as hotspots for high SERS enhancement. We grow 2D dendritic $PdSe_2$ with ample intrinsic defects to exploit it for SERS application. X-ray photoelectron spectroscopy (XPS) analysis reveals 9.3% outer layer and 4.7% interior Se vacancies. A detailed examination of atomic-scale defects revealed Se vacancy (V_{Se}) coupled with Se–Pd–Se vacancy ($V_{Se\text{-}Pd\text{-}Se}$) in monolayer $PdSe_2$ and an array of line defects (Se vacancies) and nanopores in bilayer $PdSe_2$ dendrites. Interestingly, our studies reveal that Se vacancy-rich $PdSe_2$ gives rise to line defects that act like hotspots for SERS enhancement. Remarkably, the vacancy-rich dendritic $PdSe_2$ shows a SERS enhancement factor $>10^5$ and can detect RhB at a concentration down to 10^{-8} M. We speculate that the topological line defects and the edge construction in $PdSe_2$ dendrites act as metallic wire or edge, which is partly responsible for the high enhancement in the SERS signal. The high SERS sensitivity is explained based on multiple charge transfer processes combined with the predicted metal-like behavior of the defected 2D $PdSe_2$. This metal-like behavior is fully supported by the density functional theory calculation of the electronic density of states of the defective bilayer $PdSe_2$, which remarkably exhibits metallic character.

Chapter 5:

This chapter particularizes the activity toward the scrolling and unscrolling of bilayer $PdSe_2$. Controlled scrolling in response to external environmental stimuli, such as mild temperature compatible with biological systems, is yet to be demonstrated. Such controlled water-assisted scrolling is extremely difficult to achieve with graphene, TMDs, and NTMDs. Here, we show that thermal activation in an H_2O environment can have a more marked effect on the behavior, leading to spontaneous sliding, tearing, and peeling of $PdSe_2$ from the mica substrate. The $PdSe_2$

nanoscrolls (PSNS) are formed from the edges of the bilayer $PdSe_2$ sheet. The catalytic conversion of bilayer $PdSe_2$ into PSNS via Pd nanoparticles and unscrolling into sheet structures are fully controlled under the H_2O environment. The structures are characterized using spectroscopy and microscopy. We highlight its applicability by encapsulating live cancer cells, where Pd nanoparticles attack the cancer cell, leading to cancer cells' nuclear arrest and death.

Chapter 6:

In this chapter, we studied the strain-induced properties of $PdSe_2$ and discovered the phase transition from $PdSe_2$ to Pd_2Se_3. While the exfoliation of almost all layered materials results in a monolayer with the same atomic geometry as its bulk counterpart, the exfoliation of $PdSe_2$ presents a puzzle in a monolayer with a different nuclear geometry and a new stoichiometry, Pd_2Se_3, which is a fusion of two $PdSe_2$ monolayers mediated by Se emission. $PdSe_2$ is often transformed to Pd_2Se_3, which is discovered experimentally and computationally. Each phase has a separate and unique application as the band gap changes from indirect to quasi-direct. In addition, transfer of the ultrathin layer from a growth substrate to a desired substrate is essential for further use of the layer. Here, we develop a facile transfer method of the ultrathin film of the $PdSe_2$ layer and subsequently study the phonon responses under uniaxial tensile strain. We discover the phase evolution of Pd_2Se_3 from the van der Waal $PdSe_2$ layer under the uniaxial tensile strain of > 0.5 % in the case of water-assisted transfer and of > 0.2 % in the case of scotch tape transfer. The precise strain engineering can evolve the $PdSe_2$ layer into a Pd_2Se_3 probed by Raman fingerprints.

Chapter 7:

This chapter summarizes the work done in the thesis. It highlights our contributions to studying the controlled growth of monolayer to multilayer 2D $PdSe_2$, catalytic growth, phase change from $PdSe_2$ to Pd_2Se_3 and their applications in the field of SERS, Cancer biology, strain sensor, and thermally active robots. Finally, the outlook for future studies on different NTMDs such as $PdSe_2$, PdS_2, and $PdTe_2$ is presented.

LIST OF PUBLICATIONS

Journal Papers (Thesis relevant)

1. Tadasha Jena, Md Tarik Hossain, P. K. Giri, Temperature-dependent Raman study and determination of anisotropy ratio and in-plane thermal conductivity of low-temperature CVD grown $PdSe_2$ using unpolarized laser excitation, J. Mater. Chem. C 9, 16693-16708 (2021).
2. Tadasha Jena, Md Tarik Hossain, Upasana Nath, Hiroshi Sugimoto, Minoru Fujii, Manabendra Sarma, P. K. Giri, Evidence for intrinsic defects and nanopores as hotspots in 2D $PdSe_2$ dendrites for plasmon free SERS substrate with a high enhancement factor, NPJ 2D Mater. Appl. 7, 8 (2023).
3. Tadasha Jena, Garima Choudhary, Md Tarik Hossain, Upasana Nath, Manabendra Sarma, P. K. Giri, Salt-Catalyzed Directed Growth of Bilayer Palladium Diselenide ($PdSe_2$) Dendrites and Pd nanoparticle Decorated $PdSe_2$-Pd_2Se_3 Junction Exhibiting Very High SERS Sensitivity. Chem. Mater. 2024, 36, 5922−5934 (2024).

Other publications

1. Md Tarik Hossain, Tadasha Jena, Subhankar Debnath, P. K. Giri, Defect-induced Photogating effect and its modulation in ultrathin freestanding Bi_2O_2Se Nanosheets with Visible Near-infrared photoresponse, J. Mater. Chem. C 11, 6670-6684 (2023).
2. Md Tarik Hossain, Tadasha Jena, Upasana Nath, Manabendra Sarma, P. K. Giri, Room temperature exciton formation and robust optical properties in ultrathin Bi_2O_2Se crystals on arbitrary substrates, Nanoscale 15, 11222-11236 (2023).
3. Md Tarik Hossain, Larionette P. L. Mawlong, Tadasha Jena, Abhilasha Bora, Upasana Nath, Manabendra Sarma, P. K. Giri, Interlayer Charge-Transfer-Induced Photoluminescence Quenching and Enhanced Photoconduction in Two-Dimensional Bi_2O_2Se/MoS_2 Type-II Heterojunction, ACS Appl. Nano Mater. 6, 13, 11023–11036 (2023).
4. Md Tarik Hossain, Tadasha Jena, P. K. Giri, Recent Advances in the Growth Strategies, Multifunctional Properties, and Emerging Applications of Two-Dimensional Non-van der Waals Bismuth Oxychalcogenides and Prospective Heterostructures, Small Struct., 2300511, (2024).

Manuscript under preparation

1. Tadasha Jena, Hirakjyoti Roy, Siddhartha S Ghosh P. K. Giri, Water-assisted scrolling and unscrolling of bilayer $PdSe_2$ for selective killing of cancer cells.
2. Tadasha Jena, Md Tarik Hossain, P. K. Giri, Layer-dependent Raman studies and strain-induced phase transition of bilayer $PdSe_2$ to Pd_2Se_3.

Oral/poster presentation at Conferences

1. Tadasha Jena, P. K. Giri, "Self-scrolling and unscrolling of $PdSe_2$ nanoscrolls for selective killing of cancer cells via nucleus arrest", (**ICANN 2023, IIT Guwahati, India**) Oral.
2. Tadasha Jena, P. K. Giri, "Defects in 2D $PdSe_2$ dendrites as hotspots towards plasmon-free SERS sensing", (**RIC 2023, IIT Guwahati, India**) Oral.
3. Tadasha Jena, Md Tarik Hossain, P. K. Giri, Line defects and nanopores as hotspots in dendritic $PdSe_2$ towards plasmon free SERS substrate (**2D TMDs 2023, Cambridge, UK**) Poster.
4. Tadasha Jena, P. K. Giri, Optical studies on thermal conductivity and anisotropic ratio calculations using unpolarized laser excitation in low-temperature CVD grown two dimensional $PdSe_2$ (**NERC-2022, IIT Guwahati, India**) Oral.
5. Tadasha Jena, Md Tarik Hossain, P. K. Giri, Low temperature CVD growth and optical characterization of 2D few layer $PdSe_2$ on arbitrary substrates, International Conference on Materials for the Millennium (**MATCON-2021, Cochin University, India**) Poster.

Conference/Workshops attended

1. '8^{th} International conference on Advanced Nanomaterials and Nanotechnology - **ICANN 2023**, November 29 – December 1, 2023, IIT Guwahati, India.
2. Research & Industrial Conclave-Integration 2023 - **RIC 2023**, May 14 - 16, 2023, IIT Guwahati, India.
3. International Conference on 2D Transition Metal Dichalcogenides - **2D TMDs 2023**, June 26 - 29, 2023, University of Cambridge, United Kingdom.
4. North-East Research Conclave and Assam Biotech Conclave 2022 - **NERC 2022**, May 20 - 22, 2022, IIT Guwahati, India.

5. Virtual scientific lecture series jointly organized by the Indian Association for the Cultivation of Science (IACS) and HORIBA Scientific - **Optical School 2021**, September 6 - 8, 2021, Kolkata, India.
6. International Conference on Materials for the Millennium (online) - **MATCON 2021**, March 15 - 19, 2021, Cochin University of Science and Technology, India
7. DAE-BRNS 5th National Workshop on Materials Chemistry - **NWMC 2019**, November 8 - 9, 2019, Manipal University Jaipur, Rajasthan, India.

LIST OF ABBREVIATIONS

Abbreviation	Description
2D	Two dimensional
1L	Monolayer
2L	Bilayer
CVD	Chemical Vapor Deposition
$PdSe_2$	Palladium diselenide
SERS	Surface Enhanced Raman Scattering
NTMDs	Noble transition metal dichalcogenides
AFM	Atomic force microscope
EDX	Energy Dispersive X-ray Analysis
FESEM	Field Emission Scanning Electron Microscopy
HRTEM	High Resolution Transmission Electron Microscopy
KPFM	Kelvin Probe Force Microscopy
STEM	Scanning Transmission Electron Microscopy
SAED	Selected Area Electron Diffraction
XPS	X-ray Photoelectron Spectroscopy
XRD	X-ray diffraction
RTA	Rapid Thermal Annealing
DFT	Density functional theory
NIR	Near-infrared
PL	Photoluminescence
Se_{TLU}	Top layer upper Se atom
Pd	Palladium
Pd NPs	Palladium nanoparticles
MB	Methylene blue
RhB	Rhodamine B
EF	Enhancement factor
PMMA	Poly methyl methacrylate
NaCl	Sodium chloride
PSNS	$PdSe_2$ nanoscrolls

Chapter 1 - Introduction

Since the discovery of graphene and its pioneering applications in various fields, such as optoelectronic devices, energy conversion devices, chemical and biological sensors, and high-frequency electronic and optical devices, many researchers have been attracted to the world of two-dimensional materials.[1-3] As a very stable and conducting material, graphene exhibits an immensely high thermal conductivity of ~5300 W/m. K.[4] This partly limits their applications in various fields and led to the search for alternative 2D materials, such as hBN, black phosphorous, and group IV-X TMDs.[5-13]

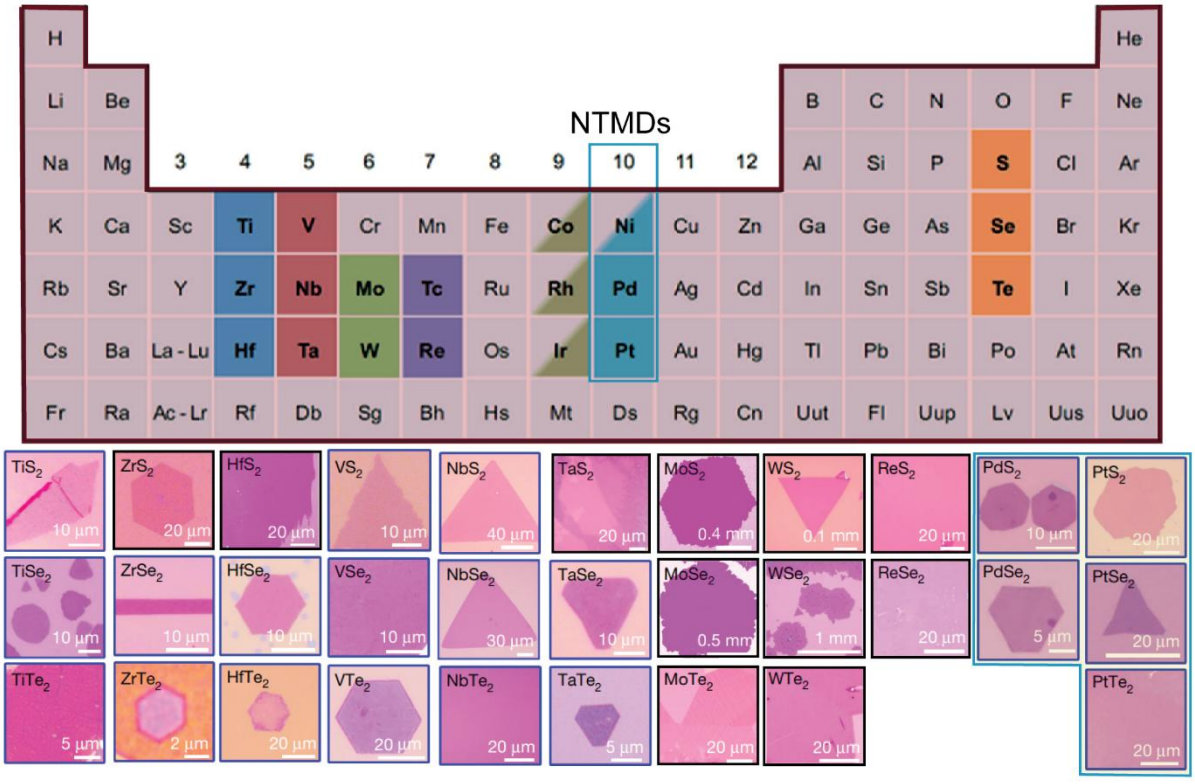

Figure 1.1 Overview of metals and chalcogens associated with TMDs and NTMDS (adopted from Ref[14]) and their Optical images.

The commonality between graphene and most other 2D materials is that they are mostly symmetric due to their isotropic lattice structure. Over the past decade, several experimentally reachable 2D materials exhibit in-plane isotropic behavior.[15] However, in 2014, the discovery of black phosphorous (BP) as an anisotropic material pinned scientists to search for alternative materials exhibiting anisotropic behavior.[16] This characteristic of BP ignites a new era of 2D materials with

low-symmetry structures and in-plane anisotropic properties. On this basis, they offer more affluent and more unique low-dimensional physics compared to conventional isotropic 2D materials, thus providing a fertile ground for novel applications, including electronics, optoelectronics, molecular detection, thermoelectric, piezoelectric, and ferroelectric concerning in-plane anisotropy. In this revolutionary track, noble transition metal dichalcogenides (NTMDs) provide a fertile ground for many applications.[17-23] 2D $PdSe_2$, a relatively new member in the NTMD family, has outstanding properties such as high air stability, making it uniquely favorable for electronics, medical, energy, sensor, SERS, and artificial synapse applications. An overview of metals and chalcogens associated with TMDs and NTMDS and their optical images are given in **Figure 1.1**.

1.1. Properties of $PdSe_2$

1.1.1. Crystal structure of $PdSe_2$

$PdSe_2$ has an uncommon structure, where Pd atoms coordinate with four Se atoms, forming a square backbone network with two Se atoms at the top and two Se atoms at the bottom. The two Se atoms located in the top and bottom planes of the $PdSe_2$ structure form a tilted Se-Se dumbbell crossing the Pd layer (shown in **Figure 1.2**), which results in the lack of rotational symmetry. $PdSe_2$ adopts a puckered pentagonal structure with an orthorhombic lattice.[24]

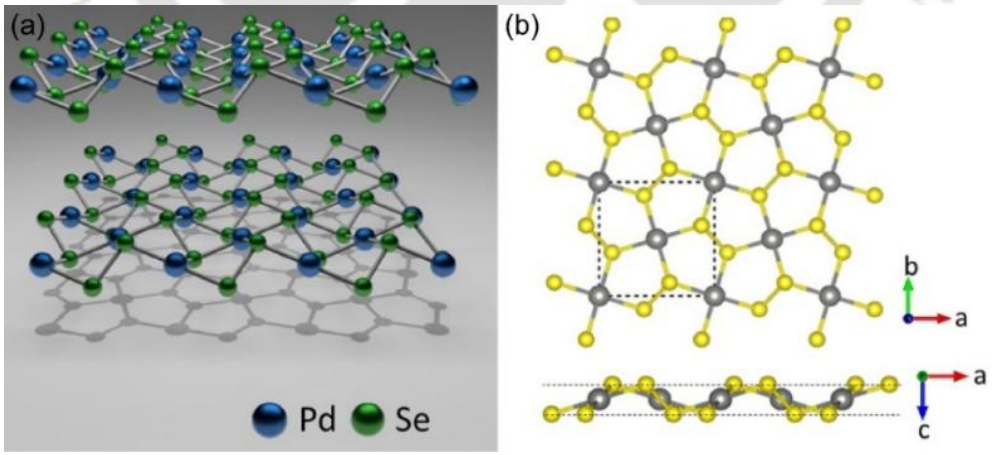

Figure 1.2 (a) Crystallographic structure of $PdSe_2$. (b) The top and side views of the crystal structure of monolayer $PdSe_2$.(Adopted from Ref[20])

Pentagons are usually treated as topological defects or geometrical frustrations. Bulk $PdSe_2$ crystallizes in an orthorhombic structure with space group Pbca, with a unit cell of a = 5.7457 Å,

b = 5.8679 Å, and c = 7.6976 Å. The 2D Se-Pd-Se layers are stacked by van der Waals (vdW) interactions, and one unit cell contains two $PdSe_2$ layers.[25] In each layer, Pd traces at the center of the square while Se occupies the vertices. The bond length between the intralayer Pd and Se atoms takes the value of 2.49 Å.

1.1.2. 2D $PdSe_2$ puzzle

While the monolayer of almost all layered materials has the same atomic stoichiometry as its bulk counterpart, the monolayer of bulk $PdSe_2$ is not $PdSe_2$. The monolayer of $PdSe_2$ has a different atomic stoichiometry similar to Pd_2Se_3, which is a fusion of two $PdSe_2$ monolayers. The formation of the Pd_2Se_3 monolayer has its roots in Se vacancies in the $PdSe_2$ system. In most 2D layered materials, such as graphene and TMDs, the layers interact only through weak van der Waal forces, even in the presence of defects. In contrast, for $PdSe_2$, Se vacancies reduce the distance between layers, causing the melding of two layers into one, resulting in the formation of the new atomic stoichiometry Pd_2Se_3 (**Figure 1.3**).[26]

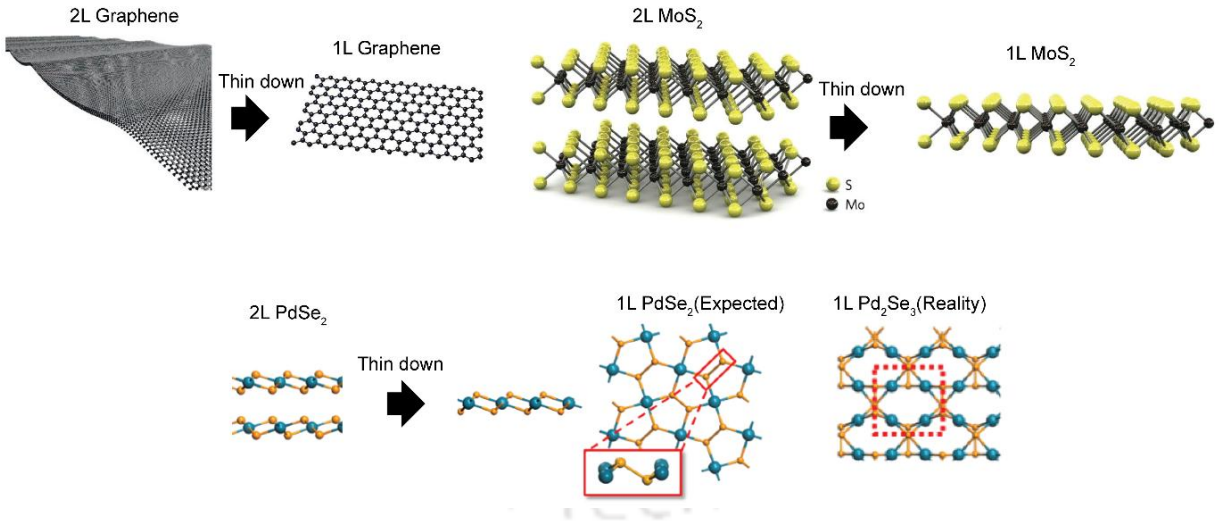

Figure 1.3 The Thinning down of graphene and MoS_2 results in the exact stoichiometry as their bulk counterparts, whereas the thinning down of $PdSe_2$ consequences a new stoichiometry 1L Pd_2Se_3 (Adopted from Ref[26])

1.1.3. Band structure of 2D $PdSe_2$

$PdSe_2$ is one of these novel 2D noble-metal dichalcogenides known for its remarkable layer-dependent electronic structure. Monolayer $PdSe_2$ is predicted to be an indirect band gap

semiconductor with a band gap of 1.3 eV, while the bulk exhibits a band gap of 0.03 eV. The 1.3 eV indirect band gap for a monolayer is quite close to its direct band gap of 1.43 eV, making it promising for optoelectronic applications. Similar indirect band gaps are observed in few-layer $PdSe_2$ as well, indicating the intrinsic nature of this indirect band gap semiconductor. The valence band maximum (VBM) is located between the high-symmetry Γ and X points, while the conduction band minimum (CBM) is located between Γ and M points. The inset of **Figure 1.4** shows the rectangular shape of the first Brillouin zone of bulk $PdSe_2$.[20]

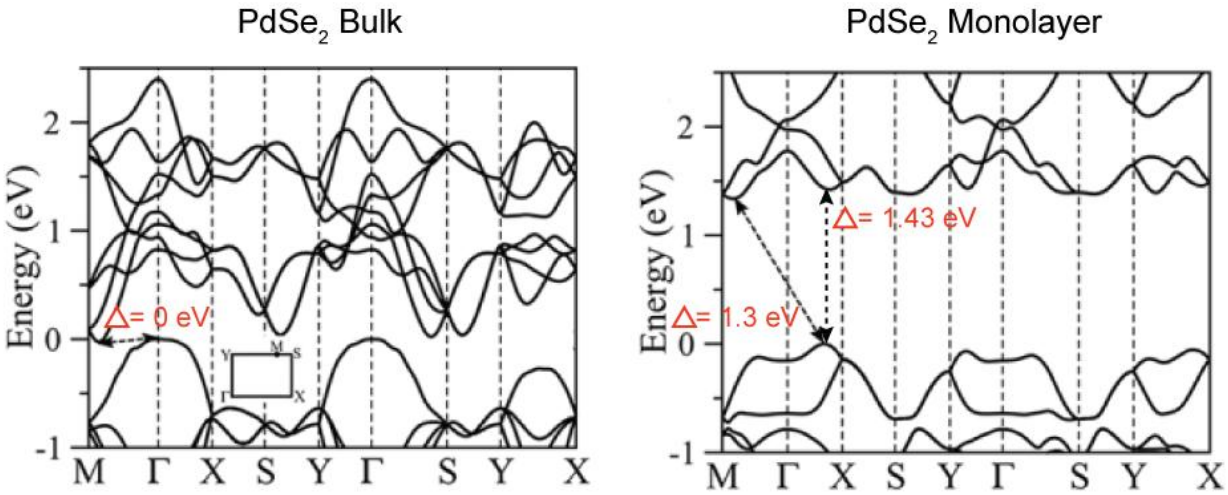

Figure 1.4 Band structures of bulk and monolayer $PdSe_2$ (Adopted from Ref[20])

1.1.4. In-plane anisotropy

2D $PdSe_2$, a member of the NTMD family, exhibits in-plane anisotropy, which enables the unique electrical, optical, and thermoelectric properties of the material. Because of the anisotropic pentagonal structure, the electrical, mechanical, and optical properties of $PdSe_2$ are also anticipated to exhibit in-plane anisotropy. For bulk $PdSe_2$, only the A_g and B_{1g} phonon modes with in-plane vibrations are Raman-active in the backscattering geometry. Polarization-resolved Raman measurements provide a non-destructive optical measurement for identifying the crystallographic orientation of the few-layer samples.

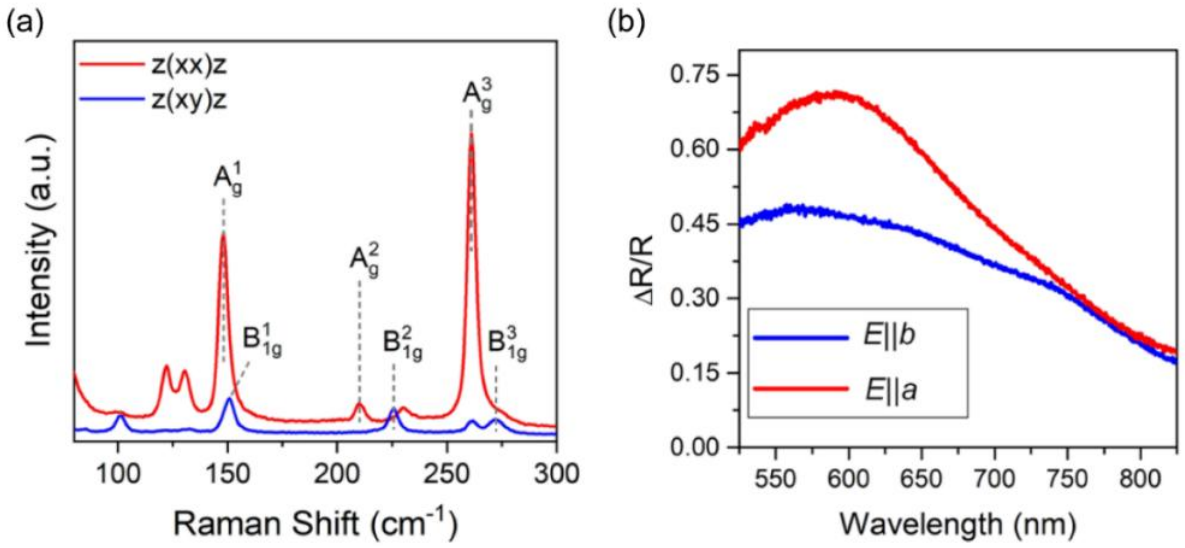

Figure 1.5 Polarization-resolved (a) Raman spectra, (b) optical reflection spectra of the 4L $PdSe_2$ flake with polarization along a (red) and b (blue) crystallographic axes. (Adopted from Ref[24])

Figure 1.5a shows the Raman spectra acquired from a 2D $PdSe_2$ in the $z(xx)\bar{z}$ and $z(xy)\bar{z}$ measurement configurations. **Figure 1.5b** shows the optical contrast spectra for the $PdSe_2$ crystal with polarization along a and b axes. Linear dichroism occurs in the visible range from 500 to 700 nm with an anisotropic ratio up to ~1.5 at 600 nm.

1.1.5. Raman spectra of 2D $PdSe_2$

Raman spectroscopy is a non-invasive and powerful tool to characterize the crystal phase and structure and is an excellent approach to determining the layer number of various 2D materials. Through analyzing the Raman spectra in $PdSe_2$, the layer number of a thin sample can be identified quickly, precisely, and non-destructively. The theoretical and experimental Raman spectra of the bulk to monolayer $PdSe_2$ are shown in **Figures 1.6a and 1.6b**. The Raman spectrum of bulk $PdSe_2$ exhibits four distinct Raman peaks at ~143, ~206, ~222, and ~256 cm^{-1}. These four Raman peaks will blueshift as the thickness decreases from multilayer to few-layer. Two additional A_1^1, A_1^2 modes were observed in the 2L- 4L layer $PdSe_2$. In 2L- 4L $PdSe_2$, it is worth affirming that the Raman peaks in the low-frequency region 60-140 cm^{-1} vary considerably.[20] The atomic vibrations of A_g^1, A_g^2, A_g^3, B_{1g}^1, B_{1g}^2, B_{1g}^3 Raman modes are illustrated in **Figure 1.6c**. It is interesting to point out that all of them mainly involve the vibrations of the Se atoms.

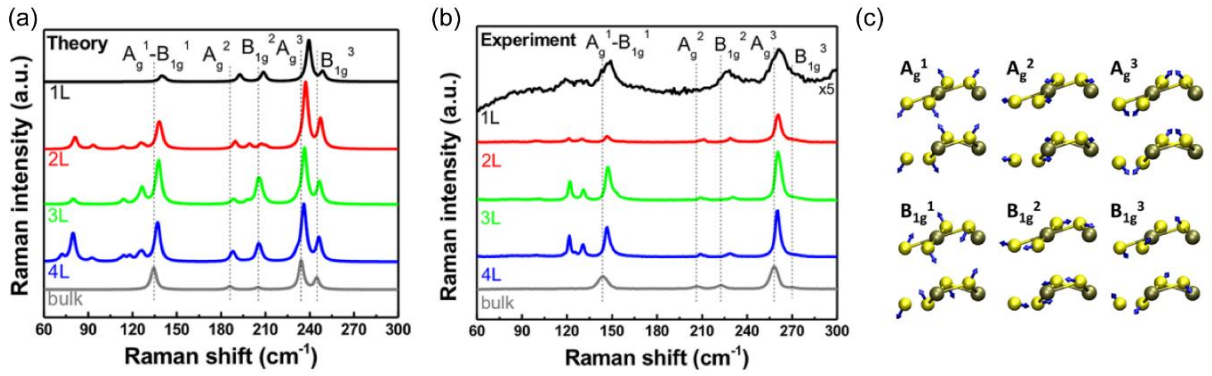

Figure 1.6 (a) Theoretical and (b) Experimental Raman spectra of $PdSe_2$ from 1L to bulk. (c) Atomic displacements of six Raman modes in bulk $PdSe_2$. (Adopted from Ref[20])

1.1.6. Defect-induced and phase transformation properties

The unique puckered pentagonal structure of $PdSe_2$ possesses imperfect rotational symmetry, resulting in high defect sensitivity, particularly Se vacancies, which facilitates the occurrence of different phase transitions.[27] The natural cleavage surface of $PdSe_2$ is never defect-free. Many interesting physical properties originate from the existence of various defects in the crystal. Fu et al. reported top-layer Se atom vacancies, sublayer Pd atoms, and the intrinsic Pd and Se vacancy defects (**Figures 1.7a, 1.7b)**, which induce defect states near the Fermi level.[28] The reported nanoflakes comprised monolayer Pd_2Se_3 and bilayer $PdSe_2$, inferring that monolayer Pd_2Se_3 was thermodynamically favorable in a Se-rich environment. (**Figure 1.7c**).[29] Monolayer Pd_2Se_3 is more physically stable than monolayer $PdSe_2$. Chen et al. reported the phase transition of the few-layer $PdSe_2$ films to Pd_2Se_3 monolayers by heating to 350 °C at the in-situ heating holder loaded in STEM (**Figure 1.7d**).[30] **Figure 1.7e** shows that the exfoliation of $PdSe_2$ from bulk results in tri-layer and bi-layer $PdSe_2$. Unexpectedly, the monolayer $PdSe_2$ changed its stoichiometry to Pd_2Se_3 and has its roots in the vacancies in the $PdSe_2$ system.[26] Such a feature is absent in conventional TMDs: WS_2, MoS_2, and $MoSe_2$. Further, Zuluaga et al. reported that the exfoliated $PdSe_2$ changed its geometry to Pd_2Se_3, a fusion of two $PdSe_2$ monolayers mediated by Se emission (**Figure 1.7f**).[31] A phase transformation from $PdSe_2$ to Pd_2Se_3 for creating 2D striated lattice systems is revealed in **Figure 1.7g**; where controlled thermal annealing induces Se loss in few-layered $PdSe_2$ which leads to $PdSe_{2-x}$, which results in Pd_2Se_3.[32]

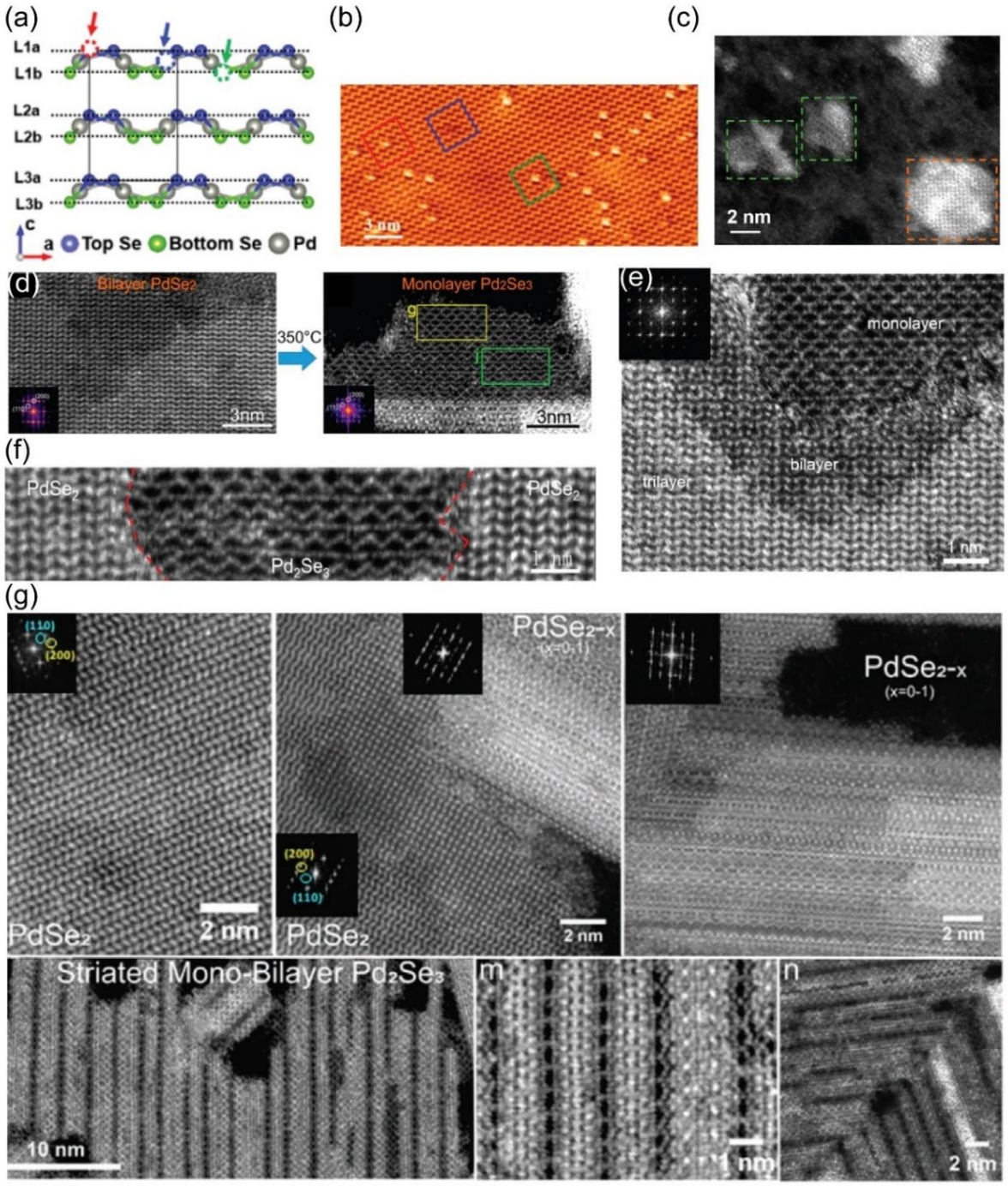

Figure 1.7 (a) Side view of the lattice structure of $PdSe_2$ (b) STM topographic image of $PdSe_2$ surface, where defects are outlined (Adopted from Ref[28]) ADF-STEM image showing the (c) as-grown sample consisting of $PdSe_2$ and Pd_2Se_3 nanoflakes, where $PdSe_2$ and Pd_2Se_3 are marked as orange dotted and green dotted rectangles, respectively. (Adopted from Ref[29]), (d) the phase transformation from a few-layer $PdSe_2$ to monolayer Pd_2Se_3 with in situ heating at 350 °C. (Adopted from Ref[30]). (e) the few layers of exfoliated $PdSe_2$ region, where the monolayer possesses different stoichiometry. (Adopted from Ref[26]) (f) STEM image shows two regions: $PdSe_2$ bilayer and Pd_2Se_3 monolayer. (Adopted from Ref[31]). (g) ADF-STEM images show the intermediate phase transition states from $PdSe_2$ to Pd_2Se_3. (Adopted from Ref[32])

1.1.7. Other inherent properties

Carrier transport characteristics and carrier mobility

Field-effect transistors (FETs) based on TMDs have demonstrated high current on−off ratios and sizable carrier mobility.[33] However, the reported mobility values are still far below the predicted intrinsic mobility,[34] primarily due to poor metal contacts. $PdSe_2$, owing to their predicted high carrier mobility (up to $\sim 10^3$ cm^2 V^{-1} s^{-1})[35]. FETs based on few-layer $PdSe_2$ have shown high electron mobility ($\sim$216 and$\sim$158 cm^2 V^{-1} s^{-1}) [19,20] and high current on/off ratios, demonstrating their potential in electronic devices. $PdSe_2$-based photo-detectors have revealed an ultra-broad band extending from visible to mid-infrared and unique anisotropic responses.[36]

Air stability of $PdSe_2$

DFT calculations for the binding energies of physisorbed H_2O and O_2 on pristine monolayer $PdSe_2$ results appreciable electron transfers per adsorbed molecule from the surface.[37] A pristine $PdSe_2$ device behaving n-type, after short-term (<160 h) ambient aging effect exhibits a decrease in n-type conduction and increase in p-type conduction. The aging is arrested by placing it in vacuum condition, confirming the ambient exposure affects the electrical behaviour. Longer term aging (>430h) produces a complete suppression of the n-type conduction and an increase in the p- DFT calculations for the binding energies of physisorbed H_2O and O_2 on pristine monolayer $PdSe_2$ result in appreciable electron transfers per adsorbed molecule from the surface.[37] A pristine $PdSe_2$ device behaving n-type, after a short-term (<160 h) ambient aging effect, exhibits a decrease in n-type conduction and an increase in p-type conduction. The aging is arrested by placing it in a vacuum condition, confirming that ambient exposure affects the electrical behavior. Longer-term type conduction. This long-term aging is ascribed to a dissociative O_2 chemisorption, where PdO_2 is formed. However, the PdO_2 is volatile at low temperatures and thus can be sublimated with a low-temperature anneal. The sublimation of the PdO_2 formed on the devices decreases the p-type conduction and restores some n-type conduction. Any short-term aging in $PdSe_2$ devices in atmospheric conditions can be reversible.

Mechanical properties

The monolayer $PdSe_2$ is a very ductile material. Large deformation causes nonlinearity of the strain−stress relation, and ultra-large deformation sometimes leads to plastic deformation or

fracture. Under large deformation, mechanical nonlinearity causes significant changes in Young's modulus. The Young's modulus for $PdSe_2$ demonstrates a non-linear performance, meaning the Young's modulus has a slightly reducing trend, representing the material softening property.[23]

1.2. Synthesis of 2D $PdSe_2$

1.2.1. Chemical vapor deposition

Three-zone CVD

The growth of 2D $PdSe_2$ flakes were reported by an ambient-pressure CVD method in a three-zone tube furnace. Pd powder (35 mg) and Se powder (500 mg) were selected as precursors and were put in the central zone. The upstream zone of a three zones furnace, respectively, with the substrate in the downstream zone of the furnace (**Figure 1.8**). Argon gas of 600 sccm was filled to the tube furnace for 10 minutes to clean the O_2 gas before heating. The temperature of the Se and Pd sources were kept at 450 °C and 815 °C, respectively. The reaction was conducted for 30 minutes with 90 sccm. After the reaction was finished, the tube furnace was naturally cooled to room temperature.[38]

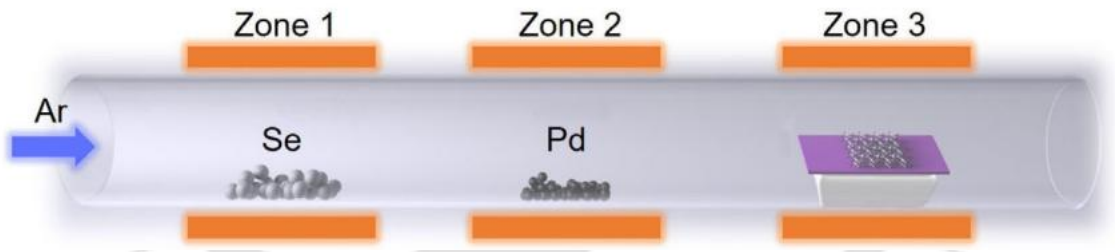

Figure 1.8. Schematic of the CVD synthesis process for $PdSe_2$ sheets. (Adopted from Ref[38])

1.2.2. Solution assisted CVD

Instead of Pd powder as the Pd source, $PdCl_2$ solution is used here. $PdSe_2$ is synthesized using $PdCl_2$ solution and Se powder as source precursors. $PdCl_2$ is first dissolved in deionized water to form a saturated solution. The substrate is spread with the $PdCl_2$ solution and then dried at 80 °C on a hot plate. The Se powder and the substrate were placed at the center of the quartz tube and heated to 300 °C to grow $PdSe_2$ for 10 mins. [24]

1.2.3. NaCl assisted CVD

NaCl-assisted CVD has been widely used to synthesize TMDs due to the following unique features:

(1) NaCl reduces reaction temperature significantly.

(2) NaCl is highly water-soluble, making it easily removable without residue after the growth.

(3) NaCl can assist a large area of growth.

Powders of Se and $PdCl_2$/NaCl (10 mg and 1 mg) were used as sources. Se powder (350 ℃) was put upstream, and $PdCl_2$/NaCl powders (850 ℃) were placed in the center of the furnace with mica put above them as growth substrate (shown in **Figure 1.9**).[39]

Figure 1.9. Schematic showing the NaCl assisted Synthesis of $PdSe_2$ flakes on mica substrate by APCVD. (Adopted from Ref[39])

1.2.4. CVD on gold foil

2D $PdSe_2$ was grown on Au foils using a three-zone tube furnace under atmospheric pressure. $PdCl_2$ power mixed with NaCl powder in a quartz boat was located at the center, and Se powder was located upstream of the furnace, with Au foils placed above the $PdCl_2$/NaCl mixture. The temperature of the Se powder and $PdCl_2$/NaCl mixture with Au foils were set at 400 °C and at 850–900 °C respectively.[40]

1.2.5. Self-flux method

Bulk $PdSe_2$ single crystals were grown by a self-flux method through melting stoichiometric amounts of Pd powder and Se powder. The palladium and selenium powder were mixed with an atomic ratio of Pd: Se = 1:2 and further compressed into tablets. The tablets were placed into a quartz tube sealed under 10^{-5} mbar. After that, the sealed quartz was set in a muffle furnace and

gradually heated in steps to the synthesis temperature of 1100 K. Then, it was held at this temperature for 78 h to grow $PdSe_2$ crystal bulk. The $PdSe_2$ nanosheets can then be obtained by exfoliating the $PdSe_2$ bulk with the aid of an ultrasonic wave (shown in **Figure 1.10**).[41]

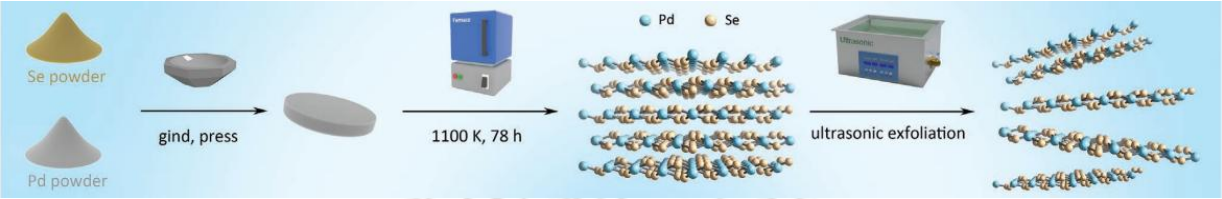

Figure 1.10. Schematic showing the synthesis of $PdSe_2$ flakes by self-flux method. (Adopted from Ref[41])

1.2.6. Mechanical exfoliation method

Bulk $PdSe_2$ was synthesized using self-flux and CVD methods. $PdSe_2$ thin flakes were mechanically exfoliated from the bulk $PdSe_2$ using blue tape, adhesive tape, and polydimethylsiloxane stamp.[20,42,43]

1.2.7. Liquid phase exfoliation

The preparation process is provided in **Figure 1.11** and described as follows: 10 mg $PdSe_2$ bulk powder is added into 100 ml of ethanol for soaking for about 96 hrs. The soaked solution is kept under ice-bath sonication for 24 hrs. Next, the suspension is centrifuged for 30 minutes at 5000 rpm to attain a few-layered $PdSe_2$ nanosheet dispersion.

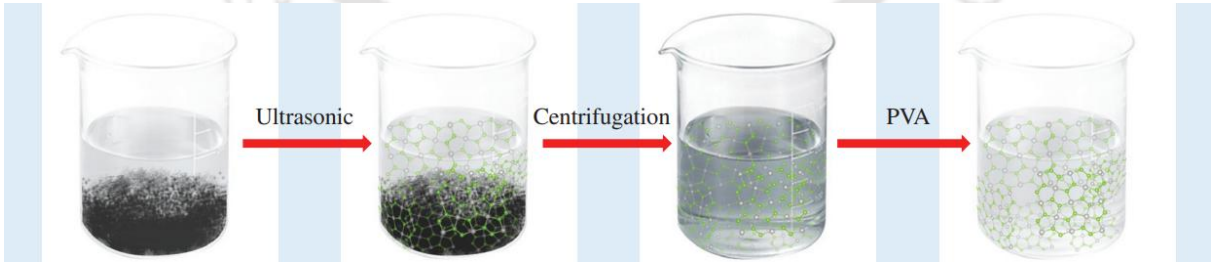

Figure 1.11. Schematic showing the synthesis of $PdSe_2$ flakes by ultrasonication. (Adopted from Ref[44])

Finally, the dispersed $PdSe_2$ nanosheets are mixed with 100 ml of 5 wt% polyvinyl alcohol (PVA) solution and placed in the ultrasonic cleaner for another six h to obtain a uniform $PdSe_2$-PVA solution.[44]

Table 1.1. Summary of the important growth parameters, substrate used, thickness, advantages, and limitations of the discussed growth techniques.

Growth Techniques	Growth Parameters	Thickness (nm)	Advantage	Limitation
CVD 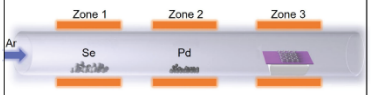	Pd: 35 mg Se: 500 mg Pd: 815 °C Se: 450 °C Ar: 90 sccm,30 min Substrate: SiO_2/Si	4-27	Sheet size: 30 μm	Growth temperature: High
NaCl assisted CVD 	$PdCl_2$/NaCl: 1 mg Se: 10 mg $PdCl_2$/NaCl: 850 °C Se 350 °C Ar: 80 sccm, 5-10 min H_2: 15 sccm, 5-10 min Substrate: mica	2.2-16.5	Sheet size: 3-28 μm	Growth temperature: High
Self-flux 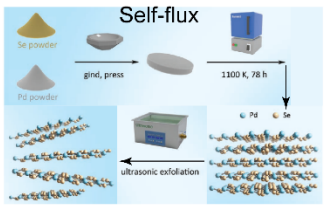	Pd+Se: 1g Pd+Se tablet 826 °C 78 hrs DMSO: 25 ml, Ultrasonication: 2 hrs.	1.65	Easy optimization	Growth temperature: High Reaction time: Long
Liquid phase exfoliation 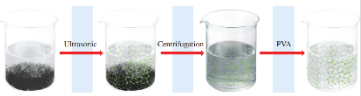	$PdSe_2$: 10 mg PVA:100 ml 96 hrs Centrifuged: 30 min, 5000 rpm Substrate: sapphire	6-12	Large scale production	Large area flake ✗
Sputtering 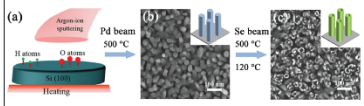	Pd beam: 500 °C Pd beam: 60 min 45 s Se beam: 500 °C and 120 °C Se beam: 3 min 16 s Substrate: Si(100)	50–60	Less defect Air-stable >6 months	Difficult optimization Uncontrolled nucleation

1.2.1. Sputtering

The $PdSe_2$ film was synthesized by a straightforward selenization approach. In brief, Pd metal layers were first deposited on Si substrate using a magnetron sputtering system. The as-deposited Pd films were placed at the center zone of the furnace. The base silicon was at a steady temperature of 500 °C during this process. The thickness of Pd is around 50.00 Å. The Pd beam was turned off, and the Se beam was turned on for 3 min 16 s in a steady state, which resulted in a Se film

with a thickness of around 10.00 Å. Finally, the substrate temperature was decreased to 120 °C, and then the Se beam was turned on under these conditions to grow a 10.00 Å thickness of Se stably. The pre-deposited Pd nanorods, as shown in **Figure 1.12** on a Si(100) substrate, are transformed into $PdSe_2$ nanotubes after selenization.[45] **Table 1.1.** show a comparative study on the essential parameters, substrate used, thickness, advantages, and limitations of the above-discussed growth techniques.

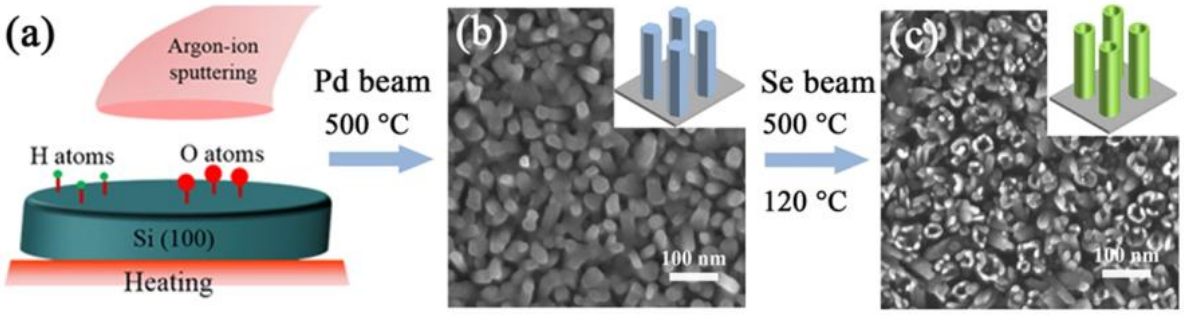

Figure 1.12. (a) Schematic showing repeatedly bombarded Si(100) substrate with argon-ion sputtering. (b) Top view of as-grown Pd nanorods and (c) $PdSe_2$ nanotubes after selenization of Pd nanorods. (Adopted from Ref[45])

1.3. Transfer of 2D Layers to arbitrary substrates

1.3.1. PMMA-assisted transfer

PMMA-assisted transfer process is commonly used to transfer $PdSe_2$.[46-48]. The as-grown $PdSe_2$ layer on the mica substrate was transferred to a Cu grid. The following steps involve the transfer of the $PdSe_2$ layer from the parent substrate to the required substrate using drop-casting of a PMMA solution and then immersion into KOH solution.

(1) The PMMA solution is drop-cast onto the $PdSe_2$ layer and then spin-coated at 1500 rpm for 60 seconds.

(2) The PMMA-adhered spin-coated sample is baked at 110 ℃ on a hot plate.

(3) Next, the dried PMMA with the immovable spin-coated $PdSe_2$ is immersed in KOH solution for 3 hours.

(4) the PMMA-coated $PdSe_2$ is dipped into a Petri dish containing distilled water to separate the $PdSe_2$ film easily.

(5) Finally, the PMMA-adhered $PdSe_2$ film is 'fished' onto a required foreign substrate. Subsequently, the $PdSe_2$-supporting foreign substrate is dipped in acetone for 6 hours to remove the PMMA layer from the $PdSe_2$ flakes.

(6) In the end, it is dried for a few hours.

This method is the most widely employed transfer technique. The PMMA residues and KOH solution partially damage the $PdSe_2$ layer quality and hamper the device's performance. Therefore, the transferred samples must be verified to confirm they are PMMA residue-free and good quality for device fabrications and subsequent applications.

1.4. Applications of 2D $PdSe_2$

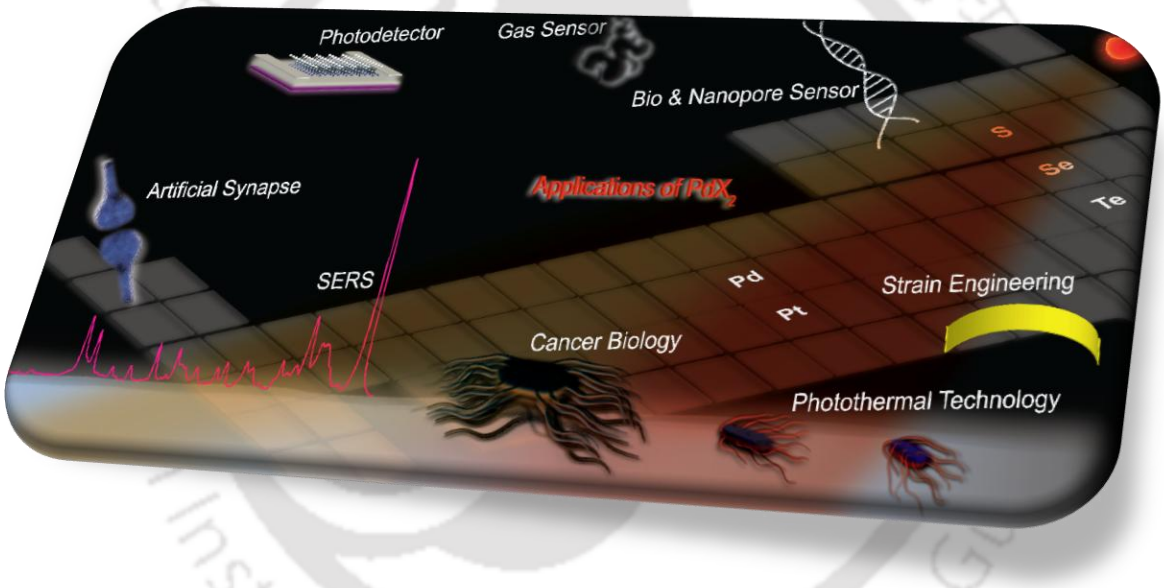

Figure 1.13. Schematic diagram showing various applications of 2D $PdSe_2$.

The remarkable air stability of $PdSe_2$ brings excellent advantages for practical applications, which is an advantage over many 2D materials suffering from fast degradation in the air. High carrier mobility[19] (up to $\sim 10^3$ cm^2 V^{-1} s^{-1}) makes $PdSe_2$ a feasible candidate for many applications, such as photodetectors, sensors, thermoelectric applications, field effect transistors, hydrogen evolution reactions, etc. (**Figure 1.13**) A few reported applications are highlighted in the following section.

1.4.1. Ultra-broadband photodetectors

This section discusses the structure and performance of different photodetectors based on 2D $PdSe_2$. Liang et al. reported a high-performance broadband photodetector based on a few-layer $PdSe_2$. The responsivity is 7.08×10^2 A $W^{-1,}$ and the detectivity is 1.31×10^9 Jones under 1064 nm laser illumination.[36] $PdSe_2$ heterojunction-based photodetectors improve their performance in photodetection. Heterojunction can effectively suppress the dark current, which makes up for enhancing the detectivity of photodetectors. Ge nanocones (GeNCs) in heterojunction photodetectors can absorb photons more efficiently. $PdSe_2$/GeNCs exhibit responsivity 530.2 mA W^{-1} and detectivity 1.45×10^{11} Jones under 1550 nm illumination.[49] The $PdSe_2$/pyramid Si heterojunction arrays, which are fabricated through simple selenization of pre-deposited Pd nanofilm, exhibit responsivity of 456 mA W^{-1} and a detectivity of up to 9.97×10^{13} Jones under 980 nm illumination at zero bias.[50] The $PdSe_2$/Si nanowire array (SiNWA) based photodetector reaches a maximum responsivity of 726 mA W^{-1} and detectivity 3.19×10^{14} Jones. Notably, the $PdSe_2$/Si NWA photodetector significantly responds to weak light signals with a broad spectral detection range from deep ultraviolet to mid-infrared.[51] $PdSe_2$/Si NWA demonstrated a high detectivity.

1.4.2. Photodetection with orientation selectivity

The pentagonal structure of $PdSe_2$ results in anisotropic electrical transport behavior. The angular-dependent behavior in the transfer curves is noticeably observed. To experimentally verify the electrical anisotropy of the $PdSe_2$ flake, angle-resolved electrical transport measurements data are provided in **Figure 1.14**. Twelve electrodes in **Figure 1.14a** have a circular distribution with identical angles, and one pair of electrodes along the b-axis is defined as a 0° reference. The optical image of the $PdSe_2$ device with a thickness of ~9.6 nm is displayed in the inset of **Figure 1.14b**. The I_{ds}-V_{ds} curves at different angles exhibit good Ohmic contact and angular dependence, proving the in-plane anisotropic behavior of the $PdSe_2$ flake.[52]

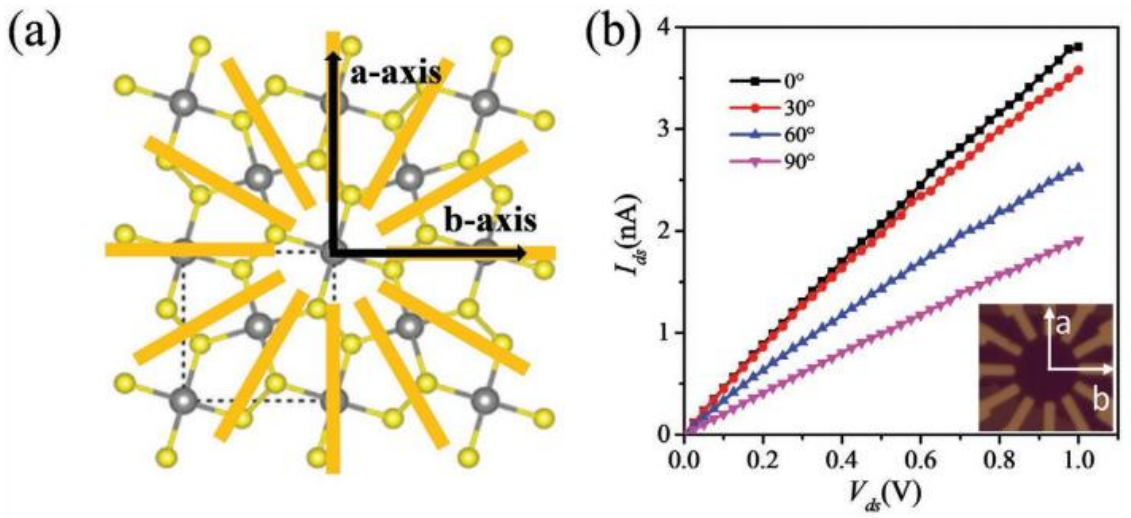

Figure 1.14. Angle-resolved electrical transport measurement: (a) Schematic view of a device structure with six pairs of electrodes spaced at 30°apart. (b) Typical output curves at different angles between different electrode pairs; inset: the optical image of a few-layer $PdSe_2$ device with a-axis and b-axis directions are labeled. (Adopted from Ref[52])

1.4.3. 2D $PdSe_2$-based sensors

Humidity sensor

Due to the large surface-to-volume ratio of the 2D $PdSe_2$ and the SiNWA, the $PdSe_2$/SiNWA heterostructure device shows high sensitivity to the surrounding atmosphere's relative humidity (RH). The humidity sensing properties of the $PdSe_2$/SiNWA heterostructure to different RH values from 11% to 95% in the dark and under 780 nm illumination, respectively, are shown in **Figure 1.15a**. It is observed that a significant current response with good stability and repeatability is achieved at each of the RH values, where I_{RH} and I_{Dry} are the currents of the sensor under humid and dry air conditions, respectively.[51]

NO_2 gas sensor

The NO_2 gas-sensing performance of the sensors based on $PdSe_2$ film and the $PdSe_2$/Si heterostructure is given in **Figure 1.15b**. Here, the sensors based on the $PdSe_2$/Si heterojunctions with thicknesses of 2, 6, 8, 14, and 28 nm of $PdSe_2$ are denoted as $PdSe_2$/Si-2, $PdSe_2$/Si-6, $PdSe_2$/Si-8, $PdSe_2$/Si-14, and $PdSe_2$/Si-28, respectively. The response increases with the increasing NO_2 concentrations from 0.1 to 5 ppm for $PdSe_2$/Si-8. In $PdSe_2$/Si heterostructure, p-type $PdSe_2$ is contacted with n-type Si from the p−n type $PdSe_2$/Si heterojunction.

Table 1.2. 2D $PdSe_2$-based Sensors showing their corresponding response properties to different RH values. (Adopted from Ref[51,53,49])

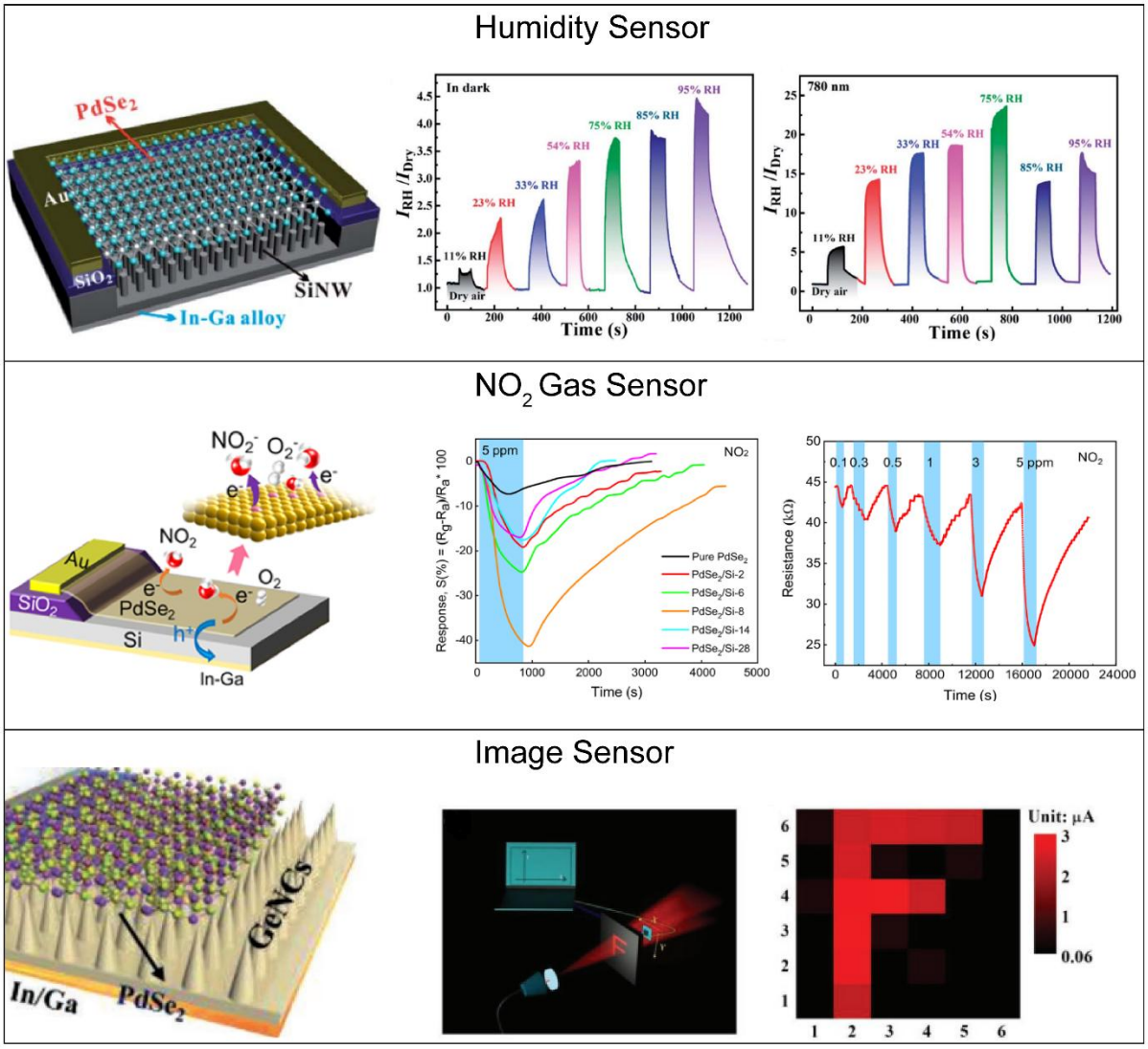

The Fermi level of Si is higher than that of $PdSe_2$; due to the difference in Fermi levels, when the two materials are connected, the electrons will diffuse from Si to $PdSe_2$, forming a depletion layer in the interfaces of the two materials. When the $PdSe_2$/Si sensor is exposed to air, the absorbed oxygen molecules can trap electrons from the $PdSe_2$ surface. The sensor based on $PdSe_2$/Si-8 heterostructure exhibited the best response of approximately 7.2% toward 100 ppb NO_2 gas.[53]

Image sensor

$PdSe_2$/ germanium nanocones (GeNCs) hybrid heterojunction photodetector can record images, essential in optical areas such as cameras and fax machines. Using the setup shown in **Figure 1.15c**, the $PdSe_2$/GeNCs can record the simple "F" image projected to the image sensor, suggesting the promising application of the $PdSe_2$/GeNCs heterojunction photodetector in future infrared optoelectronic systems.[49]

1.4.4. Other applications

$PdSe_2$ photodetector shows high responsivity from the visible-infrared to terahertz (THz) region. In the visible-infrared region, the photogenerated electron-hole pairs in the $PdSe_2$ body achieve high responsivities of 28 A W^{-1} at 405 nm, 4 A W^{-1} at 635 nm, 0.9 A W^{-1} at 1550 nm, and[36] 0.4 A W^{-1} at 1850 nm. In the THz region, $PdSe_2$ photodetectors achieved an efficient detection for THz waves under the assistance of hot carriers, with responsivities of 400 mA W^{-1} at 0.03 THz, 20 mA W^{-1} at 0.10 THz and five mA W^{-1} at 0.24 THz. The incident THz radiation heats the carriers in $PdSe_2$, and the metal electrodes act as the heat sinks, generating a temperature gradient distribution as a function of position along the channel (**Figure 1.15**).

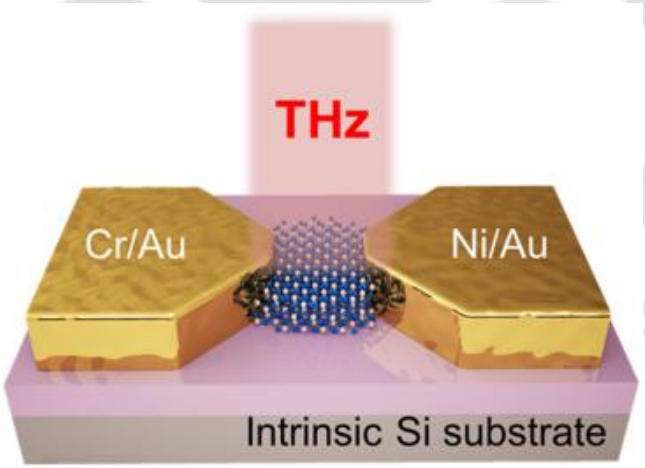

Figure 1.15. Schematic of the $PdSe_2$-based photodetector under THz illumination. (Adopted from Ref[54])

High-resolution THz transmission imaging was also performed, illustrating the potential of fast and large-area imaging applications.[54] $PdSe_2$-based photodetectors are promising for applications in remote sensing, security checking, environmental monitoring, optical communication, etc. **Table 1.3.** summarizes of the applications/properties.of some reported $PdSe_2$.

Table 1.3. A summary of reported $PdSe_2$ applications/properties.

Sample type	Growth method	Applications/properties	Key results	Ref
2D $PdSe_2$	Selenizaton	$PdSe_2$/n-Si heterojunction photodetector	Responsivity ~ 300.2 mA W^{-1}, specific detectivity ~10^{13} Jones	55
2D $PdSe_2$ /1D Si nanowire arrays	Selenizaton	Broadband (Deep UV-Mid IR) photodetector, image and humidity sensor	Responsivity of 726 mA W^{-1}, specific detectivity of 3.19×10^{14} Jones, response speed of 25.1/34 μs, polarization sensitivity of 75	51
bilayer to few-layer $PdSe_2$	Atmospheric pressure CVD	Field-effect transistors	Electron mobility up to ~ 294 cm^2 V^{-1} s^{-1}	46
Few-layer $PdSe_2$	Mechanical exfoliation	FET-based pressure sensor	Conductivity switches between n- and p-type.	42
$PdSe_2$ nanosheets	Mechanical exfoliation	Field-effect transistors	n-type transistors Electron mobility ≈20 cm^2 V^{-1} s^{-1}	56
Few-layer $PdSe_2$	Solid state reaction (850 °C)	SERS	Enhancement factor of 10^5 for R6G	57
$PdSe_2$ nanosheet	exfoliation	Memristor	Low-voltage resistive switching of $PdSeO_x$/$PdSe_2$ heterostructures	58
2D $PdSe_2$	DFT	Gas sensor	NO_2 sensing	59
$PdSe_2$ Quantum dots	Liquid phase exfoliation	Photoluminescence	Excitation wavelength-dependent behaviors and large Stokes shifts	60

1.5. Tailoring defects in $PdSe_2$

However, the presence of defects in the as grown samples represents one of the main limiting factors for commercial applications. At the same time, $PdSe_2$ properties are frequently tailored by defects. For example;

1. The optical bandgap of non-defective 2L $PdSe_2$ is 1.89 eV and that of defective 2L $PdSe_2$ is 1.55 eV.

2. The monolayer $PdSe_2$ has an indirect band gap of 2.25 eV, however after introducing Pd or Se defects, the band gaps are 1.45 and 1.91 eV, respectively.
3. Se and Pd vacancies in $PdSe_2$ can significantly improve HER performance than $PdSe_2$ without vacancies.

1.6. Challenges in 2D $PdSe_2$ research

The constitutional unit of the pentagon instead of the hexagon endows pentagonal $PdSe_2$ with distinctive properties as compared to common hexagonal 2D materials. Although some vital progress has been made, more efforts are essential to accelerate the development of $PdSe_2$ in many rapidly growing fields.

1. The quality of 2D $PdSe_2$ determines its properties and device applications. Synthesizing high-quality samples with decent control over the structural characteristics, including crystallinity, layer number, size, and phase, is still a challenge in 2D $PdSe_2$.
2. Massive production and wafer-scale growth are also vital for future practical applications. Strategies for preparing other NTMDs as well as the understanding of growth kinetics, selection of appropriate substrates, and precise control over synthesis parameters are still challenging.
3. Engineering the defects, phase, and strain in 2D $PdSe_2$ remains challenging.
4. Black phosphorous (BP), an in-plane anisotropic material, has been reported as a very promising candidate in the biomedical field. However, poor stability in ambient conditions limits its applications. Due to the great air stability of $PdSe_2$, it may replace the BP in the field of biomedicine; which needs plenty of research.
5. 2D pentagonal magnets with critical Curie temperatures above room temperature can be potential candidates for quantum computing. $PdSe_2$ with a pentagonal crystal structure is observed to possess anisotropic magnetoresistance.[61] Combining magnetic properties, strain, and stress, 2D $PdSe_2$ may find potential applications in smart structures, including nanoactuators, spintronic nanodevices, and nano-sensors, which are yet to be studied.
6. Furthermore, the construction of heterostructures of $PdSe_2$ may find cutting-edge potential in functional applications.

1.7. Scopes and objective of the present thesis

Although 2D $PdSe_2$ holds great promise for several applications, the controlled synthesis of bilayer $PdSe_2$ remains challenging. Therefore, the present dissertation started with the controlled growth of bilayer $PdSe_2$, and mainly focuses on the following:

1. CVD growth of bilayer $PdSe_2$ without pre-treatment of NaCl and dendritic bilayer $PdSe_2$ with the NaCl pre-treatment.
2. $PdSe_2$ can never be defect-free; we exploit intrinsic defects in bilayer $PdSe_2$ dendrites and $PdSe_2$-Pd_2Se_3 junction towards Surface-enhanced Raman spectroscopy (SERS) applications.
3. Estimation of in-plane thermal conductivity by non-destructive Raman measurement technique without the use of polarized lasers.
4. CVD growth of other NTMDs: PdS_2, $PdTe_2$ on mica substrate.
5. Phase evolution of $PdSe_2$ by strain engineering.
6. Scrolling and unscrolling of bilayer $PdSe_2$ for selective killing of cancer cells via attacking filopodia.
7. Polymer-free transfer techniques for 2D PdSe2 to arbitrary substrates.

1.8. Organization of thesis

The thesis work contains seven chapters.

Chapter 1 briefly introduces 2D $PdSe_2$ with reported research on crystal structure, unique, extraordinary properties, different synthesis routes, and applications in different areas. It ends with stating the challenges in the research on 2D $PdSe_2$ and the focus of the present thesis.

In **Chapter 2**, we discuss the successful synthesis of 2D layered PdX_2 (X: S, Se, Te) on varieties of substrates by adopting a bottom-up chemical vapor deposition technique at relatively low temperatures (250-310 °C). Several structural and optical studies have confirmed the morphology of as-grown $PdSe_2$ over a large area. We developed a novel low-cost salt solution-assisted catalytic growth of dendritic strictly bilayer $PdSe_2$ and other NTMDs on mica substrate. The pinned contact line and electrostatic force play an important role in the dynamics and evolution of dendritic structure, which is catalyzed by NaCl. The orientation of the dendrite is primarily guided by the NaCl crystals and electrostatic forces between Cl^- ions and K^+ ions, Pd^{2+}/ Na^+ ions, and K^+ ion cavities in a mica substrate. We develop a novel and facile growth strategy where a pre-patterned

edge Pd NP is a mobile microreactor in the thermal CVD process, favoring the continuous extension of bilayer $PdSe_2$ dendrites. Utilizing the advantages of water solubility of NaCl, we have demonstrated a chemical etchant-free and large-area transfer of $PdSe_2$ dendrites, which fully overcomes the limitations of the well-known PMMA-assisted transfer technique. The SERS spectrum of MB molecules at the $PdSe_2$-Pd_2Se_3 junction region decorated with Pd NPs (~50 nm) shows significantly higher SERS enhancement. The mechanism of SERS enhancement is described with the help of FEM simulation and Raman mapping. A detailed analysis revealed a SERS enhancement factor of 3×10^5, which is contributed by both EM and CM mechanisms. According to the FEM simulation, the EM enhancement is 5.546×10^3 for Pd NPs on bilayer $PdSe_2$. The attachment of Pd NPs at the $PdSe_2$-Pd_2Se_3 junction further enhances the SERS signal for MB molecules due to the combined role of electromagnetic and chemical enhancement mechanisms.

In **Chapter 3,** present the growth of ultrathin sheet-like bilayer and ribbon-like few-layer $PdSe_2$ on mica substrate with high chemical and structural uniformity. Temperature-dependent Raman studies have been carried out to understand the phonon-phonon interactions in the as-grown bilayer and few-layer (5-layer) $PdSe_2$. In the case of as-grown bilayer and five-layer $PdSe_2$ film, it ranges from -0.006 $cm^{-1}K^{-1}$ to -0.024 $cm^{-1}K^{-1}$. For 2D $PdSe_2$, as layer number increases, the Raman temperature coefficient increases for A_g^3, B_{1g}^3 modes and decreases for A_g^1, B_{1g}^1 modes, which is unique due to its ubiquitous in-plane anisotropy. CVD synthesized group VI TMDs have temperature coefficients from -0.0114 cm^{-1} K^{-1} to -0.0135 cm^{-1} K^{-1}, where the variation is significantly less compared to our as-grown $PdSe_2$. Layer thickness-dependent anisotropic ratio is determined through Raman studies, and the origin of lower anisotropic ratio for increasing layer number is discussed. Using the Raman spectroscopic measurement technique, we have estimated the thermal conductivity of bilayer and few-layer $PdSe_2$. At room temperature, the estimated thermal conductivity is ~36.8 W/m. K and ~10.1 W/m. K for bi-layer and few-layer (~5L) $PdSe_2$, respectively.

In **Chapter 4**, demonstrated a simple low-temperature CVD synthesis technique to grow 2D $PdSe_2$ with attractive dendritic edges. The precise layer number and structure have been identified through AFM and Raman analyses. XPS analysis reveals about 9.3% outer layer Se vacancies, 4.7 % inner Se vacancies, and 4.7% Pd vacancies in dendritic 2D $PdSe_2$. In 2D $PdSe_2$, two Se atoms in the top layer and two Se atoms in the bottom layer are joined by a tilted structure with one Pd

in-between. Se atoms cover the outer surface by forming a protecting layer to $PdSe_2$. We addressed the high vacancies of upper Se atoms, and we know surface Se atoms can escape more easily from the TEM and AFM image analysis on various defects, edge geometry, and nanopores in dendritic $PdSe_2$. Near-infrared (NIR) PL studies revealed a decrease in bandgap in monolayer and bilayer dendritic $PdSe_2$, further supporting Se vacancies. In addition, an additional peak in the XPS spectrum confirms the presence of defects in $PdSe_2$. It is shown that defects, nanopores, and edge geometry in dendritic $PdSe_2$ act as trapping/binding sites for foreign atoms/molecules. These active sites and vacancies play a crucial role in the enhanced Raman signal of Rhodamine B.[62] SERS signal associated photoluminescence of RhB/$PdSe_2$ hybrid system confirms that the Se vacancy sites in defective dendritic $PdSe_2$ act as hotspots for SERS of RhB molecule. The density functional theory (DFT) calculations show that including the Se-defect in the $PdSe_2$ system alters its electronic behavior from semiconductor to metallic. The topological line defect of Se_{TLU} (top layer upper Se atom) in $PdSe_2$ in the presence of excess Pd behaves as a quasi-one-dimensional metallic wire, which is responsible for the high SERS enhancement.

In **Chapter 5,** we delve deep into understanding the scrolling of bilayer $PdSe_2$ and unscrolling using an external stimulus: heat. The nanoscrolls are formed from the edges of the bilayer $PdSe_2$ sheet. Controlled scrolling of $PdSe_2$ in response to external environmental stimuli, such as mild temperature compatible with biological systems, has yet to be demonstrated. Such controlled water-assisted crolling is extremely difficult to achieve in the case of other 2D materials such as graphene, TMDs, and NTMDs. Here, we show that thermal activation inside an H_2O environment can have a more marked effect on the behavior, leading to spontaneous sliding, tearing, and peeling of directly CVD-grown $PdSe_2$ from mica substrate. The $PdSe_2$ nanoscrolls (PSNS) are formed from the edges of the bilayer $PdSe_2$ sheet. The conversion of $PdSe_2$ into PSNS via Pd nanoparticles and unscrolling into sheet structures are fully controlled under an H_2O environment. The structures are characterized using spectroscopy and microscopy. We have observed that the PSNS tends to unscroll its free outer layer, which is helpful for cargo delivery under specific conditions. We highlight applicability by encapsulating live cancer cells, where Pd nanoparticles attack the cancer cell, leading to cancer cells' nuclear arrest and death.

In **Chapter 6**, we investigated the uniaxial tensile strain-mediated evolution of new Pd_2Se_3 phase from the high-quality $PdSe_2$ bilayer. To obtain stable bilayer $PdSe_2$, we employ a two-step growth

method. To perform strain engineering on $PdSe_2$, we have transferred it onto a flexible PET substrate after growth on a mica substrate. A scotch-tape assisted transfer technique is introduced to eliminate any unwanted effects by polymers. Using Raman spectroscopy, we have shown that bilayer $PdSe_2$ can undergo phase transition into Pd_2Se_3 due to Se vacancies and interlayer fusion of two $PdSe_2$ layers when subject to tensile strain. This phase transition arose in the case of polymer-free transfer methods like water-assisted and scotch tape-assisted transfer techniques. In contrast, the phase transition is unachievable in the case of polymer-assisted transfer techniques. Under the uniaxial tensile strain of > 0.5 % in the case of water-assisted transfer and of > 0.2 % in the case of scotch tape transfer, $PdSe_2$ changes its phase to Pd_2Se_3. Further RTA analyses confirmed the transition of the $PdSe_2$ phase to Pd_2Se_3 with the generation of new peaks at 157 cm^{-1}, 189 cm^{-1}, 198 $cm^{-1,}$ and 212 cm^{-1}.

Chapter 7 summarizes the work done in the thesis and highlights its contributions to the study of bilayer $PdSe_2$, the discovery of $PdSe_2$ dendrite and $PdSe_2$ nanoscroll (PSNS) for applications in the fields of SERS and cancer biology. Finally, we discuss the future scopes of $PdSe_2$, $PdSe_{2,}$ and PSNS in the era of 2D materials.

References

1 Duan, X., Wang, C., Pan, A., Yu, R., & Duan, X. (2015). Two-dimensional transition metal dichalcogenides as atomically thin semiconductors: opportunities and challenges. Chemical Society Reviews, 44(24), 8859–8876. https://doi.org/10.1039/c5cs00507h.

2 Zhou, X., Zhang, Q., Gan, L., Li, H., Xiong, J., & Zhai, T. (2016). Booming Development of Group IV–VI Semiconductors: Fresh Blood of 2D Family. Advanced Science, 3(12). https://doi.org/10.1002/advs.201600177.

3 Sun, Z., Martinez, A., & Wang, F. (2016). Optical modulators with 2D layered materials. Nature Photonics, 10(4), 227–238. https://doi.org/10.1038/nphoton.2016.15.

4 Balandin, A. A., Ghosh, S., Bao, W., Calizo, I., Teweldebrhan, D., Miao, F., & Lau, C. N. (2008). Superior Thermal Conductivity of Single-Layer Graphene. Nano Letters, 8(3), 902–907. https://doi.org/10.1021/nl0731872.

5 Cai, Q., Scullion, D., Gan, W., Falin, A., Zhang, S., Watanabe, K., Taniguchi, T., Chen, Y., Santos, E. J. G., & Li, L. H. (2019c). High thermal conductivity of high-quality monolayer boron nitride and its thermal expansion. Science Advances, 5(6). https://doi.org/10.1126/sciadv.aav0129.

6 Luo, Z., Maassen, J., Deng, Y., Du, Y., Garrelts, R. P., Lundstrom, M. S., Ye, P. D., & Xu, X. (2015). Anisotropic in-plane thermal conductivity observed in few-layer black phosphorus. Nature Communications, 6(1). https://doi.org/10.1038/ncomms9572

7 Zhang, X., Sun, D., Li, Y., Lee, G., Cui, X., Chenet, D., You, Y., Heinz, T. F., & Hone, J. C. (2015). Measurement of Lateral and Interfacial Thermal Conductivity of Single- and Bilayer MoS2 and MoSe2 Using Refined Optothermal Raman Technique. ACS Applied Materials & Interfaces, 7(46), 25923–25929. https://doi.org/10.1021/acsami.5b08580.

8 Easy, E., Gao, Y., Wang, Y., Yan, D., Goushehgir, S. M., Yang, E., Xu, B., & Zhang, X. (2021). Experimental and Computational Investigation of Layer-Dependent Thermal Conductivities and Interfacial Thermal Conductance of One- to Three-Layer WSe2. ACS Applied Materials & Interfaces, 13(11), 13063–13071. https://doi.org/10.1021/acsami.0c21045.

9 Peimyoo, N., Shang, J., Yang, W., Wang, Y., Cong, C., & Yu, T. (2014). Thermal conductivity determination of suspended mono- and bilayer WS2 by Raman spectroscopy. Nano Research, 8(4), 1210–1221. https://doi.org/10.1007/s12274-014-0602-0.

10 Hossain, M. T., & Giri, P. K. (2021). Temperature-dependent Raman studies and thermal conductivity of direct CVD grown non-van der Waals layered Bi2O2Se. Journal of Applied Physics, 129(17). https://doi.org/10.1063/5.0049368.

11 Wang, F., Luo, P., Zhang, Y., Huang, Y., Zhang, Q., Li, Y., & Zhai, T. (2020b). Band structure engineered tunneling heterostructures for high-performance visible and near-infrared photodetection. Science China Materials, 63(8), 1537–1547. https://doi.org/10.1007/s40843-020-1353-3.

12 Wang, F., Yang, S., Wu, J., Hu, X., Li, Y., Li, H., Liu, X., Luo, J., & Zhai, T. (2021). Emerging two-dimensional bismuth oxychalcogenides for electronics and optoelectronics. InfoMat, 3(11), 1251–1271. https://doi.org/10.1002/inf2.12215.

13 Wang, Y., Pang, J., Cheng, Q., Han, L., Li, Y., Meng, X., Ibarlucea, B., Zhao, H., Yang, F., Liu, H., Liu, H., Zhou, W., Wang, X., Rummeli, M. H., Zhang, Y., & Cuniberti, G. (2021). Applications of 2D-Layered Palladium Diselenide and Its van der Waals Heterostructures in Electronics and Optoelectronics. Nano-Micro Letters, 13(1). https://doi.org/10.1007/s40820-021-00660-0.

14 Zhou, J., Lin, J., Huang, X., Zhou, Y., Chen, Y., Xia, J., Wang, H., Xie, Y., Yu, H., Lei, J., Wu, D., Liu, F., Fu, Q., Zeng, Q., Hsu, C., Yang, C., Lu, L., Yu, T., Shen, Z., . . . Liu, Z. (2018). A library of atomically

thin metal chalcogenides. Nature, 556(7701), 355–359. https://doi.org/10.1038/s41586-018-0008-3.

15 Neupane, G. P., Zhou, K., Chen, S., Yildirim, T., Zhang, P., & Lu, Y. (2019). In-Plane Isotropic/Anisotropic 2D van der Waals Heterostructures for Future Devices. Small, 15(11). https://doi.org/10.1002/smll.201804733.

16 Xu, Y., Shi, Z., Shi, X., Zhang, K., & Zhang, H. (2019). Recent progress in black phosphorus and black-phosphorus-analogue materials: properties, synthesis and applications. Nanoscale, 11(31), 14491–14527. https://doi.org/10.1039/c9nr04348a.

17 W Wang, Y., Li, L., Yao, W., Song, S., Sun, J. T., Pan, J., Ren, X., Li, C., Okunishi, E., Wang, Y., Wang, E., Shao, Y., Zhang, Y. Y., Yang, H., Schwier, E. F., Iwasawa, H., Shimada, K., Taniguchi, M., Cheng, Z., . . . Gao, H. (2015). Monolayer PtSe2, a New Semiconducting Transition-Metal-Dichalcogenide, Epitaxially Grown by Direct Selenization of Pt. Nano Letters, 15(6), 4013–4018. https://doi.org/10.1021/acs.nanolett.5b00964.

18 Zhao, Y., Qiao, J., Yu, Z., Yu, P., Xu, K., Lau, S. P., Zhou, W., Liu, Z., Wang, X., Ji, W., & Chai, Y. (2016). High-Electron-Mobility and Air-Stable 2D Layered PtSe2 FETs. Advanced Materials, 29(5). https://doi.org/10.1002/adma.201604230.

19 Chow, W. L., Yu, P., Liu, F., Hong, J., Wang, X., Zeng, Q., Hsu, C., Zhu, C., Zhou, J., Wang, X., Xia, J., Yan, J., Chen, Y., Wu, D., Yu, T., Shen, Z., Lin, H., Jin, C., Tay, B. K., & Liu, Z. (2017). High Mobility 2D Palladium Diselenide Field-Effect Transistors with Tunable Ambipolar Characteristics. Advanced Materials, 29(21). https://doi.org/10.1002/adma.201602969.

20 Oyedele, A. D., Yang, S., Liang, L., Puretzky, A. A., Wang, K., Zhang, J., Yu, P., Pudasaini, P. R., Ghosh, A. W., Liu, Z., Rouleau, C. M., Sumpter, B. G., Chisholm, M. F., Zhou, W., Rack, P. D., Geohegan, D. B., & Xiao, K. (2017b). PdSe2: Pentagonal Two-Dimensional Layers with High Air Stability for Electronics. Journal of the American Chemical Society, 139(40), 14090–14097. https://doi.org/10.1021/jacs.7b04865.

21 Zhao, Y., Qiao, J., Yu, P., Hu, Z., Lin, Z., Lau, S. P., Liu, Z., Ji, W., & Chai, Y. (2016). Extraordinarily Strong Interlayer Interaction in 2D Layered PtS2. Advanced Materials, 28(12), 2399–2407. https://doi.org/10.1002/adma.201504572.

22 Li, L., Wang, W., Chai, Y., Li, H., Tian, M., & Zhai, T. (2017). Few-Layered PtS2 Phototransistor on h-BN with High Gain. Advanced Functional Materials, 27(27). https://doi.org/10.1002/adfm.201701011.

23 Deng, S., Li, L., & Zhang, Y. (2018). Strain Modulated Electronic, Mechanical, and Optical Properties of the Monolayer PdS2, PdSe2, and PtSe2 for Tunable Devices. ACS Applied Nano Materials, 1(4), 1932–1939. https://doi.org/10.1021/acsanm.8b00363.

24 Lu, L., Chen, G., Cheng, H., Chuu, C., Lu, K., Chen, C., Lu, M., Chuang, T., Wei, D., Chueh, W., Jian, W., Li, M., Chang, Y., Li, L., & Chang, W. (2020). Layer-Dependent and In-Plane Anisotropic Properties of Low-Temperature Synthesized Few-Layer PdSe2 Single Crystals. ACS Nano, 14(4), 4963–4972. https://doi.org/10.1021/acsnano.0c01139.

25 Li, E., Wang, D., Fan, P., Zhang, R., Zhang, Y., Li, G., Mao, J., Wang, Y., Lin, X., Du, S., & Gao, H. (2018). Construction of bilayer PdSe2 on epitaxial graphene. Nano Research, 11(11), 5858–5865. https://doi.org/10.1007/s12274-018-2090-0.

26 Lin, J., Zuluaga, S., Yu, P., Liu, Z., Pantelides, S. T., & Suenaga, K. (2017c). Novel Pd2Se3 Two-Dimensional Phase Driven by Interlayer Fusion in Layered PdSe. Physical Review Letters, 119(1). https://doi.org/10.1103/physrevlett.119.016101.

27 Nguyen, G. D., Liang, L., Zou, Q., Fu, M., Oyedele, A. D., Sumpter, B. G., Liu, Z., Gai, Z., Xiao, K., & Li, A. (2018). 3D Imaging and Manipulation of Subsurface Selenium Vacancies in PdSe2. Physical Review Letters, 121(8). https://doi.org/10.1103/physrevlett.121.086101.

28 Fu, M., Liang, L., Zou, Q., Nguyen, G. D., Xiao, K., Li, A., Kang, J., Wu, Z., & Gai, Z. (2019c). Defects in Highly Anisotropic Transition-Metal Dichalcogenide PdSe2. The Journal of Physical Chemistry Letters, 11(3), 740–746. https://doi.org/10.1021/acs.jpclett.9b03312.

29 Tai, K., Chen, J., Wen, Y., Park, H., Zhang, Q., Lu, Y., Chang, R., Tang, P., Allen, C. S., Wu, W., & Warner, J. H. (2020c). Phase Variations and Layer Epitaxy of 2D PdSe2 Grown on 2D Monolayers by Direct Selenization of Molecular Pd Precursors. ACS Nano, 14(9), 11677–11690. https://doi.org/10.1021/acsnano.0c04230.

30 Chen, J., Ryu, G. H., Sinha, S., & Warner, J. H. (2019b). Atomic Structure and Dynamics of Defects and Grain Boundaries in 2D Pd2Se3 Monolayers. ACS Nano, 13(7), 8256–8264. https://doi.org/10.1021/acsnano.9b03645.

31 Zuluaga, S., Lin, J., Suenaga, K., & Pantelides, S. T. (2018c). Two-dimensional PdSe 2 -Pd 2 Se 3 junctions can serve as nanowires. 2D Materials, 5(3), 035025. https://doi.org/10.1088/2053-1583/aac34c.

32 Ryu, G. H., Zhu, T., Chen, J., Sinha, S., Shautsova, V., Grossman, J. C., & Warner, J. H. (2019b). Striated 2D Lattice with Sub-nm 1D Etch Channels by Controlled Thermally Induced Phase Transformations of PdSe2. Advanced Materials, 31(46). https://doi.org/10.1002/adma.201904251.

33 Li, S., Tsukagoshi, K., Orgiu, E., & Samorì, P. (2015). Charge transport and mobility engineering in two-dimensional transition metal chalcogenide semiconductors. Chemical Society Reviews, 45(1), 118–151. https://doi.org/10.1039/c5cs00517e.

34 Kaasbjerg, K., Thygesen, K. S., & Jacobsen, K. W. (2012). Phonon-limited mobility inn-type single-layer MoS2from first principles. Physical Review B, 85(11). https://doi.org/10.1103/physrevb.85.115317.

35 Zhang, W., Huang, Z., Zhang, W., & Li, Y. (2014). Two-dimensional semiconductors with possible high room temperature mobility. Nano Research, 7(12), 1731–1737. https://doi.org/10.1007/s12274-014-0532-x.

36 Liang, Q., Wang, Q., Zhang, Q., Wei, J., Lim, S. X., Zhu, R., Hu, J., Wei, W., Lee, C., Sow, C., Zhang, W., & Wee, A. T. S. (2019). High-Performance, Room Temperature, Ultra-Broadband Photodetectors Based on Air-Stable PdSe2. Advanced Materials, 31(24). https://doi.org/10.1002/adma.201807609.

37 Hoffman, A. N., Gu, Y., Liang, L., Fowlkes, J. D., Xiao, K., & Rack, P. D. (2019). Exploring the air stability of PdSe2 via electrical transport measurements and defect calculations. Npj 2D Materials and Applications, 3(1). https://doi.org/10.1038/s41699-019-0132-4.

38 Xu, W., Jiang, J., Ma, H., Zhang, Z., Li, J., Zhao, B., Wu, R., Yang, X., Zhang, H., Li, B., Shu, W., Zhang, Z., Li, B., Liu, Y., Liao, L., & Duan, X. (2020). Vapor phase growth of two-dimensional PdSe2 nanosheets for high-photoresponsivity near-infrared photodetectors. Nano Research, 13(8), 2091–2097. https://doi.org/10.1007/s12274-020-2815-8.

39 Jiang, S., Zhang, C., Zhao, E., Han, M., Zhu, L., & Zhao, Y. (2021). Synthesis of ultrathin PdSe2 flakes for hydrogen evolution reaction. Applied Surface Science, 570, 151178. https://doi.org/10.1016/j.apsusc.2021.151178.

40 Jiang, S., Xie, C., Gu, Y., Zhang, Q., Wu, X., Sun, Y., Li, W., Shi, Y., Zhao, L., Pan, S., Yang, P., Huan, Y., Xie, D., Zhang, Q., Liu, X., Zou, X., Gu, L., & Zhang, Y. (2019). Anisotropic Growth and Scanning Tunneling Microscopy Identification of Ultrathin Even-Layered PdSe2 Ribbons. Small, 15(45). https://doi.org/10.1002/smll.201902789.

41 Lin, Z., Xiao, B., Wang, Z., Tao, W., Shen, S., Huang, L., Zhang, J., Meng, F., Zhang, Q., Gu, L., & Zhong, W. (2021). Planar-Coordination PdSe2 Nanosheets as Highly Active Electrocatalyst for Hydrogen Evolution Reaction. Advanced Functional Materials, 31(32). https://doi.org/10.1002/adfm.202102321.

42 Di Bartolomeo, A., Pelella, A., Liu, X., Miao, F., Passacantando, M., Giubileo, F., Grillo, A., Iemmo, L., Urban, F., & Liang, S. (2019). Pressure-Tunable Ambipolar Conduction and Hysteresis in Thin Palladium Diselenide Field Effect Transistors. Advanced Functional Materials, 29(29). https://doi.org/10.1002/adfm.201902483.

43 Long, M., Wang, Y., Wang, P., Zhou, X., Xia, H., Luo, C., Huang, S., Zhang, G., Yan, H., Fan, Z., Wu, X., Chen, X., Lu, W., & Hu, W. (2019). Palladium Diselenide Long-Wavelength Infrared Photodetector with High Sensitivity and Stability. ACS Nano. https://doi.org/10.1021/acsnano.8b09476.

44 Z Zhang, H., Ma, P., Zhu, M., Zhang, W., Wang, G., & Fu, S. (2020). Palladium selenide as a broadband saturable absorber for ultra-fast photonics. Nanophotonics, 9(8), 2557–2567. https://doi.org/10.1515/nanoph-2020-0116.

45 Wu, Z., Lu, L., Liang, X., Dun, C., Yan, S., Mu, E., Liu, Y., & Hu, Z. (2020). Formation of Hexagonal PdSe2 for Electronics and Catalysis. The Journal of Physical Chemistry C, 124(20), 10935–10940. https://doi.org/10.1021/acs.jpcc.0c00521.

46 Gu, Y., Cai, H., Dong, J., Yu, Y., Hoffman, A. N., Liu, C., Oyedele, A. D., Lin, Y., Ge, Z., Puretzky, A. A., Duscher, G., Chisholm, M. F., Rack, P. D., Rouleau, C. M., Gai, Z., Meng, X., Ding, F., Geohegan, D. B., & Xiao, K. (2020). Two-Dimensional Palladium Diselenide with Strong In-Plane Optical Anisotropy and High Mobility Grown by Chemical Vapor Deposition. Advanced Materials, 32(19). https://doi.org/10.1002/adma.201906238.

47 Xie, C., Jiang, S., Gao, Y., Hong, M., Pan, S., Zhao, J., & Zhang, Y. (2020). Giant Thickness-Tunable Bandgap and Robust Air Stability of 2D Palladium Diselenide. Small, 16(19). https://doi.org/10.1002/smll.202000754.

48 Li, M., Sun, H., Zhou, J., & Zhao, Y. (2023). Engineering phonon thermal transport in few-layer PdSe2. Frontiers of Physics, 19(3). https://doi.org/10.1007/s11467-023-1351-x.

49 Luo, L., Wang, D., Xie, C., Hu, J., Zhao, X., & Liang, F. (2019). PdSe2 Multilayer on Germanium Nanocones Array with Light Trapping Effect for Sensitive Infrared Photodetector and Image Sensing Application. Advanced Functional Materials, 29(22). https://doi.org/10.1002/adfm.201900849.

50 Liang, F., Zhao, X., Jiang, J., Hu, J., Xie, W., Lv, J., Zhang, Z., Wu, D., & Luo, L. (2019). Light Confinement Effect Induced Highly Sensitive, Self-Driven Near-Infrared Photodetector and Image Sensor Based on Multilayer PdSe2/Pyramid Si Heterojunction. Small, 15(44). https://doi.org/10.1002/smll.201903831.

51 Wu, D., Jia, C., Shi, F., Zeng, L., Lin, P., Dong, L., Shi, Z., Tian, Y., Li, X., & Jie, J. (2020). Mixed-dimensional PdSe2/SiNWA heterostructure based photovoltaic detectors for self-driven, broadband photodetection, infrared imaging and humidity sensing. Journal of Materials Chemistry A, 8(7), 3632–3642. https://doi.org/10.1039/c9ta13611h.

52 Pi, L., Hu, C., Shen, W., Li, L., Luo, P., Hu, X., Chen, P., Li, D., Li, Z., Zhou, X., & Zhai, T. (2020). Highly In-Plane Anisotropic 2D PdSe2 for Polarized Photodetection with Orientation Selectivity. Advanced Functional Materials, 31(3). https://doi.org/10.1002/adfm.202006774.

53 Fan, J., Hu, X., Fu, C., Qin, W., Min, X., Zhao, J., Luo, L., & Zhang, W. (2021). Few-Layer PdSe2 Nanofilm/Si Heterojunction for Sensing NO2 at Room Temperature. ACS Applied Nano Materials, 4(7), 7358–7370. https://doi.org/10.1021/acsanm.1c01339.

54 Dong, Z., Yu, W., Zhang, L., Mu, H., Xie, L., Li, J., Zhang, Y., Huang, L., He, X., Wang, L., Lin, S., & Zhang, K. (2021). Highly Efficient, Ultrabroad PdSe2 Phototransistors from Visible to Terahertz Driven by Mutiphysical Mechanism. ACS Nano, 15(12), 20403–20413. https://doi.org/10.1021/acsnano.1c08756.

55 Zeng, L., Wu, D., Lin, S., Xie, C., Yuan, H., Lu, W., Lau, S. P., Chai, Y., Luo, L., Li, Z., & Tsang, Y. H. (2018b). Controlled Synthesis of 2D Palladium Diselenide for Sensitive Photodetector Applications. Advanced Functional Materials, 29(1). https://doi.org/10.1002/adfm.201806878.

56 Di Bartolomeo, A., Pelella, A., Urban, F., Grillo, A., Iemmo, L., Passacantando, M., Liu, X., & Giubileo, F. (2020). Field Emission in Ultrathin PdSe2 Back-Gated Transistors. Advanced Electronic Materials, 6(7). https://doi.org/10.1002/aelm.202000094.

57 Lei, Z., Zhang, X., Zhao, Y., Wei, A., Tao, L., Yang, Y., Zheng, Z., Tao, L., Yu, P., & Li, J. (2022). Enhanced Raman scattering on two-dimensional palladium diselenide. Nanoscale, 14(11), 4181–4187. https://doi.org/10.1039/d1nr07126b.

58 Li, Y., Chen, S., Yu, Z., Li, S., Xiong, Y., Pam, M., Zhang, Y., & Ang, K. (2022). In-Memory Computing using Memristor Arrays with Ultrathin 2D PdSeOx/PdSe2 Heterostructure. Advanced Materials, 34(26). https://doi.org/10.1002/adma.202201488.

59 Xia, X., Guo, S., Xu, L., Guo, T., Wu, Z., & Zhang, S. (2021). Sensing Performance of SO_2, SO_3 and NO_2 Gas Molecules on 2D Pentagonal $PdSe_2$: A First-Principle Study. IEEE Electron Device Letters, 42(4), 573–576. https://doi.org/10.1109/led.2021.3059667.

60 Wang, X., Qarony, W., Cheng, P. K., Ismail, M., & Tsang, Y. H. (2019). Photoluminescence of PdS2 and PdSe2 quantum dots. RSC Advances, 9(65), 38077–38084. https://doi.org/10.1039/c9ra07445g.

61 Zhu, R., Gao, Z., Liang, Q., Hu, J., Wang, J., Qiu, C., & Wee, A. T. S. (2021). Observation of Anisotropic Magnetoresistance in Layered Nonmagnetic Semiconducting PdSe2. ACS Applied Materials & Interfaces, 13(31), 37527–37534. https://doi.org/10.1021/acsami.1c10500.

62 Vicarelli, L., Heerema, S. J., Dekker, C., & Zandbergen, H. W. (2015). Controlling Defects in Graphene for Optimizing the Electrical Properties of Graphene Nanodevices. ACS Nano, 9(4), 3428–3435. https://doi.org/10.1021/acsnano.5b01762.

Chapter 2 - Salt-catalyzed directed growth of bilayer $PdSe_2$ and Pd nanoparticle-decorated $PdSe_2$-Pd_2Se_3 junction exhibiting high SERS sensitivity

In this chapter, we advocate for NaCl as a catalyst underpinning the controlled growth of 2D $PdSe_2$. A pre-patterned edge Pd NPs serves as a mobile microreactor in the thermal CVD process, favoring the continuous extension of bilayer $PdSe_2$ dendrites. While the chemical stoichiometry does not change with a reduction in layer numbers for most of the 2D layered materials, the multi-layer Pd_2Se_3 in the NTMDs group changes its stoichiometry to $PdSe_2$ in the bilayer form under Se-rich growth conditions. The experimental realization of $PdSe_2$-Pd_2Se_3 junctions and their application in various sensing applications are yet to be explored. We introduce a NaCl catalyzed CVD growth of 2L $PdSe_2$ dendrites and $PdSe_2$-Pd_2Se_3 junctions on the mica substrate through the salt solution pre-treatment. The pre-treated structure triggers the formation of molten Pd-O droplets, which undergo a phase evolution from Pd NPs to Pd_2Se_3 (in Se-poor condition) to $PdSe_2$ (in Se-rich condition). Remarkably, Pd NPs hotspots on $PdSe_2$-Pd_2Se_3 junctions enable significant SERS enhancement with an enhancement factor (EF$\sim 3\times10^5$), which is more than one order of magnitude higher than that of 2L $PdSe_2$ to detect methylene blue molecules due to multiple factors, such as charge transfer and electromagnetic field enhancement. This is confirmed by DFT calculations and Finite element method (FEM) simulation, along with Raman imaging. The FEM simulations revealed an electric field enhancement factor of 5.546×10^3 for Pd NPs decorated bilayer $PdSe_2$, and the remaining enhancement factor is expected to be contributed by charge transfer mechanisms.

2.1. Introduction

Two-dimensional (2D) materials are at the forefront of research due to their fascinating properties and diverse emerging applications. 2D materials exhibit a wide variety of morphologies, including dendritic, snowflake, and flower, similar to snowflakes and pine trees in nature. [1-6] Among these, dendritic morphology has attracted significant research interest due to its complex morphologies[7, 8], unique synthesis mechanism[9-14], and, more importantly, highly sensitive edges[5]. In addition, these nanostructures are interesting because of their quantum confinement effect and space-confined transport phenomena, which hold promise for potential applications in future

nanodevices.[15] In recent years, nanoscale dendrites have received much attention due to their efficient applications in the field of cancer research [16, 17], bioimaging [18, 19], catalysis [20-22], sensing [23, 24]. Understanding the dendrite formation mechanisms may enable fine control of the fractal morphology and enhance their properties. Theoretically, a plethora of growth dynamics have been explored, and many theoretical predictions have corroborated the intricate pattern selection rules in micro and macro-scale dendrites. [25-29] However, it is challenging to determine whether classical dendrite growth theories are applicable at the nanoscale due to the lack of proper information on the growth dynamics of the experimentally reported nanoscale dendrites.

Recent advances in the chemical vapor deposition (CVD) method have been utilized to synthesize dendritic transition metal dichalcogenides (TMDs) [14]. Over and above the most investigated TMDs, noble transition metal dichalcogenides [30, 31] (NTMDs: $PdSe_2$, Pd_2Se_3, $PdTe_2$, PdS_2, $PtSe_2$) have been attracting increasing attention in the last few years. 2D $PdSe_2$ has sparked as the star NTMD due to its low symmetry puckered pentagonal structure, easily exfoliated, thickness tunable bandgap (0 eV to 1.43 eV), in-plane anisotropy similar to 2D black phosphorous [32], high carrier mobility, high air stability [33], direction-dependent physical properties, etc. Although 2D $PdSe_2$ holds great promise for several applications, the controlled synthesis of bilayer $PdSe_2$ remains challenging. Catalytic growth with a pre-determined morphology is a feasible way to control the layer number and the kinetics of a nanostructure. Recently, catalysts such as reduced graphene oxide [34], nickel (Ni) [35], sodium chloride (NaCl) [36, 37], and potassium chloride (KCl) [38] salts have been employed for controlled growth of TMDs. To our knowledge, there is no report on the catalyzed growth of bilayer $PdSe_2$ dendrites. Among the catalysts, salts are efficient candidates for constructing an *in-situ* patterned structure along with control over the number of layers during the CVD growth. NaCl salt has been widely used to catalyze the synthesis of TMDs due to the following unique features: (1) NaCl reduces reaction temperature significantly from very high (>1200 °C) to much lower (~700 °C) value,[39] (2) NaCl is highly water soluble, making them easily removable without any residue after the growth, (3) NaCl can assist an H_2O-assisted polymer-free transfer technique. In the growth of $PdSe_2$, the role of the NaCl catalyst in the CVD growth needs a thorough investigation. To the best of our knowledge, to date, the majority of the reported articles on 2D $PdSe_2$ use poly methyl methacrylate (PMMA)-assisted transfer technique for post-growth transfer.[40-42] However, the post-growth transfer techniques significantly degrade the properties as well as the performance of ultrathin CVD-grown 2D materials due to the polymer

residue, such as PMMA, poly(bisphenol A carbonate) (PC), polystyrene (PS), and poly di-methyl siloxane (PDMS), and reactive etchants, such as KOH, and HF solutions used during the transfer process.[43, 44] Therefore, besides the limitations of using hazardous chemicals, the development of a water-based transfer strategy is highly desirable for CVD-grown 2D materials.

2.2. Material and methods

2.2.1. Growth of $PdSe_2$ dendrites

$PdCl_2$ powder (99.999%), Se powder purchased from Sigma Aldrich, and NaCl powder (> 99.0 %, Merck) were used for experiments without further purification. 7.6×10^{-3} mol L^{-1} $PdCl_2$ was first added into 20 mL distilled water. Na_2PdCl_4 solution was prepared by mixing and dissolving 3 mg of NaCl with the $PdCl_2$ solution, which undergoes vigorous stirring (180 r/min) for about 45 min at room temperature using a magnetic stirrer. After ultrasonic irradiation of the final 10.17×10^{-3} mol L^{-1} Na_2PdCl_4 solution for 3 hrs, the color of the solution turned from initial pale yellow to dark brown. This observation indicates the reduction of Pd (II) ions to palladium Pd (0). Then, pre-patterning of Na_2PdCl_4 is done with the support of a quartz mask with circular openings. The quartz mask was placed on a freshly cleaved mica substrate. Then, under heating conditions (heat at 50 °C on a hot plate), the as-prepared Na_2PdCl_4 solution was drop-cast in the circular opening area of the quartz mask. Na_2PdCl_4 solution on mica is heated at 50 °C on a hotplate for 45 mins. Then, the pre-patterned mica substrate is placed inside a tube (quartz) furnace for CVD. Before the growth, the quartz chamber was cleaned by purging Argon gas (300 sccm) via a rotary pump. In the CVD process, the temperature of the center zone is ramped up to 500 ℃, and Se powder is kept at 1 cm away towards the upstream (temperature ~240 ℃) to vaporize the Se and transport it to the growth substrate (~240 ℃) with a carrier gas (Argon) flow (110 sccm) in a single-zone tube furnace with precise temperature control. The temperature profile is given in the **Figure 2.1**. This resulted in the growth of 2D $PdSe_2$ dendritic structure on mica substrates.

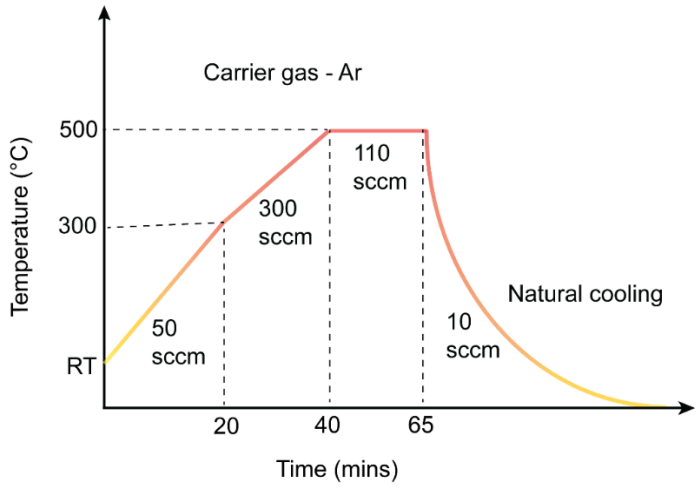

Figure 2.1. Temperature profile for the CVD synthesis of $PdSe_2$ dendrites

2.2.2. SERS measurement

Methylene blue (MB) water solutions were prepared, drop-casted over the CVD-grown dendrites, and kept for 30 minutes to soak the MB molecule completely. The drop cast sample was analyzed after drying. Micro-Raman spectroscopy (LabRam HR800, Jobin Yvon) with an excitation wavelength (λ_{ex}) of 532 nm (Ar ion laser) was conducted to record the SERS spectra of MB on the 2D $PdSe_2$ dendrites and $PdSe_2$-Pd_2Se_3 junction for comparison. A 100X objective lens focused to a spot size of 1 μm along with a laser power of 1.5 mW at the sample (which discards the possibility of laser heating-induced damage) was used for the Raman measurements. The acquisition time and accumulations were kept at 10 s and two, respectively, and 600 grating per mm was used for all the measurements.

2.2.3. TEM sample preparation

The as-prepared 2D $PdSe_2$ dendritic samples were transferred to the TEM grid using a polymer-free water-assisted transfer technique. The detailed transfer process and mechanism of the water-assisted transfer technique are discussed later.

2.2.4. Characterization technique

Field emission scanning electron microscopy (FESEM, Sigma, Zeiss) imaging has been performed for structural analyses of the as-synthesized dendrites. The thickness of the dendrites was evaluated via atomic force microscopy (AFM) (Cypher, Oxford Instruments) in non-contact mode scanning. The atomic resolution surface morphology of the dendritic $PdSe_2$_Pd_2Se_3 junction has been confirmed by a transmission electron microscope (TEM) (JEOL-JEM 2010 operated at 200 kV) analysis. Micro-Raman spectroscopy (LabRam HR800, Jobin Yvon) with an excitation wavelength (λ_{ex}) of 532 nm (Ar ion laser) was conducted to confirm the crystallinity and phase evolution across the dendrites. A 100X objective lens focused to a spot size of 1 μm along with a laser power of 1.5 mW at the sample (which discards the possibility of laser heating-induced damage) was used for the Raman measurements. The acquisition time and accumulations were kept at 10 s and 2, respectively, and 600 grating per mm was used for all the measurements. A charge-coupled device attached to the same system was used to collect the Raman scattered signals sent through a multimode fiber grating of 1800 grooves mm^{-1}. X-ray diffraction pattern of $PdSe_2$ dendrites was collected in a standard XRD instrument (Rigaku RINT 2500 TTRAX-III, Cu k_α radiation).

2.3. Computational details

We have carried out DFT based electronic structure calculations with the Quantum ESPRESSO software package by implementing the projector-augmented wave (PAW) method.[45] The Perdew-Burke-Ernzerhof (PBE) functional in the generalized gradient approximation (GGA)[46,47] takes into account the exchange-correlation. A 30 Å vacuum space was created along the Z-axis to eliminate the interactions between the periodic layers. Brillouin zone samples were taken using a 5×5×1 k-point grid, with a cut-off of 680 eV for plane waves. The D3 approach of Grimme was used to incorporate van der Waals interactions (DFT-D3).[48] The calculated lattice constant of the $PdSe_2$ bilayer is found to be 5.75×5.87 Å, whereas the Pd_2Se_3 monolayer exhibits a lattice constant of 5.89×6.02 Å.[49] While constructing the $PdSe_2$-Pd_2Se_3 junction, we experienced lattice mismatches of 2.95% and 0.5% along the X-axis. Accordingly, a $PdSe_2$-Pd_2Se_3 junction was created with dimensions 17.76 Å × 22.00 Å × 30.00 Å for our calculations.

Electromagnetic FEM simulations were performed in a CST microwave studio design environment. A plane wave source of 532 nm wavelength was made incident on the nanoparticle along the negative Z direction, and PML (perfectly matched layer) boundary conditions were used along the Z direction. The boundary conditions for magnetic and electric fields were taken along the x and y directions, respectively. A tetrahedral meshing was employed to carry out the simulations.

2.4. Results and discussion

2.4.1. Growth on various substrates with and without pretreatment of NaCl

Using a CVD method in a tube furnace system, bilayer (2L) $PdSe_2$ was grown on various substrates with and without pre-treatment of NaCl under a moisture-controlled gas flow (for details, see supplementary information). The growth results with different conditions (without and with NaCl pre-treatment) were compared. For the CVD-grown samples with no NaCl pre-treatment, the conventional, irregular 2D $PdSe_2$ flakes can be fabricated on different substrates. **Figures 2.2 and 2.3** demonstrate the AFM images and Raman spectra of as-grown, few-layer $PdSe_2$ on a variety of substrates.

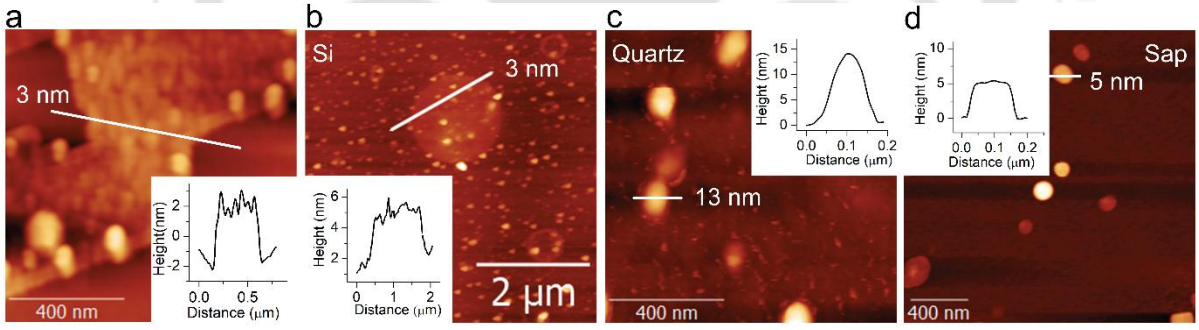

Figure 2.2. AFM images of $PdSe_2$ flakes on (a) Mica, (b) Silicon, (c) Quartz, and (d) Sapphire substrates without any NaCl treatment.

Without NaCl treatment, there is an absence of directed growth (**Figure 2.2**). **Figure 2.2** shows the AFM images of $PdSe_2$ grown on mica, Si, quartz, and sapphire substrates with thicknesses ranging from 3 -13 nm, and the corresponding Raman spectra are shown in **Figure 2.3**. Next, we conducted salt solution-assisted CVD growth of 2L $PdSe_2$ on a freshly cleaved mica surface, which involved two steps: (1) pre-CVD patterning and (2) post-CVD growth of 2L $PdSe_2$ from the edge of the dendrite. In the primary stage of the pre-CVD process, ultrasonication of the Na_2PdCl_4

results in a color alteration of the solution from the initial pale yellow to a dark brown. This observation indicates the reduction of Pd^{2+} ions to Pd NPs, according to the mechanism proposed by Okitsu et al. [50]

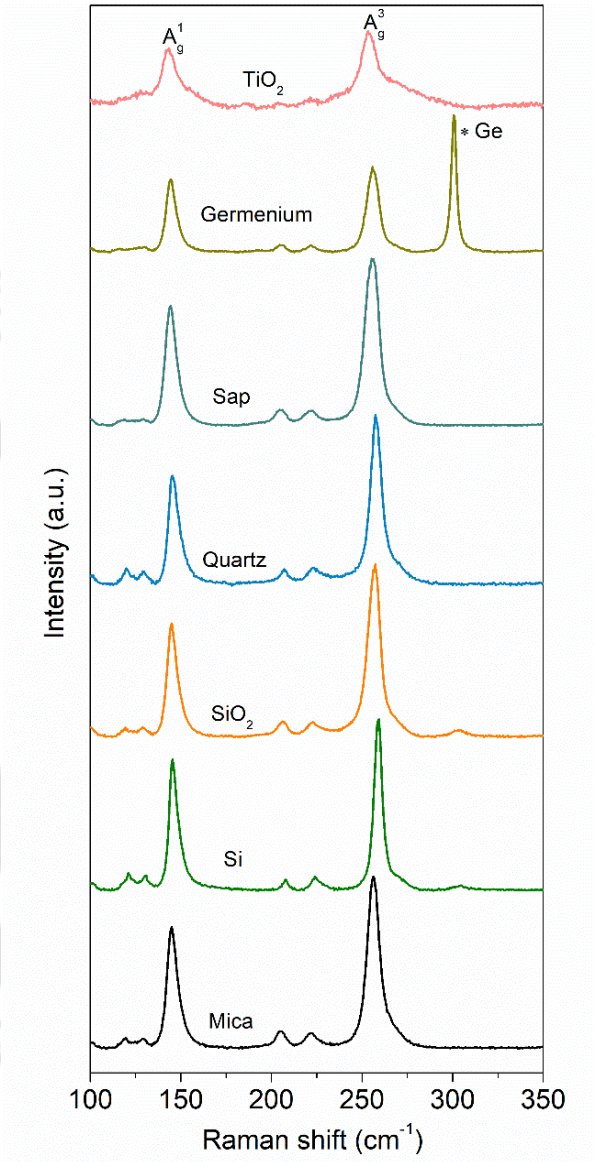

Figure 2.3. Raman spectra of $PdSe_2$ on different growth substrates (without NaCl treatment): Mica, Si, SiO_2, quartz, sapphire, Ge, and TiO_2 showing the characteristic peaks of $PdSe_2$.

Subsequently, (Na_2PdCl_4+Pd NPs) solution was patterned at one corner of the mica substrate to give adequate space for dendrite growth. When the (Na_2PdCl_4+Pd NPs) solution on mica is heated on a hotplate, it results in anisotropy of surface tension and temperature gradient (due to variation in temperature from the center of the hotplate towards edges. The concentration gradient favors the tip growth, which leads to one-armed dendrite formation.

2.4.2. Contact angles on various substrates

We have calculated the contact angles of (Na_2PdCl_4+Pd NPs) on varieties of substrates to better understand the substrate that is best suited for growth. The measured contact angles of (Na_2PdCl_4+Pd NPs) droplets on mica, Si, quartz, glass, Ge, and TiO_2 substrates are 15°, 35°, 39°, 42°, 53°, and 90°, respectively (see **Figure 2.4**)

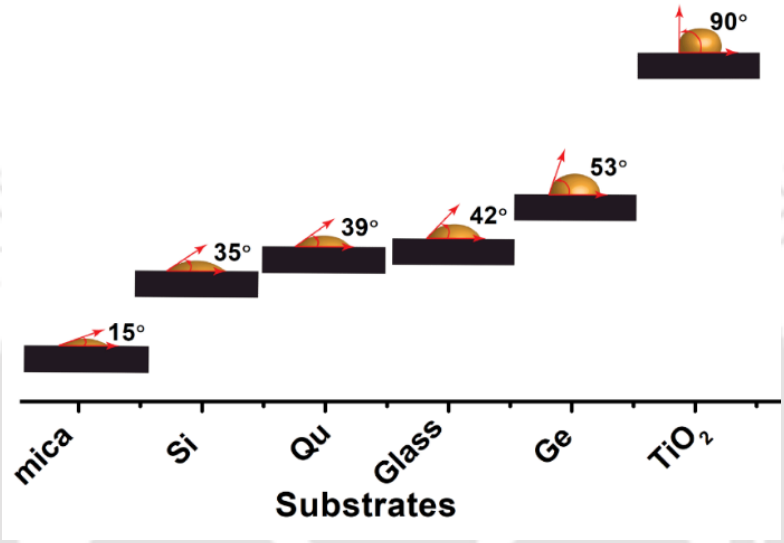

Figure 2.4. Contact angles of (Na_2PdCl_4+ Pd NPs) droplet on different substrates.

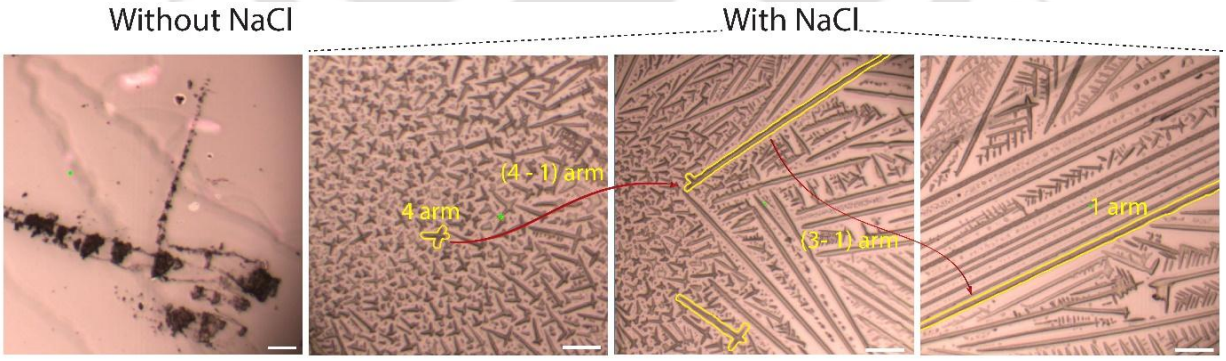

Figure 2.5. Optical images show a non-dendritic pattern (after heating) of drop-cast $PdCl_2$ without NaCl pre-treatment and a dendritic pattern of drop-cast $PdCl_2$ with NaCl pre-treatment on a mica substrate. The scale bar is 5 μm.

Among all the substrates, the mica substrate exhibits the highest wettability, inducing minimum contact angle, and it favors good growth compared to all others. Evidently, during heating, competitive four-armed dendritic growth occurred at the beginning (**Figure 2.5**).

2.4.3. Mechanism for the pre-CVD growth of Na_2PdCl_4 with Pd NPs

To better understand the dendritic path that depends on the temperature gradient, we have divided the growth of (Na_2PdCl_4+Pd NPs) dendrites into three zones of temperature (zone 1- 48 °C, zone 2- 49 °C, zone 3- 50 °C) (**Figure 2.6a**). In zone 1, the four-armed dendritic growth occurs, and the side branching dendrites are affected by neighboring dendrites (**Figure 2.6b**). Due to limited space availability in the inter-dendritic region, some arms collapse and disappear. In zone 2, some parallel dendrites with similar orientations survive in the competition and block others (**Figure 2.6c**). As the temperature increases, the 4-armed dendrite spacing adjusts with neighboring dendrites and grows steadily. As the evaporation proceeds, solute content increases, so the growth of dendrites is not affected by the flow much. The tip of the dendritic arm goes in the direction where it gets maximum velocity. In zone 3, mostly parallel dendrites are rapidly visualized. As we move from zone 1 to zone 3, one of the dendritic arms dominates and captains the growth. Zone 1 behaves as the initiator of four-armed dendritic growth, which finally ends up with one-arm. As we can see in zone 3, there exist many long-branched parallel equi-spaced one-armed dendrites (**Figure 2.6d, e**) due to the availability of adequate growing space. Observing the sword-like morphology of the $PdSe_2$ dendrites (**Figure 2.6d, f**) suggests the termination of dendrites when the precursor was entirely consumed. The terminated dendrite size matches well with a NaCl square (**Figure 2.6f**), mimicking the dendrite width. To confirm the composition of the edge particles in the dendrite, we have conducted EDX mapping, shown in **Figure 2.6f,** and the corresponding spectrum given in **Figure 2.6g**. **Figure 2.6f** shows the FESEM EDX mapping of a single dendrite; the corresponding Na, Cl, and Pd mapping analyses (red square of **Figure 2.6f**) indicate that most of the Pd NPs reside at the edge of the dendrites containing envelop of Na_2PdCl_4. EDX analysis suggests a new compound in the precursors, such as a Na_2PdCl_4 alloyed with Pd NPs (e.g., $Na_2Pd_{1+x}Cl_4$) (**Figure 2.6g**). **Figure 2.6h** shows a (Na_2PdCl_4+Pd NPs) droplet on top of the mica surface after cleaving. Due to the cleaving of the mica surface, 50% K^+ ions remain on each cleaved surface.[51]

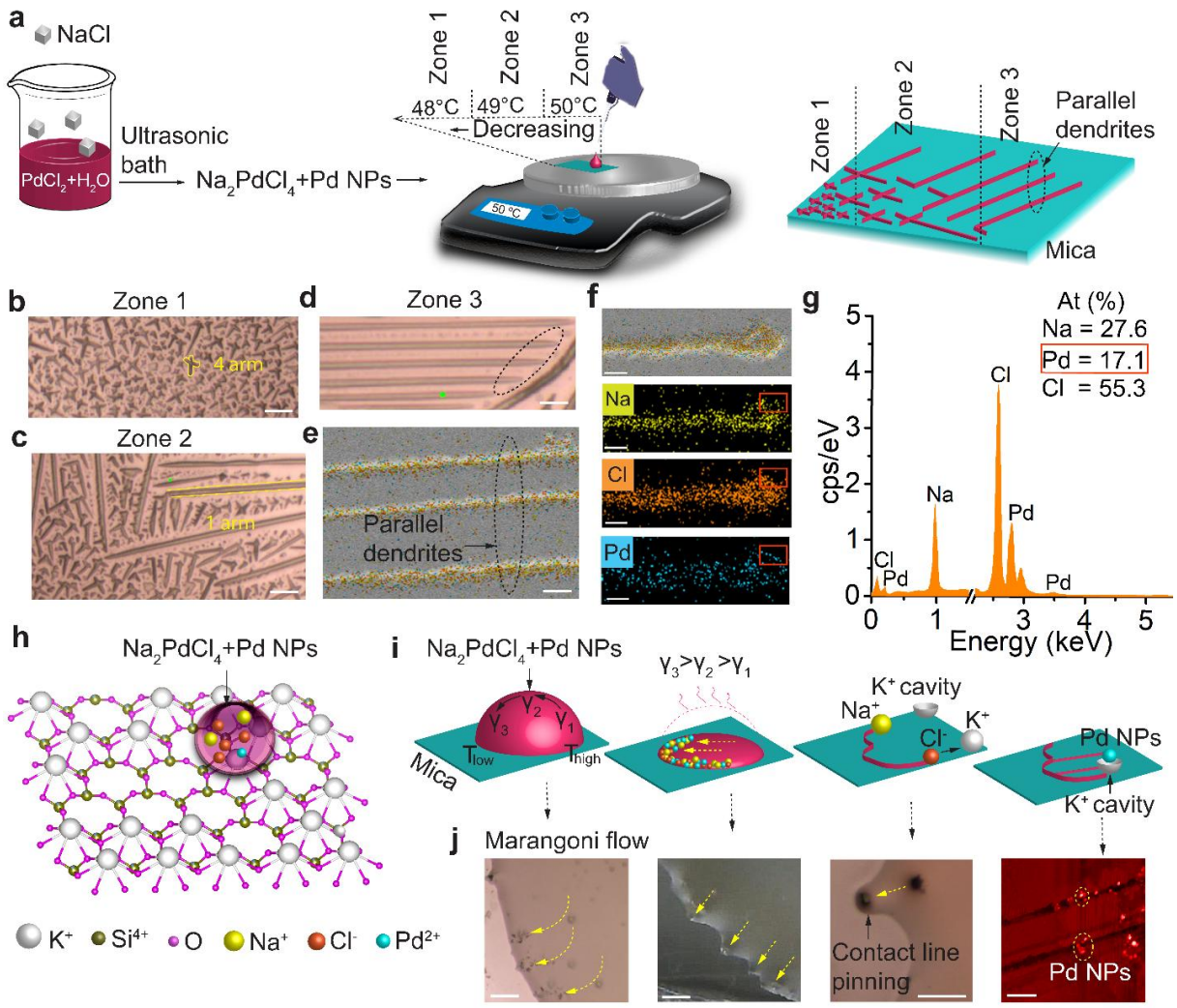

Figure 2.6. (a) Schematic illustration of various phases of pre-CVD dendritic growth of Na_2PdCl_4 with Pd NPs, (b) optical image of four-armed Na_2PdCl_4 dendrites at zone 1, (c) directional growth of Na_2PdCl_4 dendrites in zone 2, (d, e) parallel patterned Na_2PdCl_4 dendrites in zone 3, scale bar is 1 μm. (f) FESEM image (the color distribution represents Na, Cl, and Pd elemental distribution) of parallel $PdSe_2$ dendrites; scale bar is 1 μm. (g) FESEM EDX mapping of single Na_2PdCl_4 dendrite and the corresponding elemental Na, Cl, and Pd mappings. The scale bar is 1 μm. (h) Top view of mica surface after cleaving and (Na_2PdCl_4+Pd NPs) droplet on cleaved mica surface. (i) Schematic showing the Marangoni convection inside (Na_2PdCl_4+Pd NPs) droplet, contact line pinning, and electrostatic attraction between droplet Cl^- ion and mica K^+ ion, Na^+/Pd NPs, and K^+ ion cavities finally leading to dendrite formation, and (j) the corresponding experimental observation.

Figure 2.6i systematically describes the mechanism of dendrite formation and motion on the mica substrate. The corresponding optical and AFM images are shown in **Figure 2.6j**. The EDX mapping of parallel dendrites is shown in **Figure 2.7**.

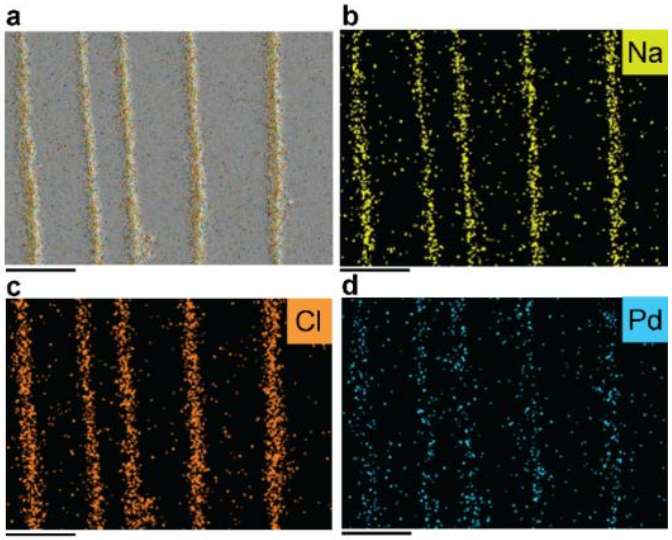

Figure 2.7. (a) FESEM image of the parallel dendrites (pre-CVD) and (b-d) Corresponding EDX mapping of dendrites showing Na, Cl, and Pd. The scale bar is 10 μm in each case.

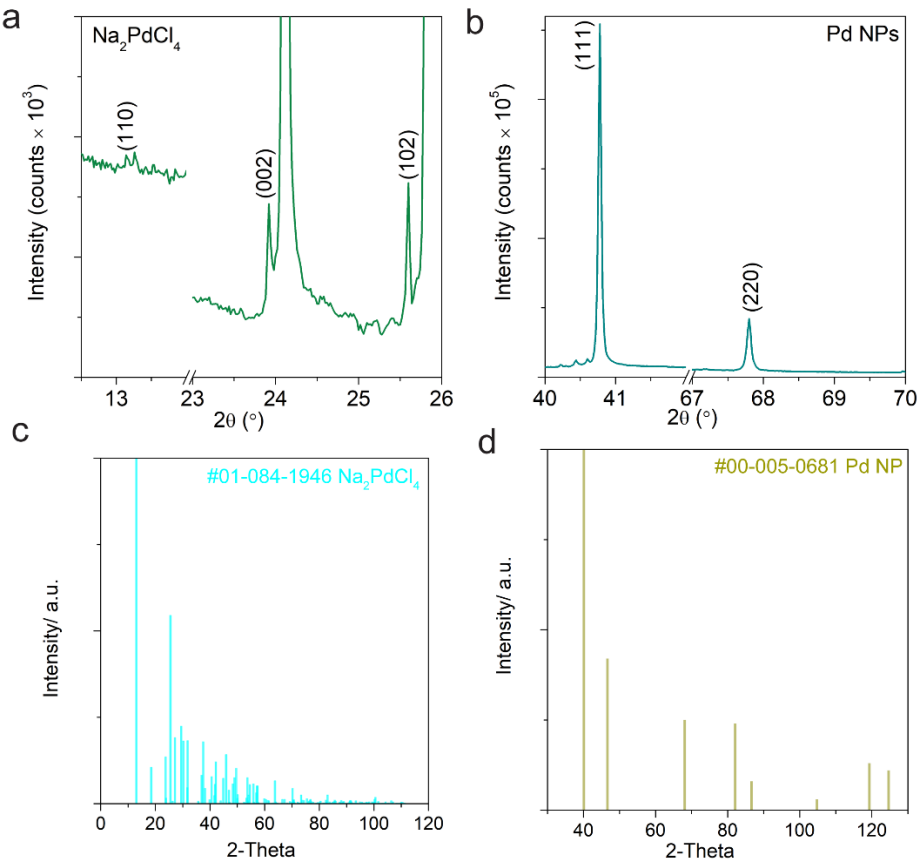

Figure 2.8. XRD pattern of pre-CVD dendrites, showing peaks of both (a) Na_2PdCl_4, (b) Pd NPs before the CVD growth, (c) Na_2PdCl_4 and (d) Pd NP standard JCPD cards.

The XRD analyses on the reaction products are given in **Figure 2.8**. XRD analysis reveals that the resulting compound of dendrite (pre-CVD) contains Na_2PdCl_4 and Pd NPs. Predominantly, the motion of precursors results from the competition between interfacial surface tensions of the solid/liquid interface γ_1 (at the hot end), liquid/gas interface γ_2 and solid/liquid interface γ_3 (at the cold end), $\gamma_3 > \gamma_2 > \gamma_1$ initiates a drag force on the droplet, leading to the Marangoni flow of precursors toward the mica substrate's colder end, forming a contact line (**Figure 2.9**).

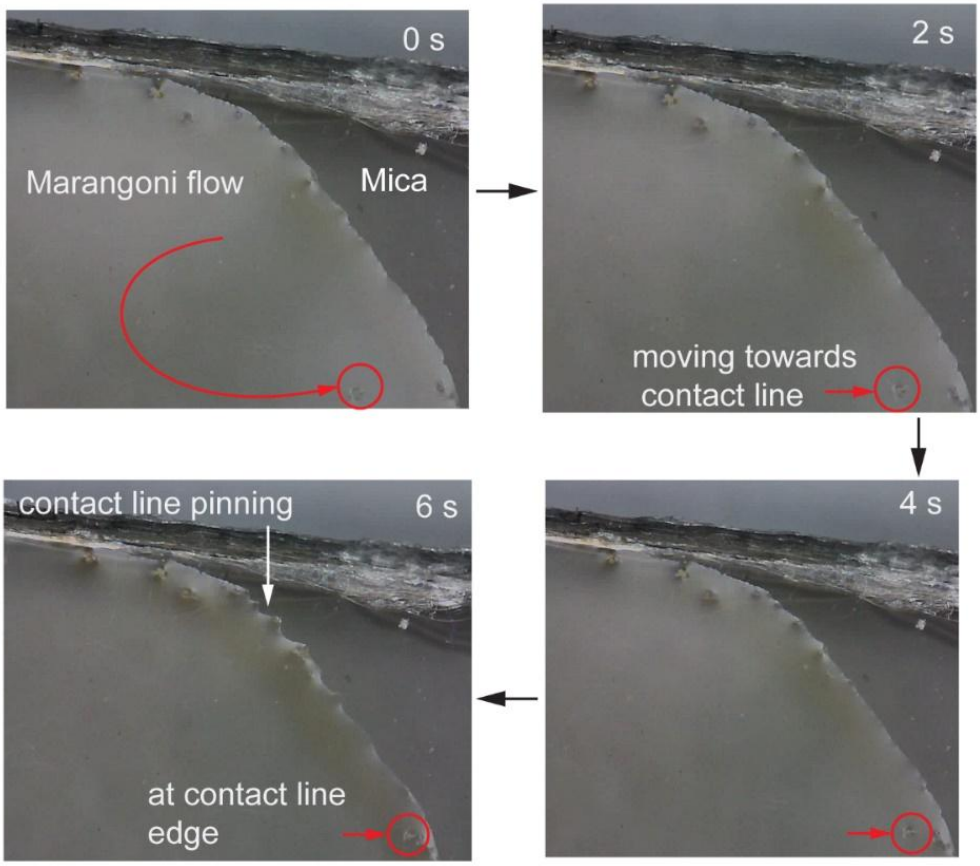

Figure 2.9. Digital microscope images of droplets showing Marangoni flow [1] of Na_2PdCl_4 particles with heating at 50℃ on a hotplate (on a cleaved mica surface); the red circle illustrates the direction of the flow within the droplet. With time, Na_2PdCl_4 particles move towards the contact line and reach the contact line after 6 seconds of heating.

As the heating proceeds, the Na_2PdCl_4 dendrite starts growing from the colder end to the hotter end of the substrate. We have observed different growth scenarios on various substrates.

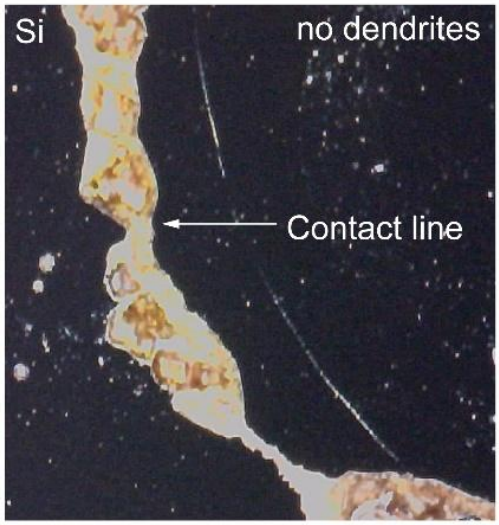

Figure 2.10. Optical image of Na_2PdCl_4 droplets showing the absence of dendrite growth on a Si substrate (due to lack of contact line pinning).

Interestingly, no dendritic growth is observed in the case of other substrates except for mica (see **Figure 2.10**, which shows no dendrites over the Si substrate). The mica surface's lower contact angle induces contact line pinning [52] (**Figure 2.11**). The system is no longer in equilibrium when NaCl is added to the $PdCl_2$ solution due to the common Cl^- ion.

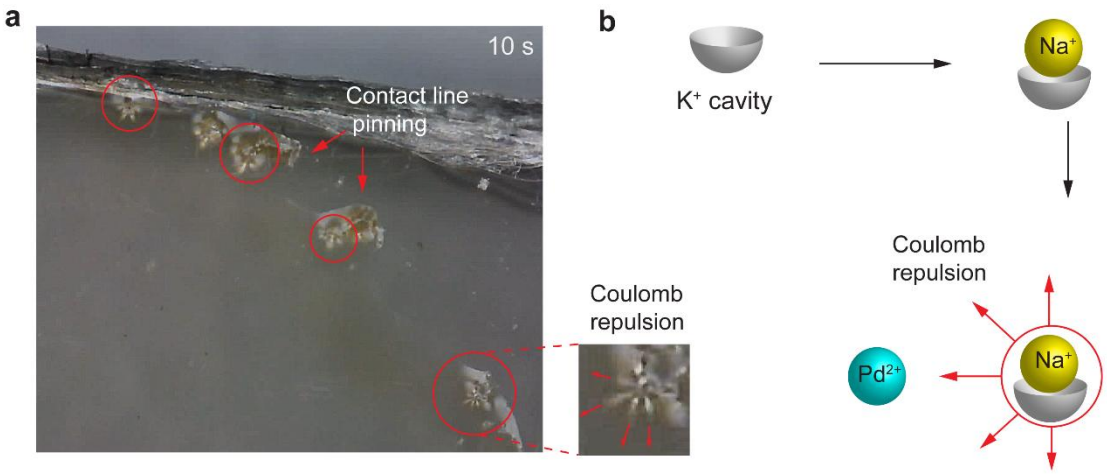

Figure 2.11. (a) Optical image of Na_2PdCl_4 droplet on mica at the time of heating showing contact line pinning and Coulomb repulsion at the droplet edge responsible for dendrite formation, (b) Schematic illustration of mechanism of Coulomb repulsion and dendrite formation; dragging of Na^+ ions towards the K^+ ion cavity and subsequent Coulomb repulsion for Pd^{2+} ions in its vicinity (red arrows show the Coulomb repulsion direction).

Therefore, increased Cl^- ions behave as stress added to the system. According to Le Chatelier's principle [53], the system will move in a direction that decreases stress. Since surface cations occupy approximately 50% of the surface sites of mica, it's natural to expect electrostatic interaction between surface K^+ ions (on the mica surface) and Cl^- ions (in Na_2PdCl_4 droplet). Likewise, the mica surface has 50% K^+ ion cavities, so we consider the possibility of co-adsorption of Na^+ and Pd^{2+} ions on the mica surface.[54] Based on our experimental observations, we propose a qualitative understanding of the *in-situ* CVD growth dynamics of dendritic $PdSe_2$. Although the growth temperature (~500°C) is well below the typical melting point of $PdCl_2$ (~670°C) and NaCl (~801°C) at atmospheric pressure, the ($NaCl+PdCl_2+H_2O$) mixture starts melting at a temperature well below the melting point of individual components because of two significant reasons, (1) pre-patterned (Na_2PdCl_4+Pd NPs) micro-structured dendrites and Pd nanoparticles have melting points much lower than that of bulk[55], (2) salt-solution assisted growth decrease the melting point[39]. A careful observation of the dendrite morphology of Na_2PdCl_4 by FESEM EDX mapping reveals that, primarily, Pd NPs aggregate along the edge of the dendrite (see **Figures 2.6f, Figure 2.12**). The Na_2PdCl_4 dendrites become immobilized during the heating and participate *in-situ* in the CVD process.

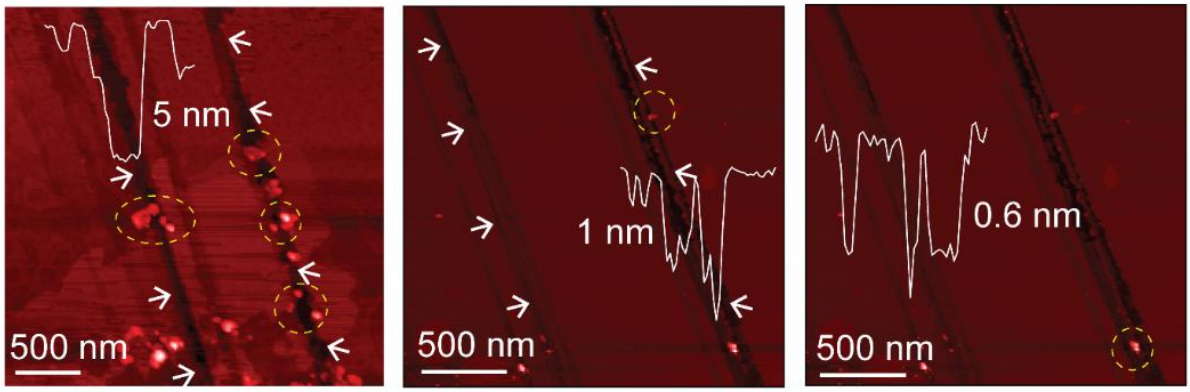

Figure 2.12. AFM image of dendrites after transfer showing Pd NPs condensed over K^+ lattice sites. White arrows indicate the edges of dendrites. The depth of the dendritic track ranges from 0.6 nm- 5 nm, as shown from the AFM height profile.

2.4.4. Mechanism for the post-CVD dendrite growth of $PdSe_2$

Careful examination of the post-CVD dendrite morphologies by FESEM (**Figure 2.13a-d**) reveals that the growth of $PdSe_2$ starts from the Pd NPs (diameter ~50 nm). **Figure 2.13a** shows a small portion of a $PdSe_2$ dendrite edge, where the expansion of $PdSe_2$ is along the movement of molten

droplet direction. AFM image in **Figure 2.13a** (inset) reveals that the thickness of the layer is 1 nm, confirming the growth of 2L $PdSe_2$. **Figures 2.13b** and **2.13c** demonstrate that the $PdSe_2$ growth direction is emulated by NaCl crystal. The squared region of **Figure 2.13c** shows a shadowy vision due to the underneath Pd NPs, which is further confirmed by the top side down FESEM image of $PdSe_2$ as shown in **Figure 2.13d**.

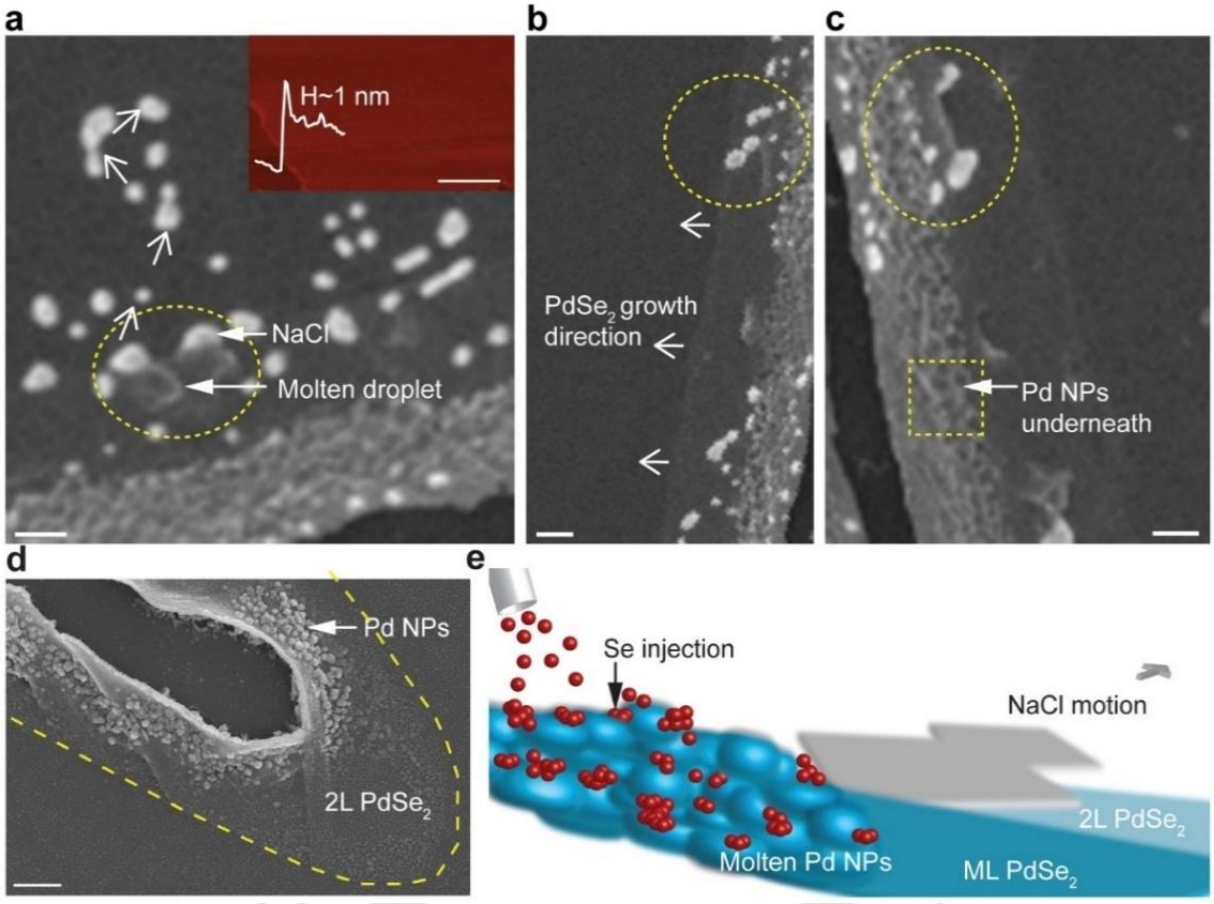

Figure 2.13. FESEM images of (a) dendritic edge showing NaCl isolation from molten droplet (yellow dotted encircled region), Inset: AFM image and height dendritic $PdSe_2$ showing a thickness of 1 nm, revealing the bilayer $PdSe_2$; scale bar is 500 nm. (b) Initiation of $PdSe_2$ growth from the Pd NPs, (c) yellow dotted square region shows shadowy vision due to underneath Pd NPs. The scale bar is 1 mm. (d) The top-side-down FESEM image of the edge of a 2L $PdSe_2$ dendrite showing top Pd NPs; the scale bar is 1 mm. (e) Schematic of the proposed mechanism for the dendrite growth of $PdSe_2$ through injection of Se atoms over molten Pd NPs during the CVD process.

Based on our experimental observations, we can provide a qualitative understanding of the growth mechanism schematically illustrated in **Figure 2.13e**. During the CVD, the immobilized Pd NPs

are the nucleation site, avoiding random nucleation, and $PdSe_2$ growth begins. Pd NPs become immobilized droplets during heating and, *in situ,* participate in the reaction. Subsequently, the upstream Se vapor is injected into the molten droplet, triggering the formation of the $PdSe_2$ nucleus. Afterward, this $PdSe_2$ nucleus gradually expands horizontally, initiating multilayer $PdSe_2$ (ML $PdSe_2$) and, finally, bilayer $PdSe_2$ growth. Further, the (Na_2PdCl_4+Pd NPs) mixture intermediate is achieved by pre-annealing the salt solution on mica without the supply of Se. Raman analysis of the annealed sample in **Figure 2.14** shows the characteristic peak of the Pd-O bond [56] at the edges.

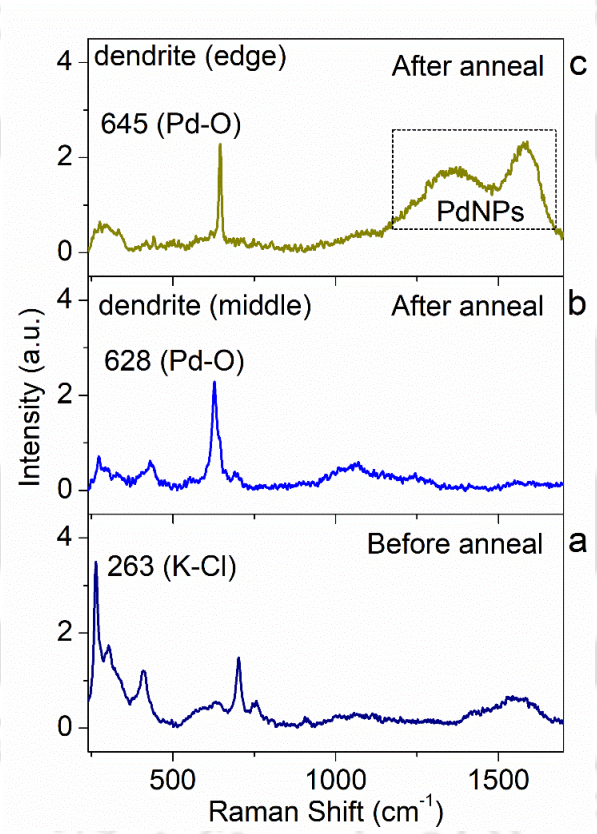

Figure 2.14. Raman spectra of Na_2PdCl_4 dendrite (a) before annealing, (b) after annealing at 400℃, (c) Pd nanoclusters at the edge of Na_2PdCl_4 dendrite after annealing at 400℃ on mica substrate.

Raman spectra suggest the formation of molten intermediate Pd-O droplets on the Pd NPs[57] (**Figure 2.14c**) before the injection of Se. The area of Pd NPs decreases, and $PdSe_2$ increases with the increase in growth time (**Figure 2.15**). As the area increases, the increase in free energy leads to a driving force for the Pd-O droplet to displace laterally till the Pd and Se are fully consumed.[58] The supersaturated precursor is prone to being driven away from the site-specific positioned Pd-O

droplets and towards the NaCl crystal-driven direction. Here, NaCl plays a key role in reducing the melting of the precursors and enabling the directed growth of bilayer $PdSe_2$. The NaCl has the property to spontaneously move from a region of low surface energy to a region of high surface energy.[59] Concurrently, the solubility of Se in NaCl decreases rapidly, which further separates the NaCl from the droplet and drives the movement of the NaCl to the edge of $PdSe_2$.

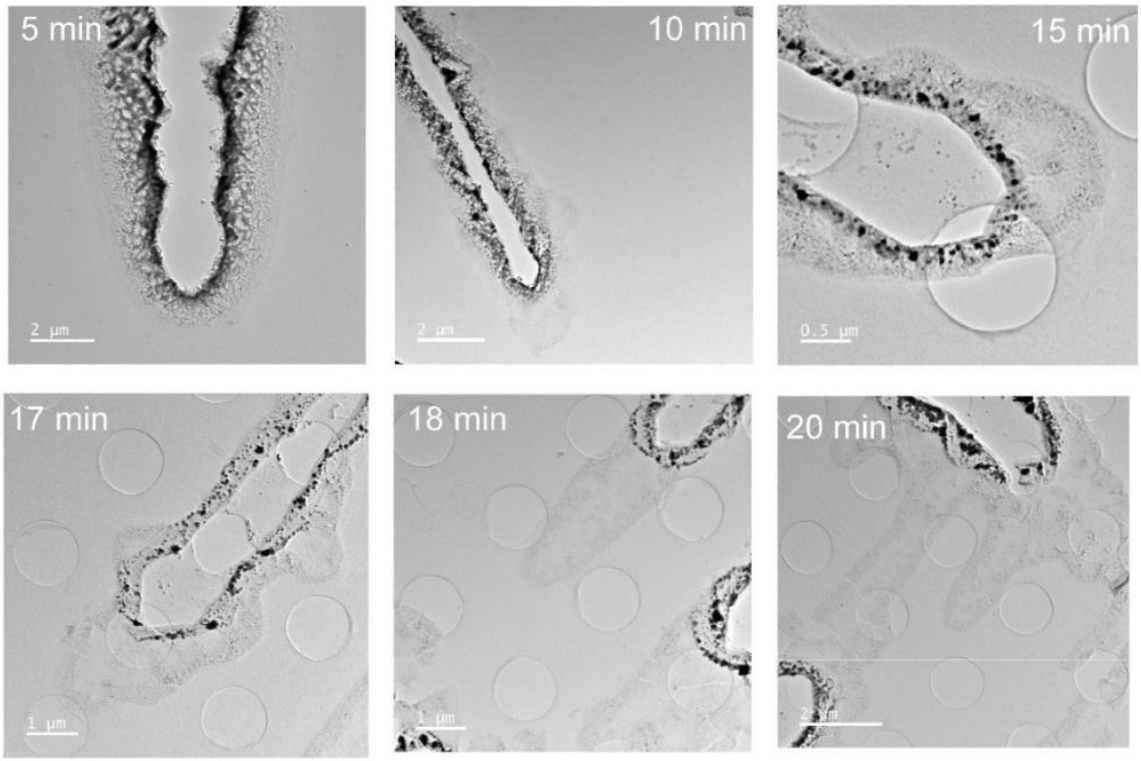

Figure 2.15. TEM images of $PdSe_2$ dendrites grown after different growth times. The area/density of Pd NPs decreases, and the area of 2D $PdSe_2$ increases with increasing growth time.

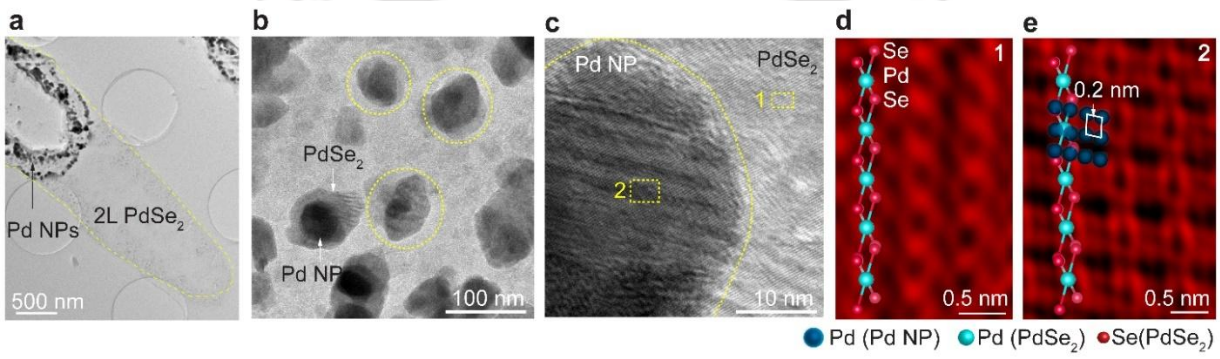

Figure 2.16. (a) Bright-field TEM image of the bilayer $PdSe_2$ dendritic end, (b) the corresponding magnified view of the Pd NPs, (c) HRTEM lattice image of Pd NPs, (d) the corresponding magnified view taken from regions 1 and 2 of dendrite edge showing $PdSe_2$ chain, and (e) Pd NP decorated $PdSe_2$ chain.

The crystal extension is not terminated until the NaCl runs out of stock. Unlike the 2L $PdSe_2$ regions, which are uniform in contrast (yellow dotted region in **Figure 2.16a**), the inner edge region of the dendrite exhibits darker regions due to the presence of Pd NPs (**Figure 2.16a**). To gain further insight, we investigate the edge structure containing Pd NPs and its precursory $PdSe_2$, as shown in **Figure 2.16b**. **Figure 2.16c** presents a Pd NP extended out of a $PdSe_2$ dendrite, and **Figures 2.16d** and **2.16e** present two types of atomic resolution HRTEM images taken from different regions from **Figure 2.16c**. In region 1, the more intense spots in the chain-like projection correspond to Pd atoms, while the two sides of the $PdSe_2$ chain with less intensity scale correspond to Se atoms. In the $PdSe_2$ chain, the Pd-Pd distance is 0.29 nm. The intensity of Pd and Se decreased in region 2, suggesting Pd NPs are on the top of the $PdSe_2$ chain. In the top layer, Pd NPs show a Pd-Pd distance of 0.2 nm, corresponding to crystalline Pd NPs.

2.4.5. Region wise growth

A further understanding of CVD-grown $PdSe_2$ dendrite morphology by SEM (**Figure 2.17a**) reveals that there exist three regions. The formation of three regions can be explained as follows. (1) Region 1: Because of pre-patterning of the mica substrate with a quartz mask using Na_2PdCl_4 solution (drop cast) followed by heating at 50 °C, which results in the formation of Pd source region (Pre-CVD), which turns into bulk $PdSe_2$ region after selenization inside CVD (region R1), (2) Region 2: At the initial stage of growth, during CVD under Se poor condition, bulk $PdSe_2$ from region R1 gradually expands to form multilayer $PdSe_2$ (region R2) and, (3) Region 3: at later stage of growth, during CVD under Se rich condition (sufficient Se vapor pressure), expansion of region R2 leads to the formation of bilayer $PdSe_2$ region (Region R3), which is away from the source region (region R1).

Interestingly, these three regions can be isolated in a controlled manner. At first, using water-assisted transfer, region R1 can be transferred on any arbitrary substrate, while region R2 and R3 remain on the mica substrate. Subsequently, region R2 can be separated by the scotch tape transfer method, and finally, region R3, containing only bilayer $PdSe_2$, remains on the parent substrate for further studies. The enlarged view of the square dotted yellow box of **Figure 2.17a** in **Figure 2.17b** illustrates different regions (marked as R1, R2, and R3). To validate our conjecture about the different regions, we have acquired position-dependent Raman spectra (**Figure 2.17c**) over the dendrite surface.

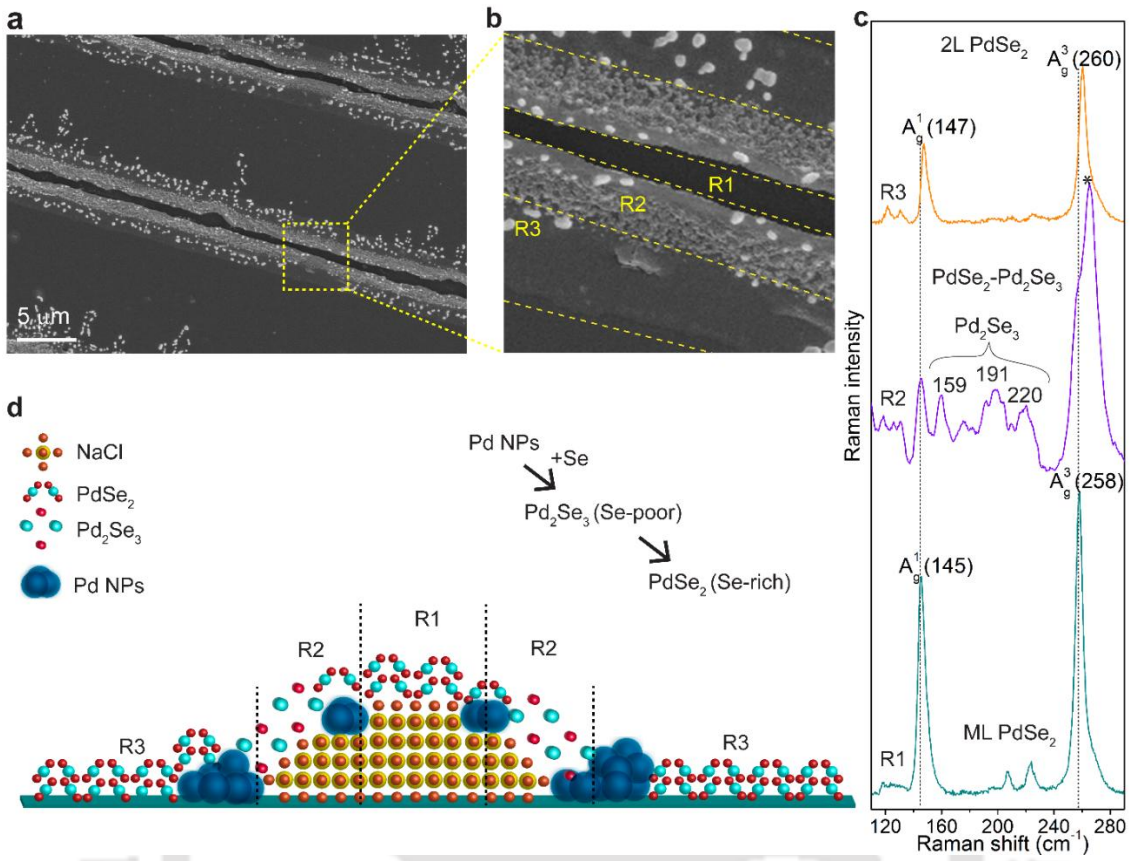

Figure 2.17. (a) FESEM image of parallel dendrites of 2L $PdSe_2$, (b) enlarged view of a dendrite along the width highlighting three regions: R1, R2, and R3. (c) Raman spectra of R1, R2, and R3 regions showing $PdSe_2$, $PdSe_2$-Pd_2Se_3 and 2L $PdSe_2$ growth, respectively, * symbol corresponds to K-Cl bond (263 cm^{-1}) of mica, (d) schematic illustration of the three regions showing the layer content; beginning of Pd_2Se_3 from Pd NPs at a Se-poor environment and $PdSe_2$ at Se-rich environment.

We found that the R1 and R3 regions contain only the 2D $PdSe_2$ phase, while the R2 region contains a mixed phase (both 2D $PdSe_2$ and 2D Pd_2Se_3 phases). The Raman spectrum of the R2 region contains all the characteristic peaks of the $PdSe_2$ and Pd_2Se_3 phases (see **Figure 2.17c**). At R1, the A^1_g and A^3_g Raman modes of the $PdSe_2$ phase lie at 144 and 257 cm^{-1}, suggesting the formation of ML $PdSe_2$. It is worth mentioning that the R1 and R2 regions show the same Raman peaks, indicating the similar thickness of the $PdSe_2$ layer in both regions. Region R1 contains multilayer $PdSe_2$, while region R2 contains multilayer $PdSe_2$ along with $PdSe_2$-Pd_2Se_3 junction and Pd NPs, whereas region R3 contains only bilayer $PdSe_2$. As the Raman peak position of bilayer $PdSe_2$ is different than the multilayer $PdSe_2$, it can be stated that regions R1 and R2 contain multilayer $PdSe_2$, consistent with the same peak position for the A^1_g mode. Note that the A^1_g mode intensity in region R2 is lower than that of R1 due to the presence of defects in $PdSe_2$ and the mixed phase of $PdSe_2$ and Pd_2Se_3. In the case of R3, the upshift of the A^1_g mode is indicative of

the lower thickness, i.e., bilayer $PdSe_2$. The thickness of different regions was confirmed by the AFM height profile analysis, which is consistent with the Raman analysis. However, there is a sudden drop in Raman intensity in the R2 region, which is attributed to the presence of NaCl and Pd NPs below the $PdSe_2$ layer in R2 (schematically shown in **Figure 2.17d**). At the R2 region, we observe the A^1_g and A^3_g Raman modes of the $PdSe_2$ phase, the same as the R1 region, along with three additional peaks at 159 cm^{-1}, 191 $cm^{-1,}$ and 220 cm^{-1} corresponding to 2D Pd_2Se_3, which is similar to the theoretical Raman modes of Pd_2Se_3.[60] FESEM and STEM EDX spectrum of the junction region of a dendrite shows an atomic stoichiometry of ~2:3, suggesting clearly the formation of the Pd_2Se_3 region (**Figure 2.18**).

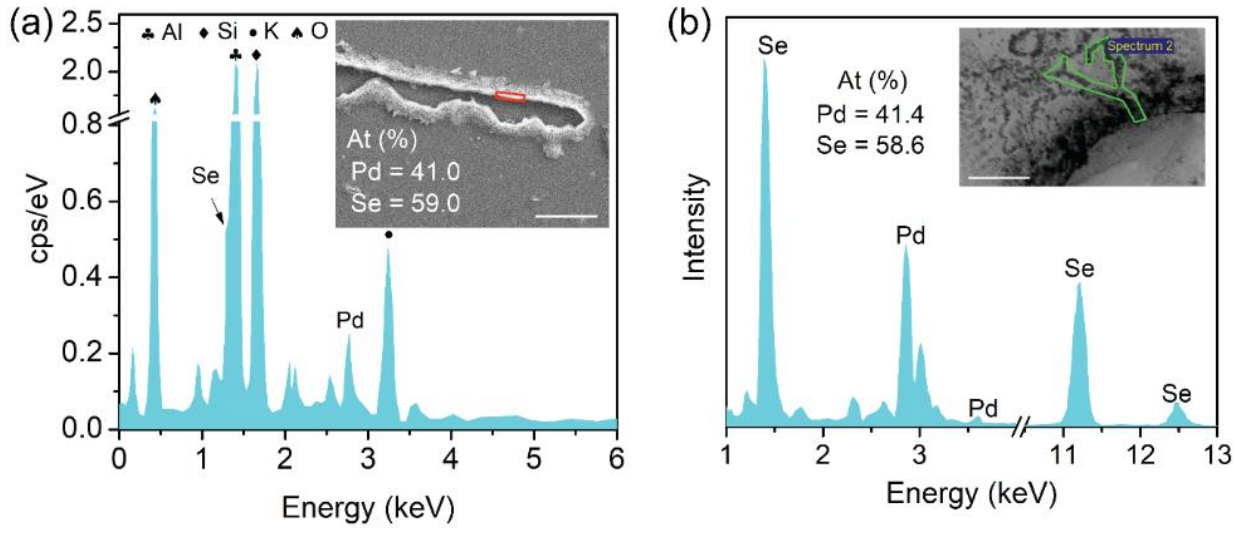

Figure 2.18. (a) EDX spectrum of the R2 region of a dendrite (marked with a red rectangle in the inset dendrite) showing the atomic composition corresponding to Pd_2Se_3 formation. (b) STEM EDX spectrum of a spitted junction region of a dendrite showing atomic stoichiometry of ~2:3. Scale bar is 5 μm for the inset of (a) and 500 nm for the inset of (b).

The B^1_{1g} mode arises due to the outer mode vibration [5], and the change of stoichiometry from $PdSe_2$ to Pd_2Se_3 shifted the B^1_{1g} mode and generation of Pd_2Se_3 peak at 159 cm^{-1}. At R3, we observe $PdSe_2$ peaks at 147 cm^{-1} and 260 cm^{-1}, confirming the formation of bilayer $PdSe_2$.[5] **Figure 2.17d** schematically shows the content of 3 different regions of the dendrites. The R1 region is comprised of the NaCl layer at the bottom and PdSe2 at the top layer. In R2, Pd NPs are the source of Pd. During the CVD, when the upstream Se vapor is injected into the molten Pd-O droplet, it triggers the formation of Pd_2Se_3 in the Se poor condition. This nucleus gradually expands horizontally, initiating continuous growth of bilayer $PdSe_2$ when further supply of Se heads to a

Se-rich atmosphere is created inside the CVD chamber. Increasing Se changes the ratio of metal: chalcogen from 1:0 to 2:3 to 1:2, first from Pd NPs to Pd_2Se_3 (in Se-poor condition) and then finally to $PdSe_2$ (in Se-rich condition). At the beginning of the CVD process, a possible Se-poor condition leads to a decrease in interlayer distance, resulting in the chemical stoichiometry of Pd_2Se_3. [61, 62]

2.4.6. H_2O assisted transfer mechanism

Since the presence of a NaCl catalyst is not desirable in the final growth product, as it degrades the film with time (**Figure 2.19**), it is essential to eliminate NaCl from $PdSe_2$ dendrites.

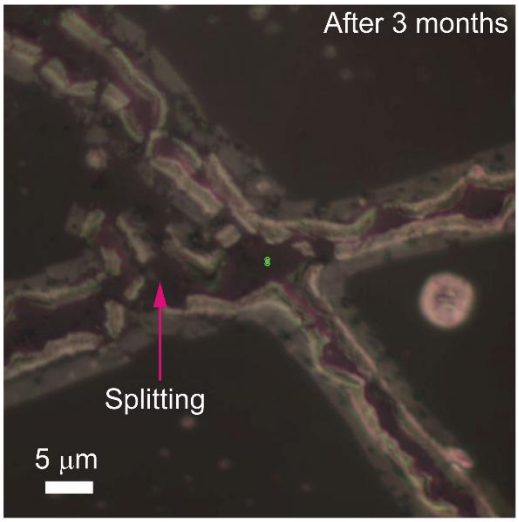

Figure 2.19. (a) Optical image of NaCl-assisted grown $PdSe_2$ dendrite after 3 months.

In general, the transfer methods of 2D materials usually involve polymer-assisted transfer, such as PVA, PMMA, etc. [63] These polymers leave a thin layer of long-chain residual molecules on the 2D material surface, and it may alter the intrinsic properties of 2D materials. It is worth noting that most of the reported $PdSe_2$ transfer techniques relied on etchants, such as KOH and HF solutions, and PMMA for detaching the samples from the growth substrates. [40-42] In contrast, in this work, we took advantage of the presence of NaCl-salt and consequently adopted a water (H_2O) assisted transfer technique that didn't involve any polymer throughout the delamination process. A critical delamination process has been recorded for a clear demonstration of the efficacy of the transfer process, and it is indeed very fast (within a few seconds) and a facile technique (Kindly refer the video here). During this process, an H_2O film bridges the $PdSe_2$ layer to the inner edges

of the mica and pulls it away from the mica surface. At the $H_2O/PdSe_2$ interface, the driving force originates from the out-of-plane shear, where the shear stress is normal to the $PdSe_2$ surface [64]. Due to the high surface tension of H_2O (72 mNm^{-1}) [65], the thin $PdSe_2$ film is successfully isolated and floated freely on the water surface. The H_2O membrane stretches until the whole $PdSe_2$ layer is lifted from the mica surface. It is worth noting that we have not used any polymer throughout the delamination process (**Figure 2.20a**), and thus our process is contamination-free. **Figures 2.20b** and **2.20c** show the FESEM images of as-grown $PdSe_2$ dendrite on the mica substrate before and after transfer. A successful transfer is confirmed from the FESEM image of the transferred $PdSe_2$ dendrite on a SiO_2 substrate (**Figure 2.20d**). The structural integrities of $PdSe_2$ dendrite detached from the growth substrates were characterized and confirmed by Raman spectroscopy. Raman spectra of $PdSe_2$ transferred on SiO_2 show (**Figure 2.20e**) all the characteristic Raman modes that exhibit higher intensity compared to mica, indicating a high-quality transfer of $PdSe_2$ and its adhesion with the SiO_2 substrate. After transfer, the remaining $PdSe_2$ in the R3 region is confirmed from the corresponding Raman spectra. **Figure 2.20f** schematically illustrates the successful transfer of $PdSe_2$ to the target substrate aided by the dissolution of underneath NaCl. For a better understanding of R3, we have measured the thickness after H_2O transfer. As the bottom layers of R1 and R2 contain NaCl, after H_2O-assisted transfer, both layers are easily removed due to the out-of-plane shear.[64] **Figure 2.20g** shows a step height (AFM) of ~1 nm for 2L $PdSe_2$ collected from the R3 region of a dendrite, confirming the formation of bilayer $PdSe_2$. Boundary line flips are commonly observed due to out-of-plane shear during H_2O transfer. **Figure 2.20h** represents dark field TEM images of a hollow (center region) $PdSe_2$ dendrite after the water-assisted transfer process. **Figures 2.20i** and **2.20j** represent the corresponding Pd and Se mappings of $PdSe_2$ dendrites, further validating that the bottom layer of R1 contains NaCl. Most of the NaCl crystals are fully etched out in H_2O transfer, which confirms that NaCl is underneath R1, which helps in lifting the $PdSe_2$ film.

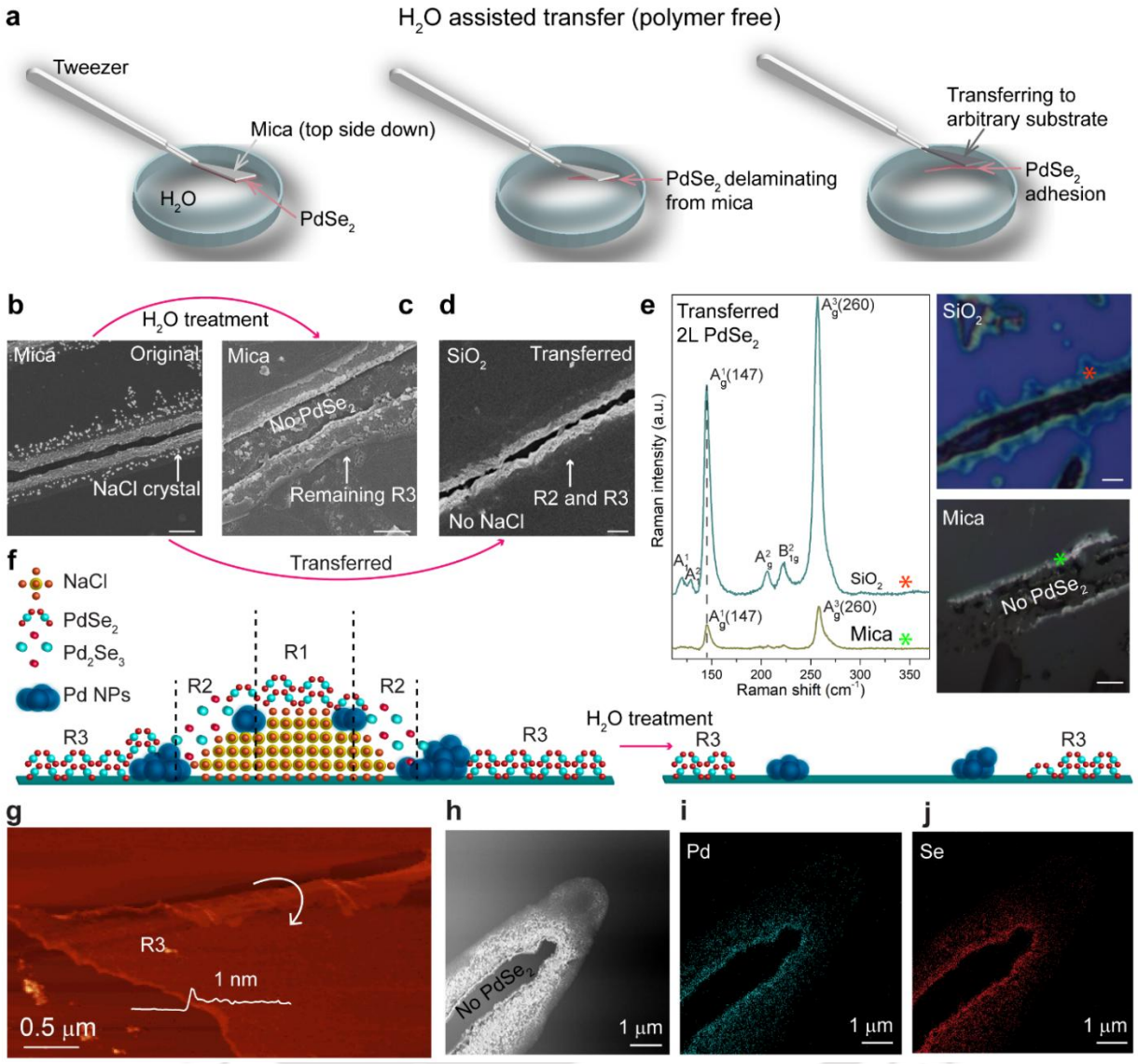

Figure 2.20. (a) Schematic illustration of H_2O-assisted transfer process of 2L $PdSe_2$ from mica substrate ($PdSe_2$ layer facing downward) to arbitrary substrate. (b) FESEM image of a $PdSe_2$ dendrite on original growth substrate before transfer, (c) FESEM image showing the successful removal of $PdSe_2$ dendrite from mica substrate after H_2O transfer, (d) transferred 2L $PdSe_2$ dendrite on SiO_2 substrate. The scale bar is 2 μm in each image. (e) Raman spectra at the marked (*) location after H_2O-assisted transfer on SiO_2 and mica substrate. (f) Schematic illustration of the different layers before and after transfer of $PdSe_2$, (g) AFM image of one edge of a dendrite after H_2O transfer reveals intact bilayer $PdSe_2$, delamination and twisting of R3 region occurs due to the out-of-plane shear. (h) Dark field TEM images of $PdSe_2$ dendrite showing removal of $PdSe_2$ from the central region, (i, j) the corresponding mapping of Pd and Se atoms, respectively.

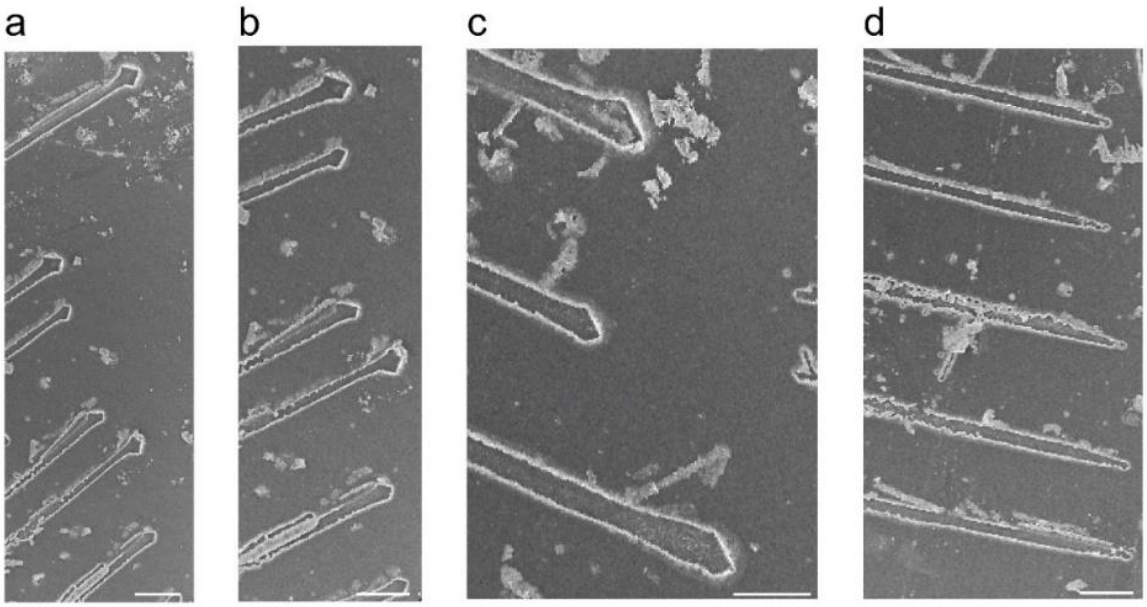

Figure 2.21. (a-d) FESEM images of *in-situ* grown parallel $PdSe_2$ dendrites after H_2O-assisted transfer. The scale bar is 5 μm.

Figure 2.21 shows the FESEM image of an array of parallel $PdSe_2$ dendrites. The terminated dendrite (**Figure 2.21**) size closely resembles a NaCl square, which is fully etched out after the H_2O transfer. AFM was employed to evaluate the detailed morphology of different regions of a dendritic $PdSe_2$ layer. Note that due to the underneath NaCl and Pd NPs layer, the thickness of the R1 and R2 regions is much higher (~200 nm, see **Figure Figures 2.22a, 2.22b**) than the R3 region.

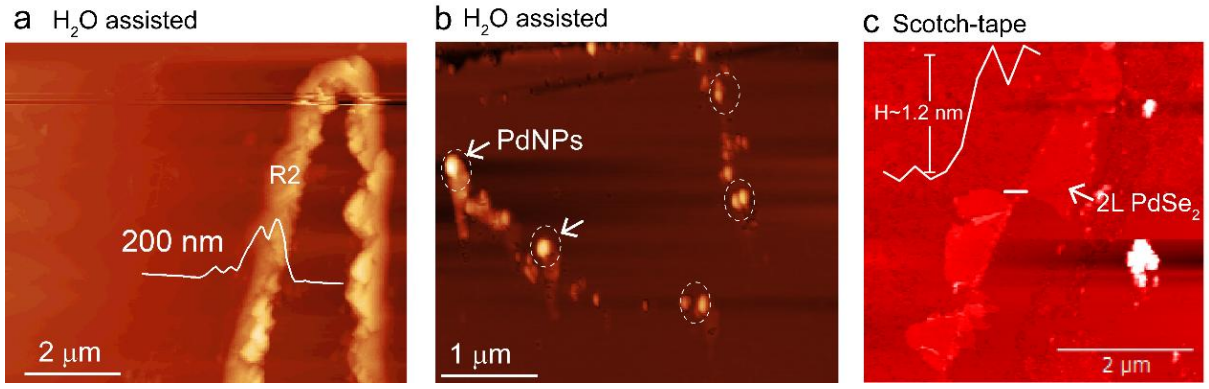

Figure 2.22. AFM topographic image of (a) R2 region of a $PdSe_2$ dendrite (showing high thickness due to the underneath NaCl layer and Pd NPs, (b) Residual Pd NPs on mica substrate after H_2O transfer. (c) Scotch tape transferred 2L $PdSe_2$, showing a thickness of 1.2 nm in the R3 region.

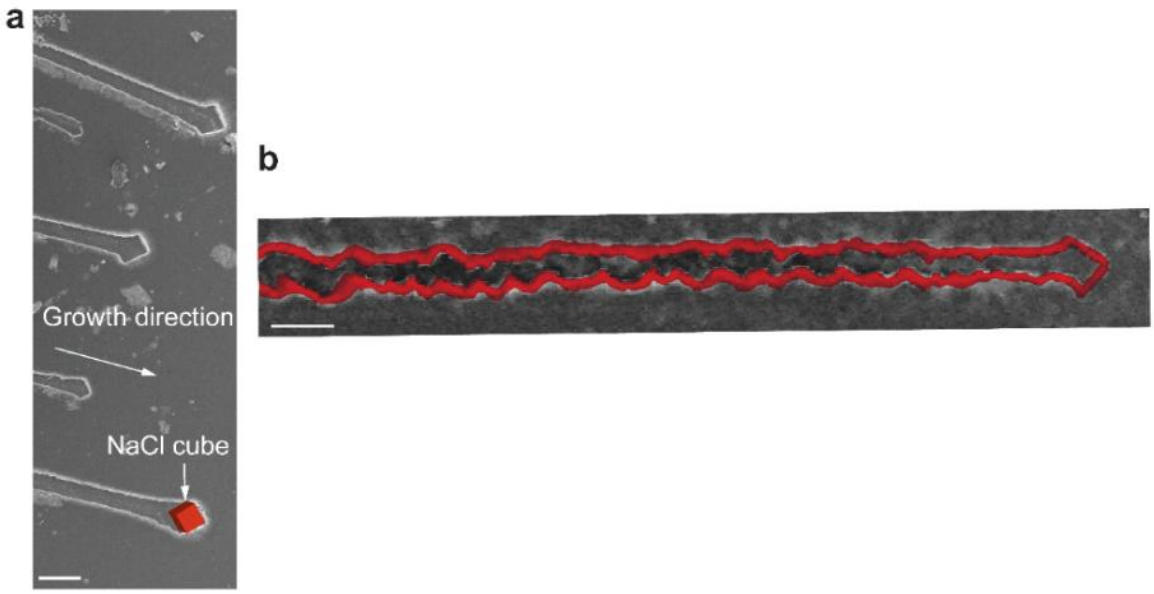

Figure 2.23. (a) FESEM images of parallel $PdSe_2$ dendrites at the end of the growth where the end shape mimics the NaCl cube shape. (b) FESEM image showing a single dendrite. The scale bar is 5 μm.

2.4.7. $PdSe_2$-Pd_2Se_3 junction region

To further investigate the Pd_2Se_3 region, we conducted scanning transmission electron microscopy (STEM) imaging/mapping of the sample. **Figure 2.24a** shows the bright field STEM image of a dendrite. Noticeably, the middle portion of the dendrite is empty due to the H_2O-assisted transfer process. As explained earlier, the R1 and R2 regions have an underneath NaCl layer; during the transfer process, the bottom layers of the R1 and R2 region form a step-climbing epitaxy. H_2O insertion begins with the layer of R2, subsequently in R1 underneath, and dissolves the NaCl layer. The insertion of H_2O below the $PdSe_2$ layer uplifts the R1 and R2 region, which is separated from R3. The R1 region is divided from R2 and R3 due to the presence of a phase transition region in R2. The R1 region was removed from the dendrite, making a hollow dendrite structure (see **Figure 2.24a**). The area of Pd_2Se_3 is the darker spilt region, which encompasses non-uniformly over the R2. Pd_2Se_3 is selectively formed at defect-rich regions containing, e.g., grain boundaries and edges around the Pd NPs. Pd_2Se_3 started forming at the edges and grain boundaries and grew to smear around the Pd NPs, forming a patch-like structure. Contrary to other 2D materials, the exfoliation of bilayer $PdSe_2$ results in the formation of the Pd_2Se_3 layer.[66] EDX spectrum of yellow shaded portion at the boundary of R2 (**Figure 2.24b**) confirms the formation of Pd_2Se_3.

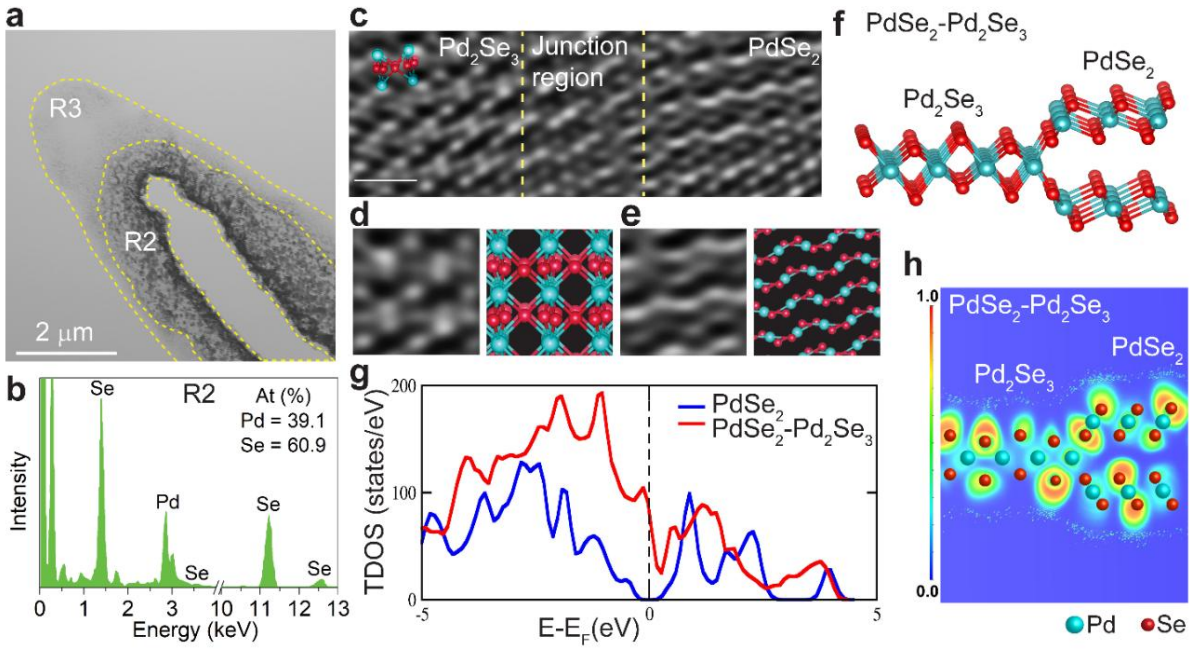

Figure 2.24. (a) TEM image of a $PdSe_2$ dendrite after water-assisted transfer, Scale bar is 2 μm. (b) EDS spectrum at R2 showing the atomic stoichiometry of Pd and Se is ~2:3, corresponding to Pd_2Se_3 formation. (c) HRTEM lattice image of sandwiched $PdSe_2$-Pd_2Se_3 junction, the junction region is highlighted by yellow dashed lines, (scale bar is 0.5 nm), (d) the enlarged view of Pd_2Se_3 (left panel of (c)) shows the butterfly-like structure and its corresponding atomic model, (e) the enlarged view of $PdSe_2$ (right panel of (c)) and its corresponding atomic model, (f) side view of the $PdSe_2$-Pd_2Se_3 junction (Pd (cyan), Se (red)), and (g) corresponding DOS plot of $PdSe_2$ and $PdSe_2$-Pd_2Se_3 junction obtained from DFT calculation, (h) electron localization function (ELF) of the $PdSe_2$-Pd_2Se_3 junction.

Atomic resolution HRTEM image (**Figure 2.24c**) at a portion of R2 reveals the existence of two types of lattice structures (Pd_2Se_3 and $PdSe_2$) with a sandwiched $PdSe_2$-Pd_2Se_3 junction. Both Pd_2Se_3 and $PdSe_2$ structures agreed well with the structure of bilayer Pd_2Se_3 with AB stacking.[67] The enlarged view of the Pd_2Se_3 structure (**Figure 2.24d**) exhibits a peculiar butterfly-like periodic array. Likewise, the enlarged view of $PdSe_2$ is shown in **Figure 2.24e** with the corresponding atomic model. The $PdSe_2$-Pd_2Se_3 junction is created by bonding between the Pd_2Se_3 monolayer and the $PdSe_2$ bilayer (**Figure 2.24f**). This structure is utilized to calculate the band structure of the junction employing DFT. Interestingly, the calculated band structure of the $PdSe_2$-Pd_2Se_3 junction exhibits a spike in the DOS at the Fermi level (see **Figure 2.24g**), depicting the metallic characteristic of the junction in contrast to the semiconducting nature of the $PdSe_2$ layer. Considering the $PdSe_2$-Pd_2Se_3 junction, we further calculated the electron localization function (ELF) at the junction. Due to the electro-negativity, electrons prefer to be located on the Se atoms, and the electron densities around Pd are low (**Figure 2.24h**). At the junction, an electric field could be built within the interface region.[68] We have analyzed AFM to confirm the presence of intrinsic

defects (**Figure 2.25**). **Figure 2.25** shows defective regions (white dotted regions) with pores-like features with a depth of ~0.4 nm.

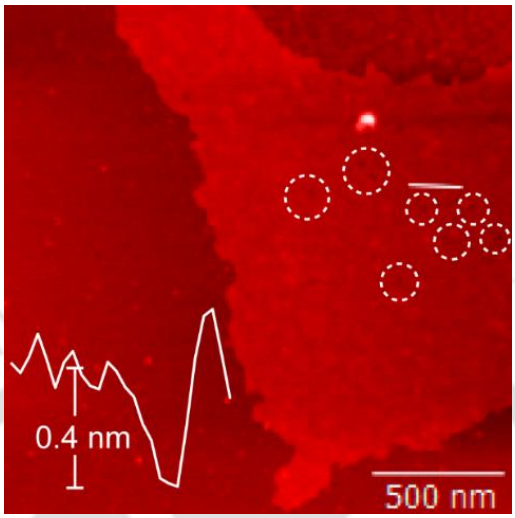

Figure 2.25. AFM image of PdS_2 shows the presence of defective regions (white dotted regions) with pores-like features with a depth of ~0.4 nm.

2.4.8. Metallic behavior of $PdSe_2$-Pd_2Se_3 junction

In light of the above discussion, the unique metallic behavior of the $PdSe_2$-Pd_2Se_3 junction was next exploited in SERS sensing of methylene blue (MB) molecule (schematically shown in **Figure 2.26a**). Micro-Raman analysis was carried out at $PdSe_2$, $PdSe_2$-Pd_2Se_3, and Pd NPs enveloped $PdSe_2$-Pd_2Se_3 ($PdSe_2$-Pd_2Se_3/Pd NPs) regions with MB molecules using a 532 nm laser line. Consistent with the theoretical calculation results of metallic behavior, we observe a higher signal of the SERS spectrum of MB molecules at the $PdSe_2$-Pd_2Se_3 junction region (**Figure 2.26b**, middle panel) than that of the bare $PdSe_2$ region (**Figure 2.26b**, lower panel). The SERS spectrum of MB molecules at the $PdSe_2$-Pd_2Se_3 junction region decorated with Pd NPs with an average diameter of 50 nm shows significantly higher enhancement of the Raman signal. It is found that the high SERS signal on $PdSe_2$-Pd_2Se_3/Pd NPs regions (**Figure 2.26b**, upper panel) is due to the dense accumulation of MB molecules along the $PdSe_2$-Pd_2Se_3 junction regions. The $PdSe_2$ peak at 147 $cm^{-1,}$ along with extra peaks of Pd_2Se_3 at 162 cm^{-1} and 193 $cm^{-1,}$ confirm the presence of both phases in the junction region. **Figure 2.26c** reveals a huge variation in SERS intensities (I) between $PdSe_2$ and $PdSe_2$-Pd_2Se_3 with $PdSe_2$-Pd_2Se_3/Pd NPs.

$$I\ (PdSe_2\text{-}Pd_2Se_3/Pd\ NPs) > I\ (PdSe_2\text{-}Pd_2Se_3) > I\ (PdSe_2).$$

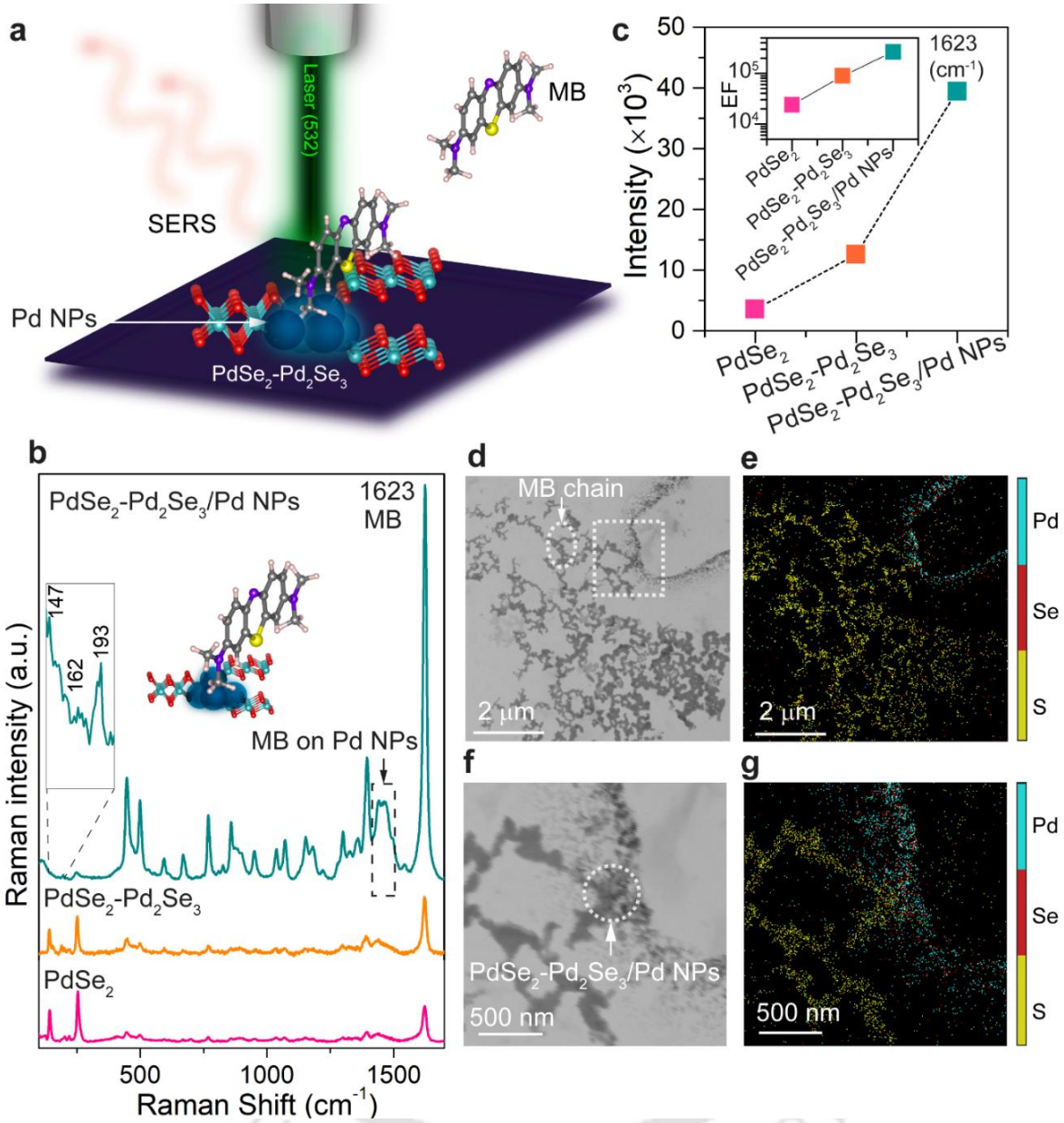

Figure 2.26. $PdSe_2$-Pd_2Se_3/Pd NPs as a SERS sensor: (a) schematic of MB SERS sensing at Pd NPs decorated $PdSe_2$-Pd_2Se_3 junction SERS signal is much higher at the $PdSe_2$-Pd_2Se_3/Pd NPs region, (b) Comparative SERS spectra of MB on $PdSe_2$, $PdSe_2$-Pd_2Se_3, and on $PdSe_2$-Pd_2Se_3/Pd NPs. For each spectrum, maximum intensity counts are fixed at 40k. (c) the corresponding intensity plot for different regions. The inset shows the log plot of the calculated enhancement factor (EF). (d) Low-resolution bright field TEM image shows that the joining of MB chains starts at the junction in a head-to-tail manner, (e) corresponding color mappings of Pd (cyan), Se (red), and S (yellow). 'S' highlights the MB chain. (f) magnified view of (d) showing the joint between the MB chain and $PdSe_2$-Pd_2Se_3/Pd NPs, and (g) the corresponding color mappings of Pd, Se, and S.

Among these, the $PdSe_2$-Pd_2Se_3/Pd NPs exhibit the highest intensity peak, which implies its highly sensitive nature towards SERS. It clearly indicates that Pd NPs on metallic $PdSe_2$-Pd_2Se_3 junction play a vital role in such a high SERS activity. Further, we performed a SERS measurement of the MB molecule to calculate the detection efficiency in different regions. The enhancement factor (EF) is calculated using the following equation, $EF = \frac{I_{SERS}}{I_{RS}} \times \frac{C_{RS}}{C_{SERS}}$ where I_{SERS} and I_{RS} are the SERS and Raman signal intensities, respectively, and C_{SERS} , C_{Rs} are the corresponding concentrations for whom the intensities are considered. The calculated enhancement factor (EF) in the inset of **Figure 2.26c** (log plot) reflects a huge change in EF from $PdSe_2$ to $PdSe_2$-Pd_2Se_3/Pd NPs. It is evident that $PdSe_2$-Pd_2Se_3/Pd NPs can serve as a SERS substrate with MB molecule detection with an enhancement factor of $\sim 3\times10^5$, which is 11 times higher than $PdSe_2$ to detect MB molecules due to the metallic nature of the junctions. MB exists in cation form in a highly polar solvent like water.[64] Because of the metallic nature, the $PdSe_2$-Pd_2Se_3 junction and Pd NPs create an electric field and attract bipolar molecules.[70] Due to the polarity of MB, further adsorption of molecules occurs in a head-to-tail manner; the process repeats and finally forms long chain aggregates (**Figure 2.26d, 2.26f**). To verify the existence of the interaction between MB molecules with $PdSe_2$-Pd_2Se_3/Pd NPs regions, we further investigated it with EDX mapping of Pd, Se, and S elements. **Figures 2.26e** and **2.26g** reveal that the signals arising from the S atoms of the foreign molecule (MB) are due to the formation of MB chains. The S mapping leads us to speculate that the joining of MB molecules originates at the Pd NPs decorated $PdSe_2$-Pd_2Se_3 junction regions (indicated as 'Joint'). Our in-situ grown $PdSe_2$-Pd_2Se_3/Pd NPs regions show ultrahigh enhancement of the characteristic peak of MB molecule (1623 cm^{-1}) with an intensity count of 40k (**Figure 2.26b**). This indicates that the Pd NPs decorated $PdSe_2$-Pd_2Se_3 junctions have high potential as an efficient SERS substrate.[71]

2.4.9. Mechanism of high SERS sensitivity

The mechanism of SERS enhancement is described with the help of FEM simulation of Pd NPs without $PdSe_2$ (**Figure 2.27**), Pd NPs on $PdSe_2$ (**Figure 2.27a**) and Raman mapping (**Figure 2.27b-d**). The signal from $PdSe_2$ with Pd NPs shows dramatic improvement of the MB Raman signal (1623 cm^{-1} peak), signifying the important contribution from the Pd NPs in SERS enhancement.

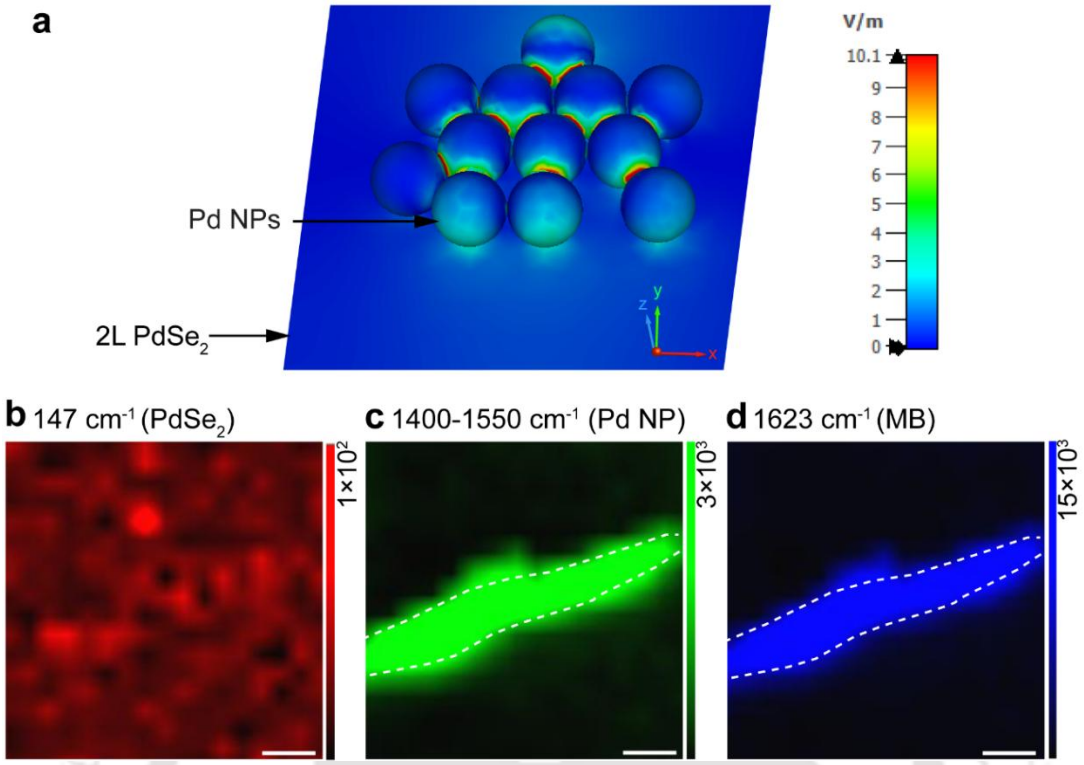

Figure 2.27. (a) FEM simulation of the electric field distribution of Pd NPs on bilayer $PdSe_2$ under 532 nm excitation. (b) The Raman intensity mapping of 147 cm^{-1} peak of $PdSe_2$, (c) 1400-1550 cm^{-1} peak of Pd NP, and (d) 1623 cm^{-1} peak of MB respectively. The scale bar is 2 μm.

Further, Raman mapping of MeB depicts that along the junction region, the Raman intensity is highest due to the presence of Pd NPs.

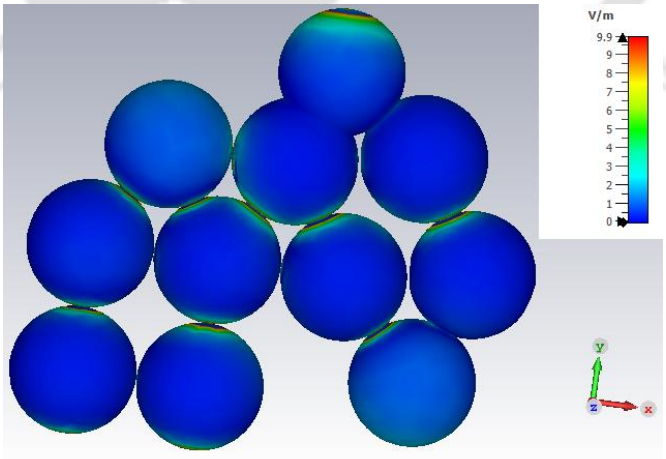

Figure 2.28. FEM simulation of the electric field distribution of Pd NPs under 532 nm excitation.

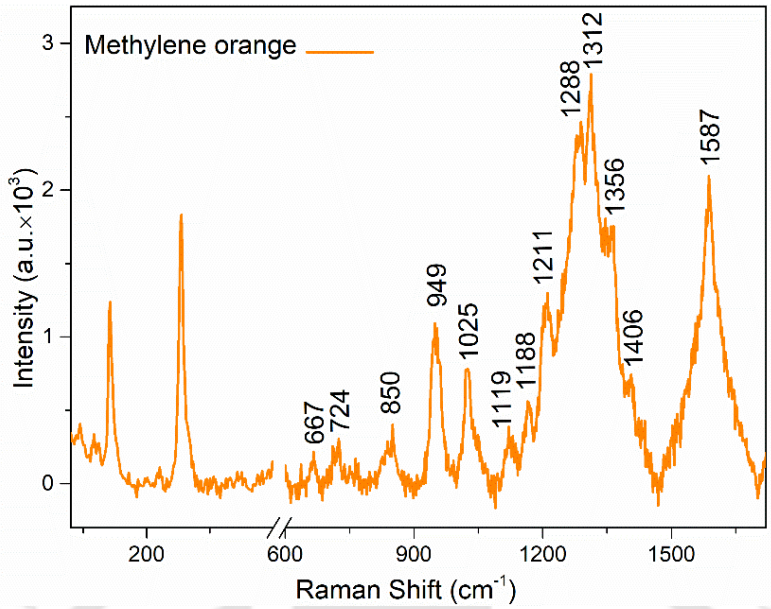

Figure 2.29. SERS spectra of 10^{-4} M of methylene orange on 2L $PdSe_2$.

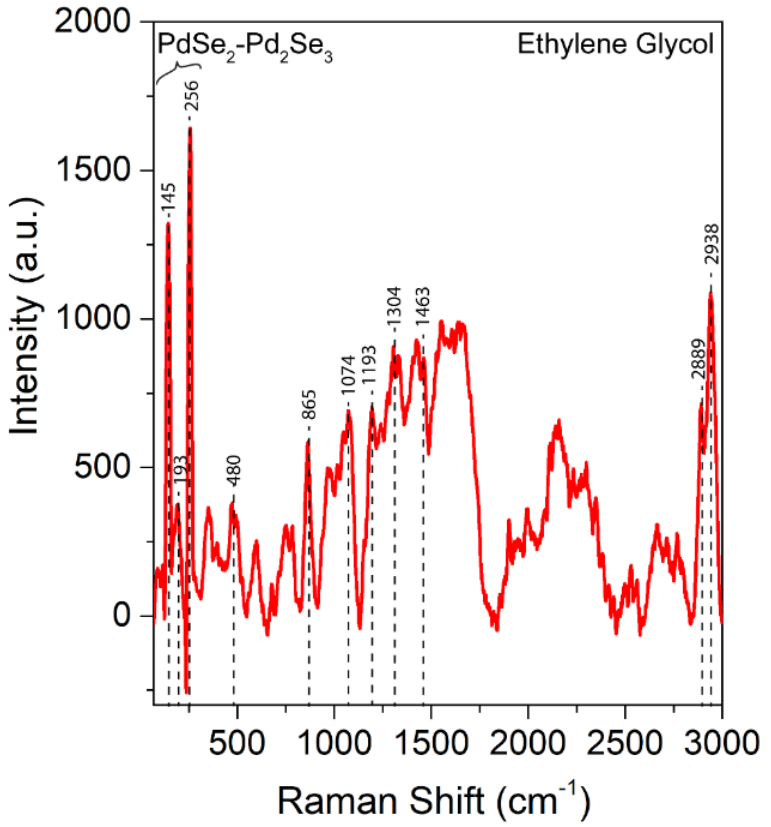

Figure 2.30. SERS spectra of Ethylene Glycol on 2L $PdSe_2$.

With the help of additional data and FEM simulation of the electromagnetic (EM) field enhancement factor, we show that the measured EF (3×10^5) is contributed by both EM and CM mechanisms. According to the FEM simulation, the EM enhancement is ~2.628×10^3 for Pd NPs without the presence of bilayer $PdSe_2$ and it goes up to 5.546×10^3 for Pd NPs on bilayer $PdSe_2$ (**Figure 2.28**). Thus, the remaining EF (~10^2) can be attributed to the CM mechanism, which is consistent with the SERS data for other dye molecules (**Figure 2.29**). SERS sensing data of one volatile organic compound, e.g., ethylene glycol on the $PdSe_2$-Pd_2Se_3/Pd NPs, is also shown in **Figure 2.30**, where the enhancement is relatively low. We measured the highest SERS EF for MB (~EF = 3×10^5) and the lowest EF (~2.3×10^3) for the Methylene orange molecule. The lowest EF case clearly represents the minimal contribution of the CM mechanism and the dominant role of the EM mechanism for SERS enhancement. The specific role of Pd NPs was explored by Raman imaging of the samples. Raman signals are acquired from two different regions containing $PdSe_2$ with Pd NPs (zone 1) and $PdSe_2$ without Pd NPs (zone 2) (**Figure 2.31**).

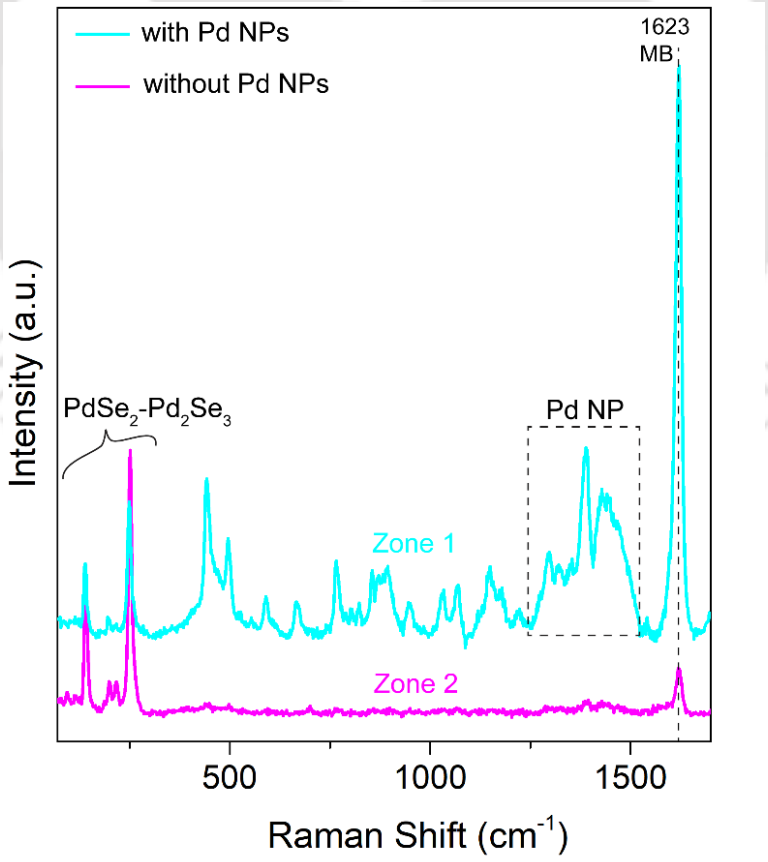

Figure 2.31. Raman signals are acquired from two different regions containing $PdSe_2$ with Pd NPs (zone 1) and $PdSe_2$ without Pd NPs (zone 2).

2.4.10. Growth of other NTMDs

Furthermore, we have tested the general applicability of this growth method by conducting the growth of other NTMDs (2D PdS_2, 2D $PdTe_2$). In 2D PdS_2 and 2D $PdTe_2$, desired patterned dendrites could be grown, indicating the versatility of this synthesis technique (**Figure 2.32**).

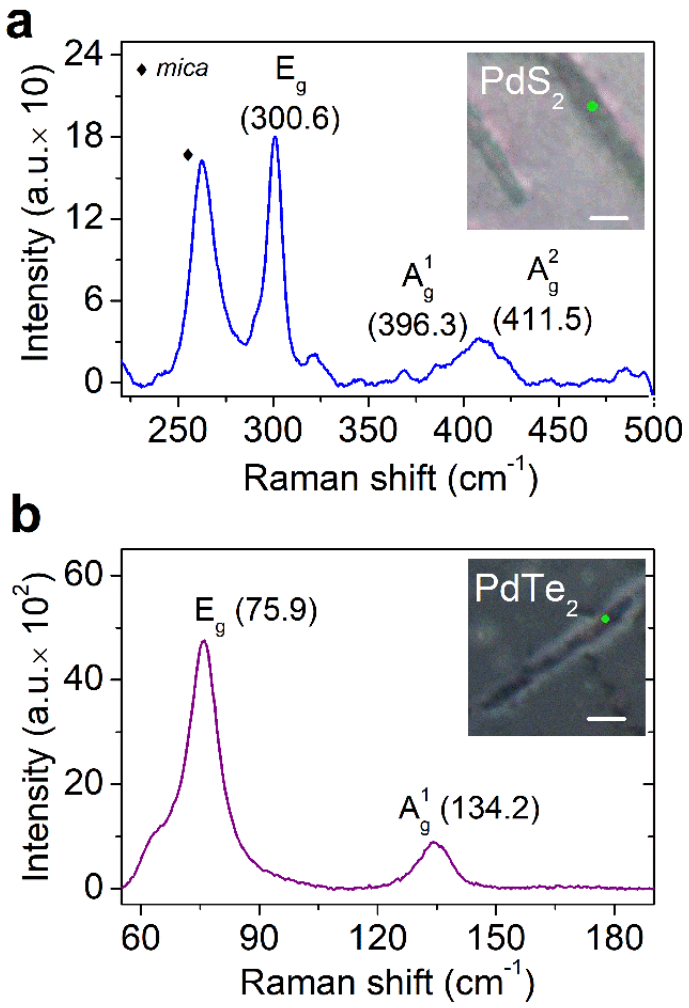

Figure 2.32. Raman spectra of (a) PdS_2 and (b) $PdTe_2$ dendrites. The inset shows the corresponding optical images. The scale bar is 2 μm

2.5. Conclusion

In summary, we developed a novel low-cost salt solution-assisted catalytic growth of dendritic strictly bilayer $PdSe_2$ and other NTMDs on mica substrate. The pinned contact line and electrostatic force play an important role in the dynamics and evolution of dendritic structure, which is catalyzed by NaCl. Utilizing the advantages of water solubility of NaCl, we have

demonstrated a chemical etchant-free and large-area transfer of $PdSe_2$ dendrites, which fully overcomes the limitations of the well-known PMMA-assisted transfer technique. Besides the growth kinetics and the easy transfer technique, we realize the $PdSe_2$-Pd_2Se_3 junction as a metallic wire using DFT calculations and experimental evidence of growing such junctions. The SERS spectrum of MB molecules at the $PdSe_2$-Pd_2Se_3 junction region decorated with Pd NPs (~ 50 nm) shows significantly higher SERS enhancement. We uncover that the attachment of Pd NPs at the $PdSe_2$-Pd_2Se_3 junction further enhances the SERS signal for MB molecules due to the combined role of electromagnetic and chemical enhancement mechanisms. Our proposed method for growing patterned dendrite morphology simply by *in-situ* CVD technique at a low temperature could potentially be applied to other NTMDs, TMDs, and 2D families, enriching this promising dendritic platform for potential applications in next-generation functional devices.

References

1. Zhang, Y.; Ji, Q.; Han, G.-F.; Ju, J.; Shi, J.; Ma, D.; Sun, J.; Zhang, Y.; Li, M.; Lang, X.-Y.; Zhang, Y.; Liu, Z., Dendritic, Transferable, Strictly Monolayer MoS2 Flakes Synthesized on SrTiO3 Single Crystals for Efficient Electrocatalytic Applications. *ACS Nano* **2014,** *8* (8), 8617-8624. https://doi.org/10.1021/nn503412w.
2. Wang, J.; Cai, X.; Shi, R.; Wu, Z.; Wang, W.; Long, G.; Tang, Y.; Cai, N.; Ouyang, W.; Geng, P.; Chandrashekar, B. N.; Amini, A.; Wang, N.; Cheng, C., Twin Defect Derived Growth of Atomically Thin MoS2 Dendrites. *ACS Nano* **2018,** *12* (1), 635-643. https://doi.org/10.1021/acsnano.7b07693.
3. Hauwiller, M. R.; Zhang, X.; Liang, W.-I.; Chiu, C.-H.; Zhang, Q.; Zheng, W.; Ophus, C.; Chan, E. M.; Czarnik, C.; Pan, M.; Ross, F. M.; Wu, W.-W.; Chu, Y.-H.; Asta, M.; Voorhees, P. W.; Alivisatos, A. P.; Zheng, H., Dynamics of Nanoscale Dendrite Formation in Solution Growth Revealed Through in Situ Liquid Cell Electron Microscopy. *Nano Lett.* **2018,** *18* (10), 6427-6433. https://doi.org/10.1021/acs.nanolett.8b02819
4. Huang, Q.; Fang, Y.; Shi, J.; Liang, Y.; Zhu, Y.; Xu, G., Flower-Like Molybdenum Disulfide for Polarity-Triggered Accumulation/Release of Small Molecules. *ACS Appl. Mater. Interfaces* **2017,** *9* (41), 36431-36437. https://doi.org/10.1021/acsami.7b11940
5. Lu, Q., Yu, Y., Ma, Q., Chen, B. and Zhang, H., 2D Transition-Metal-Dichalcogenide-Nanosheet-Based Composites for Photocatalytic and Electrocatalytic Hydrogen Evolution Reactions. Adv. Mater., **2016**, 28: 1917-1933. https://doi.org/10.1002/adma.201503270.
6. Zhang, Y.; Zhang, L.; Kim, P.; Ge, M.; Li, Z.; Zhou, C., Vapor Trapping Growth of Single-Crystalline Graphene Flowers: Synthesis, Morphology, and Electronic Properties. *Nano Lett.* **2012,** *12* (6), 2810-2816. https://doi.org/10.1021/nl300039a
7. Xu, J.; Srolovitz, D. J.; Ho, D., The Adatom Concentration Profile: A Paradigm for Understanding Two-Dimensional MoS2 Morphological Evolution in Chemical Vapor Deposition Growth. *ACS Nano* **2021,** *15* (4), 6839-6848. https://doi.org/10.1021/acsnano.0c10474 .
8. Zhang, Y.; Ji, Q.; Wen, J.; Li, J.; Li, C.; Shi, J.; Zhou, X.; Shi, K.; Chen, H.; Li, Y.; Deng, S.; Xu, N.; Liu, Z.; Zhang, Y., Monolayer MoS2 Dendrites on a Symmetry-Disparate SrTiO3 (001) Substrate: Formation Mechanism and Interface Interaction. *Adv. Funct. Mater.* **2016,** *26* (19), 3299-3305. https://doi.org/10.1002/adfm.201505571 .
9. Zhan, L.; Shen, J.; Yan, J.; Yan, R.; Zhang, X.; Long, M.; Liu, Z.; Wang, X.; Fu, S.; Zhang, L.; Cui, H.; Zhang, X., Dendritic WS2 Nanocrystal-Coated Monolayer WS2 Nanosheet Heterostructures for Phototransistors. *ACS Appl. Nano Mater.* **2021,** *4* (10), 11097-11104. https://doi.org/10.1021/acsanm.1c02568 .
10. Li, X.; Zhang, S.; Chen, S.; Zhang, X.; Gao, J.; Zhang, Y.-W.; Zhao, J.; Shen, X.; Yu, R.; Yang, Y.; He, L.; Nie, J.; Xiong, C.; Dou, R., Mo Concentration Controls the Morphological Transitions from Dendritic to Semicompact, and to Compact Growth of Monolayer Crystalline MoS2 on Various Substrates. *ACS Appl. Mater. Interfaces* **2019,** *11* (45), 42751-42759. https://doi.org/10.1021/acsami.9b14577 .
11. Felter, J.; Raths, M.; Franke, M.; Kumpf, C., In situ study of two-dimensional dendritic growth of hexagonal boron nitride. *2D Mater.* **2019,** *6* (4), 045005. DOI 10.1088/2053-1583/ab2926.
12. Goto, M.; Oaki, Y.; Imai, H., Dendritic Growth of NaCl Crystals in a Gel Matrix: Variation of Branching and Control of Bending. *Cryst. Growth Des.* **2016,** *16* (8), 4278-4284. https://doi.org/10.1021/acs.cgd.6b00323 .

13. Tian, Z. R.; Liu, J.; Voigt, J. A.; Xu, H.; McDermott, M. J., Dendritic Growth of Cubically Ordered Nanoporous Materials through Self-Assembly. *Nano Lett.* **2003,** *3* (1), 89-92. https://doi.org/10.1021/nl025828t .
14. Chowdhury, S.; Roy, A.; Bodemann, I.; Banerjee, S. K., Two-Dimensional to Three-Dimensional Growth of Transition Metal Diselenides by Chemical Vapor Deposition: Interplay between Fractal, Dendritic, and Compact Morphologies. *ACS Appl. Mater. Interfaces* **2020,** *12* (13), 15885-15892. https://doi.org/10.1021/acsami.9b23286 .
15. Kuang, D.; Xu, A.; Fang, Y.; Liu, H.; Frommen, C.; Fenske, D., Surfactant-Assisted Growth of Novel PbS Dendritic Nanostructures via Facile Hydrothermal Process. *Adv. Mater.* **2003,** *15* (20), 1747-1750. https://doi.org/10.1002/adma.200304623 .
16. Qiu, P.; Yang, M.; Qu, X.; Huai, Y.; Zhu, Y.; Mao, C., Tuning photothermal properties of gold nanodendrites for in vivo cancer therapy within a wide near infrared range by simply controlling their degree of branching. *Biomaterials* **2016,** *104*, 138-144. https://doi.org/10.1016/j.biomaterials.2016.06.033 .
17. Ma, N.; Wu, F.-G.; Zhang, X.; Jiang, Y.-W.; Jia, H.-R.; Wang, H.-Y.; Li, Y.-H.; Liu, P.; Gu, N.; Chen, Z., Shape-Dependent Radiosensitization Effect of Gold Nanostructures in Cancer Radiotherapy: Comparison of Gold Nanoparticles, Nanospikes, and Nanorods. *ACS Appl. Mater. Interfaces* **2017,** *9* (15), 13037-13048. https://doi.org/10.1021/acsami.7b01112 .
18. Jia, W.; Li, J.; Jiang, L., Synthesis of Highly Branched Gold Nanodendrites with a Narrow Size Distribution and Tunable NIR and SERS Using a Multiamine Surfactant. *ACS Appl. Mater. Interfaces* **2013,** *5* (15), 6886-6892. https://doi.org/10.1021/am401006b .
19. Liu, X.; Zhang, X.; Zhu, M.; Lin, G.; Liu, J.; Zhou, Z.; Tian, X.; Pan, Y., PEGylated Au@Pt Nanodendrites as Novel Theranostic Agents for Computed Tomography Imaging and Photothermal/Radiation Synergistic Therapy. *ACS Appl. Mater. Interfaces* **2017,** *9* (1), 279-285. https://doi.org/10.1021/acsami.6b15183 .
20. Watt, J.; Cheong, S.; Toney, M. F.; Ingham, B.; Cookson, J.; Bishop, P. T.; Tilley, R. D., Ultrafast Growth of Highly Branched Palladium Nanostructures for Catalysis. *ACS Nano* **2010,** *4* (1), 396-402. DOI 10.1021/nn901277k.
21. Lim, B.; Jiang, M.; Camargo, P. H. C.; Cho, E. C.; Tao, J.; Lu, X.; Zhu, Y.; Xia, Y., Pd-Pt Bimetallic Nanodendrites with High Activity for Oxygen Reduction. *Science* **2009,** *324* (5932), 1302-1305. https://doi.org/10.1126/science.1170377 .
22. Jiang, B.; Li, C.; Malgras, V.; Bando, Y.; Yamauchi, Y., Three-dimensional hyperbranched PdCu nanostructures with high electrocatalytic activity. *Chem. Comm.* **2016,** *52* (6), 1186-1189. https://doi.org/10.1039/C5CC08581K .
23. Zhang, N.; Yu, K.; Li, Q.; Zhu, Z. Q.; Wan, Q., Room-temperature high-sensitivity H2S gas sensor based on dendritic ZnO nanostructures with macroscale in appearance. *J. Appl. Phys.* **2008,** *103* (10), 104305. https://doi.org/10.1063/1.2924430 .
24. Ren, J.; Guo, B.; Feng, Y.; Yu, K., Few-layer MoS2 dendrites as a highly active humidity sensor. *Physica E: Low-dimens. Syst. Nanostruct.* **2020,** *116*, 113782. https://doi.org/10.1016/j.physe.2019.113782 .
25. Strickland, J.; Nenchev, B.; Dong, H., On Directional Dendritic Growth and Primary Spacing—A Review. *Crystals*, **2020**. 10(7), 627; https://doi.org/10.3390/cryst10070627 .
26. Sakane, S.; Takaki, T.; Ohno, M.; Shibuta, Y.; Aoki, T., Two-dimensional large-scale phase-field lattice Boltzmann simulation of polycrystalline equiaxed solidification with motion of a massive number of dendrites. *Comput. Mater. Sci.* **2020,** *178*, 109639. https://doi.org/10.1016/j.commatsci.2020.109639 .

27. Zhang, A.; Du, J.; Guo, Z.; Wang, Q.; Xiong, S., A Phase-Field Lattice-Boltzmann Study on Dendritic Growth of Al-Cu Alloy Under Convection. *Metal. Mater. Trans. B* **2018,** *49* (6), 3603-3615. https://doi.org/10.1007/s11663-018-1418-1 .
28. Du, J.; Zhang, A.; Guo, Z.; Yang, M.; Li, M.; Liu, F.; Xiong, S., Effect of additional solute elements (X= Al, Ca, Y, Ba, Sn, Gd and Zn) on crystallographic anisotropy during the dendritic growth of magnesium alloys. *J. Alloys Compd.* **2019,** *775*, 322-329. https://doi.org/10.1016/j.jallcom.2018.10.145 .
29. Xing, H.; Ji, M.; Dong, X.; Wang, Y.; Zhang, L.; Li, S., Growth competition between columnar dendrite and degenerate seaweed during directional solidification of alloys: Insights from multi-phase field simulations. *Mater. Des.* **2020,** *185*, 108250. https://doi.org/10.1016/j.matdes.2019.108250 .
30. Pi, L.; Li, L.; Liu, K.; Zhang, Q.; Li, H.; Zhai, T., Recent Progress on 2D Noble-Transition-Metal Dichalcogenides. *Advanced Functional Materials* **2019,** *29* (51), 1904932. https://doi.org/10.1002/adfm.201904932 .
31. Wei, M.; Lian, J.; Zhang, Y.; Wang, C.; Wang, Y.; Xu, Z., Layer-dependent optical and dielectric properties of centimeter-scale PdSe2 films grown by chemical vapor deposition. *NPJ 2D Mater. Appl.* **2022,** *6* (1), 1. https://doi.org/10.1038/s41699-021-00282-5 .
32. Liu, W.; Dong, A.; Wang, B.; Zhang, H., Current Advances in Black Phosphorus-Based Drug Delivery Systems for Cancer Therapy. *Adv. Sci.* **2021,** *8* (5), 2003033. https://doi.org/10.1002/advs.202003033 .
33. Hoffman, A. N.; Gu, Y.; Liang, L.; Fowlkes, J. D.; Xiao, K.; Rack, P. D., Exploring the air stability of PdSe2 via electrical transport measurements and defect calculations. *npj 2D Mater. Appl.* **2019,** *3* (1), 50. https://doi.org/10.1038/s41699-019-0132-4 .
34. Ling, X.; Lee, Y.-H.; Lin, Y.; Fang, W.; Yu, L.; Dresselhaus, M. S.; Kong, J., Role of the Seeding Promoter in MoS2 Growth by Chemical Vapor Deposition. *Nano Lett.* **2014,** *14* (2), 464-472. https://doi.org/10.1021/nl4033704 .
35. Li, X.; Li, B.; Lei, J.; Bets, K. V.; Sang, X.; Okogbue, E.; Liu, Y.; Unocic, R. R.; Yakobson, B. I.; Hone, J.; Harutyunyan, A. R., Nickel particle–enabled width-controlled growth of bilayer molybdenum disulfide nanoribbons. *Sci. Adv. 7* (50), eabk1892. https://doi.org/10.1126/sciadv.abk1892 .
36. Li, S.; Lin, Y.-C.; Zhao, W.; Wu, J.; Wang, Z.; Hu, Z.; Shen, Y.; Tang, D.-M.; Wang, J.; Zhang, Q.; Zhu, H.; Chu, L.; Zhao, W.; Liu, C.; Sun, Z.; Taniguchi, T.; Osada, M.; Chen, W.; Xu, Q.-H.; Wee, A. T. S.; Suenaga, K.; Ding, F.; Eda, G., Vapour–liquid–solid growth of monolayer MoS2 nanoribbons. *Nat. Mater.* **2018,** *17* (6), 535-542. https://doi.org/10.1038/s41563-018-0055-z .
37. Zhang, K.; Bersch, B. M.; Zhang, F.; Briggs, N. C.; Subramanian, S.; Xu, K.; Chubarov, M.; Wang, K.; Lerach, J. O.; Redwing, J. M.; Fullerton-Shirey, S. K.; Terrones, M.; Robinson, Considerations for Utilizing Sodium Chloride in Epitaxial Molybdenum Disulfide. J. A., *ACS Appl. Mater. Interfaces* **2018,** *10* (47), 40831-40837. https://doi.org/10.1021/acsami.8b16374 .
38. Huang, L.; Thi, Q. H.; Zheng, F.; Chen, X.; Chu, Y. W.; Lee, C.-S.; Zhao, J.; Ly, T. H., Catalyzed Kinetic Growth in Two-Dimensional MoS2. *J. Am. Chem. Soc* **2020,** *142* (30), 13130-13135. https://doi.org/10.1021/jacs.0c05057 .
39. Li, S.; Wang, S.; Tang, D.-M.; Zhao, W.; Xu, H.; Chu, L.; Bando, Y.; Golberg, D.; Eda, G., Halide-assisted atmospheric pressure growth of large WSe2 and WS2 monolayer crystals. *Appl. Mater. Today* **2015,** *1* (1), 60-66. https://doi.org/10.1016/j.apmt.2015.09.001 .
40. Gu, Y.; Zhang, L.; Cai, H.; Liang, L.; Liu, C.; Hoffman, A.; Yu, Y.; Houston, A.; Puretzky, A. A.; Duscher, G.; Rack, P. D.; Rouleau, C. M.; Meng, X.; Yoon, M.; Geohegan, D. B.; Xiao, K., Stabilized Synthesis of 2D Verbeekite: Monoclinic PdSe2 Crystals with High Mobility and In-Plane Optical and Electrical Anisotropy. *ACS Nano* **2022,** *16* (9), 13900-13910. https://doi.org/10.1021/acsnano.2c02711 .

41. Li, G.; Yin, S.; Tan, C.; Chen, L.; Yu, M.; Li, L.; Yan, F., Fast Photothermoelectric Response in CVD-Grown PdSe2 Photodetectors with In-Plane Anisotropy. *Adv. Funct. Mater.* **2021,** *31* (40), 2104787. https://doi.org/10.1002/adfm.202104787 .
42. Oyedele, A. D.; Yang, S.; Feng, T.; Haglund, A. V.; Gu, Y.; Puretzky, A. A.; Briggs, D.; Rouleau, C. M.; Chisholm, M. F.; Unocic, R. R.; Mandrus, D.; Meyer, H. M., III; Pantelides, S. T.; Geohegan, D. B.; Xiao, K., Defect-Mediated Phase Transformation in Anisotropic Two-Dimensional PdSe2 Crystals for Seamless Electrical Contacts. *J. Am. Chem. Soc.* **2019,** *141* (22), 8928-8936. https://doi.org/10.1021/jacs.9b02593 .
43. Liang, J.; Xu, K.; Toncini, B.; Bersch, B.; Jariwala, B.; Lin, Y.-C.; Robinson, J.; Fullerton-Shirey, S. K., Impact of Post-Lithography Polymer Residue on the Electrical Characteristics of MoS2 and WSe2 Field Effect Transistors. *Adv. Mater. Interfaces* **2019,** *6* (3), 1801321. https://doi.org/10.1002/admi.201801321 .
44. Gammelgaard, L.; Caridad, J. M.; Cagliani, A.; Mackenzie, D. M. A.; Petersen, D. H.; Booth, T. J.; Bøggild, P., Graphene transport properties upon exposure to PMMA processing and heat treatments. *2D Mater.* **2014,** *1* (3), 035005. https://doi.org/10.1088/2053-1583/1/3/035005 .
45. Giannozzi, P., Baroni, S., Bonini, N., Calandra, M., Car, R., Cavazzoni, C., Ceresoli, D., Chiarotti, G. L., Cococcioni, M., Dabo, I., Corso, A. D., De Gironcoli, S., Fabris, S., Fratesi, G., Gebauer, R., Gerstmann, U., Gougoussis, C., Kokalj, A., Lazzeri, M., . . . Wentzcovitch, R. M. (2009). QUANTUM ESPRESSO: a modular and open-source software project for quantum simulations of materials. Journal of Physics Condensed Matter, 21(39), 395502. https://doi.org/10.1088/0953-8984/21/39/395502
46. Xiao, F., Lei, W., Wang, W., Autieri, C., Zheng, X., Ming, X., & Luo, J. (2022). Pressure-induced structural transition, metallization, and topological superconductivity in PdSSe. Physical Review. B./Physical Review. B, 105(11). https://doi.org/10.1103/physrevb.105.115110
47. Shukla, V., Wärnå, J., Jena, N. K., Grigoriev, A., & Ahuja, R. (2017). Toward the Realization of 2D Borophene Based Gas Sensor. The Journal of Physical Chemistry C, 121(48), 26869–26876. https://doi.org/10.1021/acs.jpcc.7b09552
48. Grimme, S., Antony, J., Ehrlich, S., & Krieg, H. (2010). A consistent and accurateab initioparametrization of density functional dispersion correction (DFT-D) for the 94 elements H-Pu. The Journal of Chemical Physics, 132(15). https://doi.org/10.1063/1.3382344
49. Zuluaga, S., Lin, J., Suenaga, K., & Pantelides, S. T. (2018d). Two-dimensional PdSe 2 -Pd 2 Se 3 junctions can serve as nanowires. 2D Materials, 5(3), 035025. https://doi.org/10.1088/2053-1583/aac34c .
50. Okitsu, K.; Bandow, H.; Maeda, Y.; Nagata, Y., Sonochemical Preparation of Ultrafine Palladium Particles. *Chem. Mater.* 1996, *8* (2), 315-317. https://doi.org/10.1021/cm950285s .
51. Franceschi, G.; Kocán, P.; Conti, A.; Brandstetter, S.; Balajka, J.; Sokolović, I.; Valtiner, M.; Mittendorfer, F.; Schmid, M.; Setvín, M.; Diebold, U., Resolving the intrinsic short-range ordering of K+ ions on cleaved muscovite mica. *Nat. Comm.* 2023, *14* (1), 208. https://doi.org/10.1038/s41467-023-35872-y .
52. Sefiane, K., Patterns from drying drops. *Adv. Colloid Interface Sci.* 2014, *206*, 372-381. https://doi.org/10.1016/j.cis.2013.05.002 .
53. Treptow, R. S., Le Châtelier's principle: A reexamination and method of graphic illustration. J. Chem. Educ. 1980, 57 (6), 417. https://doi.org/10.1021/ed057p417 .
54. Sakuma, H.; Kondo, T.; Nakao, H.; Shiraki, K.; Kawamura, K., Structure of Hydrated Sodium Ions and Water Molecules Adsorbed on the Mica/Water Interface. J. Phys. Chem. C 2011, 115 (32), 15959-15964. https://doi.org/10.1021/jp111936s .
55. Qiao, Z.; Feng, H.; Zhou, J., Molecular dynamics simulations on the melting of gold nanoparticles. Ph. Transit. 2014, 87 (1), 59-70. https://doi.org/10.1080/01411594.2013.798410 .

56. Zhao, Z.; Elwood, J.; Carpenter, M. A., Phonon Anharmonicity of PdO Studied by Raman Spectrometry. J. Phys. Chem. C 2015, 119 (40), 23094-23102. https://doi.org/10.1021/acs.jpcc.5b07652 .
57. Li, Y.; Lu, G.; Wu, X.; Shi, G., Electrochemical Fabrication of Two-Dimensional Palladium Nanostructures as Substrates for Surface Enhanced Raman Scattering. J. Phys. Chem. B 2006, 110 (48), 24585-24592. https://doi.org/10.1021/jp0638787 .
58. Chaudhury, M. K.; Whitesides, G. M., How to Make Water Run Uphill. Science 1992, 256 (5063), 1539-1541. https://doi.org/10.1126/science.256.5063.1539 .
59. Brochard, F., Motions of droplets on solid surfaces induced by chemical or thermal gradients. Langmuir 1989, 5 (2), 432-438. https://doi.org/10.1021/la00086a025 .
60. Li, X.; Zhang, S.; Guo, Y.; Wang, F. Q.; Wang, Q., Physical Properties and Photovoltaic Application of Semiconducting Pd2Se3 Monolayer. Nanomater., 2018. 8(10), 832; https://doi.org/10.3390/nano8100832 .
61. Kuklin, A. V.; Ågren, H., Quasiparticle electronic structure and optical spectra of single-layer and bilayer PdSe2: Proximity and defect-induced band gap renormalization Phys. Rev. B 2019, 99 (24), 245114. https://doi.org/10.1103/PhysRevB.99.245114 .
62. Lin, J.; Zuluaga, S.; Yu, P.; Liu, Z.; Pantelides, S. T.; Suenaga, K., Novel Pd2Se3 Two-Dimensional Phase Driven by Interlayer Fusion in Layered PdSe2. Phys. Rev. Lett. 2017, 119 (1), 016101. https://doi.org/10.1103/PhysRevLett.119.016101 .
63. Schranghamer, T. F.; Sharma, M.; Singh, R.; Das, S., Review and comparison of layer transfer methods for two-dimensional materials for emerging applications. Chem. Soc. Rev. 2021, 50 (19), 11032-11054. https://doi.org/10.1039/D1CS00706H .
64. Cui, T.; Yip, K.; Hassan, A.; Wang, G.; Liu, X.; Sun, Y.; Filleter, T., Graphene fatigue through van der Waals interactions. Sci. Adv. 6 (42), eabb1335. https://doi.org/10.1126/sciadv.abb1335 .
65. Okmi, A.; Xiao, X.; Zhang, Y.; He, R.; Olunloyo, O.; Harris, S. B.; Jabegu, T.; Li, N.; Maraba, D.; Sherif, Y.; Dyck, O.; Vlassiouk, I.; Xiao, K.; Dong, P.; Xu, B.; Lei, S., Discovery of Graphene-Water Membrane Structure: Toward High-Quality Graphene Process Adv. Sci. 2022, 9 (26), 2201336. https://doi.org/10.1002/advs.202201336 .
66. Zuluaga, S.; Lin, J.; Suenaga, K.; Pantelides, S. T., Two-dimensional PdSe2-Pd2Se3 junctions can serve as nanowires. 2D Mater. 2018, 5 (3), 035025. https://doi.org/10.1088/2053-1583/aac34c
67. Ryu, G. H.; Zhu, T.; Chen, J.; Sinha, S.; Shautsova, V.; Grossman, J. C.; Warner, J. H., Striated 2D Lattice with Sub-nm 1D Etch Channels by Controlled Thermally Induced Phase Transformations of PdSe2 Adv. Mater. 2019, 31 (46), 1904251. https://doi.org/10.1002/adma.201904251 .
68. Mosleh-Shirazi, S.; Hua, G.; Akhlaghi, F.; Yan, X.; Li, D., Interfacial valence electron localization and the corrosion resistance of Al-SiC nanocomposite Sci. Rep. 2015, 5 (1), 18154. https://doi.org/10.1038/srep18154 .
69. Bruzzoniti, M. C., Appendini, M., Onida, B., Castiglioni, M., Del Bubba, M., Vanzetti, L., Jana, P., Sorarù, G. D., & Rivoira, L. (2018). Regenerable, innovative porous silicon-based polymer-derived ceramics for removal of methylene blue and rhodamine B from textile and environmental waters. Environmental Science and Pollution Research, 25(11), 10619–10629. https://doi.org/10.1007/s11356-018-1367-x .
70. Wu, J. M., Chang, W. E., Chang, Y. T., & Chang, C. (2016). Piezo-Catalytic Effect on the Enhancement of the Ultra-High Degradation Activity in the Dark by Single- and Few-Layers MoS2 Nanoflowers. Advanced Materials, 28(19), 3718–3725. https://doi.org/10.1002/adma.201505785 .
71. Chen, H.; Wei, G.; Ispas, A.; Hickey, S. G.; Eychmüller, A., Synthesis of Palladium Nanoparticles and Their Applications for Surface-Enhanced Raman Scattering and Electrocatalysis. J. Phys. Chem. C 2010, 114 (50), 21976-21981. https://doi.org/10.1021/jp106623y .

Chapter 3 - Temperature-dependent Raman study and determination of anisotropy ratio and thermal conductivity of low-temperature CVD grown $PdSe_2$ using unpolarized laser excitation

In this chapter the temperature-dependent Raman studies have been carried out to understand the phonon-phonon interactions in the as-grown bilayer and few-layer (5-layer) $PdSe_2$. In the case of as-grown bilayer and five-layer $PdSe_2$ film, it ranges from -0.006 $cm^{-1}K^{-1}$ to -0.024 $cm^{-1}K^{-1}$. For 2D $PdSe_2$, as layer number increases, the Raman temperature coefficient increases for A_g^3, B_{1g}^3 modes and decreases for A_g^1, B_{1g}^1 modes, which is unique due to its ubiquitous in-plane anisotropy. The temperature coefficient of CVD-synthesized NTMDs varies from -0.00314 cm^{-1} K^{-1} to -0.024 cm^{-1} K^{-1}, which is very wide compared to TMDs. The thermal conductivity of free-standing bi-layer and few-layer $PdSe_2$ was calculated by a simple approach by taking a laser spot as the centre of heat circulation. Heat dissipation starts from the laser spot and will go radially outward to the heat sink (Cu-grid). Layer thickness-dependent anisotropic ratio is determined through Raman studies, and the origin of lower anisotropic ratio for increasing layer number is discussed. We propose a new way to calculate the anisotropic ratio using an unpolarized laser source.

3.1. Introduction

Many researchers have been allured into the world of two-dimensional materials due to graphene's ground-breaking applications in various fields, such as optoelectronic devices, energy conversion devices, chemical and biological sensors, and high-frequency electronic and optical devices.[1-3] As a very stable material, graphene exhibits an immensely high thermal conductivity of about 5300 W/m. K.[4] This value strongly limits their electronic packaging applications and led to the search for alternative 2D materials, such as hBN, black phosphorous, group VI TMDs, and bismuth oxi-chalcogenides.[5-13] The commonality between graphene and these 2D materials is that they are highly symmetric due to their isotropic lattice structure. Over the past decade, some of the experimentally reachable 2D materials exhibit in-plane isotropic behavior.[14] However, in 2014, the revolution of black phosphorous (BP) as an anisotropic material has pinned scientists to search

for other alternative materials exhibiting anisotropic behavior.[15] In this revolutionary track, they found noble transition metal dichalcogenides (NTMDs), giving fertile ground for many applications.[16-22] Linear dichroism, linearly polarized pulse generators, high gain digital inverters, polarizer sensitive photodetectors, and high-performance thermoelectric applications separate to call NTMDs 'noble.'[23, 24] $PdSe_2$ is evidenced as NTMD which holds a noble orthorhombic pentagonal structure in a pbca space group, and it possesses a remarkable layer-tunable band gap from 0 eV in bulk to ~1.3 eV in a monolayer.[25] The in-plane anisotropy in 2D $PdSe_2$ enables unique electrical, optical, and thermoelectric properties of the material.[26, 27] A variety of methods are used to prepare layered $PdSe_2$. Many thin-film deposition technologies have proved complicated when the coating of a large surface area is required. The chemical vapor deposition technique (CVD) is a versatile tool that provides large areas, single domain sizes, chemical uniformity, structural uniformity, and protective coating to the surface.[28, 29] In recent years, CVD has had a dramatic shift towards the field of manufacturing industries.[30] To date, most of the reported $PdSe_2$ few-layers are obtained by mechanical exfoliation method, self-flux method, magnetron sputtering, direct selenization, molecular beam epitaxy etc.[13, 26, 31-33] Very few reports are there in $PdSe_2$ films using the CVD technique where growth temperatures are usually very high (some of them are mentioned here) .$PdSe_2$ nanosheet with different morphologies (Square-like, truncated square-like, heart-like) were reported on SiO_2/Si substrate depending upon the growth temperature (~ 480 °C - 620 °C).[34, 35] Anisotropic growth of ultrathin $PdSe_2$ ribbon on Au foil was demonstrated with a growth temperature of 850-900 °C.[25] Recently, Lu et al. reported a relatively lower temperature (~300 °C) CVD growth of 2D square-like $PdSe_2$ on sapphire substrate.[36] Thus, it remains challenging to grow 2D $PdSe_2$ at even lower temperatures to realize flexible optoelectronic devices. Over the past decades, Raman spectroscopy has proved to play a central role in the advancement of our knowledge about structural information thermal properties, such as temperature coefficient thermal conductivity, in a rapid and non-destructive way.[10, 37-39] Lu et al. identified the crystallographic orientation of few-layer $PdSe_2$ using polarization-resolved Raman measurement.[36] Previously reported NTMDs ($PtSe_2$, $PtTe_2$) show a red shift in all the characteristics of Raman modes as the thickness increases.[40, 41] Zeng et al. reported two additional peaks at 120.2 and 129.8 cm^{-1} would appear in the Raman spectra for 1.2 nm thickness $PdSe_2$.[42]

The temperature coefficient is a key thermal parameter that stimulates the performance of nano-based layered material devices.[27] Temperature coefficient leads us to find the thermal conductivity of a specific material. Fundamentally, thermal conductivity is an important parameter for making electronic devices.[43] Low thermal conductive materials are highly desirable in different sectors such as aerospace engineering, heat shielding, etc. Numerous experimental studies have been done on the thermal conductivities of TMDS.[9, 38, 44] However, experimental and theoretical studies on thermal conductivity are very limited for NTMDs. Recently, Chen et al. found in-plane thermal conductivity (~10.95-15.58 W/m K) experimentally in a few-layered exfoliated $PdSe_2$.[45] Note that the thermal conductivity was determined for exfoliated $PdSe_2$, and there is no report on the thermal conductivity of CVD-grown $PdSe_2$. Thought-provoking estimation of the thermal conductivity of CVD-grown suspended $PdSe_2$ in a straightforward way is highly desirable for realizing their practical applications.

3.2. Experimental details

3.2.1. Low-temperature growth of bi-layer and few-layer two-dimensional $PdSe_2$

Bi-layer and few-layer $PdSe_2$ flakes were synthesized following a two-step process. (i) Solution preparation, (ii) Low-temperature CVD growth. First, $PdCl_2$ powder (Sigma Aldrich, 99.999%) is dissolved into water to prepare a $PdCl_2$ solution. Next, the completely dissolved solution is drop-cast on the mica substrate. Subsequently, the $PdCl_2$ coated mica substrate was heated at 110 °C for 10 minutes to dry the $PdCl_2$ solution. Next, a single zone CVD system equipped with a 120 cm long quartz tube was engaged to carry out the low-temperature growth of $PdSe_2$. Se powder (Sigma Aldrich, 99.999%) was taken as a growth precursor. Firstly, Se powder was carefully placed at the center of the quartz tube. $PdCl_2$-coated mica was kept at a lower temperature between 8–12 cm away from the center. Argon was purged to carry the vapor precursor towards the down-stream. The quartz tube is initially raised up to a base pressure of 1.9 Pascal and flushed with Ar carrier gas (~300 sccm) at room temperature to make an O_2-free environment inside the quartz tube. The furnace temperature rises to ~350 °C and is held there for 18 minutes while the pressure is maintained at 50-60 kPa.

3.2.2. Sample transfer method

Various transfer methods have been proposed for the transfer of 2D layers from the growth substrate to other substrates. We have adopted a simple and effective step-wise transfer method, as follows.

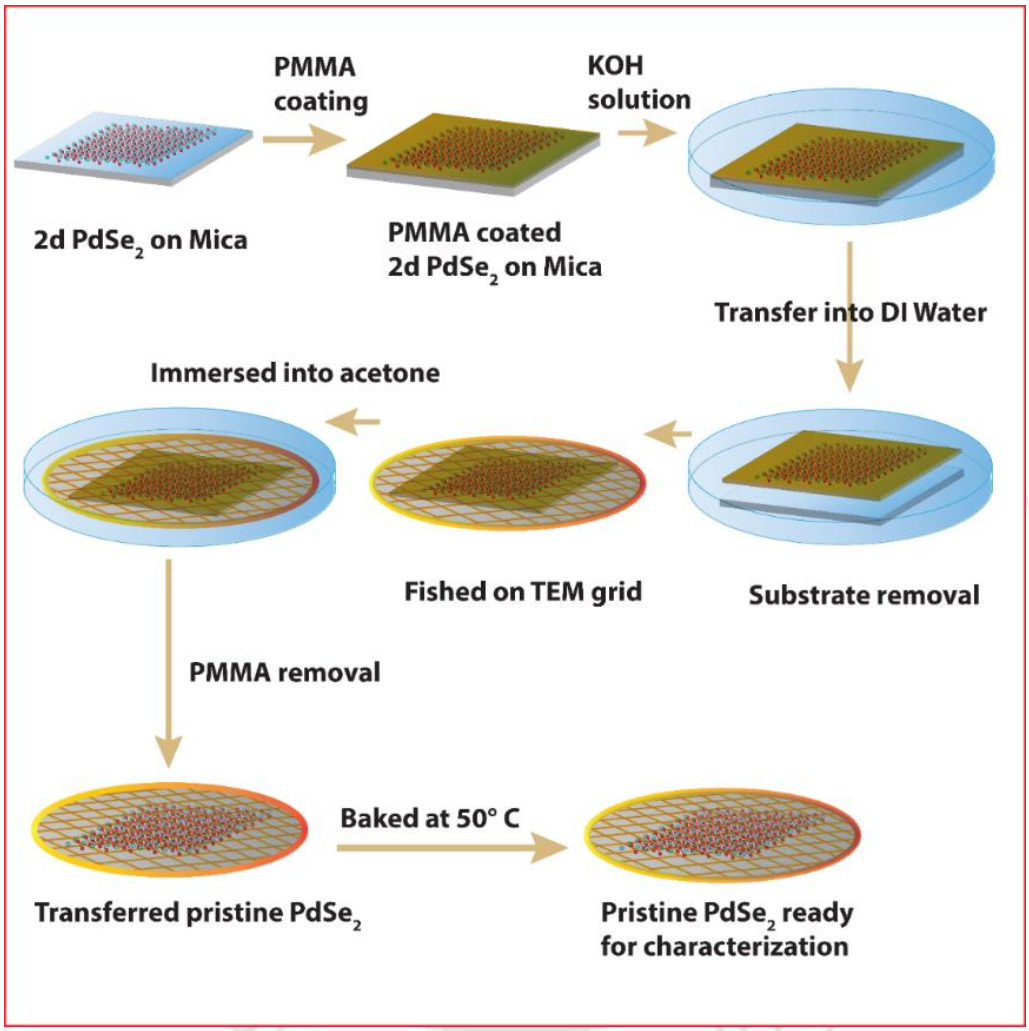

Figure 3.1. Schematic of the transfer process of 2D $PdSe_2$ flakes from mica substrate to the target substrate.

The as-grown $PdSe_2$ layer on the mica substrate has been transferred to a Cu grid to execute the TEM measurement. With the help of drop-casting of PMMA solution and then immersion into KOH solution, we separated $PdSe_2$ from the mica substrate. (1) The PMMA solution is drop cast on $PdSe_2$ and then spin-coated with 1500 rpm for 60 seconds. (2) Then, PMMA adhered spin-coated sample is baked at 110 ℃ on a hot plate. (3) Next, the dried PMMA with immovable spin-

coated $PdSe_2$ is immersed into the KOH solution for 3 hours. (4) Then, PMMA-coated $PdSe_2$ is dipped into a Petri dish with distilled water for easier separation of the $PdSe_2$ film. (5) Finally, PMMA-adhered $PdSe_2$ film is fished with a Cu grid. Consequently, the $PdSe_2$ holder Cu grid was dipped into acetone for 6 hours to eliminate the PMMA layer from the $PdSe_2$ flakes. In the end, it is dried for a few hours for further TEM characterization. For power-dependent Raman spectroscopic measurement in the suspended state, in the same way, we transferred the sample into a Cu grid. A schematic representation of the transfer process has been depicted in **Figure 3.1**.

3.2.3. Characterization techniques

The optical microscope equipped with the micro-Raman measurement system (LabRam HR800, Horiba Scientific) is used for morphological characterization of as-grown $PdSe_2$. The thickness of the as-grown $PdSe_2$ sample was estimated via a non-contact scanning mode atomic force microscope (AFM) (Cypher, Oxford Instruments). A thorough study on the crystallinity of $PdSe_2$ has been performed with the help of high-resolution micro-Raman measurement (LabRam HR800, Horiba scientific) with an excitation wavelength (λ_{ex}) of 532 nm (Ar ion laser). A 1.9 mW laser power is the source of excitation with a 100X objective lens to a spot size of ~1 μm. Collection of the generated signal is done by a charge-coupled device (CCD) in a backscattering geometry carried through a multimode fiber grating of 1800 grooves mm^{-1}. Transmission electron microscope (JEOL-JEM 2010 operated at 200 kV) gives us an opportunity to better visualize surface morphology and crystal lattice arrangement of the pristine $PdSe_2$. TEM study has been carried out on a Cu grid of 300 mesh sizes (Pacific Grid, USA). Implementing a temperature stage with a small operational span of 50X objective with liquid nitrogen as the coolant under an excitation wavelength (λ_{ex}) of 488 nm (LabRam HR800, Jobin Yvon, Ar ion laser), all the temperature-dependent Raman spectra study has been carried out. Power-dependent spectra are obtained by a 100X objective retaining NA = 0.9 by utilizing various powers of a 532 nm laser. At the laser falling spot, the exact power experienced by as-grown $PdSe_2$ was measured using a commercial power meter (Horiba).

3.3. Results and discussions

3.3.1. Low-temperature CVD Growth of 2D $PdSe_2$

Chemical vapor deposition (CVD) is an emerging tool for growing high-quality two-dimensional crystals. The parameters such as growth temperature, carrier gas, precursors, and substrate location play a dynamic role during the CVD process. By optimizing growth temperature, we achieved highly crystalline anisotropic $PdSe_2$ film on a mica substrate. Remarkably, we adopted a low-temperature CVD growth of $PdSe_2$. It follows a two-step process. (i) Substrate coating with $PdCl_2$ precursor. (ii) Selenization of $PdCl_2$ to form two-dimensional $PdSe_2$, as discussed before. More details about the nucleation are discussed in the growth mechanism section later. A schematic of the substrate preparation process is shown in **Figure 3.2**.

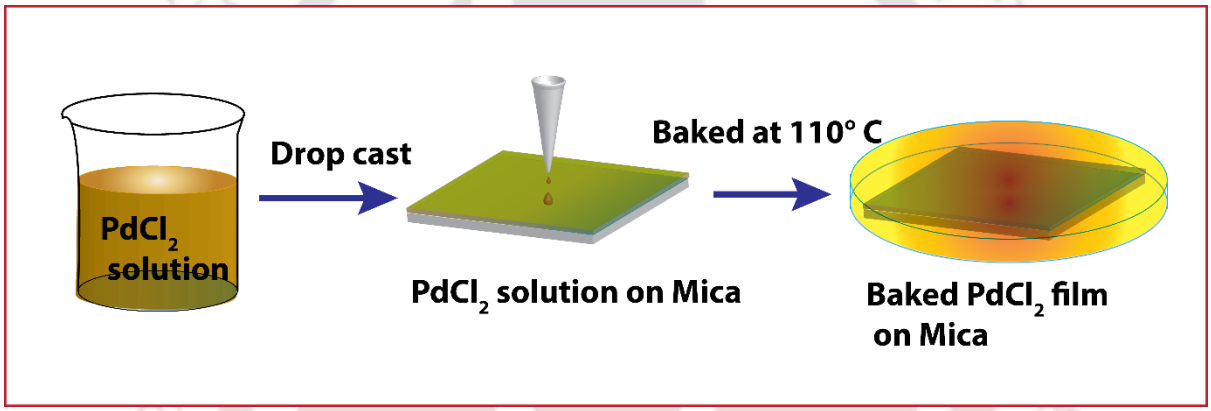

Figure 3.2. Schematic representation of substrate preparation used for the growth of 2D $PdSe_2$ flakes.

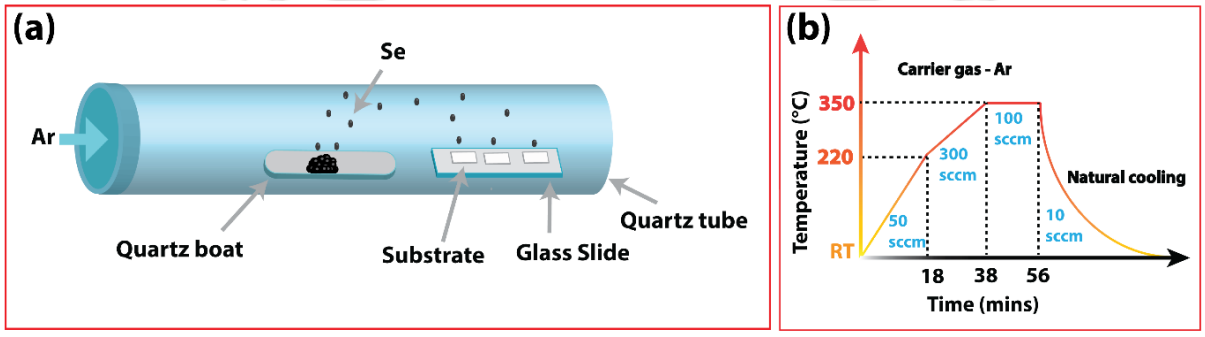

Figure 3.3 (a) Schematic representation of the CVD setup used to grow 2D $PdSe_2$ flakes. (b) Temperature profile and growth parameters of CVD grown 2D $PdSe_2$.

In the 2nd step, precursors and substrates are inserted in a quartz tube, schematically shown in **Figure 3.3a**. The growth is conducted in a single-zone tube furnace. Se powder is kept at the center of the muffle furnace (the location where the temperature is maximum). The substrates were placed downstream in a comparatively lower temperature zone. Following the temperature profile shown in **Figure 3.3b**, where we obtain large area $PdSe_2$ film.

3.3.2. Growth mechanism of sheet like and ribbon like $PdSe_2$

Following the above section **3.1**, at atmospheric condition, $PdCl_2$ coated mica substrate was dried at 110 °C for 10 minutes **Figure 3.4**.

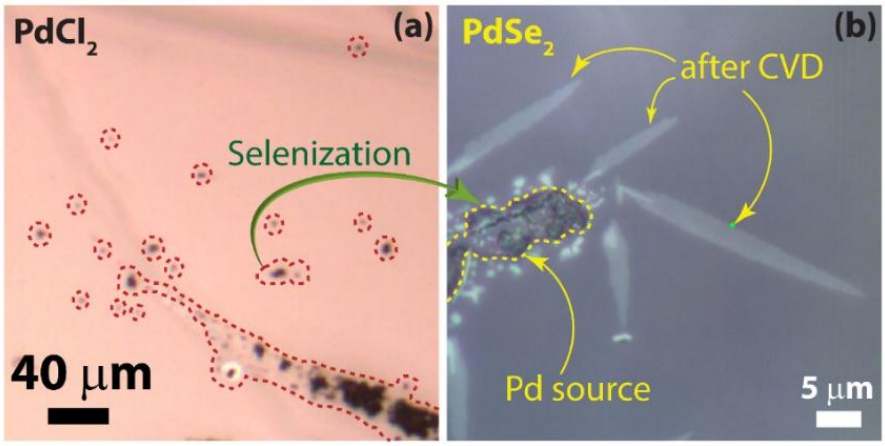

Figure 3.4 (a) Shows the inhomogeneous distribution of $PdCl_2$ solution on mica substrate after evaporation, which acts as a Pd source in CVD. (b) In CVD set up it follows a selenization process where ribbon like and sheet like $PdSe_2$ were formed after dragging Pd from Pd source.

After evaporation, an inhomogeneous distribution of $PdCl_2$ solution (**Figure 3.4a**, red dotted islands) was noticed on the mica substrate. Then it follows a low temperature CVD process in the presence of Se source. Inside CVD set-up, it follows a selenization process where $PdCl_2$ acts as a Pd source (**Figure 3.4b),** yellow dotted islands). From the edge of the Pd region, Se atoms attach to Pd to form $PdSe_2$. Thus, $PdSe_2$ begins nucleation at the edge of the Pd source, where the growth begins with a small rounded structure (at 250 °C, **Figure 3.5**), which subsequently forms a ribbon-like structure (at 270 °C), and finally forms a sheet-like structure (290 °C).

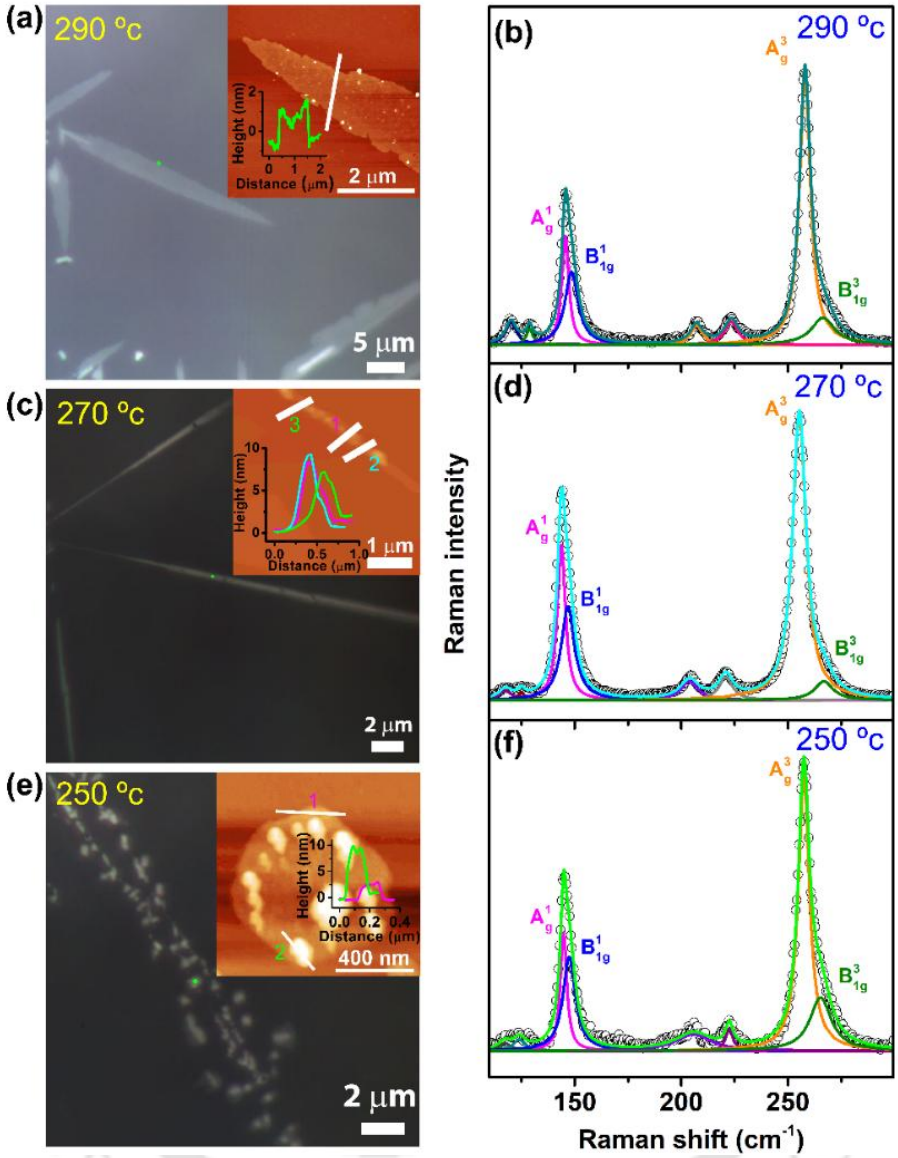

Figure 3.5. Shows optical image of (a, c, e) layered $PdSe_2$ grown with substrate temperatures 290°C, 270°C, 250°C respectively. Inset shows the corresponding AFM images with height profile. (b, d, f) represents the Raman spectra of respective images on mica substrate in different growth temperatures.

If we follow **Figure 3.5**, we can see that at a lower temperature (250 °C), rounded $PdSe_2$ is formed. These rounded structures started to form a ribbon-like structure, but the temperature did not allow this to continue. The statistics of the three types of growth, i.e., uniform sheet-like (at 290 °C), ribbon-like (at 270 °C), and non-uniform sheet-like structures (at 250 °C) are given in **Figure 3.5a, c, e**. For different growth temperatures, we can observe three types of growths, but the percentage distributions are different in each case (**Figure 3.6**).

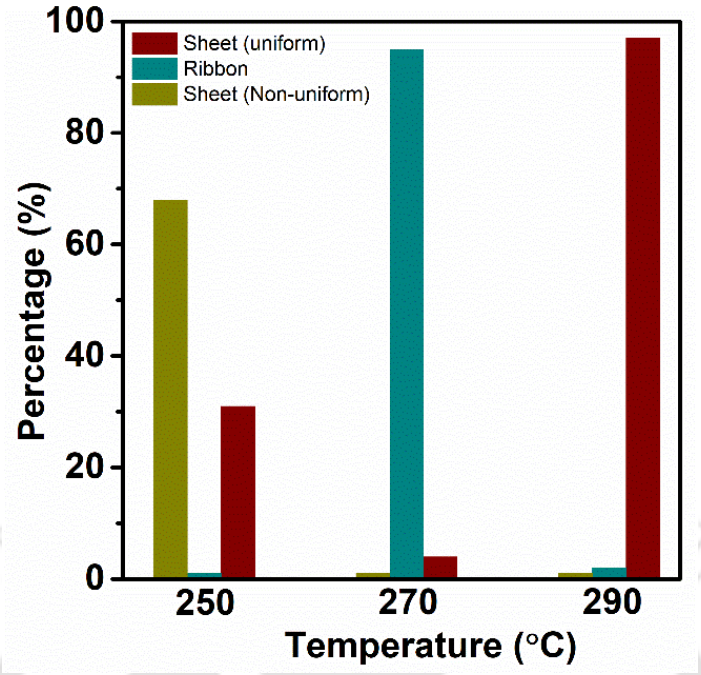

Figure 3.6. Shows distribution percentage for three types of $PdSe_2$ (uniform sheet like, ribbon like, non-uniform sheet like) structures observed at different growth temperatures 250°C, 270°C, 290°C.

At 250 °C, 270 °C, and 290 °C, we can see primarily non-uniform sheet-like, ribbon-like, and uniform sheet-like $PdSe_2$, respectively. At 250 °C, the sheet-like $PdSe_2$ is formed, but it does not have a uniform thickness throughout the sheet. Next, we discuss the characterization of these $PdSe_2$ layers. Furthermore, we fitted the spectra with Lorentzian line shape to understand the crystallinity in each case. The fitting parameters are tabulated in **Table 3.1**.

Table 3.1. Comparison of Raman peak position, FWHM of A_g^1 and A_g^3 mode in $PdSe_2$ at different growth temperatures.

Growth temperature	A^1_g (cm^{-1})	FWHM (cm^{-1})	A^3_g (cm^{-1})	FWHM (cm^{-1})
290 °C	145.6	3.99	258.1	6.2
270 °C	143.8	4.56	255.4	7.7
250 °C	144.8	3.8	257.5	6.3

3.3.3. Characterization of bilayer and few-layer $PdSe_2$

3.3.3.1. Optical microscopy of bilayer and few-layer $PdSe_2$

Optical microscopy images have been captured to evaluate the shape of the as-grown $PdSe_2$ layer. Ultrathin 'uniform sheet' like, and 'ribbon' like and 'non uniform sheet' like $PdSe_2$ flakes observed on the mica substrate, as shown in (**Figure 3.7**).

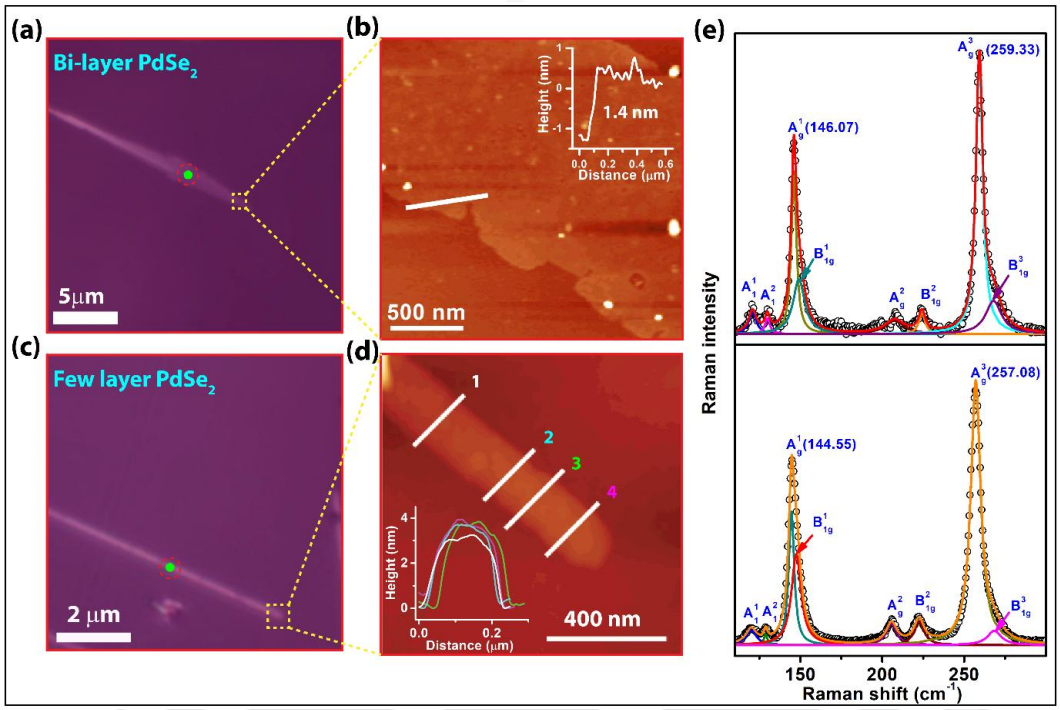

Figure 3.7. (a) Optical microscopy image of 2D $PdSe_2$ sheets. (b) AFM topography of respective $PdSe_2$ film. Inset shows its height profile revealing the bilayer $PdSe_2$. (c) Optical microscopy image of 2D $PdSe_2$ ribbon-like structure. (d) AFM topography of respective $PdSe_2$ film. Inset shows the height profiles measured along the white lines at different locations of the sample. (e) Corresponding Raman spectrum of bilayer and few-layer (~5L) $PdSe_2$. Symbols represent the experimental data, and solid lines are the Lorentzian fitted profile of Raman modes.

Different morphologies as discussed in growth mechanism section of $PdSe_2$ flakes were noticed with various substrate temperatures. Optical microscopy images are shown in **Figure 3.7a** and **c,** which indicates the ultrathin 'sheet' like and 'ribbon' like structures for bilayer and few-layer as-grown $PdSe_2$, respectively. In three growth temperatures, 'uniform sheet' like, 'ribbon' like and 'non uniform sheet' like $PdSe_2$ were observed. Note that the flow rate of Ar gas, precursor amount, source temperature, inside pressure of the quartz tube has been kept constant throughout the CVD process. By placing the mica substrate at different temperature zones, we obtain various types of growth morphology as discussed earlier. Due to the difference in the substrate temperature, a

systematic change in the morphology was noticed. As the temperature increases, the layer number decreases and more uniform $PdSe_2$ growth was observed. At a relatively higher substrate temperature of 290 °C, ultrathin 'sheet-like' morphology was observed, which is of ~2L thickness **(Figure 3.7b).** When the substrate temperature decreases to 270 °C, a 'ribbon' like structure of 5L $PdSe_2$ was obtained (**Figure 3.7d**). The optical contrast of the as-grown $PdSe_2$ at the two temperatures shows that the thickness is greater at a lower temperature than at a higher temperature.

3.3.3.2. AFM analysis

AFM analysis has been performed to measure the exact thickness of the as-grown sample. **Figure 3.7b, d** shows the AFM images of layered $PdSe_2$ on mica substrate in the temperature at 290 °C and 270 °C. The corresponding height profile (inset of **Figure 3.7b, d**) corroborates that it has a thickness of 1.4 nm and 3.2 nm, which corresponds to nearly two layers and five layers of $PdSe_2$, respectively. The average thickness of the monolayer $PdSe_2$ is 0.6 nm.[36, 46] The uniform contrast on the flake shows the uniform thickness of the flake. To validate the uniformity, we measured the thickness for multiple positions in a single flake, as shown in the inset of **Figure 3.7d**, which reveals a uniform thickness throughout the $PdSe_2$ ribbon. The AFM topography gives us a clear visualization of height profiles of $PdSe_2$ at the different growth temperatures.

3.3.3.3. Raman analysis

Micro-Raman measurements were performed to identify the characteristic Raman modes of $PdSe_2$ at the three different growth temperatures. In each case, Raman characteristic modes confirmed the presence of crystalline $PdSe_2$. In case of sheet-like morphology of $PdSe_2$ (uniform as well as non-uniform), the FWHM is lower than that of ribbon-like $PdSe_2$. This suggests that the sheet-like $PdSe_2$ is more crystalline than ribbon like $PdSe_2$. Raman spectra of bilayer and few-layer $PdSe_2$ were shown in **Figure 3.7e**. The uniformity of the bilayer and few layer as-grown $PdSe_2$ has been confirmed from **Figure 3.8**. Raman measurements at different locations of the sample shows identical spectra revealing the high uniformity of the bilayer and few-layer $PdSe_2$ throughout the sample.

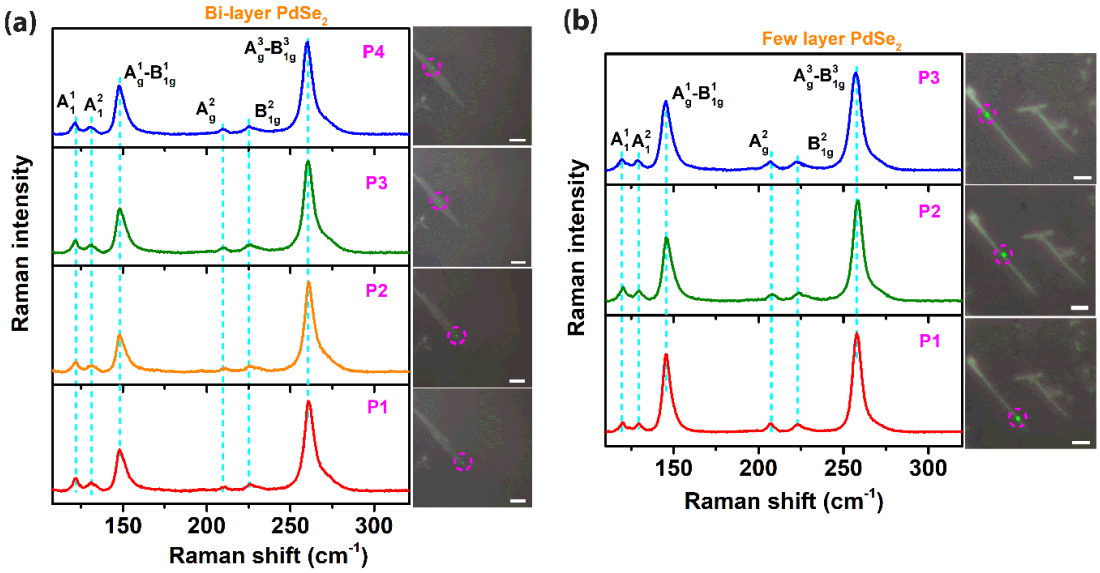

Figure 3.8. Stacked Raman spectra at different locations on (a) bilayer $PdSe_2$ (b) few-layer $PdSe_2$ showing high uniformity of the samples. In the optical images, the scale bar is 5 μm for (a) and 2 μm for (b).

All the characteristic Raman modes A_1^1, A_1^2, A_g^1, B_{1g}^1, A_g^2, B_{1g}^2, A_g^3, B_{1g}^3 reveals anisotropic orthorhombic $PdSe_2$ formation. We de-convoluted A_g^1 and A_g^3 spectra with Lorentzian line shape fitting due to asymmetry in these intense spectral peaks. Note that we have used an unpolarized laser source to perform all Raman measurements. The asymmetry behavior in spectral peaks is due to the contributions by multiple modes in the spectrum and it is partly due to the anisotropic nature of 2D $PdSe_2$. Note that optical anisotropy in $PdSe_2$ has been studied in the literature using a polarized laser only, whereas we attempt to evaluate the anisotropy using an unpolarized laser source, for the first time. A spectral peak shift is observed due to the change in thickness of anisotropic $PdSe_2$.

A comparison of spectral shift for all modes in bilayer and few-layer is given in **Table 3.2**, where we observed A_1^1 and A_1^2 peaks at 120.8 and 129.8 cm^{-1}, respectively, for 1.4 nm thickness $PdSe_2$. However, for few-layer case, we observed A_1^1 and A_1^2 peaks at 119.9 and 128.0 cm^{-1}, respectively. Zeng et al. has also reported two additional peaks at 120.2 and 129.8 cm^{-1} appear in the Raman spectra for 1.2 nm thickness $PdSe_2$, which also validates our ultrathin growth of $PdSe_2$.[42] The spectral blue shift in the B_{1g}^1 peak was the most noticeable, with a significant blue shift of 3 cm^{-1} from few-layer to bi-layer.

Table 3.2. Relative spectral shifts of different Raman modes of CVD-grown bi-layer and few-layer $PdSe_2$

Modes	Raman shift (cm^{-1})		Spectral downshift (cm^{-1})
	Bilayer $PdSe_2$	Few layer $PdSe_2$	
$\boldsymbol{A_1^1}$	120.8	119.9	0.9
$\boldsymbol{A_1^2}$	129.8	128.0	1.8
A_g^1	146.1	144.6	1.5
B_{1g}^1	150.5	147.5	3
$\boldsymbol{A_g^2}$	207.9	205.6	2.3
$\boldsymbol{B_{1g}^2}$	224.2	222.5	1.7
A_g^3	259.3	257.1	2
B_{1g}^3	268.2	268.5	-0.3

It suggests that as the layer number decreases, B_{1g}^1 plays an important role, whereas B_{1g}^3 mode is less sensitive to the outer surface. We also discerned a spectral blue shift of 1.5 cm^{-1}, 2 cm^{-1} for A_g^1 and A_g^3 modes, respectively, as we go from bilayer to few-layer $PdSe_2$. We have fitted both the spectra with Lorentz line shape, revealing the FWHM of 4.15, 5.15 cm^{-1} in bilayer $PdSe_2$ and 4.08, 7.24 cm^{-1} in a few-layer $PdSe_2$ for A_g^1, A_g^3 Raman modes, respectively. The FWHM in A_g^3 Raman modes increase due to increased inter-layer coupling as we go from bilayer to few-layer $PdSe_2$. The effect of surface defects is strong in the bilayer case, and it weakens in thicker samples because of the reduced surface-to-volume ratio, which causes narrowing behavior of the B_{1g}^1 peak with an increasing number of layers. The anomalous change in FWHM with layer number is due to low crystal symmetry in $PdSe_2$. To better understand the $PdSe_2$ crystallinity, we have carried out Raman measurement in two consecutive positions (middle and edge) of a $PdSe_2$ sheet (**Figure 3.9**). At both the positions (middle and edge) of the sheet, we got the same Raman peak positions, which

confirms that the layer numbers are same. But there is a variation in FWHM of about 1 cm^{-1} (For example, A_g^3 mode has FWHM 4.45 cm^{-1} at the middle and 5.51 cm^{-1} at the edge of sheet).

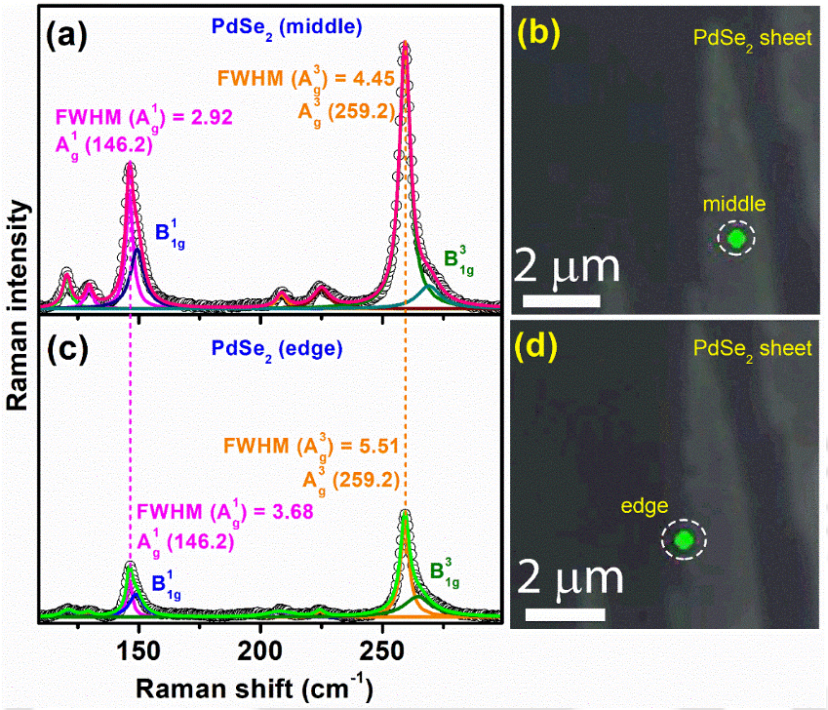

Figure 3.9. (a) Shows the Raman spectra of the demarcated spot (middle) of $PdSe_2$ sheet, (b) represents corresponding optical image. (c) Shows the Raman spectra of the demarcated spot (edge) of $PdSe_2$ sheet, (d) represents corresponding optical image. Raman intensity in both the panel is same.

It can be concluded that as the FWHM is higher, the crystallinity is lower at the edge of the sheet. Note that in $PdSe_2$, the Se atoms lie at the outer surface and at the boundaries of $PdSe_2$ and they can move out more easily than the inner atoms. This implies that Se vacancies may be the source of the low crystallinity of $PdSe_2$ at the edges. The presence of Se vacancies of as-grown $PdSe_2$ further confirmed from the EDX spectrum given in **Figure 3.10.** (Pd- 37.5 %, Se- 62.5 %). A comparison of Lorentz line shape fitted FWHM for all the modes in the bilayer and few-layer $PdSe_2$ is shown in **Table 3.3**. For the as-grown bilayer $PdSe_2$, B_{1g}^1 mode and B_{1g}^3 mode intensities are nearly identical. With the increasing layer number, the intensity of B_{1g}^1 mode increases faster than the intensity of the B_{1g}^3 mode.

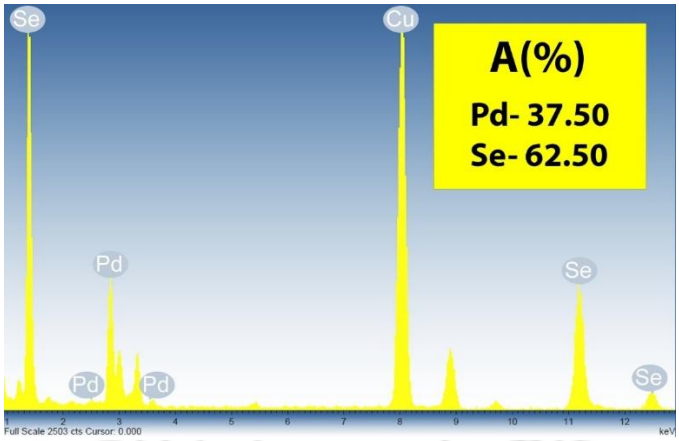

Figure 3.10. EDX spectrum for CVD grown $PdSe_2$.

Table 3.3. Relative change in linewidths with change in layer number for different Raman modes of CVD grown $PdSe_2$.

Modes	FWHM		Relative change in FWHM for few layer $PdSe_2$
	Bilayer $PdSe_2$ (cm^{-1})	Few layer $PdSe_2$ (cm^{-1})	
$\boldsymbol{A_1^1}$	5.43	7.74	Increase
$\boldsymbol{A_1^2}$	3.87	2.60	Decrease
A_g^1	4.15	4.08	Decrease
B_{1g}^1	5.43	7.16	Increase
$\boldsymbol{A_g^2}$	10.40	7.82	Decrease
$\boldsymbol{B_{1g}^2}$	4.75	7.22	Increase
A_g^3	5.15	7.24	Increase
B_{1g}^3	10.55	10.39	Decrease

The intensities of B_{1g}^1 mode and B_{1g}^3 mode in the bilayer and few-layer (5L) are 289, 175, and 1838, 291, respectively. So the intensity ratio of I(B_{1g}^1)/I(B_{1g}^3) = 289/175= 1.7 is for bilayer, but for few-layer (5L) the intensity ratio of I(B_{1g}^1)/I(B_{1g}^3) = 1838/291= 6.3. It confirms that the B_{1g}^1

mode is more sensitive and reactive to the surface. As we go from bilayer to few-layer, B_{1g}^{1} mode started playing an important role.

3.3.3.4. TEM and electron diffraction analysis:

TEM and selected area electron diffraction (SAED) analysis with atomic models further gives us a detailed picture of CVD grown $PdSe_2$. The side view crystal structure of $PdSe_2$ is shown in **Figure 3.11a** and the corresponding lattice constants are a = 0.57 nm, b = 0.58 nm, c = 0.77 nm.

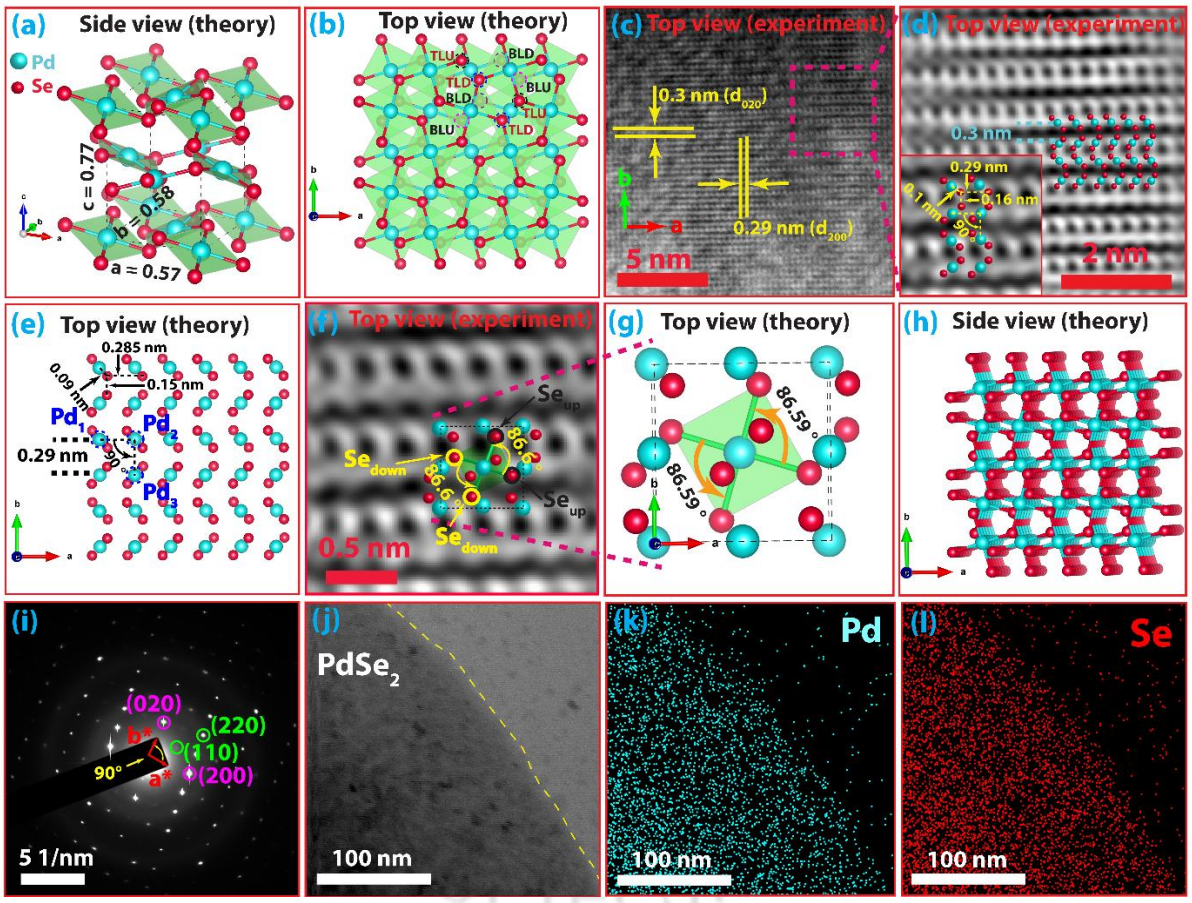

Figure 3.11. (a) Atomic model shows a side view of the $PdSe_2$ unit cell. (b) Top view of bilayer and few-layer of $PdSe_2$. (c) HRTEM of few-layer $PdSe_2$ shows the d-spacing along the x-axis and y-axis. (d) A magnified view of the dotted area of (c) shows the spacing of Pd-Se, Se-Se. Inset depicts the experimentally measured spacing value. (e) Atomic arrangement with all theoretically obtained values. (f) Experimental analysis of CVD grown 2D $PdSe_2$ showing the angles between Se_{up}-Pd-Se_{up} and Se_{down}-Pd-Se_{down}. (g) Top view of atomically arranged $PdSe_2$ with Se_{up}-Pd-Se_{up} and Se_{down}-Pd-Se_{down} angles. (h) Side view of few-layer (5L) $PdSe_2$. (i) SAED pattern for as-grown $PdSe_2$. (j) Scanning TEM image of $PdSe_2$ and (k, l) shows the STEM elemental mapping of Pd and Se atoms, respectively.

Figure 3.11b gives us a clear visualization of the top viewed bilayer and few-layer $PdSe_2$. In **Figure 3.11b**, the black dotted circles encircle the top layer up (TLU) Se atoms, and blue dotted circles encircle the top layer down (TLD) Se atoms, magenta dotted circles encircle the top layer up (BLU) Se atoms, and the purple dotted circles encircle the top layer down (BLD) Se atoms. HRTEM lattice fringes of as-grown $PdSe_2$ are illustrated in **Figure 3.11c**. The enlarged view of the dotted area of **Figure 3.11c** is shown in **Figure 3.11d**, where we can see the atomic arrangement of as-grown $PdSe_2$. We obtained the spacing between Pd-Pd is 0.3 nm along b direction. In the HRTEM image, we can only see the top view of the atomic arrangement of $PdSe_2$. The d-spacing of HRTEM image shows 0.29 nm (d_{200}) and 0.3 nm (d_{020}) along a-direction and b-direction respectively, which nearly matches with the half of theoretical value of lattice constants, that are a = 0.57 nm/2 (0.285 nm) and b = 0.58 nm/2 (0.29 nm). In **Figure 3.11c**, the atomic arrangement is along the same axes as shown in **Figure 3.11b** and **Figure 3.11e**. The inset shows the enlarged view of a small portion of **Figure 3.11d**, in which the spacing between Pd-Pd atoms and Se-Se atoms in a-direction are the same, i.e., 0.29 nm, but along b-direction, the spacing between Pd-Pd and Se-Se are not same. For Se-Se and Pd-Pd, the spacing along the b axis is 0.16 nm and 0.3 nm, respectively. For better visualization, we omitted the bonds and have shown the top view of the atomic model of $PdSe_2$ in **Figure 3.11e**. In **Figure 3.11e,** we have calculated the two-dimensional spacing of consecutive Pd and Se atoms of $PdSe_2$ from the atomic model. From the atomic model, we found that the distance between two consecutive Pd to Pd atoms (Pd-Pd) and Se to Se atoms (Se-Se) along a-direction is 0.285 nm, and the distance between two consecutive Se to Se atoms (Se-Se) along b direction is 0.15 and distance between two consecutive Pd to Pd atoms (Pd-Pd) along b direction is 0.29 nm, which are nearly same as **Figure 3.11d** values. If we see the top view of the $PdSe_2$ model **Figure 3.11e**, there are two nearest Se atoms present at a distance of 0.09 nm from Pd, which is nearly the same as the value obtained from the HRTEM image, i.e., 0.1 nm **Figure 3.11d**. **Figure 3.11f** is the magnified view of **Figure 3.11c**, where we got the angles of Se_{up}- Pd- Se_{up} as 86.6 ° and Se_{down}- Pd- Se_{down} as 86.6 °, which is nearly identical to the theoretical value Se_{up}- Pd- Se_{up} as 86.59 ° and Se_{down}- Pd- Se_{down} as 86.59 ° given in **Figure 3.11g**. **Figure 3.11h** gives the atomic model of side viewed few-layer (5L) $PdSe_2$, whose top view is the same as 2L $PdSe_2$ **Figure 3.11b**. The top view of 2L or more than 2L $PdSe_2$ given in **Figure 3.11b** is different from monolayer $PdSe_2$. **Figure 3.11i** depicts the SAED patterns of $PdSe_2$, which exposes a set of lattice orientations where the central maxima capped with an external tip. $\vec{a}^*$ and

$\vec{b}^*$ are corresponding reciprocal lattice vectors of $\vec{a}$ and $\vec{b}$ along with $\hat{x}$ and $\hat{y}$ directions, respectively. Interestingly, we got reciprocal lattice basis vectors $\vec{a}^* = 0.17\,\hat{x}$ and $\vec{b}^* = 0.16\,\hat{y}$. It confirms the magnitudes of basis vectors in reciprocal space are different from real space basis vectors. The $\left|\vec{H}_{hkl}\right|$ (reciprocal lattice vector) = 0.17 nm for (100) and $\left|\vec{H}_{hkl}\right|$ = 0.16 nm for (010). The angle between the reciprocal vectors $\vec{a}^*$ and $\vec{b}^*$ is 90°. Hence it suggests an orthorhombic crystal structure in reciprocal space. STEM image **Figure 3.11j** with corresponding elemental mapping **Figure 3.11k, l** shows the stoichiometry of each component Pd and Se in as-grown $PdSe_2$. The $PdSe_2$ film has an atomic percentage of 37.5% (Pd) and 62.5% (Se), respectively, which corresponds to the atomic ratio of about 1:2. In $PdSe_2$, we observed the deficiency of Se atoms is due to the Se vacancies exist at the boundary during growth.

3.3.4. Low temperature Raman study

3.3.4.1. Spectral shift

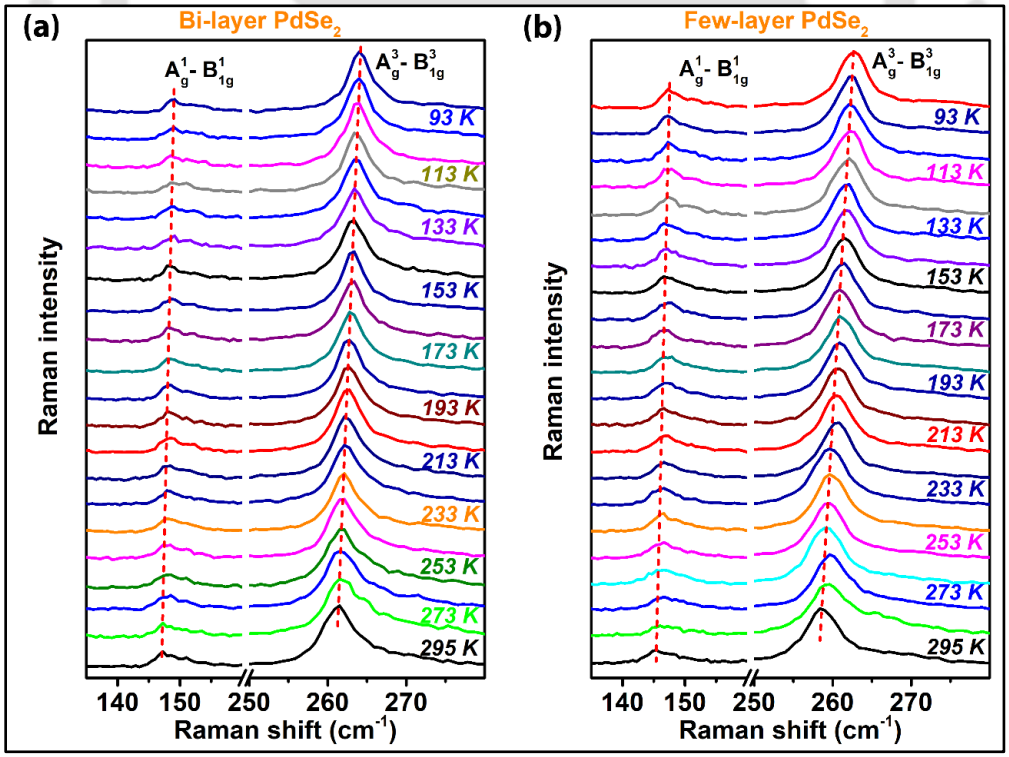

Figure 3.12. Temperature dependent Raman spectra for (a) bi-layer and (b) few-layer $PdSe_2$ grown by CVD.

Low-temperature Raman study has been carried out on CVD-grown bilayer, and few-layer $PdSe_2$ in the range of 83 K to 295 K. **Figure 3.12a, b** depicts the low-temperature Raman spectra of bilayer and few-layer $PdSe_2$, respectively. We observed a systematic blue shift of characteristic Raman peaks in the bilayer and few-layer $PdSe_2$ by decreasing the temperature. The blue shift is due to anharmonicity in the lattice vibrations.[47] The Raman spectra are fitted with the Lorentzian line shape. **Figure 3.13(a-d)** and **Figure 3.14(a-d)** show the variation in Raman peak positions with different temperatures for bilayer and few-layer $PdSe_2$, respectively. Lorentzian fit to the spectra at three different temperatures (93 K, 153 K, 273 K) are shown in **Figure 3.15**. To find out the value of temperature coefficient α, we use the following **equation 3.1**,

$$\omega = \omega_0 + \alpha\, T \qquad (3.1)$$

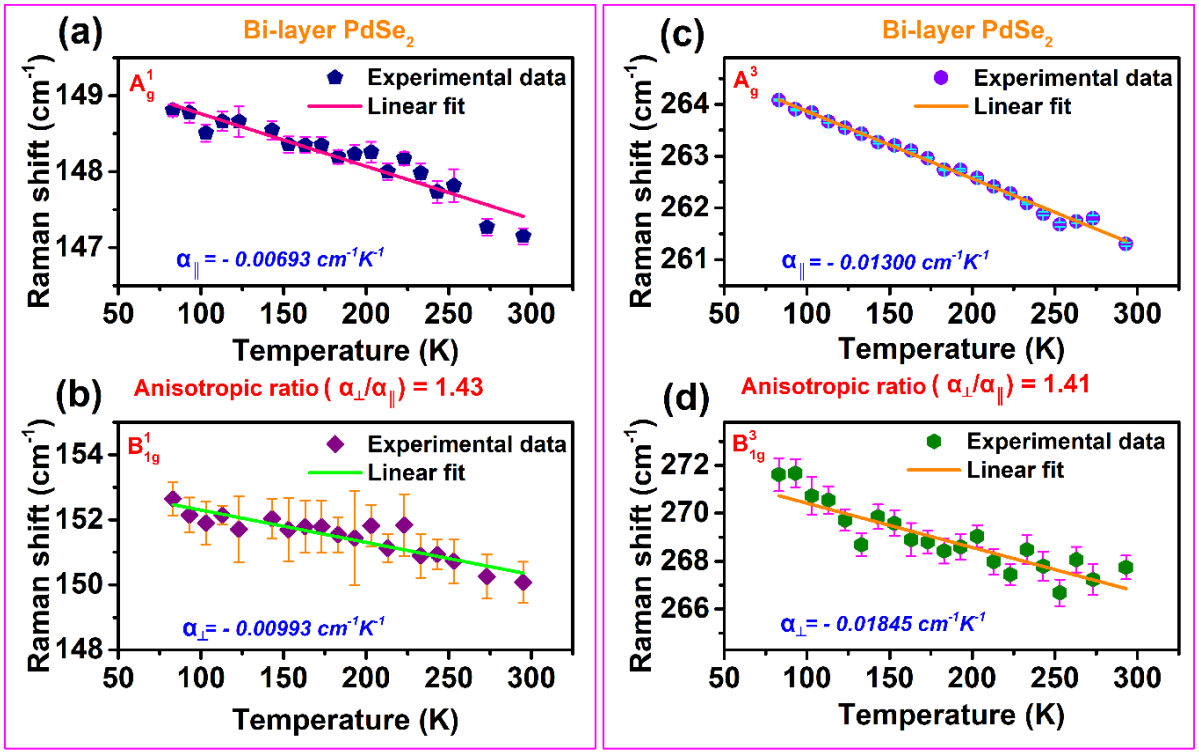

Figure 3.13. Raman shift of (a) A_g^1, (b) B_{1g}^1, (c) A_g^3, (d) B_{1g}^3 modes as a function of temperature in bi-layer $PdSe_2$. The symbols represent the experimental data, and the solid line refers to the fitted data using equation (1).

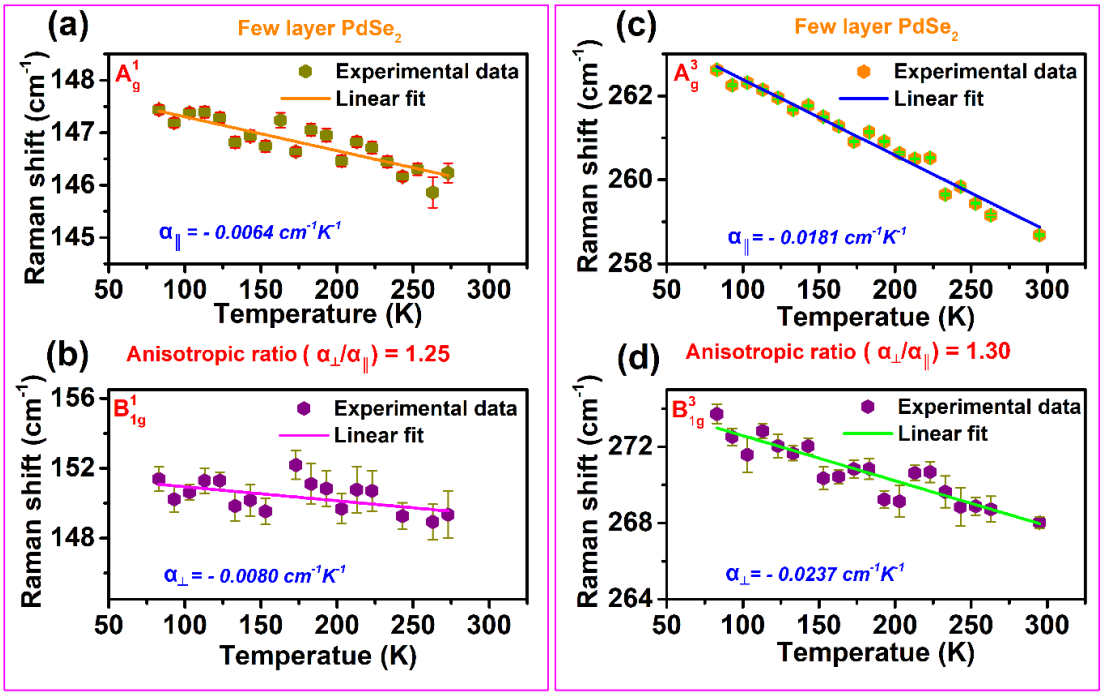

Figure 3.14. Raman shift of (a) A_g^1, (b) B_{1g}^1, (c) A_g^3, (d) B_{1g}^3 modes as a function of temperature in few-layer $PdSe_2$. The symbols represent the experimental data, and the solid line refers to the fitted data using equation (1).

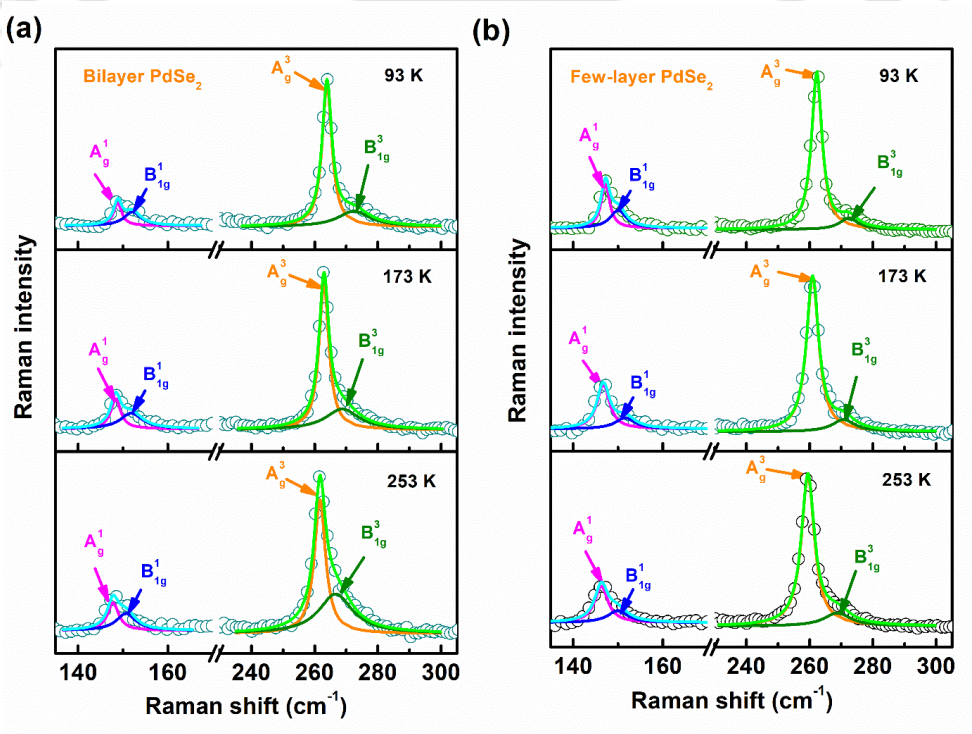

Figure 3.15. Fitted low-temperature Raman spectra for (a) bi-layer and (b) few layer $PdSe_2$ for temperatures 93 K, 173 K, 253 K.

It gives a correlation between frequency (ω) of Raman mode with temperature (T). ω_0 and α represents the frequency at absolute zero temperature and first-order temperature coefficient, respectively. From the linear plot we found out the value of first-order temperature coefficient(α) -0.00693 ± 0.00058 $cm^{-1}K^{-1}$, -0.00993 ± 0.00084 $cm^{-1}K^{-1}$, -0.01300 ± 0.00023 $cm^{-1}K^{-1}$, -0.01845 ± 0.000236 $cm^{-1}K^{-1}$, for A_g^1, B_{1g}^1, A_g^3, B_{1g}^3 modes, respectively, in bilayer $PdSe_2$. In case of few-layer $PdSe_2$, we calculated the first-order temperature coefficients (α) as -0.00640 ± 0.0007 $cm^{-1}K^{-1}$, -0.0080 ± 0.0033 $cm^{-1}K^{-1}$, -0.0181 ± 0.0007 $cm^{-1}K^{-1}$, -0.0237 ± 0.0020 $cm^{-1}K^{-1}$ for A_g^1, B_{1g}^1, A_g^3, B_{1g}^3 modes, respectively.

3.3.4.2. Anisotropic ratio calculation

In the literature different techniques (such as optical absorption and Raman scattering) have been used to calculate anisotropic ratios. Lu et al. reported the anisotropic ratio upto ~ 1.5 at 600 nm, from absorbance peak at a specific wavelength using polarized excitation. [36] Till date, there is no report regarding anisotropic ratio calculation using unpolarized laser excitation. Note that in case of Raman measurement, we obtained characteristic Raman peaks at one specific wavelength excitation. In 1962, Slack theoretically calculated the anisotropy (for T>>1K) in thermal conductivity considering $\frac{k_\perp}{k_\parallel}$. Where, $k_\perp$= thermal conductivity along the perpendicular direction, and $k_\parallel$= thermal conductivity along parallel direction.[48] It is significant to understand anisotropy with the use of an unpolarized laser excitation. In 2D materials, surface to volume ratio is more due to which in plane phonon vibration plays an important role in property change. In case of few layer $PdSe_2$, heat can be conducted through Phonon vibrations. 2D $PdSe_2$ is an anisotropic material which shows anisotropy in its properties. As the temperature decreases, the vibration of Pd and Se atoms decreases due to thermal contraction. But thermal contraction is not same in all directions because of its anisotropy. Pi et al demonstrated if the angle is 0˚ then the parallel laser source will give A_g^1 mode whereas cross polarized light will give the B_{1g}^1 mode. When we use unpolarized laser source we observe both the peaks simultaneously. The deconvolution of Lorentzian line shape gives us a new way to find out peak positions of A_g^i (parallel polarized) and B_{1g}^i (cross polarized) modes. We follow a simple process to calculate anisotropic ratio as follows. The

polarizer parallel along the a-axis gives rise to A_g^i mode, and the polarizer perpendicular to a-axis gives B_{1g}^i mode. Due to the use of unpolarized laser light, we witnessed both the modes simultaneously with asymmetric peaks. This may be because of crystallographic orientation-dependent thermal contraction in $PdSe_2$. Due to anisotropy, different crystallographic axes experience different temperature coefficients with change in temperature. Similarly, phonon transport experiences anisotropic movement due to the anisotropic crystallographic orientation of $PdSe_2$. Thus, experimental observation shows with change in temperature, A_g^1 mode shows less overall shift as compared to B_{1g}^1 mode. Hence, we can measure the anisotropic ratio for $PdSe_2$ from the temperature coefficient ratio of slope at B_{1g}^1 mode to A_g^1 mode. We de-convoluted the asymmetric Raman peaks to address these following Raman modes, A_g^1, B_{1g}^1, A_g^3, B_{1g}^3. To understand the anisotropic ratio in the as-grown bilayer and few-layer $PdSe_2$, in the first step we fitted and de-convoluted the Raman modes (A_g^1, B_{1g}^1, A_g^3, B_{1g}^3) for all the temperatures ranging from 93K to 295K. Then, in second step, we plotted Raman shift with corresponding temperatures (in **Figure 3.13, Figure 3.14**). From Slack theory [48],

$$k \propto \alpha$$

$$\Rightarrow \frac{k_\perp}{k_\parallel} \propto \frac{\alpha_\perp}{\alpha_\parallel} \qquad (3.2)$$

Taking care of the phenomena that, polarizer parallel along the a-axis gives A_g^i mode, and the polarizer perpendicular to a-axis gives B_{1g}^i mode, we have calculated anisotropic ratio from $\frac{\alpha_\perp}{\alpha_\parallel}$, where $\alpha_\perp$ is first order the temperature coefficient when the polarizer perpendicular to a-axis and $\alpha_\parallel$ is the first order temperature coefficient when the polarizer parallel to a-axis. We have calculated $\frac{\alpha_\perp}{\alpha_\parallel}$, directly from the fitted de-convoluted Raman modes (A_g^1, B_{1g}^1, A_g^3, B_{1g}^3). $\frac{\alpha_\perp}{\alpha_\parallel}$ give anisotropic ratios of 1.43 and 1.41 for bilayer $PdSe_2$ and 1.25 and 1.30 for few-layer $PdSe_2$.

3.3.4.3. Variation of temperature coefficient with layer number

Finally, we acquired a large linear ratio of $\frac{\alpha_{\perp}}{\alpha_{\parallel}}$, which gives us a layer-dependent variation of anisotropic ratio from 1.25 (for few-layer) to ~1.43 (for bilayer). Due to its exceptional anisotropic ratio, there is a wide variation in the temperature coefficient from -0.0064 $cm^{-1}K^{-1}$ to -0.0237 $cm^{-1}K^{-1}$ (which is the variation from 2L to 5L). A wide variation in temperature coefficient is expected because of the low symmetry in $PdSe_2$ crystals. A comparison table of temperature coefficient mentioning growth methods with other 2D materials is shown in **Table 3.4**.

Table 3.4. Comparison of temperature coefficients of Raman modes in different 2D materials grown by different techniques.

Material	Growth method	Raman mode	Temperature coefficient ($cm^{-1}. K^{-1}$)	Reference
2L $PdSe_2$	CVD	A_g^1	-0.00693 ± 0.00058	*This Work*
		B_{1g}^1	-0.00993 ± 0.00084	
		A_g^3	-0.01300± 0.00023	
		B_{1g}^3	-0.01845 ± 0.00236	
5L $PdSe_2$	CVD	A_g^1	-0.00640 ± 0.0007	*This Work*
		B_{1g}^1	-0.00800 ± 0.0033	
		A_g^3	-0.01810 ± 0.0007	
		B_{1g}^3	-0.02370± 0.0020	
2L PtS_2	CVD	A_{1g}^2	-0.0032	[39]
		E_g^1	-0.00335	
6L PtS_2		A_{1g}^2	-0.00314	
		E_g^1	-0.003 49	
1L WSe_2	Mechanical exfoliation	E_{2g}^1	-0.0187 ± 0.0022	[8]
2L WSe_2		E_{2g}^1	-0.0147 ± 0.0019	
3L WSe_2		E_{2g}^1	-0.0132 ± 0.0004	
1L $MoSe_2$	Mechanical exfoliation	A_g^1	-0.0111 ± 0.0005	[7]
2L $MoSe_2$		A_g^1	-0.0095 ± 0.0004	
1L MoS_2		A_g^1	-0.0167 ± 0.0007	

2L MoS_2		A_g^1	-0.0139 ± 0.0003	
1L MoS_2	CVD	E_{2g}^1	-0.0114	[44]
		A_g^1	-0.0132	
2L MoS_2		E_{2g}^1	-0.0117	
		A_g^1	-0.0121	
Multilayer MoS_2		E_{2g}^1	-0.0135	
		A_g^1	-0.0125	
1L WS_2	CVD	E_{2g}^1	-0.0125	[9]
		A_g^1	-0.0149	
2L WS_2		E_{2g}^1	-0.0133	
		A_g^1	-0.0121	
10L MoS_2	CVD	E_{2g}^1	-0.0132	[38]
		A_g	-0.0123	

We further correlated temperature coefficient with layer number extracted from different Raman modes for CVD grown and exfoliated TMDs and NTMDs, as shown in **Figures 3.16a, b**. In case of CVD synthesized TMDs and NTMDs, as we go from monolayer to few-layer, the temperature coefficient decreases for all out-of-plane Raman modes, whereas it increases for all in-plane Raman modes. For mechanically exfoliated TMDs, as the layer number increases temperature coefficient decreases for all the Raman modes. Interestingly, layer-dependent temperature coefficient variation in CVD synthesized TMDs is much lower than the exfoliated TMDs. In the case of exfoliated TMDs, the variation of temperature coefficients is more than that of CVD synthesized TMDs. In contrast, the variation of temperature coefficients is much higher in CVD synthesized $PdSe_2$, which might be attributed to the lower interlayer separation (0.38 nm) compared to TMDs (~ 0.62 nm). It may lead us to believe that the layer-dependent variation of temperature coefficient for exfoliated $PdSe_2$ might be lower than that of CVD-grown $PdSe_2$. In contrast with other TMDs, the temperature coefficients of $PdSe_2$ are proportional to layer number for A_g^3 and B_{1g}^3 modes and inversely proportional to A_g^1, B_{1g}^1 modes. It may originate from the vibration of anisotropic atomic arrangement.

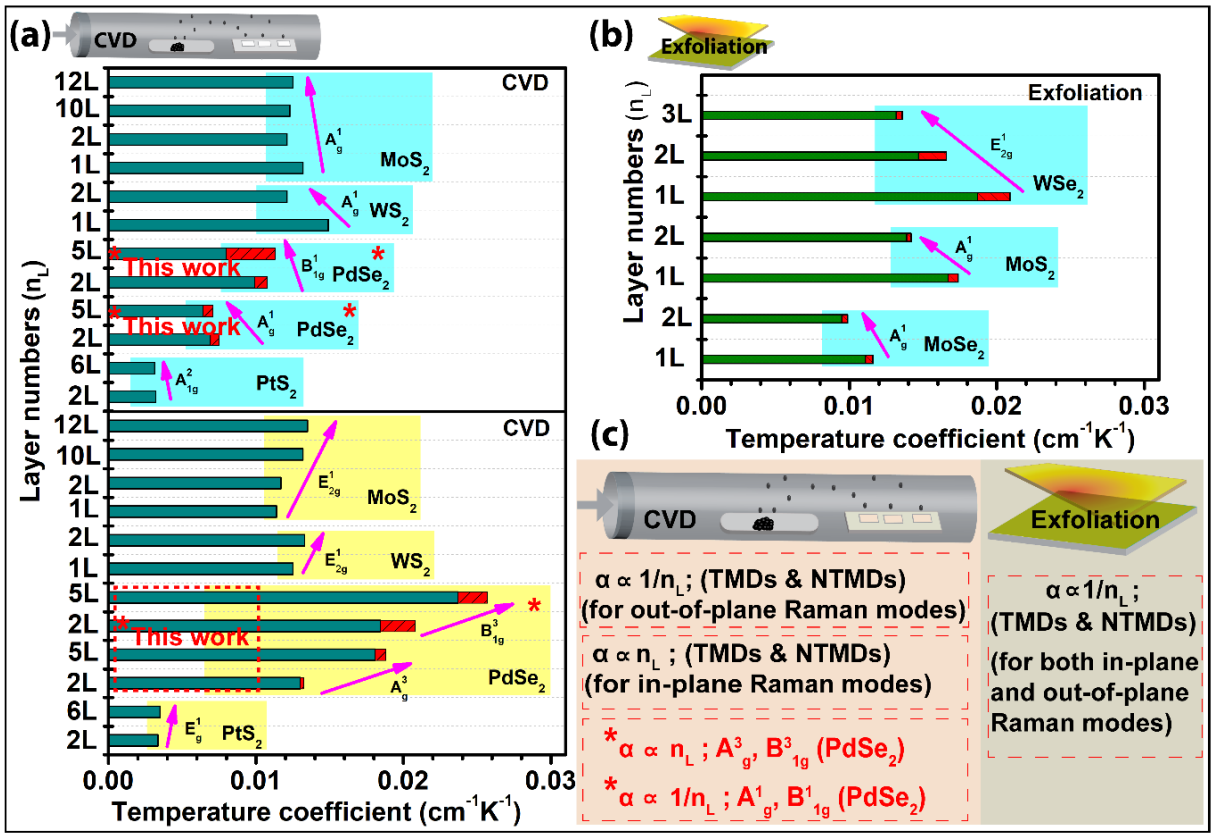

Figure 3.16. (a) CVD synthesized TMDs and NTMDs; a plot of temperature coefficients for different Raman modes. [9, 39, 44] (b) Mechanically exfoliated TMDs; a plot of temperature coefficients (α) for different Raman modes.[7, 8] (c) Schematic representation of relation between α with layer number (n_L) for CVD and exfoliation grown TMDs and NTMDs.

A relation between temperature coefficient (α) with layer number (L) has been depicted in **Figure 3.16c** to summarize our observation. 1L $PdSe_2$ consists of 2 sets of inclined mini-planes shown in **Figure 3.17** which actually acts as Pd-Se planes. 1, 2, 3, 4, 5 are the Pd-Se planes where 2 sets of planes exist. 1, 3, 5 Pd-Se planes are one set of parallel planes and 2, 4 are another set of parallel planes. From yellow shaded region in **Figure 3.16a**, we can notice that for all in-plane modes (E^1_{2g} for MoS_2, E^1_{2g} for WS_2 , and E^1_g for PtS_2), the temperature coefficients are directly proportional to layer numbers. In as-grown $PdSe_2$, A^3_g and B^3_{1g} modes are directly proportional to layer numbers. From cyan shaded region in **Figure 3.16a**, we can notice that for all out-of-plane modes (A^1_g for MoS_2 and WS_2, A^2_{1g} for PtS_2), the temperature coefficients are inversely proportional to layer number. Likewise, for our as-grown $PdSe_2$, the temperature coefficients of A^1_g and B^1_{1g} modes are inversely proportional to layer numbers. It suggests that A^1_g and B^1_{1g} modes

basically behave like out-of-plane modes in the mini-planes of $PdSe_2$, as depicted in **Figure 3.17a, b**. A_g^3 and B_{1g}^3 modes actually behave like in-plane modes in the mini-planes of $PdSe_2$ shown in **Figure 3.17d, e**.

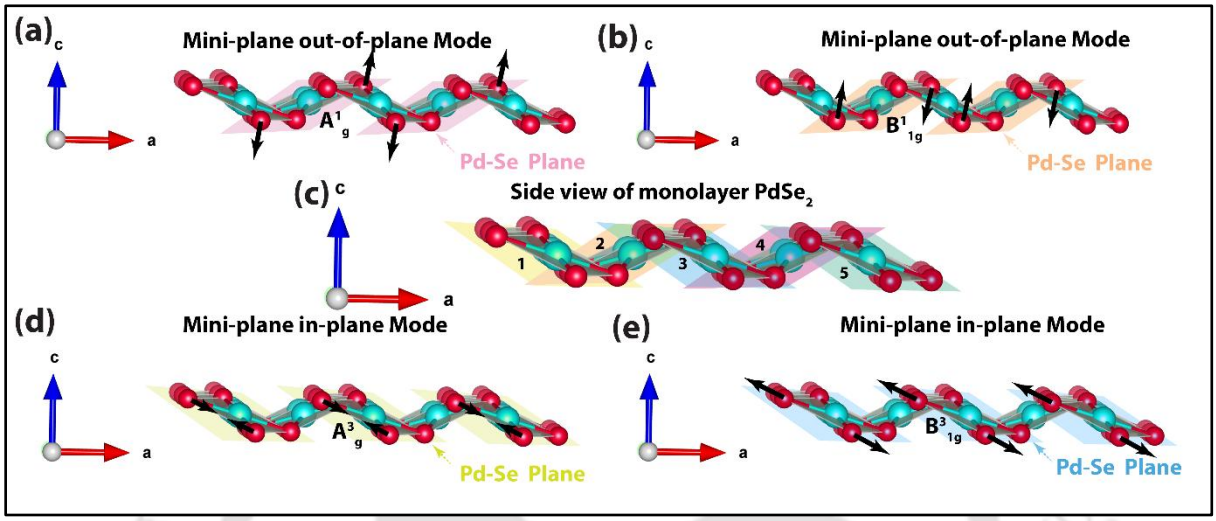

Figure 3.17. (a) Schematic illustration atomic arrangements (side-view) in monolayer $PdSe_2$. 1, 2, 3, 4, 5 are the Pd-Se planes. Schematic representation of (b) A_1^1 vibrational mode, (c) B_{1g}^1 vibrational mode, (d) A_g^3 vibrational mode, (e) B_{1g}^3 vibrational mode in monolayer $PdSe_2$.

3.3.4.4. Linewidth

In **Figure 3.18a, b** linewidth (FWHM) variation of A_g^3 Raman mode with increasing temperature for bi-layer and few-layer $PdSe_2$ has been displayed**.** We have performed an in-depth analysis of Raman modes to interpret the broadening of linewidth of the A_g^3 mode of bi-layer and few-layer $PdSe_2$. The broadening in linewidth (Γ) occurs mainly due to the anharmonic effect caused by three and four phonon processes.[49] The broadening with three and four phonon processes can be described using the following model, [10]

$$\Gamma(T) = \Gamma 0 + a\left[1 + \frac{2}{e^{c/2T}-1}\right] + b[1 + \frac{3}{e^{c/3T}-1} + \frac{3}{(e^{c/3T}-1)^2}] \quad (3.3)$$

In **equation 3.3**, Γ0 is FWHM of the Raman peak at absolute zero temperature, $c = \frac{\hbar\omega}{k_B}$, and a, b represent second and third-order anharmonic constants, respectively.[10]

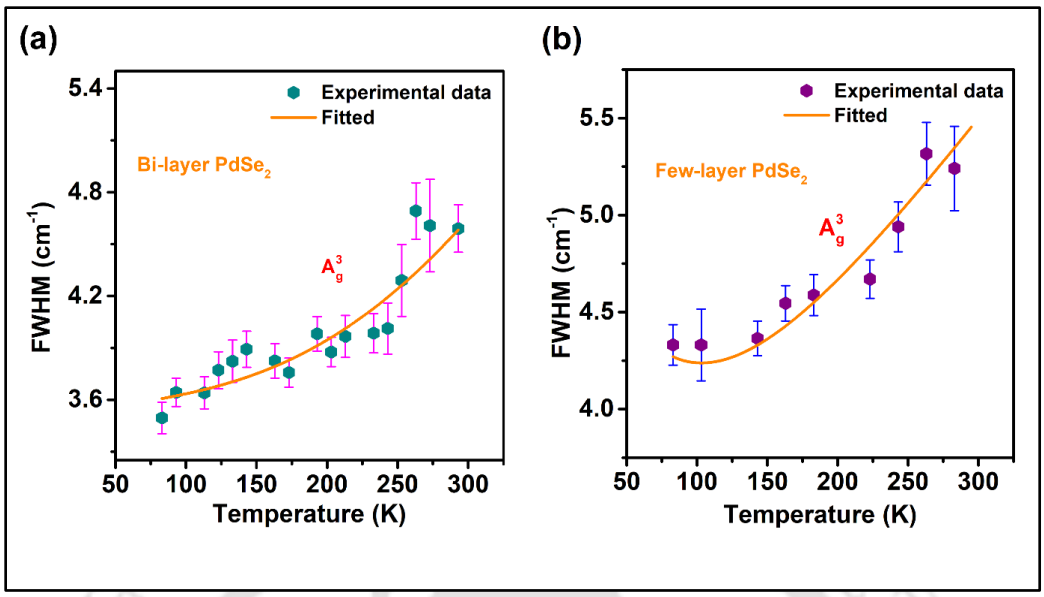

Figure 3.18. Temperature dependence of FWHM of A_g^3 mode in (a) bilayer, (b) few-layer $PdSe_2$. The symbols represent the experimental data, and the solid line refers to the fitted data using equation (3)

Equation (3) fits the variation of FWHM with temperature for three phonon decay process shown in **Figure 3.18a, b**. The FWHM of A_g^3 Raman peak at absolute zero temperature as 4.1 cm^{-1} and 3.1 cm^{-1} for bilayer and few-layer $PdSe_2$, respectively. It suggests that at low-temperature crystallinity of $PdSe_2$ increases as well as phonon dispersion decreases. The values of the second and third-order constants in A_g^3 mode are -0.88 ± 0.37 and 0.327 for bilayer, -2.21± 0.5 and 0.98 for few-layer $PdSe_2$, respectively. Phonon lifetime has been calculated by using the equation $1/\pi * \Gamma_0$, where Γ_0 is linewidth in frequency scale. We obtained the phonon lifetime as 3.4 ps and 2.6 ps for bilayer and few-layer $PdSe_2$, respectively.

3.3.4.5. Temperature-dependent Raman intensity

Next, we study the temperature variation of Raman intensity of different Raman modes in the bilayer and few-layer $PdSe_2$. **Figure 3.19 (a-c)** and **Figure 3.19 (d-f)** show the Raman intensity vs. temperature plot for A_g^1, A_g^3, B_{1g}^3 Raman modes for bilayer and few-layer $PdSe_2$, respectively. It is noticeable that all the Raman modes follow the usual trend (intensity decreases with increasing temperature) in the range 83 K to 130 K except the B_{1g}^3 mode (for bilayer $PdSe_2$). The B_{1g}^3 mode

shows anomalous behaviour above 130 K, i.e., Raman intensity does not decrease with an increase in temperature. For A_g^1 , A_g^3 modes, intensity increases in the temperature window 130 K to 220 K, which is not only related to anharmonicity from phonon-phonon scattering but also probably caused by surface defects, e.g., vacancies. After 220 K, again, it tends to follow the expected behaviour for A_g^1 , A_g^3 modes. Interestingly, the slope of the Raman intensity vs. temperature plot is significantly less for few-layer $PdSe_2$ than bilayer $PdSe_2$.

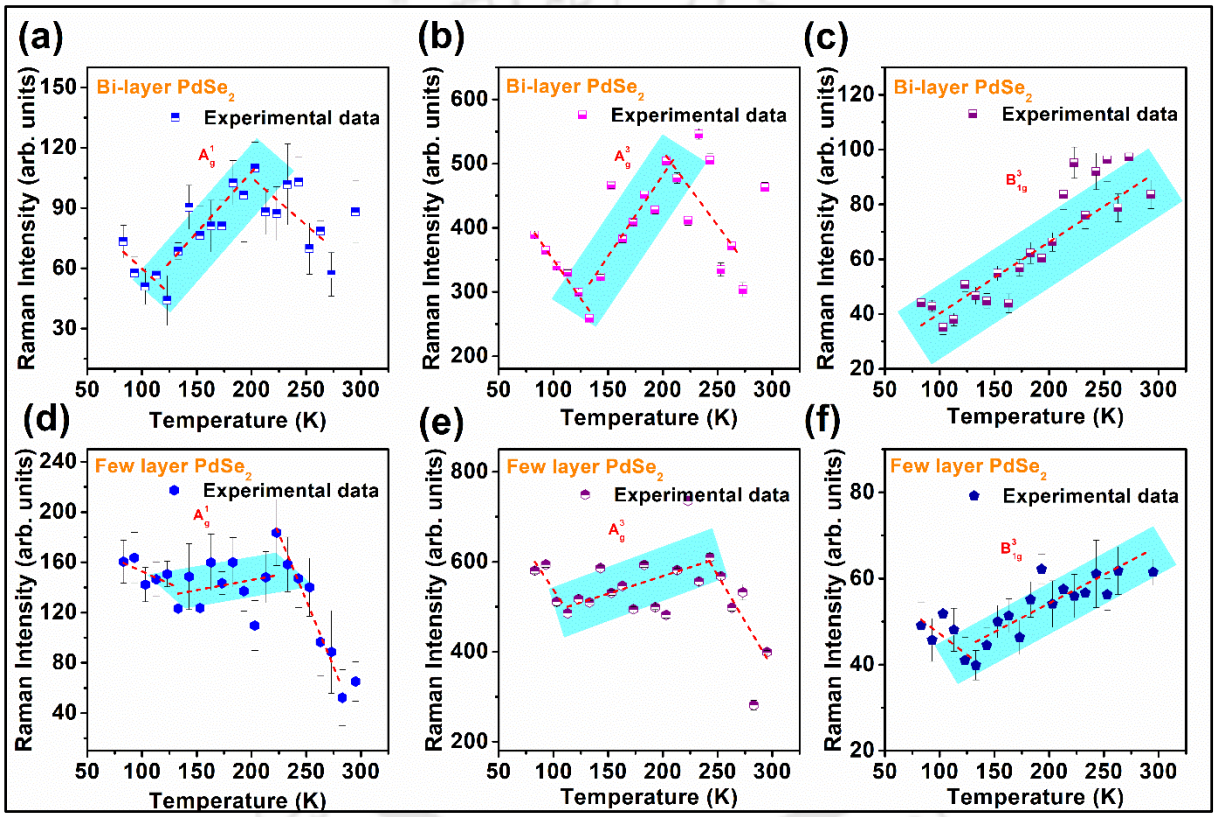

Figure 3.19. Temperature variation of Raman intensity for the characteristic (a) A_g^1 ,(b) A_g^3 ,(c) B_{1g}^3 modes in bilayer $PdSe_2$, (d) A_g^1 ,(e) A_g^3 ,(f) B_{1g}^3 modes in few-layer $PdSe_2$. The symbols represent the experimental data, and the cyan-shaded area represents the typical anomalous behaviour.

This may arise due to the lower thickness leading to more in-plane anisotropy, which lacks the phonon-phonon interaction expected due to inter-layer phonon-phonon coupling. As the temperature increases, B_{1g}^3 mode started playing an important role. When temperature increases, the intensity of the B_{1g}^3 mode increases at a higher rate, leading to B_{1g}^3 modes more sensitive and reactive to the surface. Interestingly, as the layer number increases to 5L, the increasing trend of

the B_{1g}^3 mode decreases. It reveals that as we go from few-layer to multilayer, the effect of B_{1g}^3 mode decreases. This confirms that surface defects are more dominant in the bi-layer sample and they weaken in multilayer samples because of the reduced surface-to-volume ratio. Within the temperature window, 83 K-130 K, when the temperature increases, phonon-phonon interaction between the layers increases due to phonon decay experienced by the system, which is causing in lowering the intensity and increasing the FWHM in the respective system. The usual trend of intensity variation can be understood by the Bose-Einstein distribution model, given in **equation 3.4**,

$$\eta(\omega, T) = 1/[e^x - 1] \quad (3.4)$$

Where $\eta(\omega, T)$ is the Bose-Einstein distribution function in the vibrational state and $x = \frac{\hbar\omega}{k_B T}$. [50]. In case of bilayer and few-layer $PdSe_2$, with decreasing temperature, the intensities of A_g^1, A_g^3 modes increase indicates a decreasing $\eta(\omega, T)$ value. At low temperature, detector captures more scattered photons having same frequency due to less vibrational states. It introduces additional counts in a particular Raman mode which leads to intense Raman peaks. However, the usual trend is limited to a specific temperature range in CVD-grown $PdSe_2$ because of its ubiquitous, highly anisotropic nature.

3.3.4.6. Thermal conductivity:

The excitation power-dependent Raman investigation is carried out on CVD-grown 2D $PdSe_2$ layer in a suspended state to determine its thermal conductivity. We use a 532 nm laser as an excitation source in power-dependent Raman spectroscopic measurement. Perfect laser power has a key impact on the micro-Raman experiment because laser exposure generates a central heat which can cause damage in the sample.[38] A supported few-layer $PdSe_2$ is not a good choice for finding the thermal conductivity due to the dissipation of laser-induced local heat to the substrate, which can lead to erroneous result. To affirm that the spectral shift in as-synthesized $PdSe_2$ is non-linear in the supported state, we first carried out the power-dependent Raman measurement in the supported state. A schematic of power-dependent Raman measurement on CVD grown suspended layered $PdSe_2$ is presented in **Figure 3.20a.**

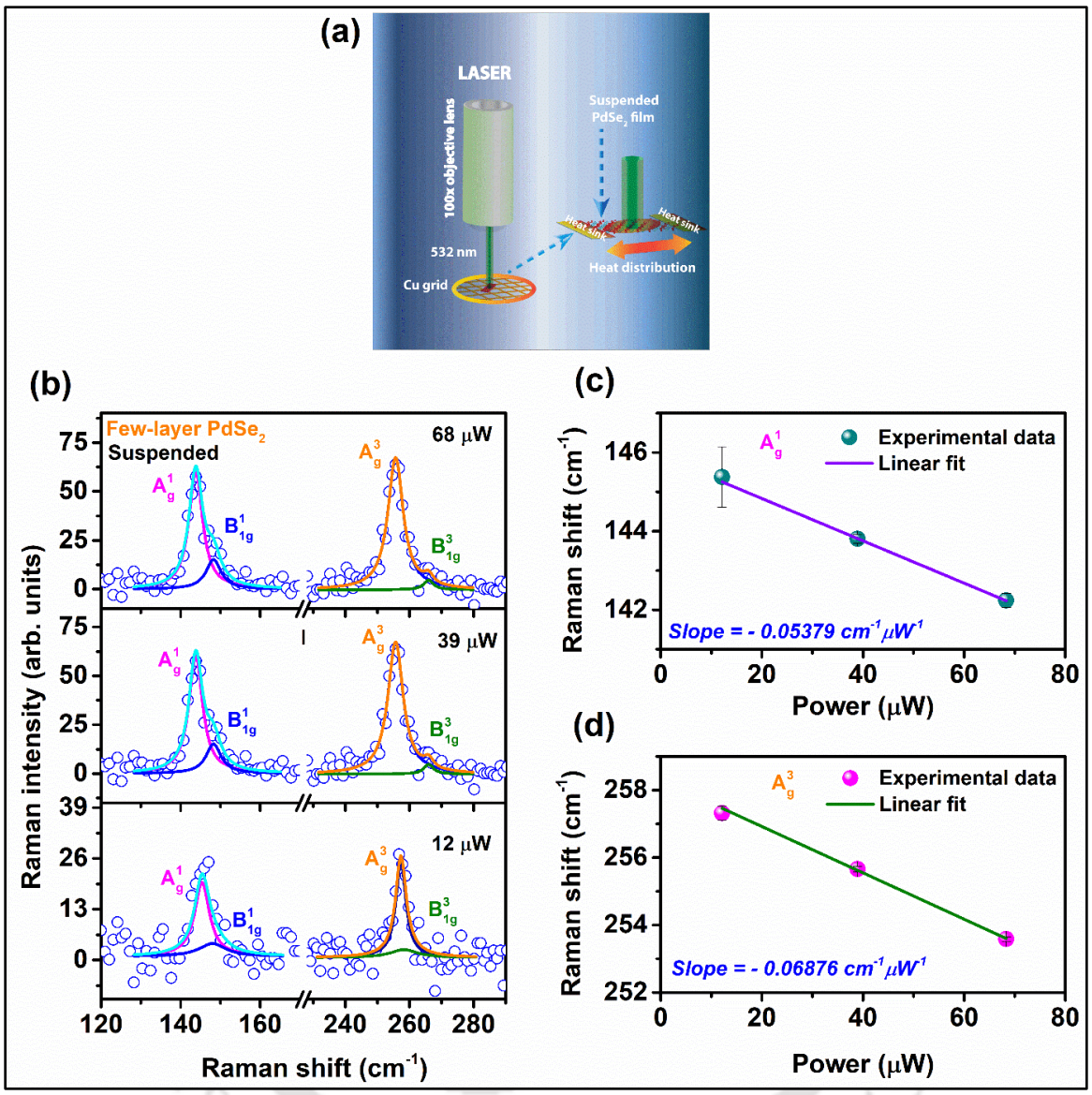

Figure 3.20. (a) Schematic of excitation power-dependent Raman measurement on suspended few-layer $PdSe_2$. (b) Laser power-dependent Raman spectra of suspended few-layer $PdSe_2$. Corresponding Raman-shift for (c) A_g^1 and (d) A_g^3 modes with laser power. Solid line indicates the linear fit.

Figure 3.20b shows the power-dependent stacked Raman spectra for suspended $PdSe_2$ film. Laser-induced heat is conducted entirely through the suspended $PdSe_2$ film, which further contributes to thermal conductivity. The thermal conductivity of few-layer $PdSe_2$ can be calculated using the following **equation 3.5**,

$$k = \frac{1}{2\pi h}\alpha\left(\frac{d\omega}{dP}\right)^{-1} \quad (3.5)$$

where we considered the laser spot transporting heat radially outward from the centre of the spot, and $d\omega$ is a shift in the frequency caused by varying the power, and 'h' is the height of the suspended $PdSe_2$ film. To estimate the thermal conductivity of suspended layered $PdSe_2$, we have extracted laser power dependence of Raman spectra by Lorentzian line-shape fitting. With the increase in excitation intensity, a systematic redshift in Raman peak position was discerned. Notably, broadening line width in Raman peak of layered $PdSe_2$ is due to increase in the lasing intensity which is caused by the localized heat-induced by the laser. Induced localized heat extends more phonon-phonon interaction in the system which leads to higher intensity in the Raman modes. [50] The shift of the A_g^1, A_g^3 peak positions with the increase in incident laser power is displayed in **Figure 3.20c, d** respectively. Redshift in Raman mode peak positions with ascending power is due to thermal conduction in the suspended $PdSe_2$. From the slope, we found the values of $d\omega/\,dP$ as -0.05379 ± 0.00118 $cm^{-1}.\mu W^{-1}$ and -0.06876 ± 0.00242 $cm^{-1}.\mu W^{-1}$ for A_g^1 and A_g^3 modes, respectively.

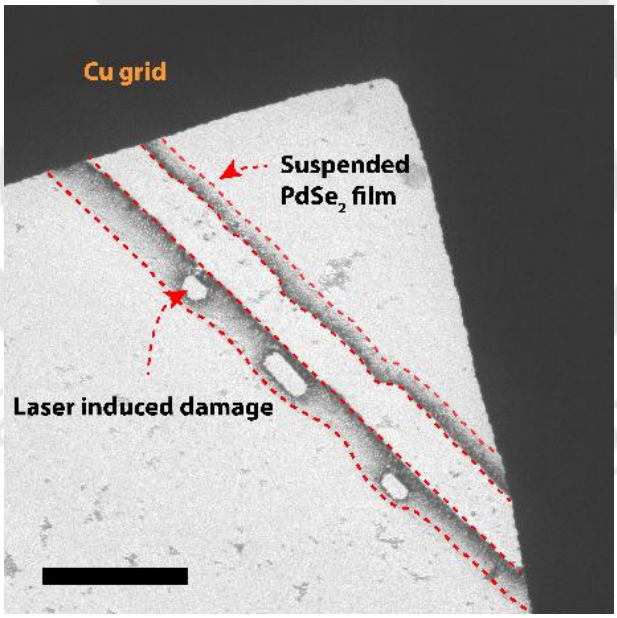

Figure 3.21. Low-resolution TEM image of suspended flakes on Cu grid. The scale bar is 10 μm.

Note that a laser induced damage witnessed during spectroscopic measurement at comparatively lower temperature in the suspended state compared to supported state. It may be due to the quiker heat dissipation in supported state. At suspended state, laser-induced damage in few-layered $PdSe_2$

observed at power >110 μW. A low-resolution TEM image of suspended CVD grown layered $PdSe_2$ on the Cu grid is shown in **Figure 3.21**.

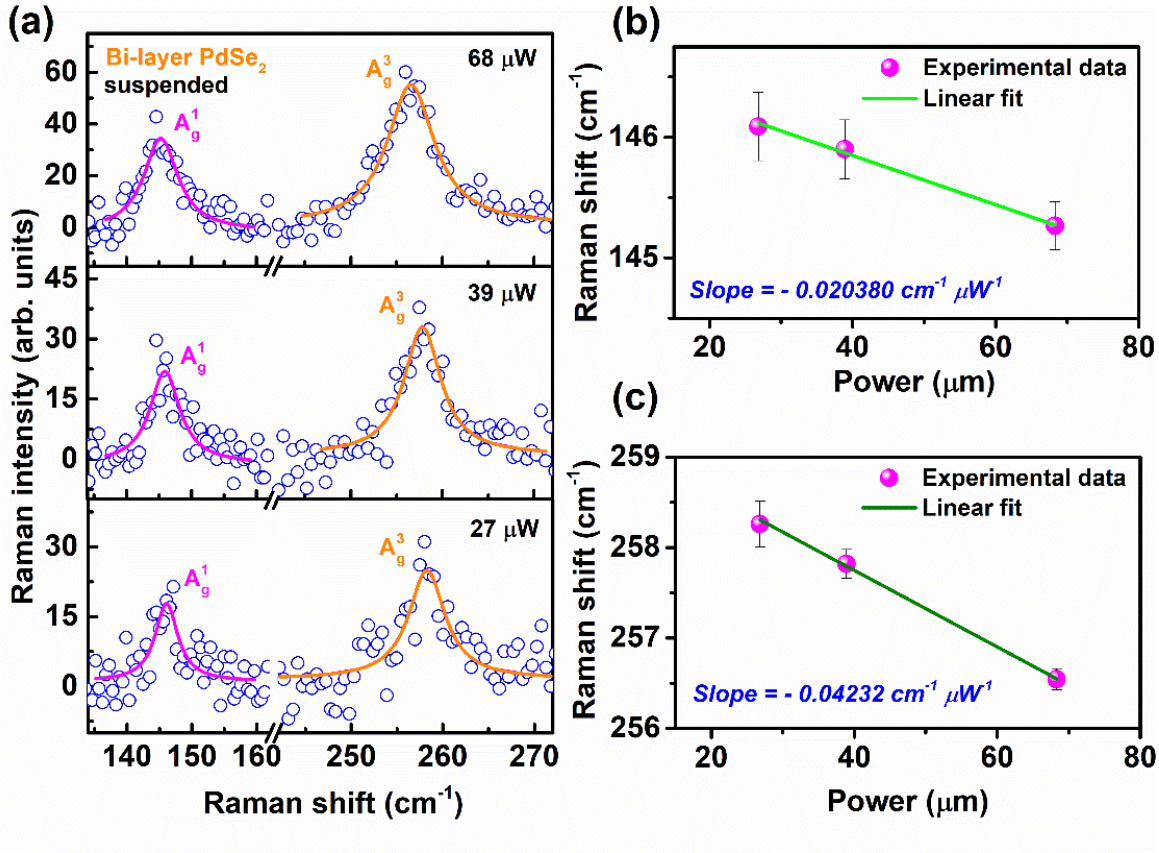

Figure 3.22. (a) Laser power-dependent Raman spectra of suspended bi-layer $PdSe_2$. Corresponding Raman shifts for (b) A_g^1 and (c) A_g^3 modes with laser power. Solid line indicates the linear fit.

In-plane thermal conductivity (k) of CVD-grown few-layer $PdSe_2$ can be estimated using the equation (5), by considering the height of few-layer $PdSe_2$ flake ~3nm, the value of first-order temperature coefficient (α) as - 0.0064 ± 0.0007 $cm^{-1}K^{-1}$, - 0.0181 ± 0.0007 $cm^{-1}K^{-1}$ and value of dω/dP as -0.05379 ± 0.00118 $cm^{-1}.\mu W^{-1}$ and -0.06876 ± 0.00242 $cm^{-1}.\mu W^{-1}$ for A_g^1 and A_g^3 modes, respectively. Thus, the thermal conductivities calculated from A_g^1 and A_g^3 of the few-layer $PdSe_2$ sample using equation (5) are ~ 6.3 ± 0.8 W/m.K and 13.9 ± 1.0 W/m.K. The variation in estimated thermal conductivity from two different modes may be due to the highly in-plane crystal anisotropic nature of $PdSe_2$.

Table 3.5. Comparison of thermal conductivity of different 2D materials grown by different techniques.

Material	Growth method	Thermal conductivity (W/m.K)	Mode	Reference
1L Graphene	Mechanical exfoliation	~ 5300	Suspended in microwells (3 μm) on SiO_2/Si substrate	[4]
1L BN	Mechanical exfoliation	~ 751	Suspended in microwells (2 μm) on SiO_2/Si substrate	[5]
2L BN		~ 646		
5L BN		~ 602		
Few layer (~11L) MoS_2	CVD	~ 52	Suspended on Cu grid	[38]
1L WS_2	CVD	~ 32	Suspended in microwells (6μm) on SiO_2 substrate	[9]
2L WS_2		~ 53		
1L $MoSe_2$	Mechanical exfoliation	~ 59 ± 18	Suspended in microwells (4μm) on SiO_2 substrate	[7]
2L $MoSe_2$		~ 42 ± 13		
1L WSe_2	Mechanical exfoliation	~ 37 ± 12	Suspended in microwells (1μm) on SiO2 substrate	[8]
2L WSe_2		~ 24 ± 12		
3L WSe_2		~ 20 ± 6		
Few layer (~11L) BP	Mechanical exfoliation	~ 10	Suspended in microwells on SiN substrate	[6]
Few layer (~17L) BP		~ 40		
Few-layer (~5L) InSe	CVD	~ 53.4	Suspended in microwells (10μm) on Si_3N_4/Si substrate	[53]
1.62 nm (~ 3L) $PdSe_2$	Mechanical exfoliation	~ 10.95 ~ 15.58	Suspended in microwells (6μm) on Si_3N_4/Si substrate	[45]
7.2 nm (~ 12L) $PdSe_2$		~ 25.35 ~ 28.45		
Few layer (~5L) $PdSe_2$	CVD	~ 10.1	Suspended in Cu grid (63μm)	*This work*

Thus, an estimated average thermal conductivity of few-layer $PdSe_2$ is 10.1 W/m.K. Similarly, calculated thermal conductivity for bilayer $PdSe_2$ is 38.7 ± 5.4 W/m.K, 34.9 ± 1.7 W/m.K (fitting details for power dependent analysis is shown in **Figure 3.22**, where, first-order temperature coefficient (α) as -0.00693 ± 0.00058 $cm^{-1}K^{-1}$, -0.01300± 0.00023 $cm^{-1}K^{-1}$ and value of dω/dP as -

0.020380 ± 0.00122 $cm^{-1}.\mu W^{-1}$ and -0.04232 ± 0.00131 $cm^{-1}.\mu W^{-1}$ for A_g^1 and A_g^3 modes, respectively). Thus, it gives average thermal conductivity of bilayer $PdSe_2$ is 36.8 W/m.K. Note that, as the intensities of all Raman modes are very low, we have fitted the peaks with only A modes due to the negligible contribution of B modes. A comparison table with growth methods and thermal conductivity measurement techniques of conventional 2D materials is given in **Table 3.5**. In **Table 3.5**, all reported thermal conductivities of 2D materials are measured in suspended mode with microwells having sizes ranging between 1 μm to 10 μm. However, in the present case, we used a Cu grid with microwell size 63 μm to support the $PdSe_2$, which is very large compared to other studies.Due to larger microwell size, laser induced heat in dissipated only through the $PdSe_2$ layer, and thus the damage in the sample caused by increasing laser power is very rapid as compared to the smaller microwell case, where the heat dissipation may be faster.

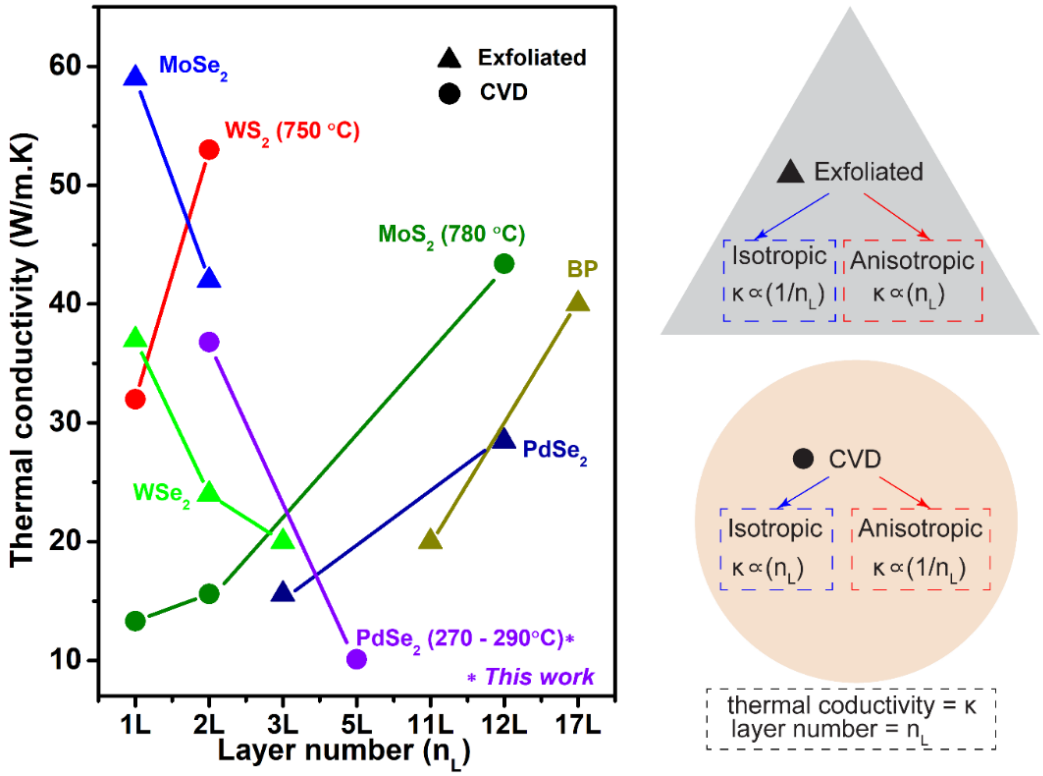

Figure 3.23. Comparison of thermal conductivity of $PdSe_2$ with other conventional 2D materials for different layer numbers.[1-6]The consecutive cartoon illustration reflects the thermal conductivity relationship with layer number for CVD grown and exfoliated isotropic and anisotropic 2D materials.

A comparison plot of thermal conductivity of different 2D materials as a function of layer number is shown **Figure 3.23**. Most of the 2D TMDs (such as $MoSe_2$, MoS_2, WS_2, WSe_2) show isotropic

behaviour due to high crystalline symmetry [14, 51, 52] whereas there are some materials show anisotropic behaviour (such as BP, $PdSe_2$).[6, 31] As the layer number increases, we may notice that thermal conductivity decreases for exfoliated isotropic 2D materials ($\kappa \propto \frac{1}{n_L}$), and as the layer number increases, the thermal conductivity increases for CVD grown isotropic 2D materials ($\kappa \propto n_L$). But anisotropic 2D materials show just the reverse trend. As layer number increases, the thermal conductivity increases for anisotropic exfoliated 2D materials, ($\kappa \propto n_L$) which is just the reverse of other isotropic 2D materials. From our work, we may notice that thermal conductivity decreases with increase in layer number i.e. $\kappa \propto \frac{1}{n_L}$ (since few-layer $PdSe_2$, κ is 10.1 W/m. K and for bilayer $PdSe_2$ it is 36.8 W/m. K). As layer number increases, the thermal conductivity decreases for anisotropic CVD grown 2D materials ($\kappa \propto n_L$), which is just the reverse of other isotropic 2D materials. Economically low-temperature CVD is a favorable, convenient, and environment-friendly technique compared to high-temperature CVD, which can bloom its empire in industrial applications. When it comes to coating a large surface area, only the CVD is a versatile tool to provide large single domain sizes, chemically uniformity, structural uniformity, and a protective coating. Thus, the low-temperature CVD grown $PdSe_2$ paves the way to be one of the low thermal conductive materials for application purposes. Very recently, Chen et al. reported the 'k' value of exfoliated few layer $PdSe_2$ flakes, whose variation of thermal conductivity with layer number is just the reverse way of our CVD grown $PdSe_2$.[45] It might be due to the variation in crystal quality in CVD grown and exfoliated $PdSe_2$. In addition, we elaborated FWHM broadening and adopted a more straightforward calculation to estimate the k value in CVD grown $PdSe_2$. Note that we used an unpolarized laser source for all the measurements, and we were able to evaluate the anisotropy for the bilayer, and few layer $PdSe_2$ in a simpler, yet powerful way.

3.4. Conclusion

There exists a wide variation of temperature co-efficient in CVD- grown $PdSe_2$ from temperature-dependent Raman measurement with an unpolarized laser source. Our work reveals that evaluating the Raman temperature co-efficient is an alternative approach to find the anisotropic ratio in $PdSe_2$ using an unpolarized laser. Using unpolarized laser source, the calculated anisotropic ratios for

bilayer and few-layer are 1.42 and 1.28 respectively. We have interpreted temperature-dependent Raman spectral linewidth of bilayer and few-layer CVD-grown $PdSe_2$ using an anharmonic phonon decay process. We revealed that the usual trend of intensity variation with temperature in the range 83 K - 130K and anomalous nature at >130 K for all the characteristic Raman modes. At room temperature, the estimated thermal conductivity is ~36.8 W/m. K and ~10.1 W/m. K for bi-layer and few-layer (~5L) $PdSe_2$. These results are crucial for exploration of temperature dependent phonon modes and intuitions of phonon-phonon and electron-phonon couplings in 2D NTMDs.

References

1. Duan, X., Wang, C., Pan, A., Yu, R., & Duan, X. (2016). ChemInform Abstract: Two-Dimensional Transition Metal Dichalcogenides as Atomically Thin Semiconductors: Opportunities and Challenges. ChemInform, 47(6). https://doi.org/10.1002/chin.201606232.
2. Zhou, X., Zhang, Q., Gan, L., Li, H., Xiong, J., & Zhai, T. (2016b). Booming Development of Group IV–VI Semiconductors: Fresh Blood of 2D Family. Advanced Science, 3(12). https://doi.org/10.1002/advs.201600177.
3. Sun, Z., Martinez, A., & Wang, F. (2016b). Optical modulators with 2D layered materials. Nature Photonics, 10(4), 227–238. https://doi.org/10.1038/nphoton.2016.15.
4. Balandin, A. A., Ghosh, S., Bao, W., Calizo, I., Teweldebrhan, D., Miao, F., & Lau, C. N. (2008b). Superior Thermal Conductivity of Single-Layer Graphene. Nano Letters, 8(3), 902–907. https://doi.org/10.1021/nl0731872.
5. Cai, Q., Scullion, D., Gan, W., Falin, A., Zhang, S., Watanabe, K., Taniguchi, T., Chen, Y., Santos, E. J. G., & Li, L. H. (2019d). High thermal conductivity of high-quality monolayer boron nitride and its thermal expansion. Science Advances, 5(6). https://doi.org/10.1126/sciadv.aav0129.
6. Luo, Z., Maassen, J., Deng, Y., Du, Y., Garrelts, R. P., Lundstrom, M. S., Ye, P. D., & Xu, X. (2015b). Anisotropic in-plane thermal conductivity observed in few-layer black phosphorus. Nature Communications, 6(1). https://doi.org/10.1038/ncomms9572.
7. Zhang, X., Sun, D., Li, Y., Lee, G., Cui, X., Chenet, D., You, Y., Heinz, T. F., & Hone, J. C. (2015b). Measurement of Lateral and Interfacial Thermal Conductivity of Single- and Bilayer MoS2 and MoSe2 Using Refined Optothermal Raman Technique. ACS Applied Materials & Interfaces, 7(46), 25923–25929. https://doi.org/10.1021/acsami.5b08580.
8. Easy, E., Gao, Y., Wang, Y., Yan, D., Goushehgir, S. M., Yang, E., Xu, B., & Zhang, X. (2021b). Experimental and Computational Investigation of Layer-Dependent Thermal Conductivities and Interfacial Thermal Conductance of One- to Three-Layer WSe2. ACS Applied Materials & Interfaces, 13(11), 13063–13071. https://doi.org/10.1021/acsami.0c21045.
9. Peimyoo, N., Shang, J., Yang, W., Wang, Y., Cong, C., & Yu, T. (2014b). Thermal conductivity determination of suspended mono- and bilayer WS2 by Raman spectroscopy. Nano Research, 8(4), 1210–1221. https://doi.org/10.1007/s12274-014-0602-0.
10. Hossain, M. T., & Giri, P. K. (2021b). Temperature-dependent Raman studies and thermal conductivity of direct CVD grown non-van der Waals layered Bi2O2Se. Journal of Applied Physics, 129(17). https://doi.org/10.1063/5.0049368.
11. Wang, F., Luo, P., Zhang, Y., Huang, Y., Zhang, Q., Li, Y., & Zhai, T. (2020c). Band structure engineered tunneling heterostructures for high-performance visible and near-infrared photodetection. Science China Materials, 63(8), 1537–1547. https://doi.org/10.1007/s40843-020-1353-3.
12. Wang, F., Yang, S., Wu, J., Hu, X., Li, Y., Li, H., Liu, X., Luo, J., & Zhai, T. (2021b). Emerging two-dimensional bismuth oxychalcogenides for electronics and optoelectronics. InfoMat, 3(11), 1251–1271. https://doi.org/10.1002/inf2.12215.
13. Wang, Y., Pang, J., Cheng, Q., Han, L., Li, Y., Meng, X., Ibarlucea, B., Zhao, H., Yang, F., Liu, H., Liu, H., Zhou, W., Wang, X., Rummeli, M. H., Zhang, Y., & Cuniberti, G. (2021b). Applications of 2D-Layered Palladium Diselenide and Its van der Waals Heterostructures in Electronics and Optoelectronics. Nano-Micro Letters, 13(1). https://doi.org/10.1007/s40820-021-00660-0.
14. Neupane, G. P., Zhou, K., Chen, S., Yildirim, T., Zhang, P., & Lu, Y. (2019b). In-Plane Isotropic/Anisotropic 2D van der Waals Heterostructures for Future Devices. Small, 15(11). https://doi.org/10.1002/smll.201804733.

15. Xu, Y., Shi, Z., Shi, X., Zhang, K., & Zhang, H. (2019b). Recent progress in black phosphorus and black-phosphorus-analogue materials: properties, synthesis and applications. Nanoscale, 11(31), 14491–14527. https://doi.org/10.1039/c9nr04348a.
16. Wang, Y., Li, L., Yao, W., Song, S., Sun, J. T., Pan, J., Ren, X., Li, C., Okunishi, E., Wang, Y., Wang, E., Shao, Y., Zhang, Y. Y., Yang, H., Schwier, E. F., Iwasawa, H., Shimada, K., Taniguchi, M., Cheng, Z., . . . Gao, H. (2015b). Monolayer PtSe2, a New Semiconducting Transition-Metal-Dichalcogenide, Epitaxially Grown by Direct Selenization of Pt. Nano Letters, 15(6), 4013–4018. https://doi.org/10.1021/acs.nanolett.5b00964.
17. Zhao, Y., Qiao, J., Yu, Z., Yu, P., Xu, K., Lau, S. P., Zhou, W., Liu, Z., Wang, X., Ji, W., & Chai, Y. (2016). High-Electron-Mobility and Air-Stable 2D Layered PtSe2 FETs. Advanced Materials, 29(5). https://doi.org/10.1002/adma.201604230.
18. Chow, W. L., Yu, P., Liu, F., Hong, J., Wang, X., Zeng, Q., Hsu, C., Zhu, C., Zhou, J., Wang, X., Xia, J., Yan, J., Chen, Y., Wu, D., Yu, T., Shen, Z., Lin, H., Jin, C., Tay, B. K., & Liu, Z. (2017). High Mobility 2D Palladium Diselenide Field-Effect Transistors with Tunable Ambipolar Characteristics. Advanced Materials, 29(21). https://doi.org/10.1002/adma.201602969.
19. Oyedele, A. D., Yang, S., Liang, L., Puretzky, A. A., Wang, K., Zhang, J., Yu, P., Pudasaini, P. R., Ghosh, A. W., Liu, Z., Rouleau, C. M., Sumpter, B. G., Chisholm, M. F., Zhou, W., Rack, P. D., Geohegan, D. B., & Xiao, K. (2017). PdSe2: Pentagonal Two-Dimensional Layers with High Air Stability for Electronics. Journal of the American Chemical Society, 139(40), 14090–14097. https://doi.org/10.1021/jacs.7b04865.
20. Zhao, Y., Qiao, J., Yu, P., Hu, Z., Lin, Z., Lau, S. P., Liu, Z., Ji, W., & Chai, Y. (2016). Extraordinarily Strong Interlayer Interaction in 2D Layered PtS2. Advanced Materials, 28(12), 2399–2407. https://doi.org/10.1002/adma.201504572.
21. Li, L., Wang, W., Chai, Y., Li, H., Tian, M., & Zhai, T. (2017). Few-Layered PtS2 Phototransistor on h-BN with High Gain. Advanced Functional Materials, 27(27). https://doi.org/10.1002/adfm.201701011.
22. Deng, S., Li, L., & Zhang, Y. (2018). Strain Modulated Electronic, Mechanical, and Optical Properties of the Monolayer PdS2, PdSe2, and PtSe2 for Tunable Devices. ACS Applied Nano Materials, 1(4), 1932–1939. https://doi.org/10.1021/acsanm.8b00363.
23. Pi, L., Li, L., Liu, K., Zhang, Q., Li, H., & Zhai, T. (2019). Recent Progress on 2D Noble-Transition-Metal Dichalcogenides. Advanced Functional Materials, 29(51). https://doi.org/10.1002/adfm.201904932.
24. Li, L., Han, W., Pi, L., Niu, P., Han, J., Wang, C., Su, B., Li, H., Xiong, J., Bando, Y., & Zhai, T. (2019). Emerging in-plane anisotropic two-dimensional materials. InfoMat, 1(1), 54–73. https://doi.org/10.1002/inf2.12005.
25. Jiang, S., Xie, C., Gu, Y., Zhang, Q., Wu, X., Sun, Y., Li, W., Shi, Y., Zhao, L., Pan, S., Yang, P., Huan, Y., Xie, D., Zhang, Q., Liu, X., Zou, X., Gu, L., & Zhang, Y. (2019). Anisotropic Growth and Scanning Tunneling Microscopy Identification of Ultrathin Even-Layered PdSe2 Ribbons. Small, 15(45). https://doi.org/10.1002/smll.201902789.
26. Liang, Q., Wang, Q., Zhang, Q., Wei, J., Lim, S. X., Zhu, R., Hu, J., Wei, W., Lee, C., Sow, C., Zhang, W., & Wee, A. T. S. (2019). High-Performance, Room Temperature, Ultra-Broadband Photodetectors Based on Air-Stable PdSe2. Advanced Materials, 31(24). https://doi.org/10.1002/adma.201807609.
27. Zhao, Y., Yu, P., Zhang, G., Sun, M., Chi, D., Hippalgaonkar, K., Thong, J. T. L., & Wu, J. (2020). Low-Symmetry PdSe2 for High Performance Thermoelectric Applications. Advanced Functional Materials, 30(52). https://doi.org/10.1002/adfm.202004896.
28. Hossain, M. T., Das, M., Ghosh, J., Ghosh, S., & Giri, P. K. (2021). Understanding the interfacial charge transfer in the CVD grown Bi2O2Se/CsPbBr3 nanocrystal heterostructure and its

exploitation in superior photodetection: experiment vs. theory. Nanoscale, 13(35), 14945–14959. https://doi.org/10.1039/d1nr04470b.

29. Yang, P., Zhang, Z., Sun, M., Lin, F., Cheng, T., Shi, J., Xie, C., Shi, Y., Jiang, S., Huan, Y., Liu, P., Ding, F., Xiong, C., Xie, D., & Zhang, Y. (2019). Thickness Tunable Wedding-Cake-like MoS2 Flakes for High-Performance Optoelectronics. ACS Nano, 13(3), 3649–3658. https://doi.org/10.1021/acsnano.9b00277.
30. Jiang, J., Li, N., Zou, J., Zhou, X., Eda, G., Zhang, Q., Zhang, H., Li, L., Zhai, T., & Wee, A. T. S. (2019). Synergistic additive-mediated CVD growth and chemical modification of 2D materials. Chemical Society Reviews, 48(17), 4639–4654. https://doi.org/10.1039/c9cs00348g.
31. Pi, L., Hu, C., Shen, W., Li, L., Luo, P., Hu, X., Chen, P., Li, D., Li, Z., Zhou, X., & Zhai, T. (2020). Highly In-Plane Anisotropic 2D PdSe2 for Polarized Photodetection with Orientation Selectivity. Advanced Functional Materials, 31(3). https://doi.org/10.1002/adfm.202006774.
32. Tai, K., Chen, J., Wen, Y., Park, H., Zhang, Q., Lu, Y., Chang, R., Tang, P., Allen, C. S., Wu, W., & Warner, J. H. (2020). Phase Variations and Layer Epitaxy of 2D PdSe2 Grown on 2D Monolayers by Direct Selenization of Molecular Pd Precursors. ACS Nano, 14(9), 11677–11690. https://doi.org/10.1021/acsnano.0c04230.
33. Li, E., Wang, D., Fan, P., Zhang, R., Zhang, Y., Li, G., Mao, J., Wang, Y., Lin, X., Du, S., & Gao, H. (2018). Construction of bilayer PdSe2 on epitaxial graphene. Nano Research, 11(11), 5858–5865. https://doi.org/10.1007/s12274-018-2090-0.
34. Gu, Y., Cai, H., Dong, J., Yu, Y., Hoffman, A. N., Liu, C., Oyedele, A. D., Lin, Y., Ge, Z., Puretzky, A. A., Duscher, G., Chisholm, M. F., Rack, P. D., Rouleau, C. M., Gai, Z., Meng, X., Ding, F., Geohegan, D. B., & Xiao, K. (2020). Two-Dimensional Palladium Diselenide with Strong In-Plane Optical Anisotropy and High Mobility Grown by Chemical Vapor Deposition. Advanced Materials, 32(19). https://doi.org/10.1002/adma.201906238.
35. Xu, W., Jiang, J., Ma, H., Zhang, Z., Li, J., Zhao, B., Wu, R., Yang, X., Zhang, H., Li, B., Shu, W., Zhang, Z., Li, B., Liu, Y., Liao, L., & Duan, X. (2020). Vapor phase growth of two-dimensional PdSe2 nanosheets for high-photoresponsivity near-infrared photodetectors. Nano Research, 13(8), 2091–2097. https://doi.org/10.1007/s12274-020-2815-8.
36. Lu, L., Chen, G., Cheng, H., Chuu, C., Lu, K., Chen, C., Lu, M., Chuang, T., Wei, D., Chueh, W., Jian, W., Li, M., Chang, Y., Li, L., & Chang, W. (2020). Layer-Dependent and In-Plane Anisotropic Properties of Low-Temperature Synthesized Few-Layer PdSe2 Single Crystals. ACS Nano, 14(4), 4963–4972. https://doi.org/10.1021/acsnano.0c01139.
37. Paillet, M., Parret, R., Sauvajol, J., & Colomban, P. (2017). Graphene and related 2D materials: An overview of the Raman studies. Journal of Raman Spectroscopy, 49(1), 8–12. https://doi.org/10.1002/jrs.5295.
38. Sahoo, S., Gaur, A. P. S., Ahmadi, M., Guinel, M. J., & Katiyar, R. S. (2013). Temperature-Dependent Raman Studies and Thermal Conductivity of Few-Layer MoS2. The Journal of Physical Chemistry C, 117(17), 9042–9047. https://doi.org/10.1021/jp402509w.
39. Pi, L., Li, L., Hu, X., Zhou, S., Li, H., & Zhai, T. (2018). Temperature dependence of Raman responses of few-layer PtS2. Nanotechnology, 29(50), 505709. https://doi.org/10.1088/1361-6528/aae41f.
40. Yan, M., Wang, E., Zhou, X., Zhang, G., Zhang, H., Zhang, K., Yao, W., Lu, N., Yang, S., Wu, S., Yoshikawa, T., Miyamoto, K., Okuda, T., Wu, Y., Yu, P., Duan, W., & Zhou, S. (2017). High quality atomically thin PtSe 2 films grown by molecular beam epitaxy. 2D Materials, 4(4), 045015. https://doi.org/10.1088/2053-1583/aa8919.
41. Ma, H., Chen, P., Li, B., Li, J., Ai, R., Zhang, Z., Sun, G., Yao, K., Lin, Z., Zhao, B., Wu, R., Tang, X., Duan, X., & Duan, X. (2018). Thickness-Tunable Synthesis of Ultrathin Type-II Dirac Semimetal PtTe2 Single Crystals and Their Thickness-Dependent Electronic Properties. Nano Letters, 18(6), 3523–3529. https://doi.org/10.1021/acs.nanolett.8b00583.

42. Zeng, L., Wu, D., Lin, S., Xie, C., Yuan, H., Lu, W., Lau, S. P., Chai, Y., Luo, L., Li, Z., & Tsang, Y. H. (2018). Controlled Synthesis of 2D Palladium Diselenide for Sensitive Photodetector Applications. Advanced Functional Materials, 29(1). https://doi.org/10.1002/adfm.201806878.
43. Pei, Y., Wang, H., & Snyder, G. J. (2012). Band Engineering of Thermoelectric Materials. Advanced Materials, 24(46), 6125–6135. https://doi.org/10.1002/adma.201202919.
44. Bae, J. J., Jeong, H. Y., Han, G. H., Kim, J., Kim, H., Kim, M. S., Moon, B. H., Lim, S. C., & Lee, Y. H. (2017). Thickness-dependent in-plane thermal conductivity of suspended MoS2 grown by chemical vapor deposition. Nanoscale, 9(7), 2541–2547. https://doi.org/10.1039/c6nr09484h.
45. Chen, L., Zhang, W., Zhang, H., Chen, J., Tan, C., Yin, S., Li, G., Zhang, Y., Gong, P., & Li, L. (2021). In-Plane Anisotropic Thermal Conductivity of Low-Symmetry PdSe2. Sustainability, 13(8), 4155. https://doi.org/10.3390/su13084155.
46. Yu, J., Kuang, X., Li, J., Zhong, J., Zeng, C., Cao, L., Liu, Z., Zeng, Z., Luo, Z., He, T., Pan, A., & Liu, Y. (2021b). Giant nonlinear optical activity in two-dimensional palladium diselenide. Nature Communications, 12(1). https://doi.org/10.1038/s41467-021-21267-4.
47. Sahoo, S., Mallik, S. K., Sahu, M. C., Joseph, A., Singh, S., Gupta, S. K., Rout, B., Pradhan, G. K., & Sahoo, S. (2020). Thermal conductivity of free-standing silicon nanowire using Raman spectroscopy. Nanotechnology, 31(50), 505701. https://doi.org/10.1088/1361-6528/abb42c.
48. Slack, G. A. (1962). Anisotropic Thermal Conductivity of Pyrolytic Graphite. Physical Review, 127(3), 694–701. https://doi.org/10.1103/physrev.127.694.
49. Balkanski, M., Wallis, R. F., & Haro, E. (1983). Anharmonic effects in light scattering due to optical phonons in silicon. Physical Review. B, Condensed Matter, 28(4), 1928–1934. https://doi.org/10.1103/physrevb.28.1928.
50. Su, Z., Sha, J., Pan, G., Liu, J., Yang, D., Dickinson, C., & Zhou, W. (2005). Temperature-Dependent Raman Scattering of Silicon Nanowires. The Journal of Physical Chemistry B, 110(3), 1229–1234. https://doi.org/10.1021/jp055869o.
51. Zhao, M., Zhang, W., Liu, M., Zou, C., Yang, K., Yang, Y., Dong, Y., Zhang, L., & Huang, S. (2016). Interlayer coupling in anisotropic/isotropic van der Waals heterostructures of ReS2 and MoS2 monolayers. Nano Research, 9(12), 3772–3780. https://doi.org/10.1007/s12274-016-1247-y.
52. Wang, Q. H., Kalantar-Zadeh, K., Kis, A., Coleman, J. N., & Strano, M. S. (2012). Electronics and optoelectronics of two-dimensional transition metal dichalcogenides. Nature Nanotechnology, 7(11), 699–712. https://doi.org/10.1038/nnano.2012.193.
53. Botcha, V. D., Zhang, M., Li, K., Gu, H., Huang, Z., Cai, J., Lu, Y., Yu, W., & Liu, X. (2017). High-K substrate effect on thermal properties of 2D InSe few layer. Journal of Alloys and Compounds, 735, 594–599. https://doi.org/10.1016/j.jallcom.2017.11.058.

Chapter 4 - Evidence for intrinsic defects and nanopores as hotspots in 2D $PdSe_2$ dendrites for plasmon-free SERS substrate with a high enhancement factor

Surface-enhanced Raman spectroscopy (SERS), a very powerful tool for the identification of molecular species, has relied mostly on noble metal-based substrates to obtain a high enhancement factor. In this chapter, we demonstrate that intrinsic defects in 2D $PdSe_2$ dendrites act as hotspots for high SERS enhancement. We grow 2D dendritic $PdSe_2$ with ample intrinsic defects to exploit it for SERS application. XPS analysis reveals 9.3% outer layer and 4.7% interior Se vacancies. A detailed examination of atomic-scale defects revealed Se vacancy (V_{Se}) coupled with Se-Pd-Se vacancy ($V_{Se\text{-}Pd\text{-}Se}$) in monolayer $PdSe_2$, and an array of line defects and nanopores in bilayer $PdSe_2$ dendrites. Our studies reveal that Se vacancy-rich $PdSe_2$ gives rise to line defects that act like hotspots for SERS enhancement. Remarkably, the vacancy-rich dendritic $PdSe_2$ shows a SERS enhancement factor $>10^5$ and can detect RhB at a concentration down to 10^{-8} M. We speculate that the topological line defects and the edge construction in $PdSe_2$ dendrites act as metallic edge, which is partly responsible for the high enhancement in the SERS signal. The high SERS sensitivity is explained on the basis of multiple charge transfer processes combined with the predicted metal-like behavior of the defected 2D $PdSe_2$.

4.1. Introduction

Recently, a new family of two-dimensional (2D) materials, namely noble transition metal di-chalcogenides (NTMDs) with atomic thickness, has received significant attention due to their unique properties, including thickness-dependent tunable-bandgaps that has potential for various optoelectronic applications.[2-7] $PdSe_2$ is one of the promising NTMDs due to its low symmetry lattice structure with highly tunable bandgap from 0 eV (bulk) to 1.43 eV (monolayer), high carrier mobility, high air stability with monolayer thickness ~0.5 nm. [8-10] $PdSe_2$ shows many distinctive properties, such as in-plane anisotropic properties similar to black phosphorus (BP).[11] BP has been reported as a very promising material in nanotechnology.[12] However, poor stability in ambient conditions limits its application in various fields.[13] We anticipate that 2D $PdSe_2$ may replace the BP in many fields due to its in-plane anisotropy with high stability in ambient conditions.

For years on end, it was believed that defects would be structurally unstable in 2D crystals according to the Mermin-Wagner theorem.[14] Defect field traced a new trajectory when graphene layer was exfoliated and isolated in 2004.[15] Structural defects, including edges and point defects, have a significant influence on mechanical, thermal, optical, electrical properties in graphene and transition metal di-chalcogenides (TMDs). Physiochemical properties of monolayer and few-layer graphene are dependent on the defect type, defect environment, and arrangements.[16] Edges have been shown to weaken the mechanical strength and degrade the electronic performance of graphene.[17] It is reported that $PdSe_2$ exhibits strong interlayer interactions, which are associated with defects.[18,19] Recently, theories predicted that $PdSe_2$ with Pd as well as Se vacancies are stable and Se vacancies are more energetically favorable than Pd vacancies.[20] However, the experimental evidence for the same has rarely been reported. In case of dendritic $PdSe_2$, the presence of dendritic edges gives rise to different Pd and Se terminations with different zigzag and armchair edges. However, defects in $PdSe_2$ have rarely been explored compared to that in graphene and other TMDs.[9,21-24]

It is well known that defects and edges are beneficial for several applications; for example, defects are essential in creating bonding and trapping sites for atoms and molecules, which can be used for sensing applications.[25] In recent years, it has been reported that a non-SERS substrate can show SERS activity only by introducing defects.[26-28] This motivates us to exploit the defects in 2D $PdSe_2$ for possible application in SERS. Conventionally, high SERS activity mainly appears in hotspots of plasmonic noble-metal materials (mostly Au and Ag). [29-35] However, there are many drawbacks of plasmonic-based SERS such as they require a well-designed hot spot, high cost, poor biocompatibility, low stability, which limits its applications in routinely used commercial products.[36] In comparison to traditional plasmonic-metal based SERS, plasmon-free SERS substrates have attracted tremendous attention due to their excellent stability, low price, recyclability, superior biocompatibility, and many promising applications in the field of biomedical diagnosis[37], metal ions and organic pollutant sensing[38], monitoring in chemical reactions. At present, there exists a big gap between plasmonic SERS substrate and plasmon-free SERS substrate, as plasmonic SERS substrate often shows higher enhancement factors. Though SERS has been a very active area of research for decades, it remains challenging to reproduce plasmon-free SERS substrates with a high enhancement factor (EF).[39] To our knowledge, no report contributed to the high SERS activity of 2D $PdSe_2$ dendrites enriched with intrinsic defects. Like

SERS, in the field of nanopore sensing techniques, there is intense research to achieve nanopores in 2D material (graphene[40], TMDs[41], boron nitride[30,42] , black phosphorus[43], etc.) instead of solid-state nanopores and biological nanopores due to their superior characteristics. [33,44]. To our knowledge, there is no experimental report on the properties and applications of intrinsic defects and nanopores in 2D $PdSe_2$.

4.2. Experimental details

4.2.1. Low-temperature CVD growth of $PdSe_2$ dendrites:

All Precursors were purchased from Sigma Aldrich and used for experiments without further purification. We adopted a novel synthesis technique with a slight addition of NaCl to obtain dendritic $PdSe_2$.[45] Briefly, we followed a two-step process, (i) $PdCl_2$ solution preparation (with adding a small amount of NaCl) and (ii) relatively low-temperature chemical vapor deposition. Firstly, we dissolve $PdCl_2$ powder (99.999%, 27 mg) in Mili Q water. When the powder was dissolved entirely, NaCl was added and stirred to dissolve completely. Then it is kept for a few hours for further use in CVD. Secondly, the solution is drop-casted on the freshly cleaved mica substrate and heated on a hot plate in atmospheric conditions to use as a CVD substrate. To conduct the CVD process, a single-zone tube furnace was used. Then, the as-prepared substrate was inserted into the quartz tube and placed at the lower temperature zone. At the center of the tube, Se precursors were kept. A rotary pump was used to evacuate the quartz tube, and Argon was purged with 300 sccm to pump out other residues from the tube. Then the furnace temperature was elevated to 450 °C to vaporize the Se precursor, and a flow rate of 110 sccm was introduced to carry the precursor to the substrate for nucleation and growth of $PdSe_2$ film.

4.2.2. SERS measurement

Water solutions of RhB were prepared with different concentrations through diluting sequentially. Further, it was drop-casted over the CVD-grown $PdSe_2$ dendrites and kept for a few minutes to soak up the RhB molecule completely. An excitation source of 532 nm equipped with the Raman instruments (LabRam HR800, Jobin Yvon) was used to obtain the SERS spectra on $PdSe_2$.

4.2.3. Sample preparation for TEM characterization

The as-prepared samples were transferred to the TEM grid following our previous report.[45] In short, PMMA based transfer process has been conducted. First, PMMA was spin-coated on the $PdSe_2$ dendrites, followed by drying. After that, it was immersed into a KOH solution till the lift-off of PMMA/$PdSe_2$ from mica substrate. Further, it was dipped into deionized water. Then the floated PMMA/$PdSe_2$ was scooped with the carbon-coated Cu-grid (300 mesh, pacific grid, USA). After that, it is rinsed with acetone to remove PMMA, followed by IPA cleaning.

4.2.4. Characterization Technique

The structural morphology is obtained using field emission electron microscopy (FESEM, Sigma, Zeiss). The as-grown sample thickness was estimated via atomic force microscopy (AFM) (Cypher, Oxford Instruments) in non-contact mode scanning. KPFM measurement was performed on conducting surface (ITO coated glass) with Ti/Ir coated silicon tip in the AFM instrument above. The high magnification surface morphology of dendritic $PdSe_2$ has been carried out by a transmission electron microscope (TEM) (JEOL-JEM 2010 operated at 200 kV). The samples for TEM analysis have been prepared on a carbon-coated Cu grid of 300 mesh size (Pacific Grid, USA). The crystallinity in the as-grown $PdSe_2$ flakes has been studied by high-resolution micro-Raman spectroscopy (LabRam HR800, Jobin Yvon) with an excitation wavelength (λ_{ex}) of 532 nm (Ar ion laser). The excitation laser light was focused with a 100X objective lens to a spot size of 1 μm, with a laser power of 1.5 mW, which discards the possibility of laser heating-induced damage. A charge-coupled device equipped with the same system collected the signal in a backscattering geometry sent through a multimode fiber grating of 1800 grooves mm^{-1}. Micro-PL in $PdSe_2$/RhB and RhB have been conducted in the Raman instrument with 532 nm laser excitation. X-ray photoelectron spectroscopy (XPS) measurement was executed using a PHI X-tool automated photoelectron spectrometer (ULVAC-PHI, Japan) with an Al Kα x-ray beam (1486.6 eV) at 20 kV, 84 W for the analysis of the chemical compositions. NIR PL has been taken with laser excitation 641 nm with a power of 50 mW. Confocal microscopy imaging was performed with 488 nm laser excitation (Zeiss LSM 880).

4.3. Computational Methods:

The calculation of the electronic properties of the bilayer $PdSe_2$ without and with line defects were performed within the framework of DFT, including van der Waals (vdW) correction with a plane-wave basis set using Quantum ESPRESSO software [64-66]. The core electrons were described using the projector-augmented-wave (PAW) pseudopotentials [67], and the exchange-correlation potential was estimated using the generalized gradient approximation (GGA) with Perdew-Burke-Ernzerhof (PBE)[68] functional. To model the Se defect in 2L $PdSe_2$ structures were built by a periodic slab geometry with a vacuum of 20 Å along the Z-direction. Subsequently, the upper Se-atom present in the upper layer of the slab was removed from the unit cell and obtained the desired structure (defective 2L $PdSe_2$). The optimized lattice constants of the unit cell of defective 2L $PdSe_2$ were a = 5.72 Å and b = 5.80 Å which are slightly lower than those of pristine 2L $PdSe_2$ (a = 5.75, and b = 5.87 [69]). Using a convergence test, a 12×12×1 k-point sampling was employed with cut-off energy of 680 eV. Additionally, the band structure as well as the DOS of the defective 2L $PdSe_2$ were calculated using the HSE06 exchange hybrid functional as it provides a more accurate description of the band structure [70]. Then 3×3×1 supercells of pristine 2L $PdSe_2$ and defective 2L $PdSe_2$ were constructed with k-point sampling 8×8×1. To achieve self-consistency, a force of 10-2 eV/Å was employed.

4.4. Results and Discussion

4.4.1. Structure and morphology of dendritic $PdSe_2$

The control of layer number in dendritic growth is crucial in 2D material's synthesis. Controlled growth of 2L and 1L is obtained via low-temperature CVD technique with minor modification. **Figure 4.1a** illustrates the FESEM micrograph of the 2L $PdSe_2$ dendrites grown on the freshly cleaved mica substrate, which is enlarged (**Figure 4.1a** inset) for better visualization. The average width of 2-4 μm was mostly grown over the mica substrate. The $PdSe_2$ dendrites begin from the dendritic zone and move along the b direction. Dendritic $PdSe_2$ extends up-to few tens of micrometers mostly along b direction, as confirmed in a later section. There exists an inter-dendritic region in-between 2L edges of bilayer $PdSe_2$, which is barely visible from the magnified FESEM micrograph (inset **Figure 4.1)**, yellow marked in the inset of FESEM micrograph).

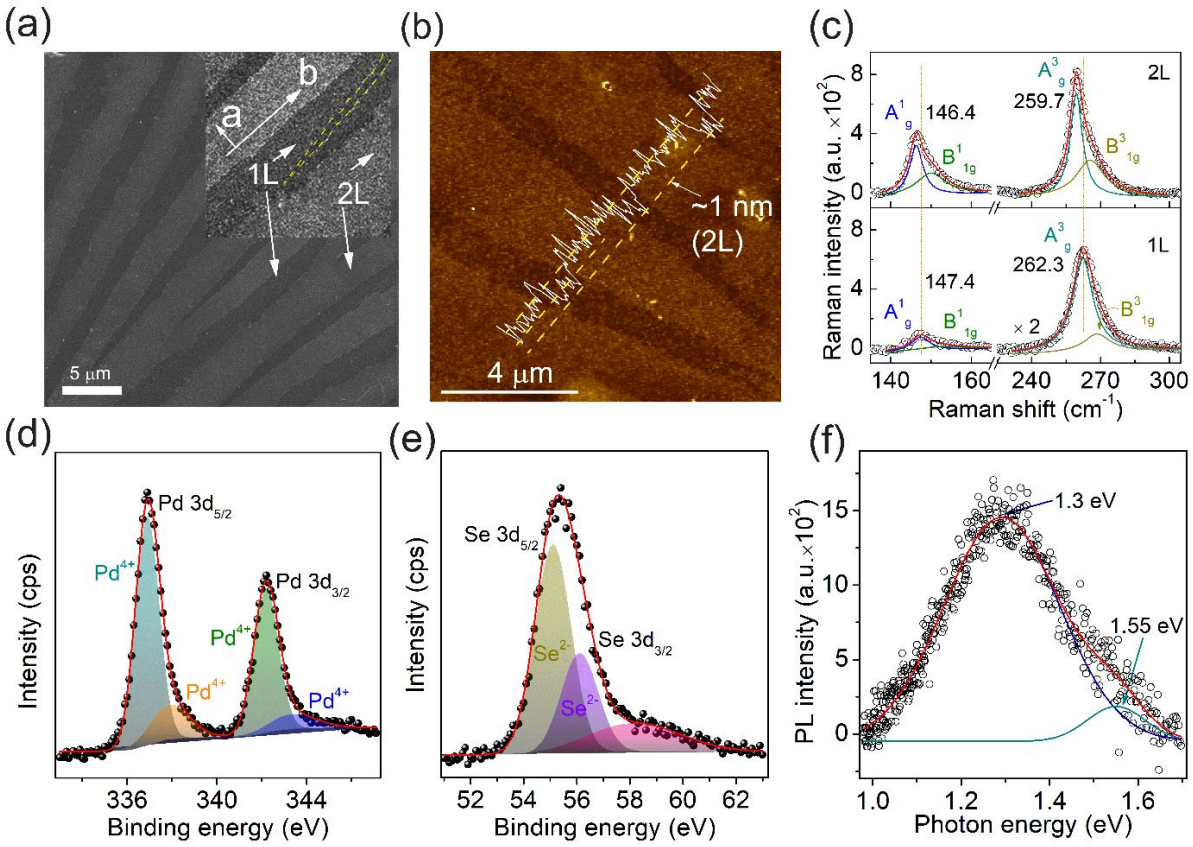

Figure 4.1. (a) FESEM image of 1L and 2L $PdSe_2$. The inset depicts the magnified view with dendrite propagation direction (along a-axis and b-axis). (b) AFM image with height profile of 2L (~1 nm), 1L (~0.5 nm) $PdSe_2$, respectively. (c) Stacked Raman spectra with Lorentzian fit for 1L and 2L $PdSe_2$, where symbols represent raw data and solid lines show fitted spectra. (d-e) XPS spectra of $PdSe_2$ dendrites for (d) Pd 3d and (e) Se 3d, with shirley baseline fitted spectra. (f) NIR photoluminosence spectrum of $PdSe_2$ dendrites with Gaussian fitting.

Later, 1L $PdSe_2$ islands in the inter-dendritic region are confirmed from Raman and TEM analyses. Atomic force microscopy (AFM) was employed to evaluate the detailed edge morphology with the thickness of the $PdSe_2$ layer. **Figure 4.1b** shows the AFM image of $PdSe_2$ dendrites. AFM height profile analysis reveals a thickness of ~1 nm in the higher contrast region, whereas for regions in between two dendrites, it is ~ 0.5 nm. The consistency of contrast or height over the large area concludes the uniform growth of dendrites. Interestingly, the thickness of 1 nm corresponds to bilayer (2L) $PdSe_2$, and ~0.5 nm corresponds to monolayer.[46] From the AFM image, we observe a highly rough surface of the $PdSe_2$ layer (estimated RMS roughness is ~0.5 nm), indicating its vacancy-contained mono and bilayer dendrite. **Figure 4.1c** shows the stacked Raman spectra of 1L and 2L $PdSe_2$ with Lorentzian line-shape fitting. The fitting parameters are presented in Table 4.1.

Table 4.1. Lorentz fitting parameters of Raman spectra of 1L and 2L $PdSe_2$ of **Figure 4.1c**

	1L		2L	
Raman modes	Peak position (cm^{-1})	FWHM (cm^{-1})	Peak position (cm^{-1})	FWHM (cm^{-1})
A_g^1	147.4	5.6	146.4	4.0
B_{1g}^1	152.3	14.4	150.0	8.9
A_g^3	262.3	10.7	259.5	6.5
B_{1g}^3	268.5	14.1	265.6	14.9

As the excitation source is unpolarized, we deconvoluted the highly intense peak $A_g^1 - B_{1g}^1$ and $A_g^3 - B_{1g}^3$ to understand the individual contribution of A_g^1, B_{1g}^1, A_g^3, B_{1g}^3 modes.[45] A_g^1 peak position (146.6 cm^{-1}) in 2L $PdSe_2$ is redshifted (1 cm^{-1}) compared to 1L A_g^1 peak position (147.4 cm^{-1}). It is obvious that a change in layer number leads to a change in phonon propagation behavior in the $PdSe_2$. As the layer thickness shrinks, the scattered photon carries higher energy due to the relaxation in the Van der Waal stacked layers in $PdSe_2$. In addition, A_g^3 mode peak positions are 259.7 cm^{-1} for 2L and 262.3 cm^{-1} for 1L. The downward peak shift in A_g^3 mode is 2.6 cm^{-1} for the same reason. FWHM of peak A_g^1 and A_g^3 modes are 5.6 cm^{-1} and 10.7 cm^{-1} in 1L and 4.0 and 6.5 cm^{-1} in 2L, respectively. The increase in FWHM for 1L compared to 2L may be attributed to the cumulative effects of higher surface defects with the decrease in layer number.

To understand the surface property, we further carried out XPS measurements. **Figures 4.1d** and **4.1e** show the Pd 3d and Se 3d high-resolution spectra with Gaussian peak fitting (Shirley baseline). The peak positions at 336.9 eV and 342.2 eV exhibit binding energy of the Pd^{4+} state, which originates due to Pd $3d_{5/2}$ and Pd $3d_{3/2}$ core label emission, respectively. The value corresponding to Pd $3d_{5/2}$ is comparatively less than the reported value.[47] This discrepancy in the binding energy might be attributed to the following reasons. The low temperature grown $PdSe_2$ dendrites contain several types of intrinsic defects. As the layer number of $PdSe_2$ decreases, a significant number of Se atoms are exposed and may detach from the surface, which gives rise to abundant Se vacancies in 2L and 1L dendrites. Further, the electronegativity of Se is lower than oxygen; as the vacancies increase, Se requires lower binding energy to break the Pd-Se bond. As

the sample is exposed to atmospheric conditions, it forms a Pd-O bond by atmospheric oxygen in place of Se vacancies. Due to the above, two additional peaks at 337.8 eV and 343.4 eV are observed and are attributed to the formation of Pd-O bond.[48] It clearly indicates that there exists a high density of Se vacancies in $PdSe_2$ dendrites. The binding energy peaks of Se 3d spectra consist of Se $3d_{5/2}$ (55.1 eV) and Se $3d_{3/2}$ (56.1 eV). Areal analysis of XPS reveals 9.3% outer Se vacancies, 4.7 % inner Se vacancies, and 4.7% Pd vacancies in dendritic $PdSe_2$. In the later section, a thorough discussion on vacancies and edge construction on dendritic $PdSe_2$ is presented and we show that, Se_{TLU} (upper layer top Se) vacancies are highest in dendritic $PdSe_2$. Deconvoluted peaks show an additional peak at 58.2 eV due to Se-O bond formation.[47] Non-bonded Se atoms in one side and Se adatoms at the dendritic edge, and fewer Pd vacancies contributed to this peak. From the above analysis, we may conclude that abundant number of Se vacancies and comparatively fewer Pd vacancies exist. Further, NIR photoluminescence (PL) measurement of as-grown $PdSe_2$ was carried out with 641 nm laser excitation. **Figure 4.1f** displays the PL spectrum with fitted two Gaussian peaks centered at 1.3 eV and 1.55 eV. As discussed earlier, there are many Se vacancies; as a result, the bandgap is reduced and it requires less photon energy to excite the electron. Depending on the concentration of vacancies, the bandgap decreases. For example, Kuklin et al. reported one vacancy per 4 unit cells of monolayer $PdSe_2$ characterized by an energy gap of 0.67 eV, whereas one vacancy per 16 unit cells corresponds to a bandgap of 1.03 eV.[3] As a result of BZ lifting and depending on the number of Se vacancies in monolayer and bilayer $PdSe_2$, the bandgap decreases to 1.3 eV for monolayer. In addition, it was stated that the optical bandgap of non-defective 2L $PdSe_2$ is 1.89 eV and that of defective 2L $PdSe_2$ is 1.55 eV. Our experimental finding revealed a bandgap of 1.55 eV for defective 2L $PdSe_2$ dendrites, which is the same as the reported theoretical value of defective $PdSe_2$.[3] Unlike other TMDs (such as MoS_2), 1L $PdSe_2$ shows comparatively higher FWHM (0.3 eV) in the PL spectrum, which may be due to the presence of defects and partly due to the distribution in the number of layers. Other possible reasons for the higher FWHM are: (1) the anisotropic lattice structure of $PdSe_2$, and (2) ten valance electrons in each Pd, which is higher than conventional TMDs. The low-intensity peak at 1.3 eV may be arising from the 2L $PdSe_2$ and/or recombination of carriers at the defects in $PdSe_2$. An optical microscopy image (**Figure 4.2**) shows the dendritic pattern growth of 2D $PdSe_2$, where the dendritic initiation zone has been shown.

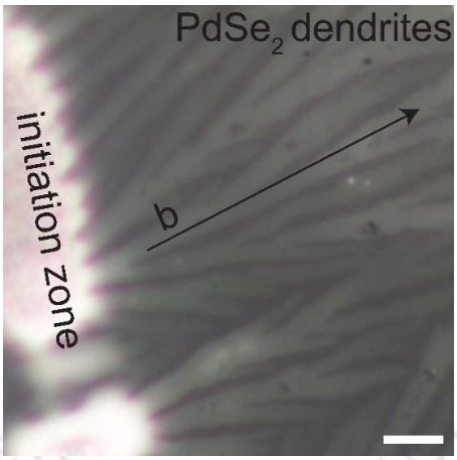

Figure 4.2. Optical microscopy image of 2D $PdSe_2$ dendrites. Scale bar 2 μm.

Further, Raman spectra were acquired to understand the details of the crystallinity of 1L and 2L $PdSe_2$ (**Figure 4.3**).

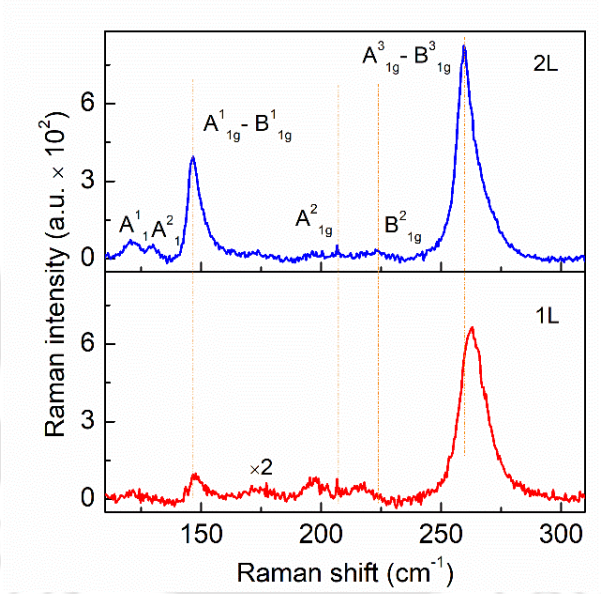

Figure 4.3. Stacked Raman spectra of 1L (inter-dendritic region) and 2L $PdSe_2$ dendrites.

The characteristics Raman modes A_1^1, A_1^2, A_g^1, B_{1g}^1, A_g^2, B_{1g}^2, A_g^3, B_{1g}^3 were observed in the 2L $PdSe_2$ dendrites. Raman mapping (**Figure 4.4**) also validates spatial uniformity over the 2L dendrites, and in-between 2L, there exist 1L $PdSe_2$ dendritic islands.

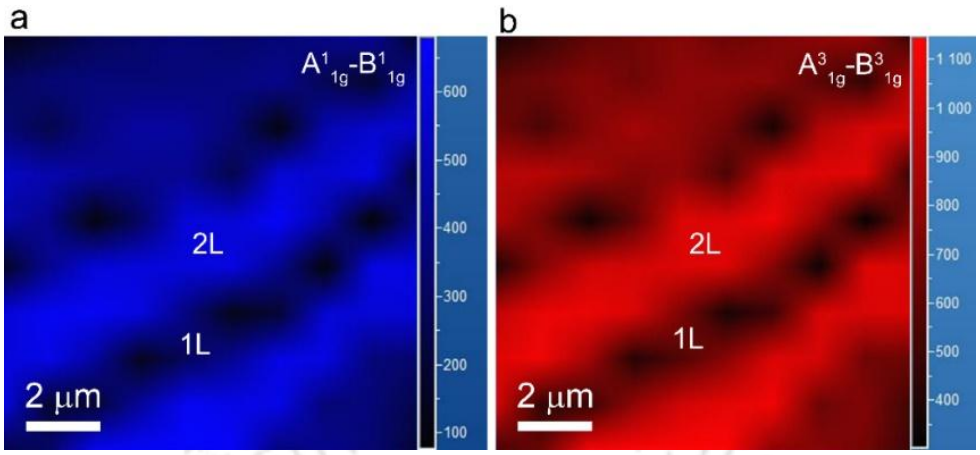

Figure 4.4. Raman mapping of 1L and 2L $PdSe_2$ dendrites (a) $A_g^1 - B_{1g}^1$ (blue map) (b) $A_g^3 - B_{1g}^3$ (red map) mode.

The XPS survey spectrum (**Figure 4.5**) highlights the presence of Pd, Se, C, O.

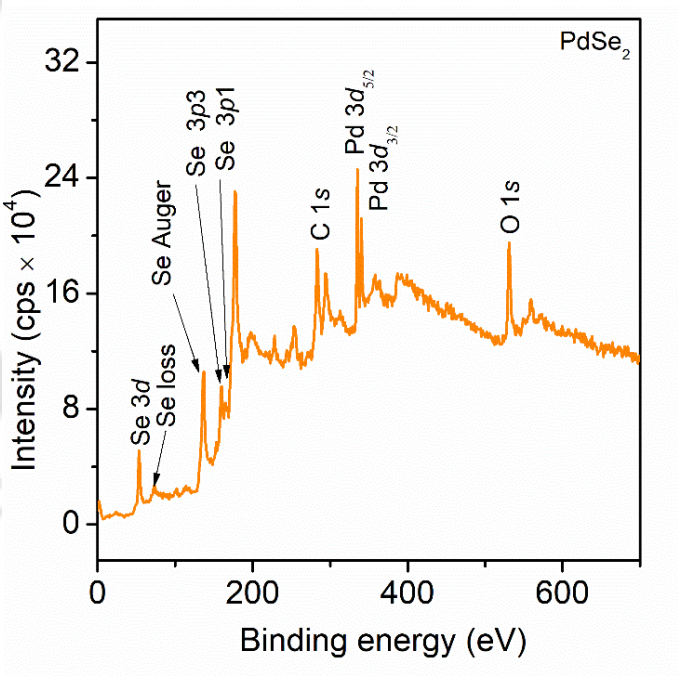

Figure 4.5. XPS survey scan for $PdSe_2$ dendrites.

The structure of the $PdSe_2$ is very different from other TMDs, where the Se-Se tilted layer crosses the Pd layer (**Figure 4.6a**). This type of structure is highly sensitive towards intrinsic defects due to the break in the symmetry of Se-Se bond. [22] One h-$PdSe_2$ contains 6 Se atoms and 2 Pd atoms. For better understanding, we divided them into top layer up Se (Se_{TLU}), top layer down Se (Se_{TLD}),

bottom layer up Se (Se_{BLU}), bottom layer down Se (Se_{BLD}), and top layer Pd (Pd_{TL}), bottom layer Pd (Pd_{BL}), as shown in **Figure 4.6b.**

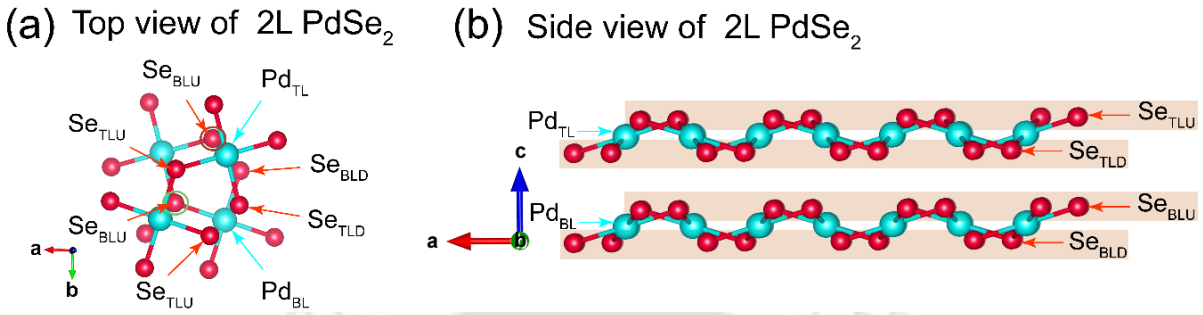

Figure 4.6. (a) Top view and (b) Side view of 2L $PdSe_2$.

4.4.2. Defects and Edge construction

Based on the signature of defects in $PdSe_2$ dendrites from XPS and PL, we undertook a detailed study of defects from electron microscopic analyses. **Figure 4.7a** illustrates the dark-field TEM image of three consecutive dendrites. The EDX mapping of Pd and Se is shown in **Figure 4.7b** and **Figure 4.7c** respectively. **Figure 4.7d** shows the atomic percentage of Pd and Se from EDX, which further confirms the presence of Se vacancies. The HRTEM image of 2L $PdSe_2$ dendrite is shown in **Figure 4.7e**, where hexagonal $PdSe_2$ (h-$PdSe_2$) is clearly visible. From the HRTEM image, we can get a two-dimensional picture of the structure. An enlarged view of a selected area of **Figure 4.7e** is shown in **Figure 4.7f**. From intensity contrast and distance measurement in **Figure 4.7f**, we obtained the arrangement of atoms with atomic distance as follows, Se_{BLU}-Se_{TLU} (tilted) = 0.21 nm, Se_{TLU}-Se_{BLU} (vertical) = 0.14 nm, Se_{TLU}-Se_{TLD} (tilted) = 0.18 nm, Se_{BLU}-Se_{BLD} (tilted) = 0.18 nm (shown in **Figure 4.7g**), which are consistent with the theoretical calculated values (shown in **Figure 4.7h**). **Figure 4.7i** illustrates a series of line defects with Se vacancies at the middle of 2L $PdSe_2$. These Se vacancies are mainly Se_{TLU} atoms, which are confirmed by HRTEM intensity analysis. To better visualize the Se_{TLU} vacancies, a small area of **Figure 4.7i** is shown in **Figure 4.7j**.

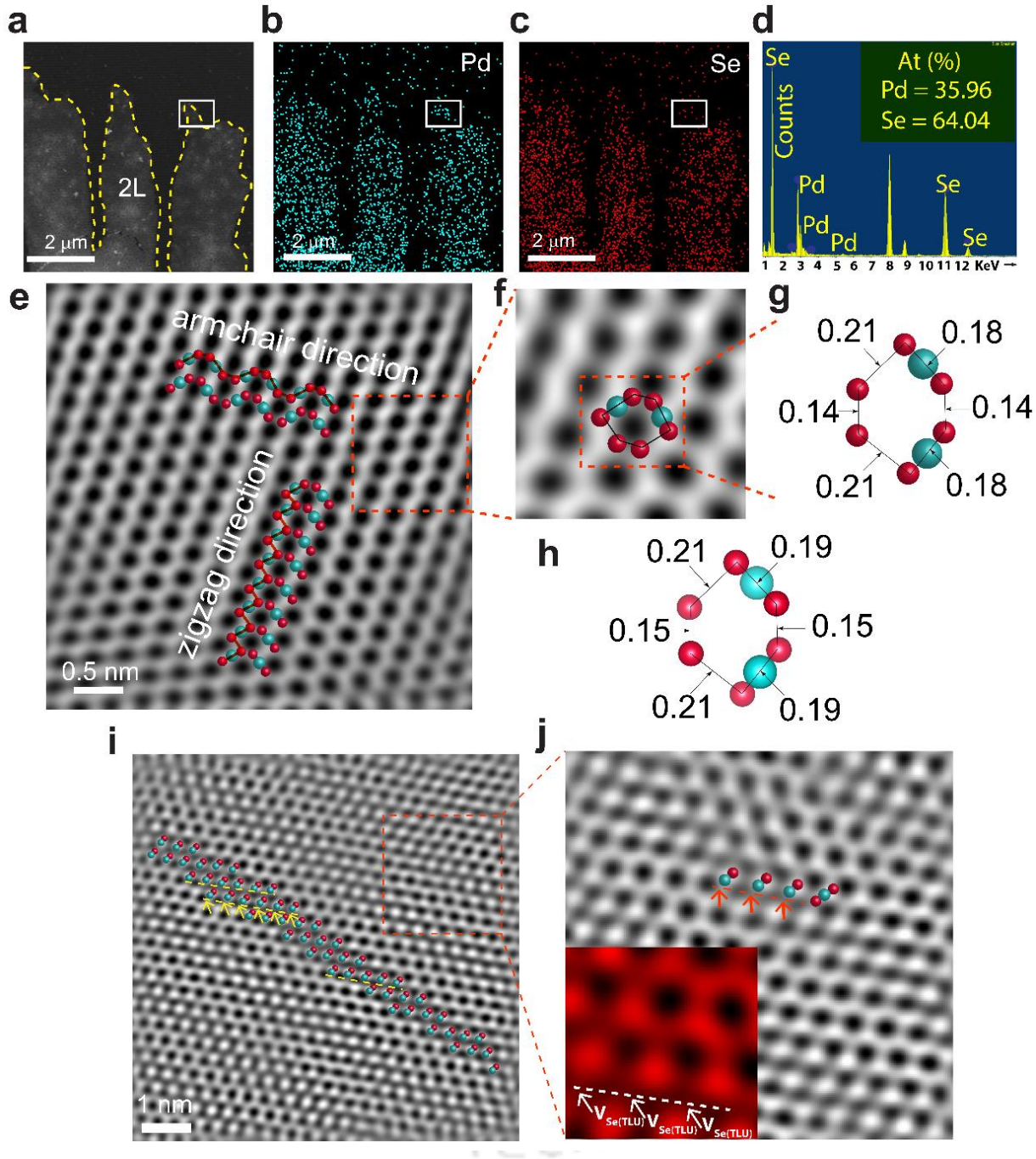

Figure 4.7. (a) Dark field TEM image of $PdSe_2$ dendrites, (b-c) the elemental distribution of Pd and Se, respectively; (d) the corresponding atomic percentage spectrum. (e) HRTEM image of defect free 2L $PdSe_2$ including armchair and zigzag edges. (f) Magnified view of HRTEM image with the atomic arrangement. (g) Atomic model representation with interatomic distance of experimental data. (h) Theoretically obtained 2D interatomic distance in the atomic model. (i) HRTEM image of defective 2L $PdSe_2$ including series of line defects. (j) Magnified view of defective 2L $PdSe_2$ showing line defects; arrow indicates Se_{TLU} vacancies,which disrupts the hexagonal structure.

4.4.3. Surface defects

The EDX mapping over a small area of bright field TEM image is shown in **Figure 4.8, Figure 4.9** and **Figure 4.10**.

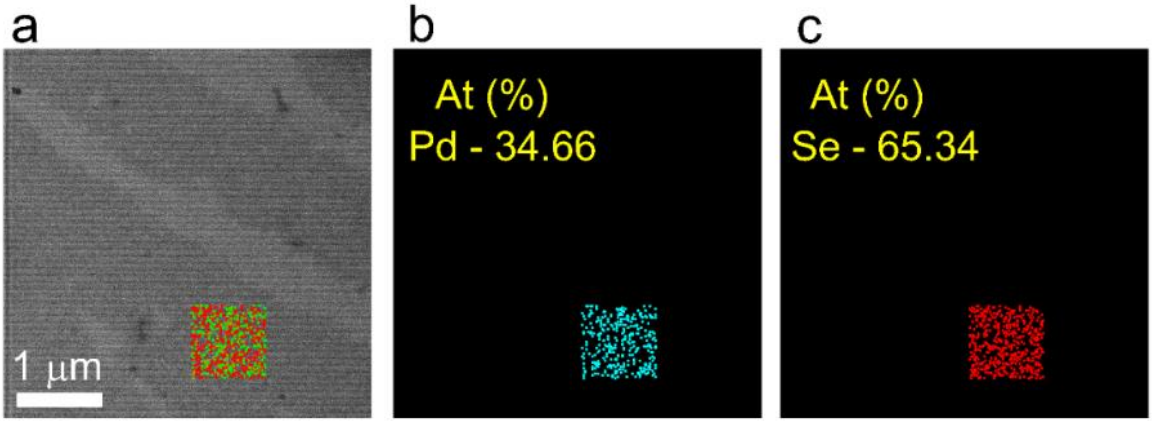

Figure 4.8. EDX elemental mapping shows (a) mix of spatial distribution of Pd and Se, (b) spatial distribution of Pd and (c) spatial distribution of Se over a small area of the bright field TEM image (a).

A careful observation of the white-shaded region (**Figure 4.7b, c)** in the mapping reveals that Pd:Se proportion increases at the end of the dendrites, implying increasing Se vacancies at the end of the dendrite. **Figure 4.8** illustrates the EDX elemental mapping of mixed spatial distribution of Pd and Se over a small area of the bright field TEM image.

In order to find the percentage of Se vacancies in the 2L middle, 2L edge, and 1L, EDX spectra were collected in different regions (**Figure 4.9**). Surface defects are more in 1L than 2L, as confirmed from EDX analysis (**Figure 4.9a-f**) of atomic percentage, where we can see the magenta rectangle enclosed the 2L edge along with 1L. Se atomic percentage is very low at the edge of the 2L (**Figure 4.9f**) than in the middle 2L region (**Figure 4.9d**).

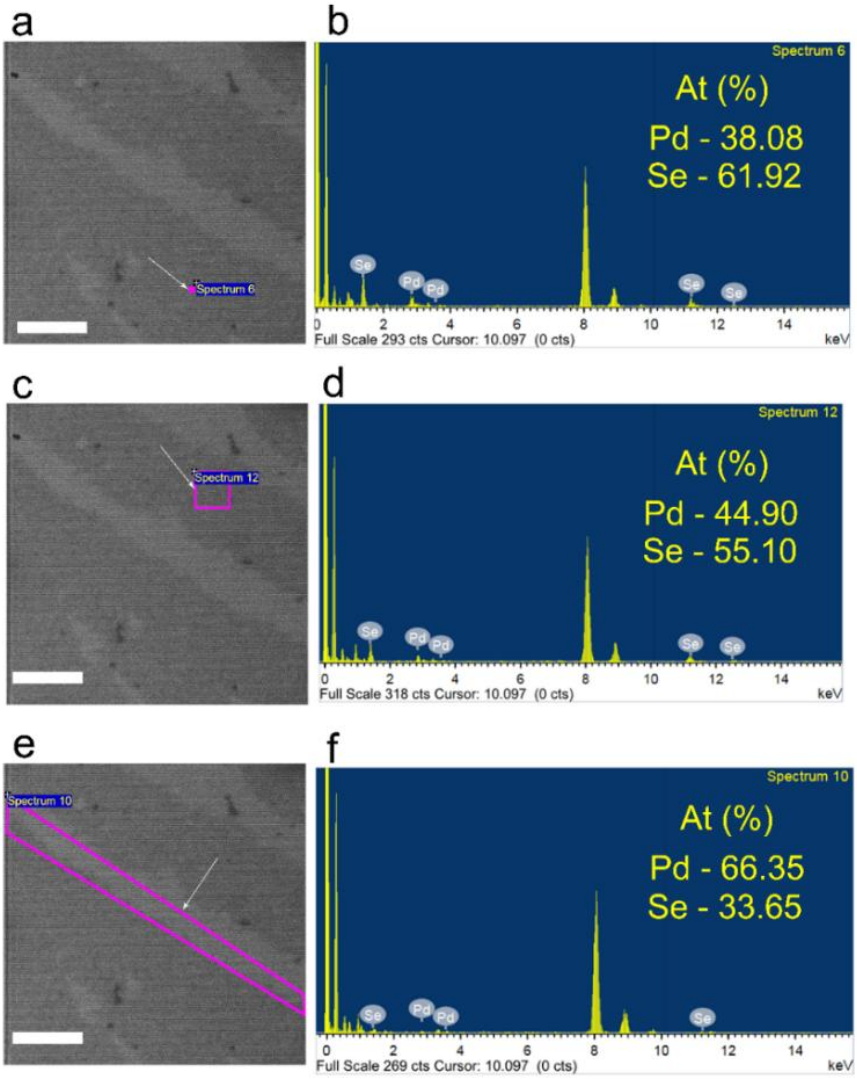

Figure 4.9. EDX analysis (a, b) shows the point spectrum on 2L $PdSe_2$. (c, d) region spectra on 2L surface and (e, f) exhibits for 2L edge. Scale bar is of 1 μm.

In **Figures 4.9a, 4.9c, and 4.9e**, spectra were recorded over a small region in the middle of 2L dendrite, a slightly larger area in the 2L dendrite, and a comparatively large area consisting of the edge of 2L dendrites as well as monolayer $PdSe_2$, respectively. From the atomic %, we believe that the vacant Se atom in the monolayer and the edge sites of $PdSe_2$ are responsible for the highest Se vacancy in **Figures 4.9e**. In **Figures 4.9a**, the density of vacancy in a small area is relatively less than in **Figures 4.9c**. In **Figures 4.9a**, there are fewer Se vacancies, whereas **Figures 4.9c** contains much Se vacancies due to existence of nanopores, which are discussed later.

4.4.4. Edge construction

As revealed by the HRTEM image; dendrites with the simplest edge orientation are mainly two types, armchair, and zigzag. However, when we move to the edge part of the dendrite, we observe different armchair and zigzag edges. Like defects, edge geometry also plays an important role in the properties of nanomaterials. Hence, it is relevant to know $PdSe_2$ edge geometries and their chemical properties beyond standard zigzag and armchair ones. Based on calculations and measurements, we found that edge construction is different at the edge of the 2L dendrite (**Figure 4.10a**). Dendrites possess mainly two types of edge structure, (1) armchair with pentagon and hexagon (one side pentagon, other side hexagon) and (2) zigzag with hexagons. We have analyzed the edge structure of a portion of the dendrite, shown in **Figure 4.10a**, with the help of the atomic model shown in **Figure 4.10b**. **Figure 4.10a** is the HRTEM image of the 2L dendritic edge. As the HRTEM image is two-dimensional, we have measured the two-dimensional distances of the edge in nanometers. To know how the edge construction happens, we have first calculated each side of edge hexagons and pentagons (1 is a pentagon, and 2, 3, 4, 5 are hexagons) from the HRTEM analysis of **Figure 4.10a**. These calculated sides from the HRTEM analysis are nearly the same as the theoretically calculated distances given in **Figure 4.10c**, which are different from the normal defect-free hexagon sides. Assuming the path initiation atom as Se_{BLU}, we have followed the distance from one atom to another in the atomic model and traced the path. For example, starting with Se_{BLU}, if Se_{BLU} follows the next Se_{TLU} then the distance will be 0.21. However, the distance of the next atom from Se_{BLU} at the edge is 0.33. If we exclude Se_{TLU}, then Se_{BLU} to the next Se_{BLU} distance is 0.33 nm. Similarly, we have traced the entire edge construction of the dendritic $PdSe_2$. Assuming the edge growth from pentagon 1 with Se_{BLU}, it follows the path excluding mostly edge Se_{TLU} atoms. The green cross marks are excluded Se_{TLU} from the followed path of the edge construction. In pentagon 1, it follows the path excluding 2 Se_{TLU}, and the distance between Se_{BLU} to Se_{BLU} is 0.33 nm, the distance between Se_{BLU} to Pd_{BL} (Se_{BLU}-Pd_{BL}) is 0.23 nm, and Pd_{BL}-Se_{TLD} = 0.09 nm. In hexagon 2, it follows the path excluding one Se_{TLU}, where Pd_{BL}-Se_{BLU} = 0.22 nm. In hexagon 3, it follows the path excluding two Se_{TLU}, where Se_{BLU}-Pd_{BL} (next hexagon Pd) = 0.23 nm, Pd_{BL}-Se_{BLU} = 0.22 nm. In hexagon 4, it follows the path excluding one Se_{TLU}, where Se_{BLU}-Pd_{BL}= 0.23 nm. In hexagon 5, nothing is excluded. Starting from pentagon 1 Se_{BLU} (encircled in blue), it follows a path as follows, $Se_{BLU} \rightarrow Se_{BLU} \rightarrow Pd_{BL} \rightarrow Se_{BLU} \rightarrow Pd_{BL} \rightarrow Se_{BLU} \rightarrow Pd_{BL} \rightarrow Se_{BLU} \rightarrow Se_{BLU} \rightarrow Pd_{BL} \rightarrow Se_{BLU} \rightarrow Se_{TLU} \rightarrow Se_{BLU} \rightarrow Pd_{BL} \rightarrow Se_{BLU} \rightarrow Pd_{TL}$

→ Se_{BLD} → Se_{TLD} → Se_{BLD} → Pd_{TL}→ Se_{BLU} → Se_{TLU} →Se_{BLU} → Pd_{TL} → Se_{BLD} → Se_{TLD} → Pd_{BL}→ Se_{BLU} → Se_{TLU} → Pd_{BL} → Se_{TLD} → Se_{BLD} → Se_{TLD} → Se_{BLD}.

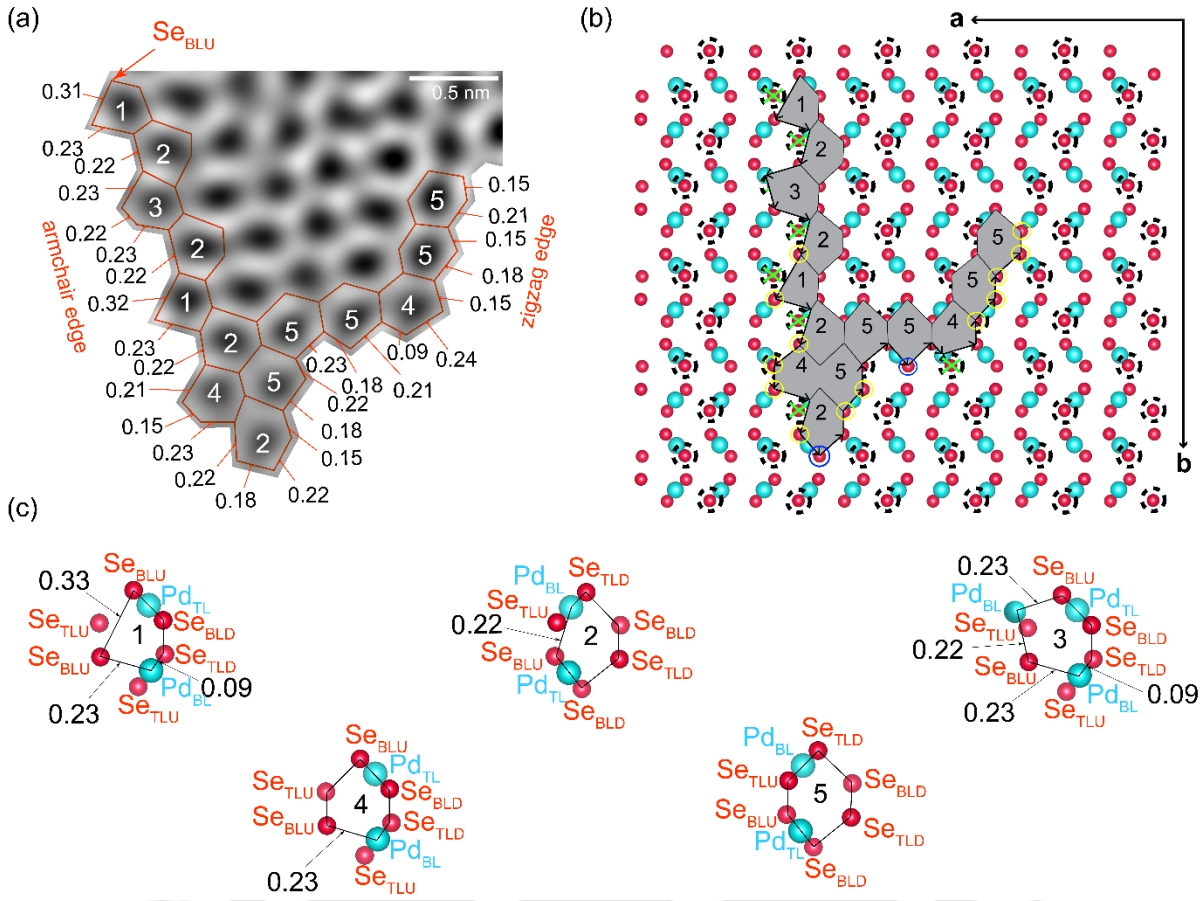

Figure 4.10. (a) High resolution TEM image of 2L $PdSe_2$ dendrites with measured edges in nanometers. (b) Theoretical model showing edge geometry of 2L dendritic $PdSe_2$, where black circles encircling the Se atoms denotes Se_{TLU}, yellow circle encircling Se denotes one side non-bonded Se-Pd, blue circle encircling Se are Se adatoms, green cross mark denotes excluded Se_{TLU} from the followed path. (c) Theoretically calculated interatomic distance (in nm), which matches well with the experimentally obtained interatomic distance from HRTEM.

The corresponding bright field high resolution TEM image of 2L $PdSe_2$ dendritic edge of **Figure 4.10a** is shown in **Figure 4.11**.

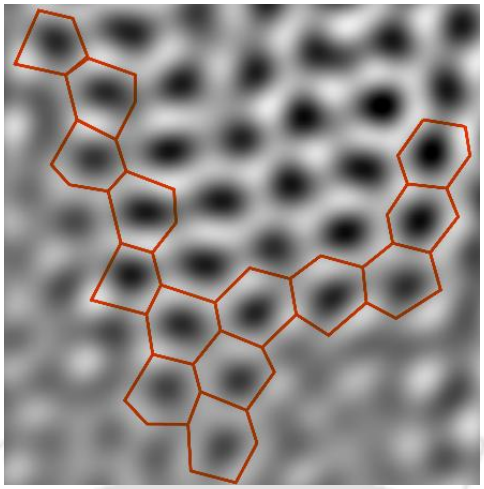

Figure 4.11. Bright field high resolution TEM image of 2L $PdSe_2$ dendritic edge.

All the calculated atomic distances from the HRTEM image match well with the theoretically calculated values shown in **Figure 4.10c**. In $PdSe_2$, each Se is bonded with one Se and two Pd atoms (Se-Pd). But, at the edge of the dendrite, there exist many Se atoms where one Se-Pd bond is absent. The yellow encircled Se atoms are bonded with one Pd atom at the edge, and one Pd-Se bond is absent. From the statistics, we concluded that 90% of edge Se atoms are bonded with only one Se-Pd bond at the edge of the dendrite. Active sites mainly exclude Se_{TLU} atoms, which is due to the fact that Se_{TLU} atoms can be removed more easily than other atoms. The most common defect is the single missing atom, called single vacancy (SV). In the case of $PdSe_2$ dendrite, we did not observe any SV from experimentally obtained TEM images. Most vacancies are associated with 2/3 V_{se} in the same row/column. Removal of more than two atoms leads to a more complex defect configuration. When the vacancy is created, the displaced atom may remain on the surface of the $PdSe_2$ layer as an adatom. Vacancies and adatoms are relatively mobile, but still unstable against recombination. From the end of the dendrite, we can notice that Se is at the propagating tip, which suggests Pd-edge is the initial nucleation edge which then is propagated by Se. However, there exist two Se adatoms at the tip of the edges encircled with blue line. The dendritic head consists of adatom, which might be the cause of ending the dendritic growth in that particular direction. **Figure 4.12** illustrates the tilted side view of monolayer $PdSe_2$.

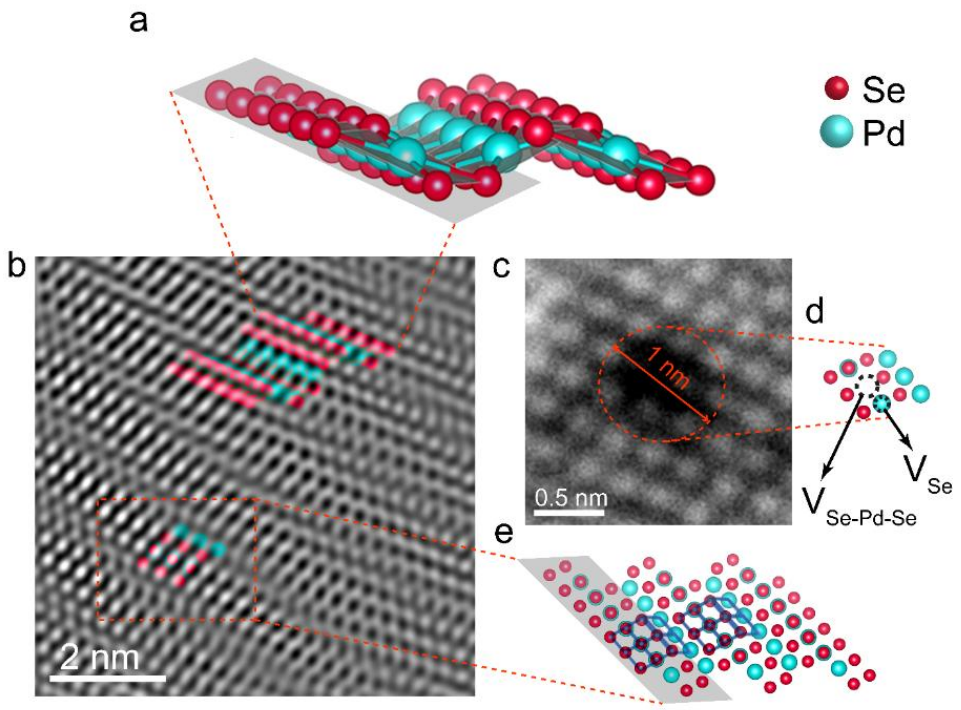

Figure 4.12. (a) Atomic model showing slightly tilted monolayer $PdSe_2$. (b) High resolution TEM image of monolayer $PdSe_2$ which well matching with atomic arrangement. (c) HRTEM image showing one Se vacancy (Vse) along with one Se-Pd-Se vacancy ($V_{Se-Pd-Se}$) (d) monolayer $PdSe_2$ atomic model showing Vse and $V_{Se-Pd-Se}$. (e) atomic model represents top view of slightly tilted monolayer $PdSe_2$ correlated with HRTEM image of 1L $PdSe_2$.

TEM imaging depends on the orientation of the material (crystal) with respect to the electron beam direction. From **Figure 4.12a, b** we can distinctly visualize the slightly tilted pattern of monolayer $PdSe_2$. We confirmed it as a monolayer by analyzing the HRTEM image intensities. **Figure 4.12c** indicates a total of three Se with one Pd vacancy in monolayer $PdSe_2$. TEM imaging enables us to identify a V_{Se} (mono Se vacancy) along with $V_{Se-Pd-Se}$ (1 upper Se 1Pd and 1 lower Se) atom vacancy from image intensity analysis (**Figure 4.12d**). In fact, it is not easy to visualize the pentagonal shape because with the tilted view of $PdSe_2$, we can see some rectangular patterns $PdSe_2$ from the tilted top (shown in **Figure 4.12e**).

4.4.5. Nanopores in dendritic $PdSe_2$

Here we notice that the vacancy exhibits closely a circular shape of about 1 nm diameter. In monolayer $PdSe_2$, we obtained two outer Se vacancies, one Pd vacancy along with one inner Se vacancy. Florina *et al.* reported that vacancies with an even number of missing atoms are energetically favorable over an odd number of missing atoms in graphene.[49] Similar to graphene,

in $PdSe_2$, mainly Pd vacancy occurs along with inner Se vacancies as an even number of vacancies are energetically favored, and more energy is required to break the Pd-Se bond. Our XPS analysis disclosed that there exist 9.3% outer Se vacancies, 4.7 % Pd vacancies, 4.7 % inner Se vacancies in dendritic $PdSe_2$. XPS analysis supports our TEM image analyses, where outer Se vacancies are dominated, whereas Pd vacancy is always associated with inner Se vacancy. In bilayer $PdSe_2$, we observe mainly Se_{TLU} vacancies or sometimes Se_{BLU} vacancies. Mostly Pd vacancies are not seen. We did not observe isolated Pd vacancy as Pd drags inner Se atoms. This is the key reason behind nanopore formation in 2L $PdSe_2$. Making a nanopore in $PdSe_2$ without any post-growth treatment and without using the electron beam radiation technique is challenging.[50,51]

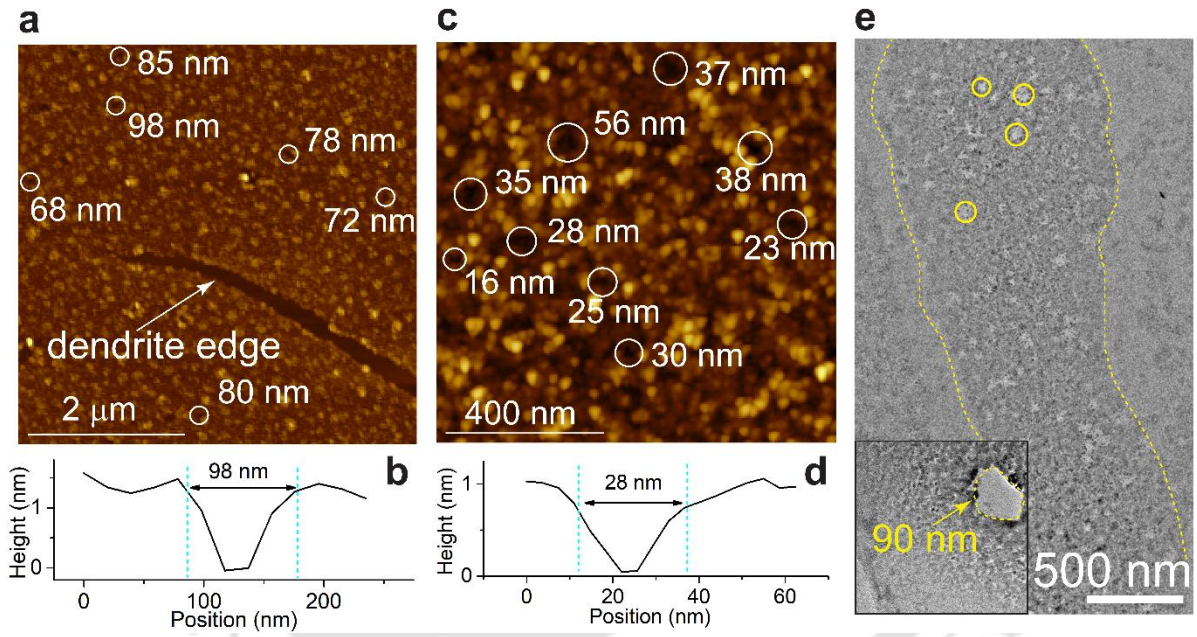

Figure 4.13. (a) Atomic force microscopy image showing the nanopores with pore diameters in the range 68-98 nm in 2L $PdSe_2$. (b) Line profile showing the diameter of 98 nm for a nanopore. (c) White circles enclosed nanopores with average diameter ranging from 16-56 nm in 2L $PdSe_2$. (d) Line profile measures the diameter of 28 nm of a nanopore. (e) Bright field low resolution TEM image of 2L $PdSe_2$ with nanopores (yellow circled) and the inset reflects nanopore with an average diameter of 90 nm.

We present a reliable, straightforward approach to synthesizing dendritic $PdSe_2$ with distributed nanopores. We consider these nanopores nearly circular, with diameters ranging from 10 nm – 90 nm (**Figures 4.13a, 4.13c, 4.13e**). **Figure 4.13a, c** shows the AFM images of dendrites with distributed nanopores in a 1 nm thickness $PdSe_2$ dendrite. **Figures 4.13 b, d** depicts height well for the estimation of nanopore diameters. **Figure 4.13e** shows the TEM image of a dendrite with many nanopores. The inset shows a magnified view of a ~90 nm diameter nanopore. We can

differentiate between reported nanopores (where voids are formed by electron beam radiation) and our nanopores (without any treatment). Nanopores in $PdSe_2$ adopt an approximately pentagonal geometry with well-defined edges (shown in the inset of **Figure 4.13e**). With the change in the ratio of $PdCl_2$ to NaCl during the growth, we observe different sizes of nanopores and defects (**Figure 4.14**).

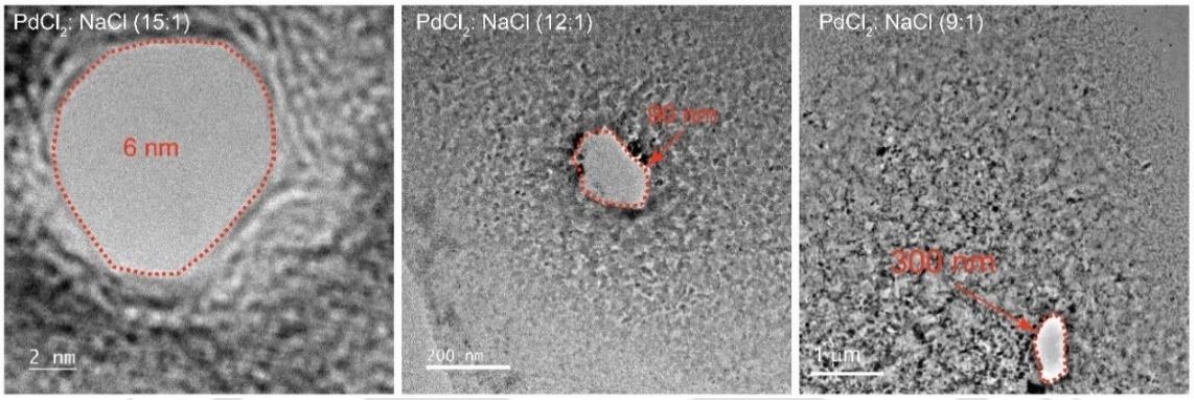

Figure 4.14. Bright field low resolution TEM image of 2L $PdSe_2$ nanopores with an average diameter of 6nm, 90 nm, and 300 nm.

4.5. Application of dendritic $PdSe_2$ in SERS sensing

Thanks to the fingerprint of Raman spectroscopy due to its remarkable sensitivity and chemical specificity. We have investigated surface-enhanced Raman scattering (SERS) of RhB on $PdSe_2$ dendrites grown on a mica substrate. To investigate the individual contribution of 2L edge, 1L vacancy, and nanopore on SERS, we carried out position-dependent SERS measurements in 3 different regions. **Figure 4.15a** represents the broad range Raman spectrum of 10^{-5} M RhB on the edge of 2L $PdSe_2$ dendrite. The presence of all the characteristic Raman modes of $PdSe_2$, including SERS of RhB molecule, makes it very interesting to find the origin of SERS sensing in novel $PdSe_2$ dendrites. Raman mapping was carried out on dendritic $PdSe_2$/RhB for better visualization of defect-induced hotspots, which are believed to be responsible for the SERS enhancement, and it is added in **Figure 4.15b, c**. **Figure 4.15b** shows the Raman intensity mapping of 258 cm^{-1} peak of $PdSe_2$, where uniform contrast is observed all over the dendritic $PdSe_2$, but contrast changes at 2L edges. The signature of rhodamine B (1647 cm^{-1}) was taken into consideration to obtain the Raman mapping of rhodamine B.

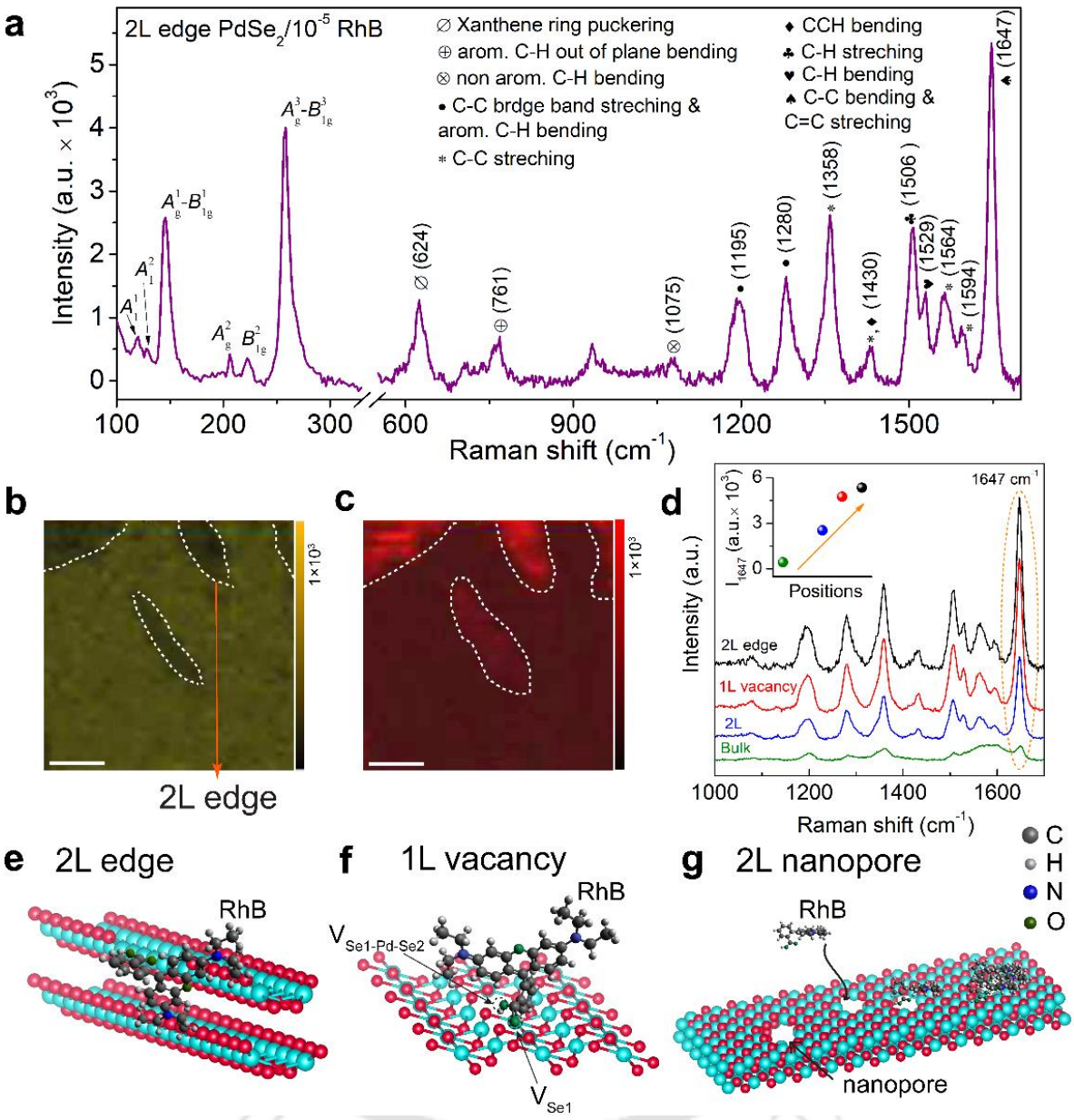

Figure 4.15. (a) Raman spectrum of 10^{-5} M RhB on the intrinsic edge of 2L $PdSe_2$. (b-c) The Raman intensity mapping of 258 cm^{-1} peak of $PdSe_2$ and 1647 cm^{-1} peak of rhodamine B, respectively. Scale bar is 2 μm. (d) Stacked Raman spectra of 10^{-5} M RhB on different spots (2L edge, 1L vacancy, 2L surface, bulk). Inset shows the position dependent Raman intensity (I_{1647}). Proposed mechanism of adsorption of RhB molecules at three different sites: (e) 2L edge, (f) 1L vacancy and (g) 2L nanopores.

Figure 4.15c shows the Raman mapping of 1647 cm^{-1} peak of rhodamine B, where distinct brighter islands are found at the 2L edge of dendritic $PdSe_2$. Interestingly, edge sites of $PdSe_2$ dendrites act as a kind of hotspot, and rhodamine B adsorption takes place at the Se vacant sites with Pd chains at the edge sites. **Figure 4.15d** shows the corresponding stacked Raman spectra of particular 2L

edge, 1L vacancy, 2L middle portions of the dendrite, and bulk $PdSe_2$. Inset shows the ascending order of peak intensities of characteristics Raman mode corresponding to C-C bending and C=C stretching (1647 cm^{-1}). **Figure 4.15d** reveals a huge variation in intensities (I) between bulk $PdSe_2$ and dendritic $PdSe_2$ (2L edge, 1L vacancy, 2L middle). Clearly, I (2L edge) > I (1L vacancy) > I (2L middle) > I (bulk). Among these, the 2L edges exhibit the highest intensity peak, which implies its highly sensitive nature toward SERS. It clearly indicates that active edges, defects, and nanopores play a vital role in SERS activity. Let us first consider the case of a 2L dendritic edge. 2L $PdSe_2$ edge is mostly terminated with one side bonded Se atom as concluded from the TEM analysis (one Se-Pd bond is absent). If an even number of atoms are removed from the dendritic edge, then bonds can be healed to preserve the connectivity. If an odd number of atoms are removed, a bond exists that makes the structure most unstable and more chemically active. Koskinen et al. reported that an armchair edge with pentagons (Ac 56) is the most expensive edge with the highest edge energy in graphene.[52] Lu et al. reported that Se-ac (110) is the most stable edge in 2L $PdSe_2$.[11] Our $PdSe_2$ edge geometry mainly consists of Se-armchair (Se-ac), which suggests us believe that it is an exclusive as well as stable edge. Edge stress can be relieved by the addition of other atoms at the stable edges.[53]

As discussed earlier, one Se-Pd bond is absent at the active sites, enhancing the dipole-dipole interaction between Se and $C=N^+$ (as N^+ ion in RhB acts as an electron deficiency site) of the RhB molecule. (**Figure 4.15 (e, f, g)**). The positively charged $C=N^+$ group in the RhB molecule will be attracted by the negatively charged Se atoms at the active edge sites. As RhB is a zwitterionic molecule, further adsorption of the RhB molecule will happen in a head-to-tail manner. To further validate the above concept, we have done an EDX analysis at three different zones. Dendritic $PdSe_2$ is dipped into KOH solution overnight in the transfer process. In an aqueous solution, KOH dissociates to form K^+ ion.

$$KOH + H_2O = K^+(aq) + OH^-(aq)$$

Interestingly K^+ adsorption happens in vacancy and edge sites of $PdSe_2$, which is confirmed by EDX. EDX analysis showed that the dendritic $PdSe_2$ contains Pd, Se, K. These results further support the validity of the above possible route. EDX analysis at three different locations (2L middle, 2L edge) of the $PdSe_2$ dendrites are shown in **Figure 4.16**. K atomic percentage is highest

at the edge of the dendrites, which indirectly confirms K^+ adsorption is more at the 2L edge and 1L.

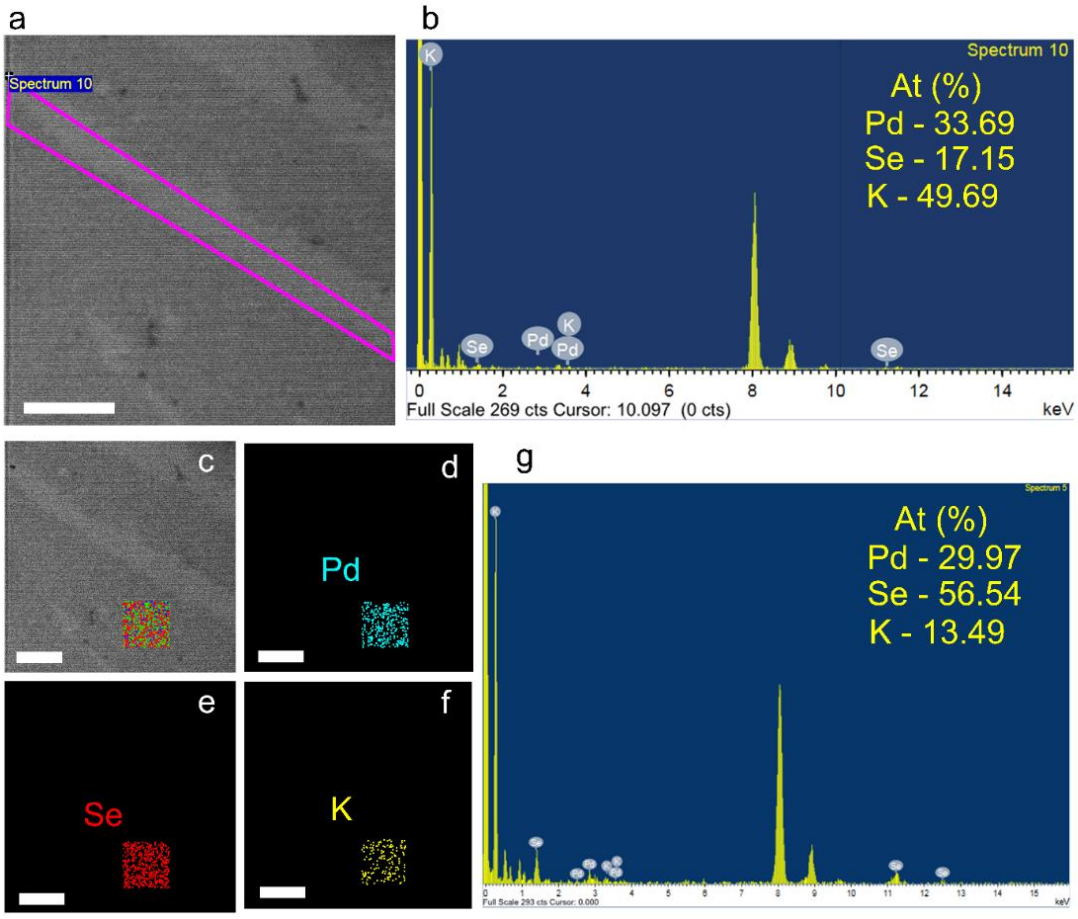

Figure 4.16. (a,b) 2L dendrite edge EDX spectrum including K. EDX elemental mapping shows (c) mix spatial distribution (d) spatial distribution of Pd and (e) spatial distribution of Se and (f) spatial distribution of K over a small area of the bright field TEM image. (g) displays corresponding spectrum. Scale bar 1 μm.

It is interesting to note that the sum of Se and K atomic percentage is exactly double the Pd atoms. This implies that Se vacancy at the active site act as a bonding site for K atoms. In the middle of a 2L dendrite, K adsorption happens with less atomic percentage (**Figure 4.16).** As K^+ and N^+ are positive ions, we can expect similar phenomena for the adsorption of N^+ ions. Thus, it indirectly indicates that the bonding of $C{=}N^+$ of RhB molecules is highest at the 2L edge. Whereas the oxygen bonding (O^{2-} of -COOH group) of RhB is highest at the 2L middle and 1L middle due to vacancies and nanopores. At Se vacancies, there is a bonding between one side non-bonded Pd with O^{2-} (-COOH group) of RhB form Pd-O bond. As Pd is a noble metal, the Pd-O bond produces a robust electronic coupling between the RhB molecule and the metal.[54] Se vacancies act as

electron trapping sites for oxygen because oxygen has the same outermost electrons as Se. At the edge, there exists a smaller number of Pd termination, which gives rise to comparatively less Pd-O bond formation. As nanopore sizes are ~10-90 nm, the chemical adsorption is more at the active sites than the middle of the nanopore void. More physisorption is expected at the center of the nanopore. The size of the RhB molecule is ~1 nm, so 1L vacancy sites act as trapping sites for RhB, which makes vacancies quite interesting for SERS activity.

4.5.1. Enhancement factor and SERS mechanism

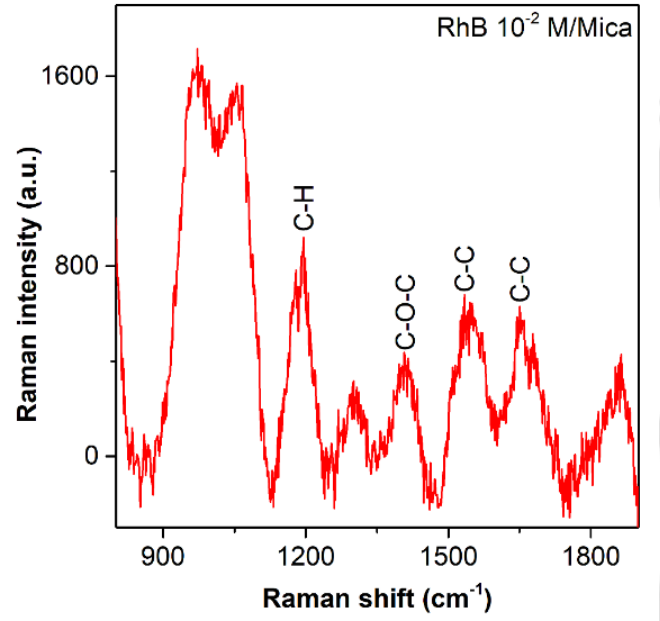

Figure 4.17. Raman spectrum of 10^{-2} M RhB on mica substrate.

The enhancement factor (EF) in SERS sensing is calculated using the following **equation 4.1**,

$$EF = \frac{I_{SERS}}{I_{RS}} \times \frac{C_{RS}}{C_{SERS}} \quad \textbf{(4.1)}$$

where I_{SERS} and I_{RS} are the SERS and Raman signal (**Figure 4.17**) intensities, respectively, and C_{SERS} , C_{Rs} are the corresponding concentrations for which the intensities are considered.

4.5.2. Cyclic voltammetry (CV)

To ascertain the same, the band positions of $PdSe_2$ were obtained using the cyclic voltammetry (CV) measurement (**Figure 4.18**).

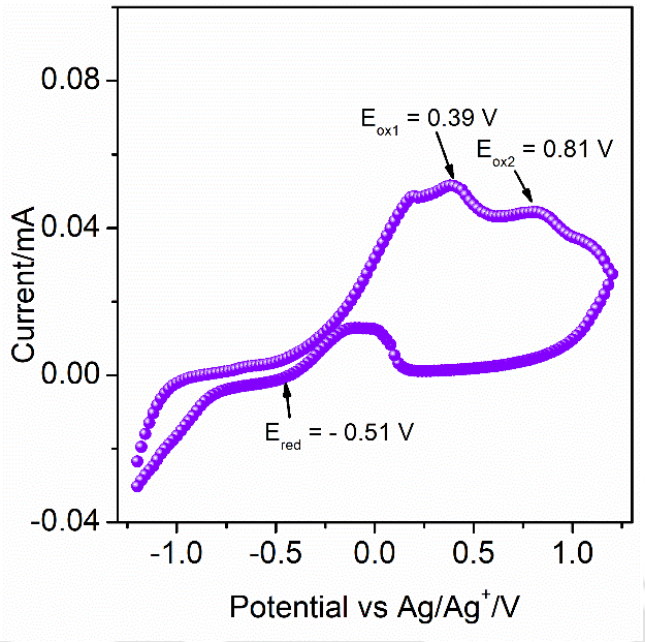

Figure 4.18. Cyclic voltammetry measurement of $PdSe_2$.

The following equations were used to calculate the band positions 2D $PdSe_2$,[55]

$E_{VB} = -(E_{ox} + 4.71)$ eV

$E_{CB} = -(E_{red} + 4.71)$ eV

Electrochemical band gap = $E_{CB} - E_{VB}$

Calculations

$E_{VB} = -(E_{ox1} + 4.71)$ eV = - (0.39 + 4.71) eV = - 5.10 eV

$E_{VB} = -(E_{ox2} + 4.71)$ eV = - (0.81 + 4.71) eV = - 5.52 eV

$E_{CB} = -(E_{red} + 4.71)$ eV = - (- 0.51 + 4.71) eV = - 4.20 eV

Calculated band gaps = (- 4.20 - (-5.10)) eV = 0.90 eV & (- 4.20 - (-5.52)) eV = 1.32 eV

Note that, obtained band gap well matches with our optically obtained band gap (PL) and also with the literature.[9] As we focused on 1L and 2L $PdSe_2$ for RhB sensing we have taken the higher band gap (1.32 eV) into our consideration to understand the transfer process in the combine system. The lower band gap comes due to few layer $PdSe_2$. $PdSe_2$ samples are transferred to the ITO glass substrate to conduct the Cyclic voltammetry (Gamry Instruments, 36083) measurements. The three electrode-based electrochemical system consists of Ag/Ag+ as the reference electrode, ITO glass

as the working electrode and Pt wire as the counter electrode. 0.5 M Na_2SO_4 was the electrolyte for the experiment. $PdSe_2$ CBM and VBM are at -4.20 eV and -5.52 eV, respectively. It has been reported that the work function for ideal monolayer $PdSe_2$ is 5.20 eV.[56]

4.5.2.1. Calculation of work function

From KPFM measurement, the measured work function of 1L and 2L $PdSe_2$ dendrites are 4.83 eV and 4.87 eV, respectively (**Figure 4.19**).

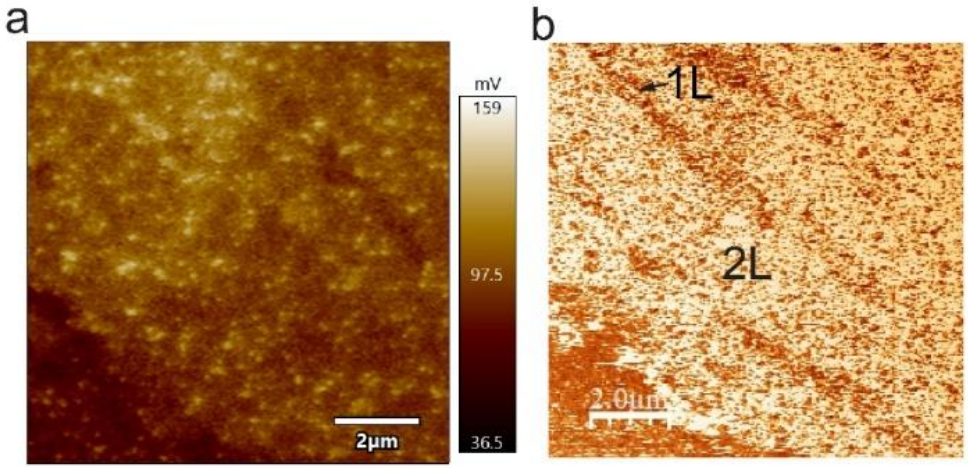

Figure 4.19. (a) KPFM surface potential image of $PdSe_2$. and (b) corresponding phase image.

Work function of $PdSe_2$ can be calculated following the below **equation 4.2**.

$$\phi_s = \phi_{tip} - eV_{CPD} \quad (4.2)$$

Where ϕ_s, ϕ_{tip} are the work function of sample and the reference tip and V_{CPD} is the contact potential difference. From **Figure 4.19**, the measured V_{CPD} is 110 mV. The reference tip has the work function 4.98 eV. Inserting all the values in the **equation 4.2**, the work function of 2L $PdSe_2$ is

$$\phi_s = (4.98 - 0.11)\ eV = 4.87\ eV$$

Notably, for 1L the work function is negligibly changed as the change in V_{CPD} is ~ (150-110) mV i.e. 40 mV. Estimated work function 1L $PdSe_2$ is ~ $\phi_s = (4.98 - 0.15)\ eV = 4.83\ eV$. The lower work function is due to the presence of defect energy states in $PdSe_2$. There exists a high density of electronic states at E_F because most edges of dendrites terminate with electron-rich Se. As the

density of vacancies increases, additional defect states appear near the Fermi level. Thus, defect states are generated close to Fermi energy (E_F). As a result, an additional charge transfer route between the RhB molecule and $PdSe_2$ is introduced.

Further, we have performed SERS measurement of different concentrations of RhB molecule to calculate the detection efficiency of $PdSe_2$ dendrites. **Figure 4.20a** shows the SERS spectra of RhB with different concentrations. The calculated enhancement factor vs. RhB concentration log plot (**Figure 4.20b**) reflects a linear increment of EF as a function of concentration. It is evident that the pristine 2L $PdSe_2$ can serve as a SERS substrate with very low concentration (10^{-8} M) RhB detection with an enhancement factor of 10^5. Such a high enhancement factor arises due to charge transfer between RhB molecules and $PdSe_2$ dendrites. A schematic illustration in **Figure 4.20c** shows the corresponding energy levels and subsequent charge transfer mechanism. According to the literature, LUMO and HOMO energy value with respect to vacuum of RhB is -3.08 eV and -5.45 eV, respectively.[57] When RhB is exposed to a laser excitation of 532 nm, the excitation energy is 2.33 eV which is less than or close to the energy difference between HOMO and LUMO (2.37 eV) of RhB. This laser excitation energy is unable to amplify the Raman signal. When RhB/$PdSe_2$ hybrid system is exposed to 532 nm laser excitation, the charge transfer process may follow three possible paths. Absorption of a photon by RhB excites an electron from the highest occupied molecular orbital (HOMO) to the lowest unoccupied molecular orbital (LUMO) through Path 1. Part of these charges may go to the conduction band (CB) of 2D $PdSe_2$ as depicted by the dashed curve in **Figure 4.20c** and partly come back to the HOMO to recombine radiatively. Experimental evidence for the electron transfer from the RhB to $PdSe_2$ comes from the photoluminescence quenching of RhB, discussed later. Next, part of these electrons in CB of $PdSe_2$ may transfer to the HOMO of RhB through Path 2 and partly through Path 3, i.e. through the defect levels of $PdSe_2$. The electronic transitions through Path 2 and Path 3 may cause lower energy recombination, which is indeed reflected in the PL emission spectra discussed below for the hybrid system. Note that with the incident laser excitation, the electrons in $PdSe_2$ are also excited from the VB to the CB as well as to defect states and these electrons also partly follow Path 2 and Path 3 for relaxation. Thus, the transitions through Path 2 and Path 3 results in high density of electrons in the HOMO and LUMO of RhB, which gives rise to the highly intense Raman signal, i.e., SERS effect from RhB.

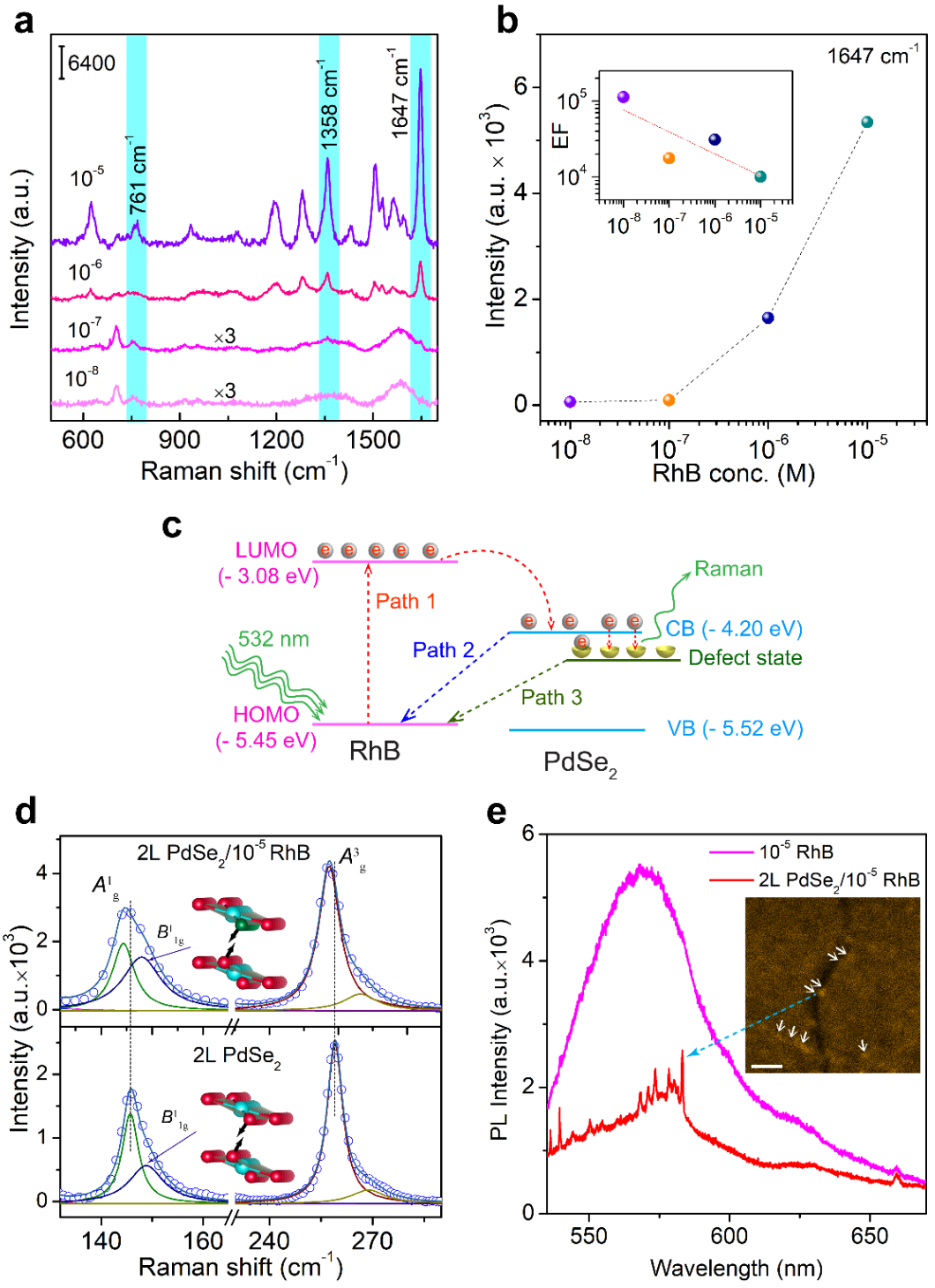

Figure 4.20. (a) Raman spectra of 10^{-5} M, 10^{-6}, 10^{-7}, 10^{-8} M RhB on $PdSe_2$, (b) the corresponding intensity semi-log plot for C-C bending and C=C stretching as a function of RhB concentration. The inset shows the log plot of calculated enhancement factor (EF). (c) Energy band diagram showing the charge transfer pathways in RhB/$PdSe_2$ hybrid system. (d) Stacked Raman spectra of 2L $Pdse_2$ and 10^{-5} RhB drop casted 2L $PdSe_2$, where the inset atomic models show the B^1_{1g} vibrational mode. (e) Measured photoluminescence spectra of 10^{-5} M RhB on mica substrate and SERS spectrum of 2L $PdSe_2/10^{-5}$ RhB. The inset shows the confocal microscopy image of RhB molecules on the defective sites (scale bar: 5 μm).

A large amount of vacancy defects result in highly intense Raman modes.[27] Evidence of charge transfer and doping is further confirmed from the Raman spectrum. **Figure 4.20d** shows the stacked Raman spectra for pristine 2L $PdSe_2$ and RhB/2L $PdSe_2$ on mica substrate. Careful observation reveals that B_{1g}^1 intensity increases in RhB/2L $PdSe_2$ system. Intensity ratio of A_g^1 / B_{1g}^1 is 2.36 in 2L $PdSe_2$, which decreases to 1.27 in the RhB/2L $PdSe_2$ system. As the RhB injection mainly happens in Se vacancy sites, among all other modes B_{1g}^1 mode becomes more intense due to the strongest coupling between RhB molecule with Se atoms. Peak shift in the Raman spectrum is a non-destructive way to understand the doping, and charge transfer.[55,58] The spectral shift in Raman peak A_g^1 (1.3 cm^{-1}) and A_g^3 (1.6 cm^{-1}) in the RhB/2L $PdSe_2$ system is definite evidence of effective charge transfer in the hybrid system. Here charge transfer between RhB molecule and $PdSe_2$ was assumed to be the dominant factor which is accompanied by a large spectral shift in 2L $PdSe_2$. For further confirmation, we have performed photoluminescence spectroscopy of the bare RhB and the RhB/ 2L $PdSe_2$ system (**Figure 4.20e**). We notice a considerable redshift along with a significant quenching (68.7%) of photoluminescence spectrum in the hybrid system. The significant quenching may be attributed to the charge transfer from the RhB LUMO to CB and defect levels of 2D $PdSe_2$. The redshift is a result of the lower energy transitions through Path 2 and Path 3, shown in **Figure 4.20c**.

Table 4.2: Lorentz fitting parameters of Raman spectra of 2L $PdSe_2$ and 2L $PdSe_2$ /10^{-5} RhB of **Figure 4.20d**.

	2L $PdSe_2$			2L $PdSe_2$/10^{-5} RhB		
Raman modes	Peak position (cm^{-1})	FWHM (cm^{-1})	Intensity (counts)	Peak position (cm^{-1})	FWHM (cm^{-1})	Intensity (counts)
A_g^1	145.7	3.9	1418	144.4	5.2	1984
B_{1g}^1	148.9	8.2	600	148.0	9.2	1563
A_g^3	259.0	5.6	2518	257.4	7.6	4236
B_{1g}^3	268.8	11.9	216	266.4	11.8	479

Recently, X. W. Zhao et al. reported that for monolayer $PdSe_2$ with Se defect, there is a reduction in the bandgap and the band of midgap state goes through the Fermi level, and the $PdSe_2$ shows metal characteristics.[10] Series of Se_{TLU} line vacancies in $PdSe_2$ act as metallic edge in the presence

of excess Pd, similar to the extended defects in graphene acting as a metallic wire[58]. Lorentz fitting parameters of Raman spectra of 2L $PdSe_2$ and 2L $PdSe_2$ /10^{-5} RhB of **Figure 4.20d** are given in **Table 4.2**.

4.5.3. Electronic band structure of 2L $PdSe_2$ without defect and with line defects

To substantiate our conjecture, we performed DFT calculation of the band structure and density of states of the bilayer $PdSe_2$ system without and with line defects (Se vacancies).

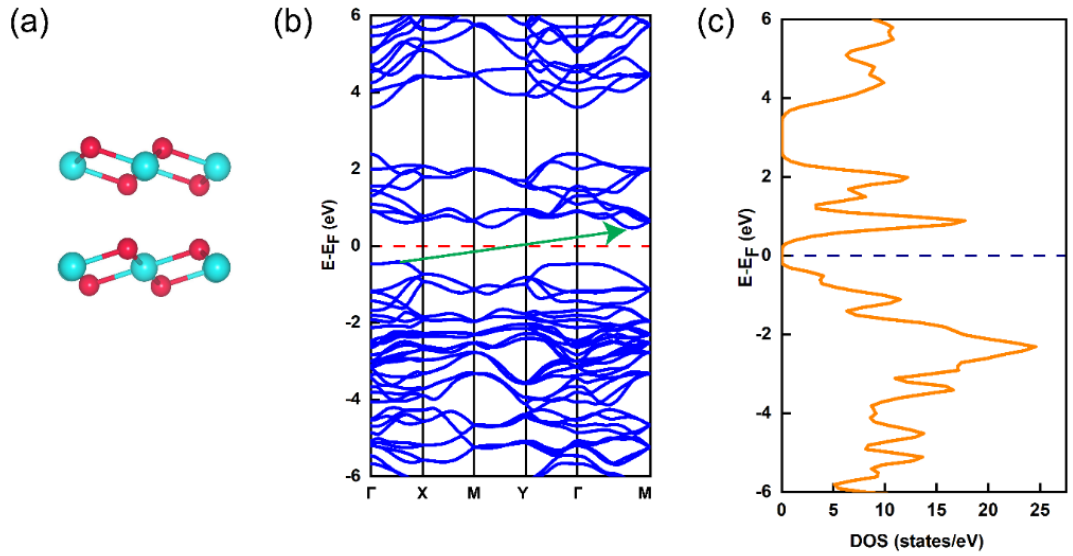

Figure 4.21 (a) Unit cell (side view) of 2L $PdSe_2$, (b) Electronic band structure and (d) DOS plot of unit-cell of 2L $PdSe_2$ using PBE-GGA. The Fermi level has been set to zero and indicated by the dashed lines.

The details of the calculations are provided in the computational methods section. We have calculated the electronic properties of bilayer $PdSe_2$ without defect (2L $PdSe_2$) and with line defects (defective 2L $PdSe_2$) using PBE-GGA (**Figure 4.21 and Figure 4.22**) and HSE06 (**Figure 4.23**) functionals. **Figure 4.21a** and **Figure 4.23a** represent the unit cell of 2L $PdSe_2$ and defective 2L $PdSe_2$, respectively. The calculated band structures along high symmetry k-points[59] illustrate an indirect band gap of 0.86 eV in 2L $PdSe_2$ (**Figure 4.21b)** and the corresponding DOS is displayed in **Figure 4.21c**. Introduction of Se defects (edge) lead to drastic change in the band structure, where some bands are seen touching the Fermi level (**Figure 4.22a**), indicating the metallic characteristics of the defective 2L $PdSe_2$ system.

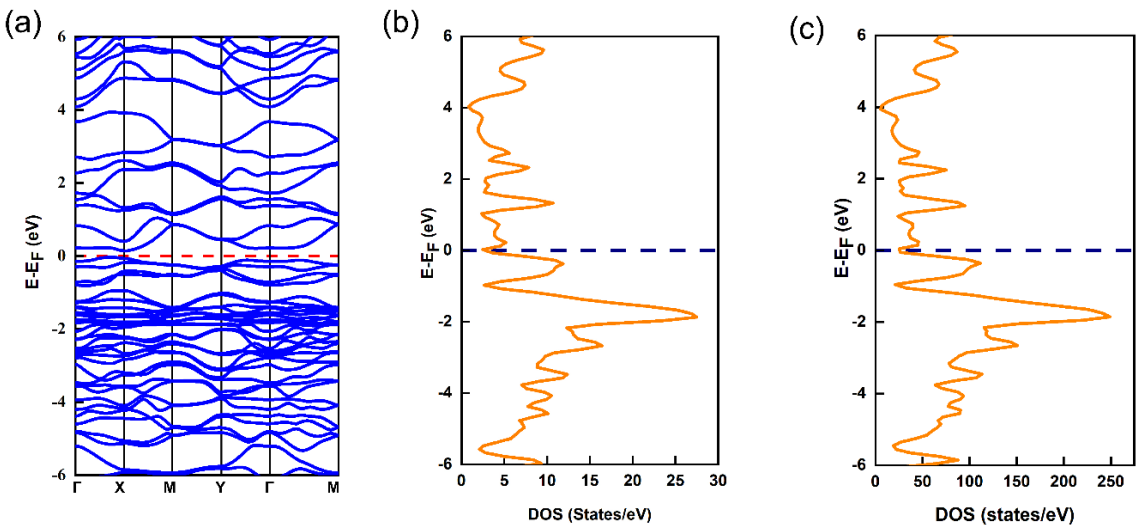

Figure 4.22 (a) Electronic band structure of unit-cell 2L $PdSe_2$ with Se vacancy, (b) DOS plot of unit-cell of defective 2L $PdSe_2$, and (c) DOS plot of 3×3 supercell of the defective 2L $PdSe_2$ using PBE-GGA. The Fermi level has been set to zero and indicated by the dashed lines.

The corresponding electronic density of states (DOS) is displayed in **Figure 4.22 b,** which shows no bandgap and it confirms the metallic behavior of the system. Further, using 3×3 supercell for PBE-GGA, we verified the electronic properties of the materials, and the DOS plot shown in **Figure 4.22c** also confirms the metallic properties of defective 2L $PdSe_2$. Since the HSE06 functional provides a more accurate description of the band structure, we have calculated the band structure and the corresponding DOS of defective 2L $PdSe_2$ using HSE06 functional and the results are shown in **Figures 4.23b, 4.23 c**. It is evident from **Figure 4.23b** that two different bands cross the Fermi energy (E_F) along X-M and Γ-M direction and it indicates the metallic nature of defective 2L $PdSe_2$. Interestingly, the density of states (DOS) plot reveals the electron occupation in the Fermi-level in the case of defective 2L $PdSe_2$, which demonstrates the metallic feature of the material. When the RhB molecule is attached to such metallic edges, the quenching is maximum due to which we observed SERS associated PL signal with lower separation between molecule - Pd.[60] Quenching of photoluminescence suggests that there is a strong interaction between RhB molecule and defective $PdSe_2$, which contributes to the efficient charge transfer in the RhB/ 2L $PdSe_2$ system. A redshift in the photoluminescence peak corresponds to lower energy emission. Due to defects and nanopores, charge transfer may take place to the lower energy and subsequent recombination (through Path 2 and Path 3) may give rise to lower energy emission band.

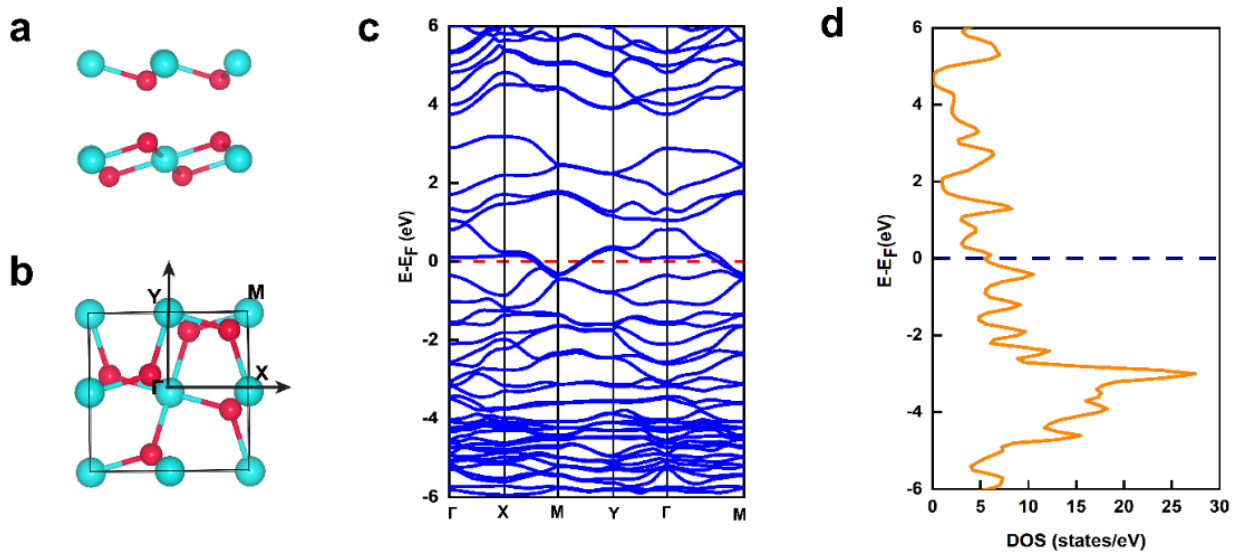

Figure 4.23. (a) Unit cell (side view) of bilayer $PdSe_2$ with Se vacancy on the top layer (Se_{TLU}). (b) Unit cell (top view) of defective 2L $PdSe_2$ showing the high symmetry K-points in the Brillouin zone. (c) Electronic band structure, and (d) DOS plot of defective 2L $PdSe_2$ using HSE06 functional showing metallic behavior. The Fermi level has been set to zero and indicated by the dashed line.

In **Figure 4.20d**, B_{1g}^{1} mode is defect-related peak, which gets intense in 2L $PdSe_2$/RhB. Thus, 2L edge sites are very crucial for the observed effect. Moreover, photoluminescence gives the intrinsic response of RhB/ 2L $PdSe_2$ system. Lin et. al. reported the difference in photoluminescence fingerprint of Au nanorods and MGTIC molecule adsorbed Au nanorods.[61] Taking TEM analysis into account, some rows of Se_{TLU} vacancies along with excess Pd behave like a metallic edge and acts as defect-induced hotspot for SERS in detecting foreign molecules. Thus, the vacant sites in $PdSe_2$ basically act as a hotspot for SERS enhancement with RhB molecule. It is worth highlighting that we observed the PL emission peak along with the SERS signal of RhB/ 2L $PdSe_2$ system. Such photoluminescence associated SERS signal retrieve a fingerprint of defects and defective dendritic $PdSe_2$ acts as defect-induced hotspot. Defect level close to the fermi level produce a local doping site for RhB molecule in a narrow stripe along the line defect (created by Se_{TLU} vacancies) which further contributes towards quasi-one dimensional metal like behavior in 2d $PdSe_2$.[62] Orange fluorescence was observed over the 2D $PdSe_2$ dendrites denoting adsorption of Rhb molecule. Confocal microscopy imaging **(**inset of **Figure 4.20e)** shows an altering contrast in fluorescence, which is due the plasmon-like behavior of vacancy rich edges, line defects, and nanopores in dendritic $PdSe_2$.

4.5.4. SERS stability

Finally, to check the stability, we carried out SERS measurements after several months on 10^{-5} M Rhodamine B deposited $PdSe_2$ sample, which was kept in the laboratory atmosphere **(Figure 4.24)**. From the distinct Raman peak, it is clear that the samples are quite stable up to a few months. Any change in signal intensity is due to the partial evaporation of the dye molecules from the sample surface.

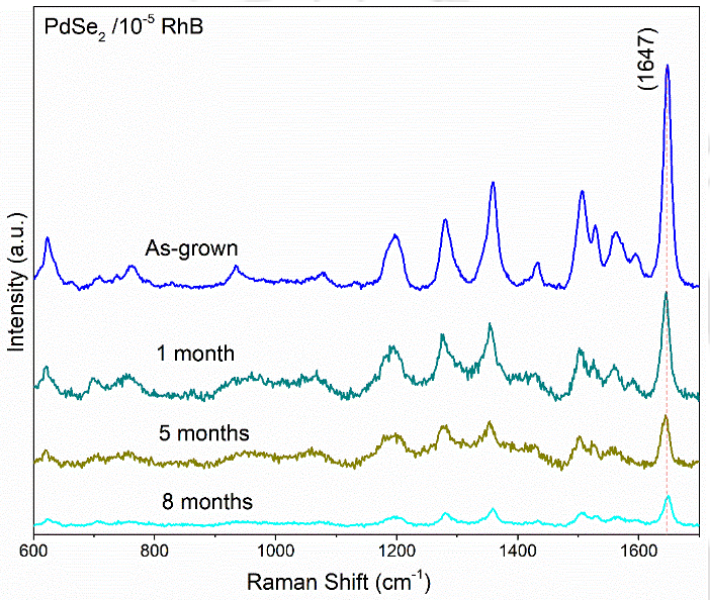

Figure 4.24. Raman spectra of 10^{-5} M rhodamine B on 2L $PdSe_2$ after 1month, 5 months and 8 months of exposer to laboratory atmosphere.

4.5.5. SERS measurement with other molecules

To prove the versatility of the as-grown defect-rich 2L $PdSe_2$ dendrites as a very powerful SERS substrate, we have also carried out the SERS measurement with other molecules, such as methylene blue and methylene orange (10^{-4} M, **Figure 4.25**). The result signifies its versatility for SERS detection with variety of probe molecules. The strong Raman signals indicate a strong interaction between 2L dendritic $PdSe_2$ with probe molecules. Thus, it has potential to be used as a commercial SERS substrate in near future.

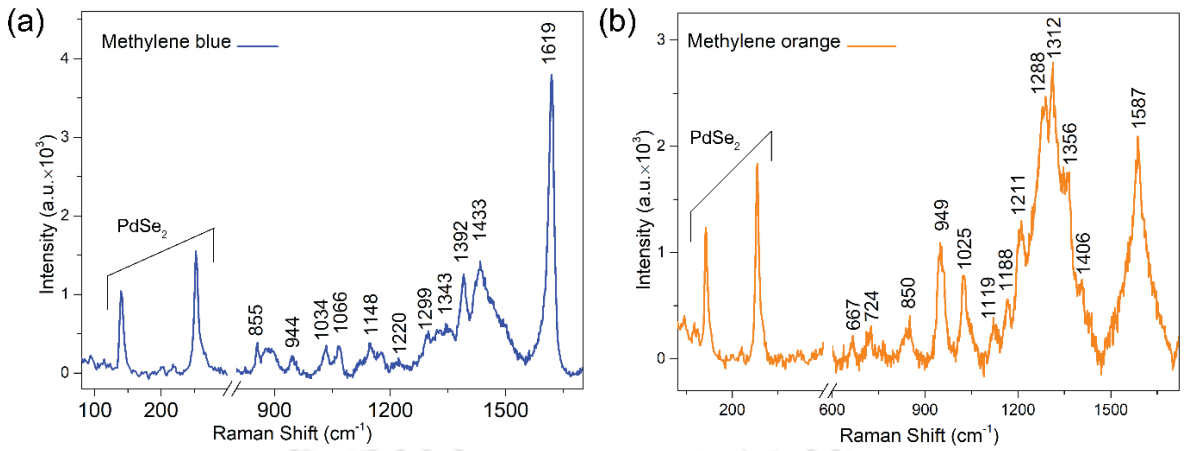

Figure 4.25 SERS spectra of 10^{-4} M (a) methylene blue and (b) methylene orange on 2L $PdSe_2$.

4.6. Conclusion

The comprehensive study on vacancies, nanopores, and edge geometry of $PdSe_2$ dendrites provides new insights into how intrinsic defects influence the properties. XPS analysis reveals about 9.3% outer layer Se vacancies, 4.7 % inner Se vacancies, and 4.7% Pd vacancies in dendritic 2D $PdSe_2$. Our finding, shows a NIR photoluminescence from dendritic $PdSe_2$ and the influence of intrinsic defects on its bandgap. We speculate that Se vacancy sites in dendritic $PdSe_2$ behave as a metallic edge and it acts as a non-plasmonic hotspot for SERS detection of RhB molecule. To validate our conjecture on the metallic behaviour of the defective $PdSe_2$, DFT calculation were performed for the electronic density of states in bilayer $PdSe_2$ with Se defects using PBE-GGA and HSE06 functionals and it clearly revealed metal-like behaviour of the dendritic $PdSe_2$. Recently, Renu et al. reported a SERS enhancement up to ~10^4 at the sculpted plasmonic hotspots in monolayer MoS_2.[63] It has constantly been debated whether plasmon-free SERS substrate can compete with plasmonic SERS substrate. Interestingly, without any post-treatment, our plasmon-free dendritic $PdSe_2$ detects RhB with a significant SERS enhancement (> 10^5), with post-growth treatment, it might exceed the plasmonic SERS substrate limit. Our findings offer insights into the field of SERS sensing, nanopore sensing, gas sensing, biosensing, and device fabrication applications, where we believe $PdSe_2$ will be a rising star in the near future. The observations, analysis, and related findings presented here show the trivial nature of dendritic $PdSe_2$, which can be expected to replace the existing plasmon-free SERS substrates in high demand in the coming generation and blossom into the affluent area of commercial products.

References

1 Vicarelli, L., Heerema, S. J., Dekker, C. & Zandbergen, H. W. Controlling Defects in Graphene for Optimizing the Electrical Properties of Graphene Nanodevices. *ACS Nano* **9**, 3428-3435 (2015). https://doi.org:10.1021/acsnano.5b01762

2 Pi, L. *et al.* Recent Progress on 2D Noble-Transition-Metal Dichalcogenides. *Advanced Functional Materials* **29**, 1904932 (2019). https://doi.org:https://doi.org/10.1002/adfm.201904932

3 Kuklin, A. V. & Ågren, H. Quasiparticle electronic structure and optical spectra of single-layer and bilayer ${\mathrm{PdSe}}_{2}$: Proximity and defect-induced band gap renormalization. *Physical Review B* **99**, 245114 (2019). https://doi.org:10.1103/PhysRevB.99.245114

4 Zhang, X. *et al.* Centimeter-Scale Few-Layer PdS2: Fabrication and Physical Properties. *ACS Applied Materials & Interfaces* **13**, 43063-43074 (2021). https://doi.org:10.1021/acsami.1c11824

5 Aftab, S. *et al.* Switching photodiodes based on (2D/3D) PdSe2/Si heterojunctions with a broadband spectral response. *Journal of Materials Chemistry C* **9**, 3998-4007 (2021). https://doi.org:10.1039/D0TC05894G

6 Aftab, S. *et al.* Platinum Disulfide (PtS2) and Silicon Pyramids: Efficient 2D/3D Heterojunction Tunneling and Breakdown Diodes. *ACS Applied Electronic Materials* **4**, 917-924 (2022). https://doi.org:10.1021/acsaelm.1c00990

7 Aftab, S. *et al.* Single nanoflake-based PtSe2 p–n junction (in-plane) formed by optical excitation of point defects in BN for ultrafast switching photodiodes. *Journal of Materials Chemistry C* **9**, 199-207 (2021). https://doi.org:10.1039/D0TC04642F

8 Pi, L. *et al.* Highly In-Plane Anisotropic 2D PdSe2 for Polarized Photodetection with Orientation Selectivity. *Advanced Functional Materials* **31**, 2006774 (2021). https://doi.org:https://doi.org/10.1002/adfm.202006774

9 Oyedele, A. D. *et al.* PdSe2: Pentagonal Two-Dimensional Layers with High Air Stability for Electronics. *Journal of the American Chemical Society* **139**, 14090-14097 (2017). https://doi.org:10.1021/jacs.7b04865

10 Zhao, Y. *et al.* Low-Symmetry PdSe2 for High Performance Thermoelectric Applications. *Advanced Functional Materials* **30**, 2004896 (2020). https://doi.org:https://doi.org/10.1002/adfm.202004896

11 Lu, L.-S. *et al.* Layer-Dependent and In-Plane Anisotropic Properties of Low-Temperature Synthesized Few-Layer PdSe2 Single Crystals. *ACS Nano* **14**, 4963-4972 (2020). https://doi.org:10.1021/acsnano.0c01139

12 Illarionov, Y. Y. *et al.* Long-Term Stability and Reliability of Black Phosphorus Field-Effect Transistors. *ACS Nano* **10**, 9543-9549 (2016). https://doi.org:10.1021/acsnano.6b04814

13 Wood, J. D. *et al.* Effective Passivation of Exfoliated Black Phosphorus Transistors against Ambient Degradation. *Nano Letters* **14**, 6964-6970 (2014). https://doi.org:10.1021/nl5032293

14 Mermin, N. D. Crystalline Order in Two Dimensions. *Physical Review* **176**, 250-254 (1968). https://doi.org:10.1103/PhysRev.176.250

15 Novoselov, K. S. *et al.* Electric Field Effect in Atomically Thin Carbon Films. *Science* **306**, 666-669 (2004). https://doi.org:10.1126/science.1102896

16 Terrones, H., Lv, R., Terrones, M. & Dresselhaus, M. S. The role of defects and doping in 2D graphene sheets and 1D nanoribbons. *Reports on Progress in Physics* **75**, 062501 (2012). https://doi.org:10.1088/0034-4885/75/6/062501

17 Zhou, W. *et al.* Intrinsic Structural Defects in Monolayer Molybdenum Disulfide. *Nano Letters* **13**, 2615-2622 (2013). https://doi.org:10.1021/nl4007479

18 Xu, X., Robertson, J. & Li, H. Semiconducting few-layer PdSe2 and Pd2Se3: native point defects and contacts with native metallic Pd17Se15. *Physical Chemistry Chemical Physics* **22**, 7365-7373 (2020). https://doi.org:10.1039/C9CP06654C

19 Oyedele, A. D. *et al.* Defect-Mediated Phase Transformation in Anisotropic Two-Dimensional PdSe2 Crystals for Seamless Electrical Contacts. *Journal of the American Chemical Society* **141**, 8928-8936 (2019). https://doi.org:10.1021/jacs.9b02593

20 Zhao, X. W. *et al.* Tuning electronic and optical properties of monolayer PdSe2 by introducing defects: first-principles calculations. *Scientific Reports* **10**, 4028 (2020). https://doi.org:10.1038/s41598-020-60949-9

21 Shautsova, V. *et al.* Direct Laser Patterning and Phase Transformation of 2D PdSe2 Films for On-Demand Device Fabrication. *ACS Nano* **13**, 14162-14171 (2019). https://doi.org:10.1021/acsnano.9b06892

22 Nguyen, G. D. *et al.* 3D Imaging and Manipulation of Subsurface Selenium Vacancies in ${\mathrm{PdSe}}_{2}$. *Physical Review Letters* **121**, 086101 (2018). https://doi.org:10.1103/PhysRevLett.121.086101

23 Jakhar, M., Singh, J., Kumar, A. & Pandey, R. First-Principles Study of the Hexagonal T-Phase PdSe2 Monolayer and Its Application in Solar Cells. *The Journal of Physical Chemistry C* **124**, 26565-26571 (2020). https://doi.org:10.1021/acs.jpcc.0c05632

24 Fu, M. *et al.* Defects in Highly Anisotropic Transition-Metal Dichalcogenide PdSe2. *The Journal of Physical Chemistry Letters* **11**, 740-746 (2020). https://doi.org:10.1021/acs.jpclett.9b03312

25 Liang, Q., Zhang, Q., Zhao, X., Liu, M. & Wee, A. T. S. Defect Engineering of Two-Dimensional Transition-Metal Dichalcogenides: Applications, Challenges, and Opportunities. *ACS Nano* **15**, 2165-2181 (2021). https://doi.org:10.1021/acsnano.0c09666

26 Zheng, Z. *et al.* Semiconductor SERS enhancement enabled by oxygen incorporation. *Nature Communications* **8**, 1993 (2017). https://doi.org:10.1038/s41467-017-02166-z

27 Lin, J. *et al.* Ultrasensitive SERS Detection by Defect Engineering on Single Cu2O Superstructure Particle. *Advanced Materials* **29**, 1604797 (2017). https://doi.org:https://doi.org/10.1002/adma.201604797

28 Cong, S. *et al.* Noble metal-comparable SERS enhancement from semiconducting metal oxides by making oxygen vacancies. *Nature Communications* **6**, 7800 (2015). https://doi.org:10.1038/ncomms8800

29 Danda, G. & Drndić, M. Two-dimensional nanopores and nanoporous membranes for ion and molecule transport. *Current Opinion in Biotechnology* **55**, 124-133 (2019). https://doi.org:https://doi.org/10.1016/j.copbio.2018.09.002

30 Liu, K. *et al.* Geometrical Effect in 2D Nanopores. *Nano Letters* **17**, 4223-4230 (2017). https://doi.org:10.1021/acs.nanolett.7b01091

31 Garoli, D., Yamazaki, H., Maccaferri, N. & Wanunu, M. Plasmonic Nanopores for Single-Molecule Detection and Manipulation: Toward Sequencing Applications. *Nano Letters* **19**, 7553-7562 (2019). https://doi.org:10.1021/acs.nanolett.9b02759

32 Qiu, H., Zhou, W. & Guo, W. Nanopores in Graphene and Other 2D Materials: A Decade's Journey toward Sequencing. *ACS Nano* **15**, 18848-18864 (2021). https://doi.org:10.1021/acsnano.1c07960

33 Lee, K. *et al.* Recent Progress in Solid-State Nanopores. *Advanced Materials* **30**, 1704680 (2018). https://doi.org:https://doi.org/10.1002/adma.201704680

34 Su, S., Wang, X. & Xue, J. Nanopores in two-dimensional materials: accurate fabrication. *Materials Horizons* **8**, 1390-1408 (2021). https://doi.org:10.1039/D0MH01412E

35 Wanunu, M. & Meller, A. Chemically Modified Solid-State Nanopores. *Nano Letters* **7**, 1580-1585 (2007). https://doi.org:10.1021/nl070462b

36 Lan, L., Hou, X., Gao, Y., Fan, X. & Qiu, T. Inkjet-printed paper-based semiconducting substrates for surface-enhanced Raman spectroscopy. *Nanotechnology* **31**, 055502 (2019). https://doi.org:10.1088/1361-6528/ab4f11

37 Qiu, Y. *et al.* Photodegradable CuS SERS Probes for Intraoperative Residual Tumor Detection, Ablation, and Self-Clearance. *ACS Applied Materials & Interfaces* **11**, 23436-23444 (2019). https://doi.org:10.1021/acsami.9b00469

38 Alvarez-Puebla, R. A. & Liz-Marzán, L. M. SERS Detection of Small Inorganic Molecules and Ions. *Angewandte Chemie International Edition* **51**, 11214-11223 (2012). https://doi.org:https://doi.org/10.1002/anie.201204438

39 Han, X. X., Ji, W., Zhao, B. & Ozaki, Y. Semiconductor-enhanced Raman scattering: active nanomaterials and applications. *Nanoscale* **9**, 4847-4861 (2017). https://doi.org:10.1039/C6NR08693D

40 Shankla, M. & Aksimentiev, A. Step-defect guided delivery of DNA to a graphene nanopore. *Nature Nanotechnology* **14**, 858-865 (2019). https://doi.org:10.1038/s41565-019-0514-y

41 Danda, G. *et al.* Monolayer WS2 Nanopores for DNA Translocation with Light-Adjustable Sizes. *ACS Nano* **11**, 1937-1945 (2017). https://doi.org:10.1021/acsnano.6b08028

42 Zhang, L. & Wang, X. DNA Sequencing by Hexagonal Boron Nitride Nanopore: A Computational Study. *Nanomaterials* **6** (2016). https://doi.org:10.3390/nano6060111

43 Masih Das, P. *et al.* Controlled Sculpture of Black Phosphorus Nanoribbons. *ACS Nano* **10**, 5687-5695 (2016). https://doi.org:10.1021/acsnano.6b02435

44 Govind Rajan, A. *et al.* Addressing the isomer cataloguing problem for nanopores in two-dimensional materials. *Nature Materials* **18**, 129-135 (2019). https://doi.org:10.1038/s41563-018-0258-3

45 W. Luo, A. D. Oyedele, Y. Gu, T. Li, X. Wang, A. V. Haglund, D. Mandrus, A. A. Puretzky, K. Xiao, L. Liang, X. Ling, Anisotropic Phonon Response of Few-Layer PdSe2 under Uniaxial Strain. Adv. Funct. Mater. 2020, 30, 2003215. https://doi.org/10.1002/adfm.202003215

46 Yu, J. *et al.* Giant nonlinear optical activity in two-dimensional palladium diselenide. *Nature Communications* **12**, 1083 (2021). https://doi.org:10.1038/s41467-021-21267-4

47 Liang, Q. *et al.* Performance Improvement by Ozone Treatment of 2D PdSe2. *ACS Nano* **14**, 5668-5677 (2020). https://doi.org:10.1021/acsnano.0c00180

48 Hoffman, A. N. *et al.* Exploring the air stability of PdSe2 via electrical transport measurements and defect calculations. *npj 2D Materials and Applications* **3**, 50 (2019). https://doi.org:10.1038/s41699-019-0132-4

49 Banhart, F., Kotakoski, J. & Krasheninnikov, A. V. Structural Defects in Graphene. *ACS Nano* **5**, 26-41 (2011). https://doi.org:10.1021/nn102598m

50 Jeong, M.-H. *et al.* Multilayer WSe2/MoS2 Heterojunction Phototransistors through Periodically Arrayed Nanopore Structures for Bandgap Engineering. *Advanced Materials* **n/a**, 2108412 (2022). https://doi.org:https://doi.org/10.1002/adma.202108412

51 Merchant, C. A. *et al.* DNA Translocation through Graphene Nanopores. *Nano Letters* **10**, 2915-2921 (2010). https://doi.org:10.1021/nl101046t

52 Koskinen, P., Malola, S. & Häkkinen, H. Self-Passivating Edge Reconstructions of Graphene. *Physical Review Letters* **101**, 115502 (2008). https://doi.org:10.1103/PhysRevLett.101.115502

53 Huang, Q. *et al.* Flower-Like Molybdenum Disulfide for Polarity-Triggered Accumulation/Release of Small Molecules. *ACS Applied Materials & Interfaces* **9**, 36431-36437 (2017). https://doi.org:10.1021/acsami.7b11940

54 Karthick Kannan, P., Shankar, P., Blackman, C. & Chung, C.-H. Recent Advances in 2D Inorganic Nanomaterials for SERS Sensing. *Advanced Materials* **31**, 1803432 (2019). https://doi.org:https://doi.org/10.1002/adma.201803432

55 Hossain, M. T., Das, M., Ghosh, J., Ghosh, S. & Giri, P. K. Understanding the interfacial charge transfer in the CVD grown Bi2O2Se/CsPbBr3 nanocrystal heterostructure and its exploitation in superior photodetection: experiment vs. theory. *Nanoscale* **13**, 14945-14959 (2021). https://doi.org:10.1039/D1NR04470B

56 Liu, X., Zhou, H., Yang, B., Qu, Y. & Zhao, M. Strain-Modulated Electronic Structure and Infrared Light Adsorption in Palladium Diselenide Monolayer. *Scientific Reports* **7**, 39995 (2017). https://doi.org:10.1038/srep39995

57 Qiu, H. *et al.* Wrinkled 2H-phase MoS2 sheet decorated with graphene-microflowers for ultrasensitive molecular sensing by plasmon-free SERS enhancement. *Sensors and Actuators B: Chemical* **320**, 128445 (2020). https://doi.org:https://doi.org/10.1016/j.snb.2020.128445

58 Dhakal, K. P. *et al.* Confocal absorption spectral imaging of MoS2: optical transitions depending on the atomic thickness of intrinsic and chemically doped MoS2. *Nanoscale* **6**, 13028-13035 (2014). https://doi.org:10.1039/C4NR03703K

59 Zhao, X. *et al.* Electronic and optical properties of PdSe2 from monolayer to trilayer. *Superlattices and Microstructures* **142**, 106514 (2020). https://doi.org:https://doi.org/10.1016/j.spmi.2020.106514

60 Johansson, P., Xu, H. & Käll, M. Surface-enhanced Raman scattering and fluorescence near metal nanoparticles. *Physical Review B* **72**, 035427 (2005). https://doi.org:10.1103/PhysRevB.72.035427

61 Lin, K.-Q. *et al.* Plasmonic photoluminescence for recovering native chemical information from surface-enhanced Raman scattering. *Nature Communications* **8**, 14891 (2017). https://doi.org:10.1038/ncomms14891

62 Lahiri, J., Lin, Y., Bozkurt, P., Oleynik, I. I. & Batzill, M. An extended defect in graphene as a metallic wire. *Nature Nanotechnology* **5**, 326-329 (2010). https://doi.org:10.1038/nnano.2010.53

63 Rani, R. *et al.* Sculpting Artificial Edges in Monolayer MoS2 for Controlled Formation of Surface-Enhanced Raman Hotspots. *ACS Nano* **14**, 6258-6268 (2020). https://doi.org:10.1021/acsnano.0c02418

64 Kresse, G. & Furthmüller, J. Efficient iterative schemes for ab initio total-energy calculations using a plane-wave basis set. *Physical Review B* **54**, 11169-11186 (1996). https://doi.org:10.1103/PhysRevB.54.11169

65 Parr, R. G. Density Functional Theory. *Annual Review of Physical Chemistry* **34**, 631-656 (1983). https://doi.org:10.1146/annurev.pc.34.100183.003215

66 Giannozzi, P. *et al.* J. Phys.: Condens. Matter 21 395502. (2009).

67 Blöchl, P. E. Projector augmented-wave method. *Physical Review B* **50**, 17953-17979 (1994). https://doi.org:10.1103/PhysRevB.50.17953

68 Perdew, J. P., Burke, K. & Ernzerhof, M. Generalized Gradient Approximation Made Simple. *Physical Review Letters* **77**, 3865-3868 (1996). https://doi.org:10.1103/PhysRevLett.77.3865

69 Oyedele, A. D. *et al.* PdSe2: pentagonal two-dimensional layers with high air stability for electronics. *Journal of the American Chemical Society* **139**, 14090-14097 (2017) https://doi.org/10.1021/jacs.7b04865.

70 Heyd, J., Scuseria, G. E. & Ernzerhof, M. Hybrid functionals based on a screened Coulomb potential. *The Journal of chemical physics* **118**, 8207-8215 (2003) https://doi.org/10.1063/1.1564060.

Chapter 5 - Water-assisted scrolling and unscrolling of bilayer $PdSe_2$ for selective killing of cancer cells

In this chapter, we introduce the scrolling and unscrolling of bilayer $PdSe_2$ on a mica substrate. It has been suggested that the transformation of these atomically planar materials to three-dimensional (3D) geometries by bending, wrinkling, or scrolling could significantly alter their properties and lead to novel structures and devices with compact form factors, but strategies to enable this shape change remain limited. Origami-like and kirigami-like graphene have been demonstrated, and shapes such as springs, stretchable electrodes, and hinges have been formed using external mechanical forces. However, controlled scrolling in response to external environmental stimuli, such as mild temperature compatible with biological systems, has yet to be demonstrated. Such controlled scrolling is extremely difficult to achieve with graphene, TMDs, and NTMDs. Here, we show that thermal activation inside an H_2O environment can have a more marked effect on the behavior, leading to spontaneous sliding, tearing, and peeling of directly CVD-grown $PdSe_2$ from mica substrate. The $PdSe_2$ nanoscrolls (PSNS) are formed from the edges of the bilayer $PdSe_2$ sheet. The conversion of $PdSe_2$ into PSNS via Pd nanoparticles and unscrolling into sheet structures are fully controlled under H_2O environment.

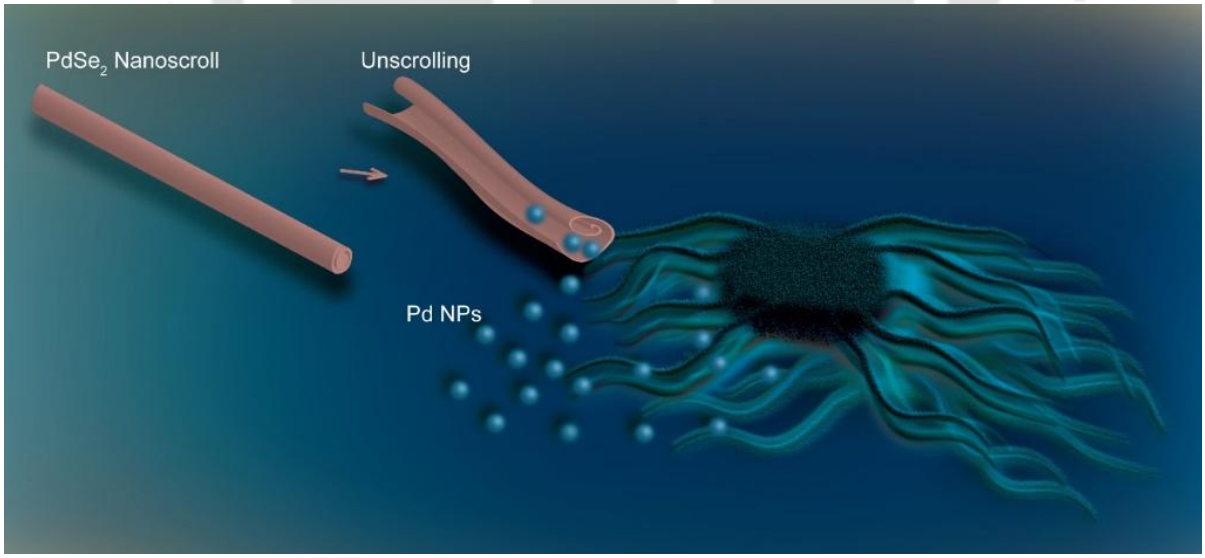

Scheme 5.1. Scheme describing the scrolling of $PdSe_2$ nanoscrolls (PSNS) enclosed by Pd NPs and attacking cancer cells by unscrolling PSNS.

We highlight its application in selective killing of cancer cells; where Pd nanoparticles attack the cancer cell leading to the nuclear arrest and death of the cells. We anticipate that this general approach is highly tunable and can be used to fabricate a range of structures of relevance in foldable electronics, biosensing, and thermally active robots. These results pave the way for the discovery of various properties and applications of $PdSe_2$ nano-scrolls and nano-ribbons.

5.1. Introduction

In the recent era of 2D materials, papyrus like Graphene nanoscrolls (GNS) is one of the emerging nanomaterials.[1] GNS is morphologically similar to multiwalled carbon nanotubes, however scrolling with tunable inter-layer spacing affords a unique opportunity to inherit favorable properties of both carbon nanotubes and graphene.[1-6] After GNS, many effective methods have been employed to fabricate the nanoscrolls of h-BN, MoS_2, WS_2, black phosphorus and these were investigated by researchers, theoretically and experimentally.[7-14] The nanoscroll diameter can easily expand or contract making them extremely radially flexible results tuning inter-layer spacing affords a unique opportunity to inherit favorable properties, which can be exploited for a variety of applications in the catalytic, sensors, energy storage,[15] supercapacitors,[16] hydrogen storage, seawater desalination, bioengineering, drug delivery, and harvesting, etc. The road to understanding nanoscrolls remains arduous still, but recent progress provides reasons for cautious optimism. However, controlled scrolling in response to external environmental stimuli, such as mild temperature compatible with biological systems, is yet to be demonstrated. Such controlled scrolling is extremely difficult to achieve in most of the 2D materials.[17]

Traditional anticancer treatments have several limitations, but cancer is still one of the deadliest diseases. Metal nanoparticle mediated photothermal therapy has attracted extensive interest in recent years by virtue of its noninvasive feature and minimal side effects as compared to traditional chemotherapy.[18, 19] The use of metal nanoparticles absorb photon energy, then convert it to heat locally, resulting in a local temperature rise which causes the death of cancer cells. Among the metallic nanoparticles, Pd is a rare earth metals that have attracted researchers owing to their outstanding bioactive properties [20, 21] In biomedicine, Pd is very frequently used in dentistry appliances and especially its needles are mostly applied in the health center for prostate cancer therapy and choroidal melanoma therapies.[22, 23] Pd NPs exert prominent inhibition of several cancer cell lines and bacterial strains. Pd NPs can be used as substitutes for gold

nanoparticles in the treatment of tumours due to their extraordinary catalytic, antitumor applications, drug carriers, biosensors, and prodrug activators[24] and high stability under near-infrared region light. In addition, the noble Pd-NPs have shown excellent physicochemical features like high photocatalytic activity, remarkable chemical stability, good thermal stability, optical and electronic properties.[23, 25-27]

5.2. Experimental details

5.2.1. Synthesis of $PdSe_2$ nanoscrolls (PSNS)

Bilayer $PdSe_2$ flakes were synthesized following a two-step CVD synthesis process, (i) Solution preparation, (ii) Low-temperature CVD growth. First, $PdCl_2$ powder (99.999%), Se powder purchased from Sigma Aldrich, and NaCl powder (> 99.0 %, Merck) were used for experiments without further purification. 7.6×10^{-3} mol L^{-1} $PdCl_2$ was first added into 20 mL distilled water. Na_2PdCl_4 solution was prepared by mixing and dissolving 3 mg of NaCl with the $PdCl_2$ solution, which undergoes vigorous stirring (180 r/min) for about 45 min at room temperature using a magnetic stirrer. After ultrasonic irradiation of the final 10.17×10^{-3} mol L^{-1} Na_2PdCl_4 solution for 3 hrs, the color of the solution turned from initial pale yellow to dark brown. This observation indicates the reduction of Pd (II) ions to palladium Pd (0). Then, pre-patterning of Na_2PdCl_4 is done with the support of a quartz mask with circular openings. The quartz mask was placed on a freshly cleaved mica substrate. Then, under heating conditions, the as-prepared Na_2PdCl_4 solution was drop-cast in the circular opening area of the quartz mask. Na_2PdCl_4 solution on mica is heated at 50 °C on a hotplate for 45 mins. Then, the pre-patterned mica substrate is placed inside a quartz furnace for CVD. Before the growth, the quartz chamber was cleaned by purging Argon gas (300 sccm) via a rotary pump. In the CVD process, the temperature of the center zone is ramped up to 500 ℃, and Se powder is kept at 1 cm away towards the upstream (temperature ~240 ℃) to vaporize the Se and transport it to the growth substrate (~240 ℃) with a carrier gas (Argon) flow (110 sccm) in a single-zone tube furnace with precise temperature control.

Then, the as grown $PdSe_2$ flakes were scrolled in just 5 s with a 100% yield by touching the sample top side down onto a water surface. Under the built-in strain, the edge part of the flake curved out of the plane and continued to roll up to a complete PSNS. The scrolling

proceeded with time and formed $PdSe_2$ nanoscrolls (PSNS). Freshly synthesized $PdSe_2$ flakes on mica were more prone to scroll, while the aged samples exhibited slightly decreased scrolling rate.

5.2.2. In vitro cell culture

HeLa and A549 cells were procured from National Centre for Cell Science, Pune and were cultured in Dulbecco's Modified Eagle's Medium (DMEM, 10% FBS) and incubated in a humidified atmosphere at 37 °C supplied with 5% CO_2.

5.2.3. Cell viability assay

For determining cell viability, Hela cells were seeded in a 96 well plates at a density of 5000 cells/well. Following attachment, cells were treated with 10, 20, 30, 40, 50 and 75 µM of Pd NPs and PSNS for 48 h. After incubation, about 500 µg/mL of 3-(4,5-Dimethylthiazol-2-yl)-2,5-Diphenyltetrazolium Bromide (MTT) was added to each well and incubated for another 1.5 h. After incubation, the media was carefully discarded, and the purple colour tetrazolium salt formed due to cellular respiration, was dissolved in 100 µL DMSO. The colorimetric measurement was performed in multi-well plate reader (Promega microplate reader) by recording the absorbance at 560 nm for sample and 600 nm for background subtraction.

5.2.4. Characterization techniques

The details of the AFM, and micro-Raman measurements are discussed in **Chapter 2** (**Section 2.2.4**). The morphology and structural properties of the CVD-grown bilayer $PdSe_2$ have been studied using a transmission electron microscope. The morphology of the bilayer $PdSe_2$ is studied using FESEM.

5.3. Results and discussion

Bilayer $PdSe_2$ nanosheets are grown on mica substrate by salt-assisted CVD method as described in Chapter 2. Due to the underneath NaCl layer, $PdSe_2$ has weak van der Waals interaction with mica substrate, which results in a easily transformed $PdSe_2$ nanoscroll structure. A schematic of the formation of $PdSe_2$ nanoscrolls is proposed in **Figure 5.1a**. The mica substrate with $PdSe_2$ nanosheets with underneath NaCl touched to the surface of a water-surface with an angle of 30 ° in top side down manner. The bilayer $PdSe_2$ is hydrophobic with a water contact angle of ~90 °.

Thus, the low friction between the water and bilayer $PdSe_2$ facilitates the sliding of the water droplet. Due to the high surface tension of water, the edge of bilayer $PdSe_2$ tends to rolling up when the water droplet slides across it (**Figure 5.1b**). After treatment with deionized (DI) water, it was shaken for 5 mins inside water medium. As the water had an unbalanced teeter-totter movement across the nanosheet, the adhesion force was overcome and the edge of $PdSe_2$ nanosheet was curled first. With the directional movement of the water droplet, the bilayer $PdSe_2$ rolled up completely to form the PSNS (**Figure 5.1c**). Then, the substrate with $PdSe_2$ was put on a hot plate at 50 °C for 10 hrs, thus obtaining a H_2O free $PdSe_2$ nanoscrolls.

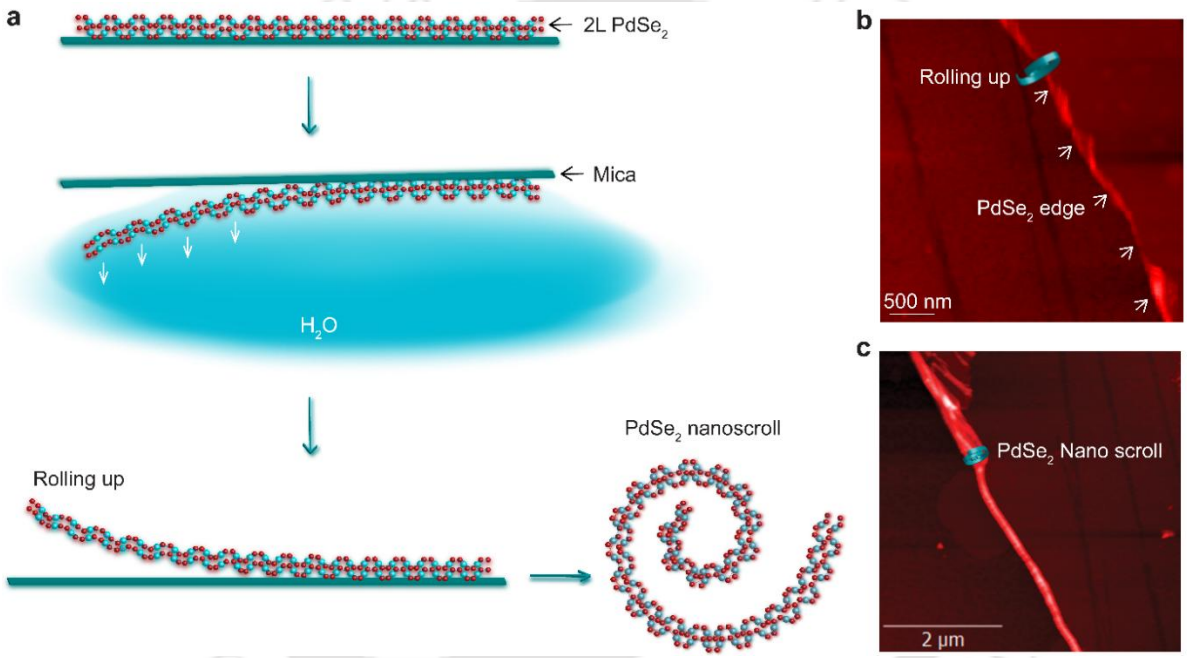

Figure 5.1. (a) Schematic illustration of $PdSe_2$ nanoscroll synthesis. (b) AFM image showing the rolling up process begins from the edge of bilayer $PdSe_2$. (c) AFM image illustrates a single $PdSe_2$ nanoscroll.

AFM was employed to study $PdSe_2$ before and after transfer to monitor the PSNS formation. The AFM image **Figure 5.2** shows the as-grown bilayer $PdSe_2$ flakes with edge Pd NPs having a thickness in 8 nm. We believe that the edge Pd NPs significantly influenced the scrolling of bilayer $PdSe_2$ from the edges. The van der Waals interaction between the Pd NPs and bilayer $PdSe_2$ is critical in the scrolling process. [28, 29] Our study suggests that $PdSe_2$ is highly active and attached to the surface of Pd NPs. Sliding $PdSe_2$ encounter the Pd NPs, which act as obstructions. The bilayer $PdSe_2$ sheet develops a spontaneous curvature at its edges, which leads to an initial wrapping of the sheet. This wrapping is driven by the minimization of surface energy, where the

edges curl toward the center. As the curling progresses, the nanosheet forms a cylindrical or scroll-like structure by rolling itself up along the edges encapsulating Pd NPs. This allows the $PdSe_2$ nanosheet to form a scroll-like shape. The formation of the scroll minimizes the overall surface energy. A completely rolled-up $PdSe_2$ scroll is energetically favorable because it reduces the exposed edge surface area and stabilizes the structure. Additionally, the presence of topological defects in bilayer $PdSe_2$ is expected to promote the scrolling behavior.[30] A defect can create a weak point where the material is more-likely to roll into a nanoscroll. When atoms are missing from the lattice, it creates a local region of strain. This strain can make the region more flexible, leading to scrolling.

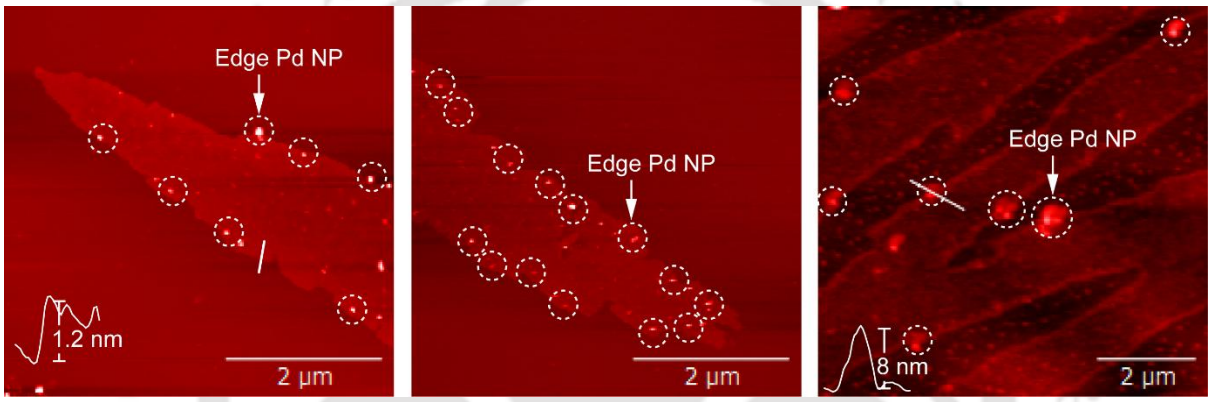

Figure 5.2. AFM showing bilayer $PdSe_2$ with edge Pd NPs.

The AFM image in **Figure 5.3a** demonstrates the rolling up of bilayer $PdSe_2$ from both the edges of a $PdSe_2$ sheet, due to the sliding of water from one end to other in both the directions. **Figure 5.3b** shows a Fish like structure because of faster rolling from the other end. From the evaluation of AFM images of PSNS, we obtain height of 3-4 nm at the curled edges, and 1.2 nm (Confirms the 2L $PdSe_2$) at the middle of the $PdSe_2$ sheet (**Figures 5.3a, 5.3b**). In order to investigate the inner structure of PSNS, transmission electron microscopy (TEM) cross-section is carried out, and the corresponding high-resolution TEM image is shown in **Figure 5.3c**. The adjacent layer distances are measured, and the average $PdSe_2$ layer spacing of 0.44 nm is obtained (**Figure 5.3c**). After keeping the water-treated sample on hotplate for 10 hrs, again AFM height profiles were carried out. Surprisingly, we found that the $PdSe_2$ sheet had turned into a nanoscroll structure (**Figure 5.3d**).

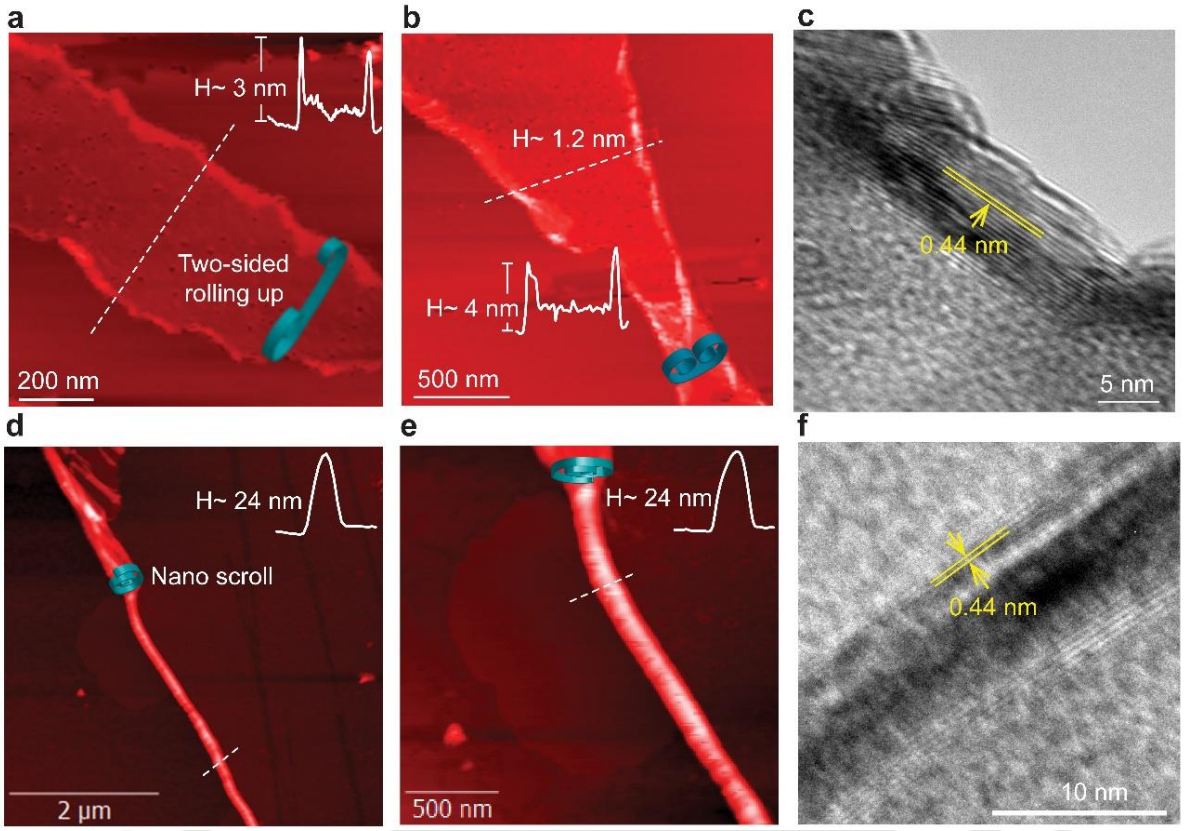

Figure 5.3. (a) AFM image showing two-sided rolling up, which started at both the $PdSe_2$ edges; the edge height is 3 nm. (b) AFM image of a fish like structure, confirming the bilayer $PdSe_2$ sheet at the middle and 4 nm rolling height at the edges. (c) HRTEM image of sidewalls of scrolled $PdSe_2$. (d, e) AFM image of a fully scrolled PSNS; with a thickness of 24 nm. (f) HRTEM image of sidewalls of part of a PSNS.

AFM confirms the height of 24 nm (**Figure 5.3d, 5.3e**) of a PSNS. To clarify this PSNS structure, we transferred it to a TEM grid for the TEM study. The TEM image (**Figure 5.3f**) shows that it possesses a tube-like structure with a hollow core surrounded by thick walls consisting of $PdSe_2$ layers. As shown in **Figure 5.3f**, the interlayer distance between adjacent $PdSe_2$ layers is about 0.44 nm, which is well matched with the reported article [31], confirming the presence of $PdSe_2$ layer at the outer region of the PSNS. The interlayer spacing decreases towards the inner region of the PSNS due to the transition of phase of $PdSe_2$ to Pd_2Se_3 (confirmed in later section). Raman spectra of the PSNS was recorded using 532 nm excitation. The Raman spectra obtained from two spots (spot 1: $PdSe_2$ sheet, spot 2: PSNS) of the optical image are shown in **Figure 5.4a**. **Figure 5.4b** demonstrates the Raman mapping of 147 cm^{-1} mode of PSNS. Raman spectra of spot 1 and spot 2 are given in **Figure 5.4c** (Upper panel: PSNS, Lower panel: 2L $PdSe_2$). We now present the interesting case of PSNS; where we observe a curvature-induced enhancement of 100 cm^{-1} peak,

and also the appearance of a new peak at 125 cm^{-1}. In flat $PdSe_2$, the layers are primarily held together by weak van der Waals forces.

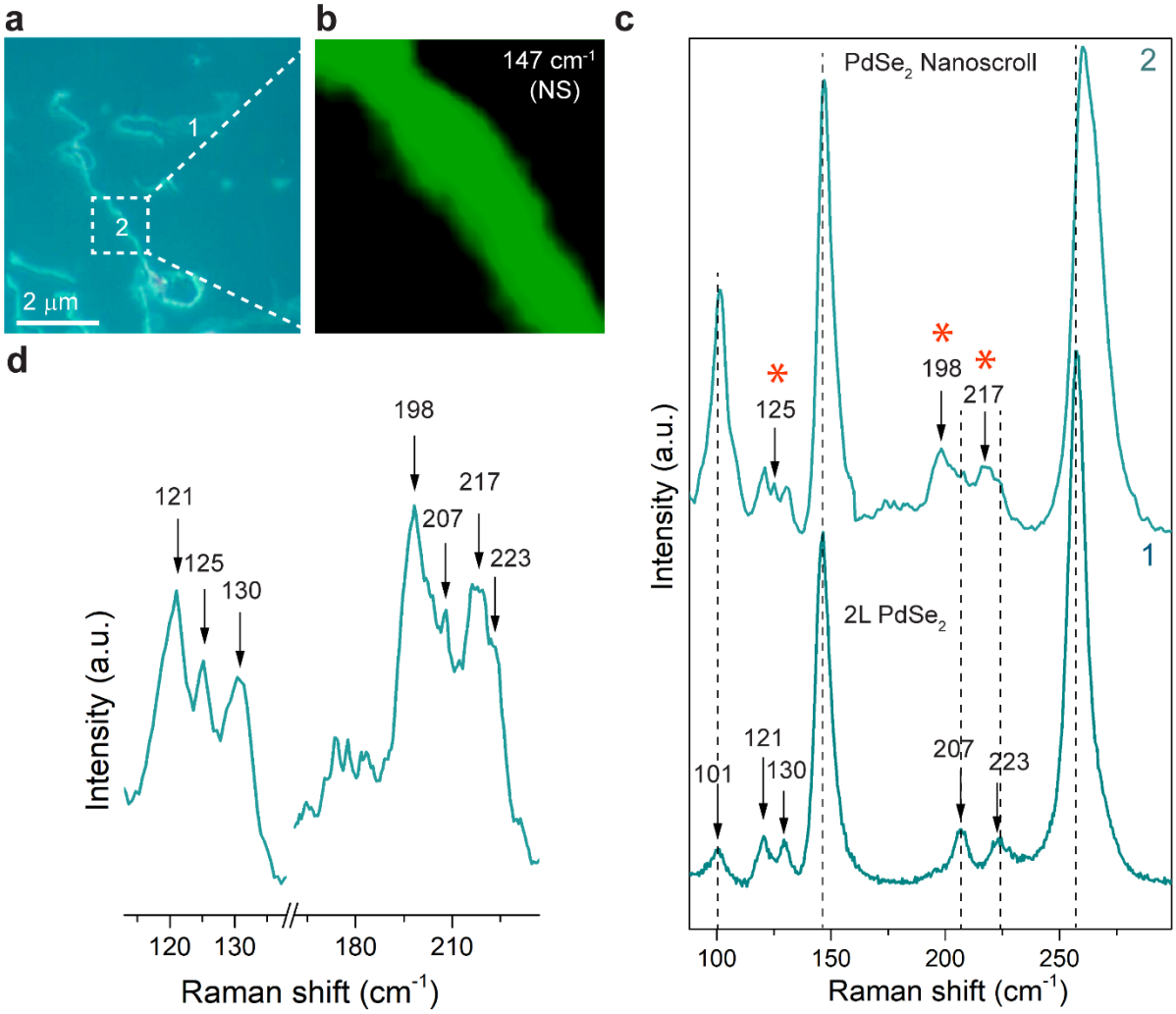

Figure 5.4. (a) Optical image of bilayer $PdSe_2$ (position 1) and PSNS (position 2), (b) 147 cm^{-1} Raman mapping of PSNS, (c) Raman spectra of marked spot 1 and spot 2, (d) PSNS Raman spectra showing extra peak (*) generation.

When $PdSe_2$ undergoes scrolling, the interaction between the layers becomes altered due to the curvature. This can lead to the appearance of new interlayer vibrational modes, which are typically seen at lower frequencies (at 125 cm^{-1}) in the Raman spectrum.The new peak at 125 cm^{-1} can be attributed to the PSNS formation. In addition, we also observe signature of Pd_2Se_3 peaks (198 cm^{-1}, 217 cm^{-1}) (**Figure 5.4d**). Interestingly, the Raman peak of A^1_g and A^3_g modes are also blueshifted; this shift was attributed to the van der Waals interactions between neighboring

nanoscroll layers, which also suggests the decrease in layer number in the nanoscroll. This furthermore advocates the formation of Pd_2Se_3 structure at the inner wall of the PSNS. During the nanoscroll formation a slight tension owing to the bending of the flake provides a strain-induced effect in the Raman spectrum.

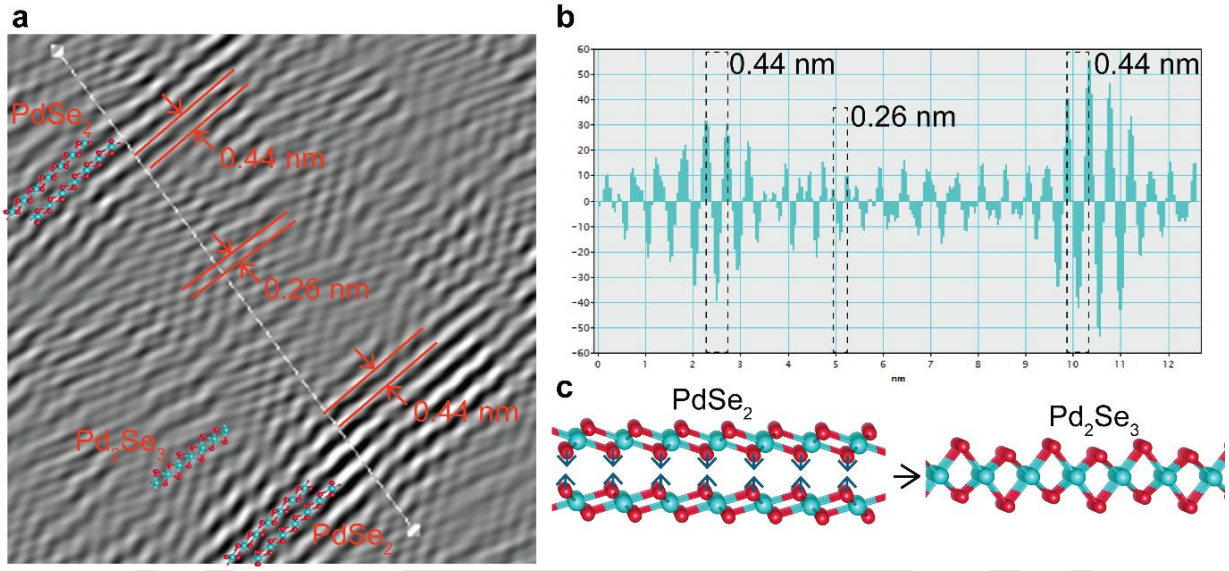

Figure 5.5. (a) HRTEM of a portion of PSNS showing two different regions; $PdSe_2$ and Pd_2Se_3, (b) intensity profile along the dotted white line showing decrease in interlayer spacing at the middle. (c) Schematics shows the interlayer spacing of two consecutive $PdSe_2$ layers decrease results merging into one Pd_2Se_3 layer.

The PSNS structure is further validated by HRTEM studies. **Figure 5.5a** shows the HRTEM image of a typical sample transferred onto a TEM grid after PSNS formation. It can be clearly seen that the PSNS has a tubular structure with interlayer spacing ~0.44 nm. The tubular structure of PSNS can be divided into two zones; (1) Outer zone: the spacing of two consecutive $PdSe_2$ layer is 0.44 nm. (2) Inner Zone: the interlayer spacing decreases from 0.44 nm to 0.26 nm; which indicates the Se atom removal. When the Se atom removal increases, the interlayer distance decreases, providing the foundation for the merging of two $PdSe_2$ layers [32]. The reconstruction of Pd atoms in the two consecutive layers is promoted by the strain owing to the bending induced formation of PSNS. The intensity profile shown in **Figure 5.5b** presented a remarkable drop of intensity at the middle of the PSNS; which also suggests a reduction in atomic density and it corresponds to monolayer Pd_2Se_3 due to the conversion from bilayer $PdSe_2$. A schematic of the reconstruction mechanism from bilayer $PdSe_2$ to monolayer Pd_2Se_3 is given in **Figure 5.5c**.

Figure 5.6a presents a schematic representation showing formation of PSNS from bilayer $PdSe_2$ and PSNS unscrolls after heating as an external stimulus. AFM image in **Figure 5.6b** shows the height of $PdSe_2$ at the middle as 1.2 nm confirming bilayer $PdSe_2$, and at the edge 4 nm confirms scrolling initation from the edge of bilayer $PdSe_2$. **Figure 5.6c** illustrate the $PdSe_2$ nanoscroll with a thickness of 24 nm. After heating the partially unscrolled $PdSe_2$ step height is 9 nm as shown in **Figure 5.6d**. unscrolling of the PSNS was triggered by increasing the temperature to nearly 55 °C in H_2O environment. We observe that the PSNS tends to unscroll through its free outer edge, which is useful for the delivery of cargo in certain specific conditions. One of the highlights of this chapter is that, scrolling and unscrolling process utilizes benign thermo-responsive conditions compatible with cell biology. Here, we exploit 2D $PdSe_2$ towards living cancer cells to monitor its activity.

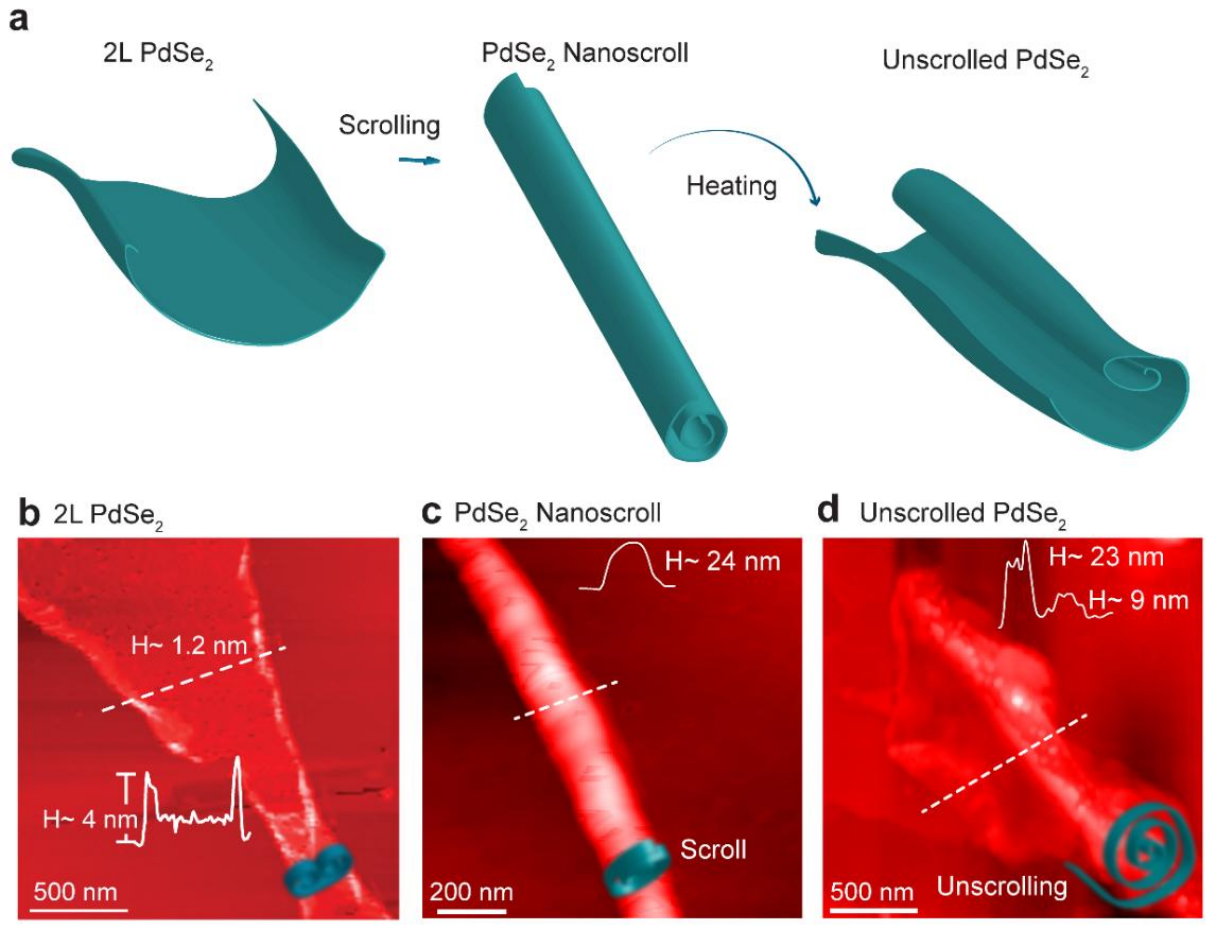

Figure 5.6. (a) Schematic showing the $PdSe_2$ nanoscroll formation from bilayer $PdSe_2$ and unscrolling after heating, AFM image showing the height of $PdSe_2$ (b) at the middle as1.2 nm, and at the edge as 4 nm, (c) $PdSe_2$ nanoscroll thickness: 24 nm, (d) partially unscrolled $PdSe_2$ height: 9 nm and 23 nm after heating.

5.3.1. Raman Spectra of HeLa Cells

Topical advances in Raman spectroscopy have given way to an extensive range of biomedical applications including cancer diagnostics. Its ability to detect variance related to DNA, RNA, proteins, and lipids have made it an excellent tool for differentiating between various cells.[33]The collection of Raman spectra from HeLa cells produces a fingerprint representing the molecular vibrations specific to chemical bonds. The Raman spectra between 500 and 1800 cm^{-1}, is the region of the Raman spectrum, which correlates to the molecular vibrations of biochemical importance. We extend Raman scattering spectroscopy to enable imaging of living cells with high temporal and spatial resolution. By investigating the wavelength dependencies of Raman background signals, we found that 532 nm wavelength excitation is best for Raman imaging and for suppressing the background signals from autofluorescence. **Figure 5.7a** show Raman mapping of PSNS before HeLa cell treatment. 125 cm^{-1}, 147 cm^{-1} and 258 cm^{-1} mapping confirms the formation of PSNS. 258 cm^{-1} mapping shows that it comes mostly from the edge of the PSNS. Due to the bending, the 258 cm^{-1} mode is more active at the curved edges. **Figure 5.7b** shows the Raman spectra of HeLa cells on PSNS. 141 cm^{-1} and 253 cm^{-1} suggests the presence of HeLa cell on PSNS. Again, the Raman mappings at 125 cm^{-1} and 141 cm^{-1} confirms the PSNS. The spectral region between 1000 cm^{-1} and 1200 cm^{-1} are due to C–C stretching vibrations. 1443 cm^{-1} is due to C–H_2 bending. The 1578 cm^{-1} band arises from the stretch vibration of the carotenoid's C=C in the carbohydrate.[34] The 1659 cm^{-1} band comes from C=C stretching mode in unsaturated fatty acids.[35] One of the advantages of Raman microscopy is its capability for label-free imaging by detecting vibrations of molecules. We follow the response of HeLa cells to the PSNS, which is provided by Raman mapping. Raman maps enabled us to distinguish the clear difference between PSNS before and after HeLa cell treatment. After treatment, the intensity of 125 cm^{-1} and 141 cm^{-1} is not symmetric all over the PSNS, which is due to the exit window for Pd NPs removal. The Raman mappings between 800-1100 cm^{-1} and 1100-1620 cm^{-1} suggests that more HeLa cells are attached on the PSNS region, where the brighter Raman mapping is coming from the PSNS hotspot regions.[36]

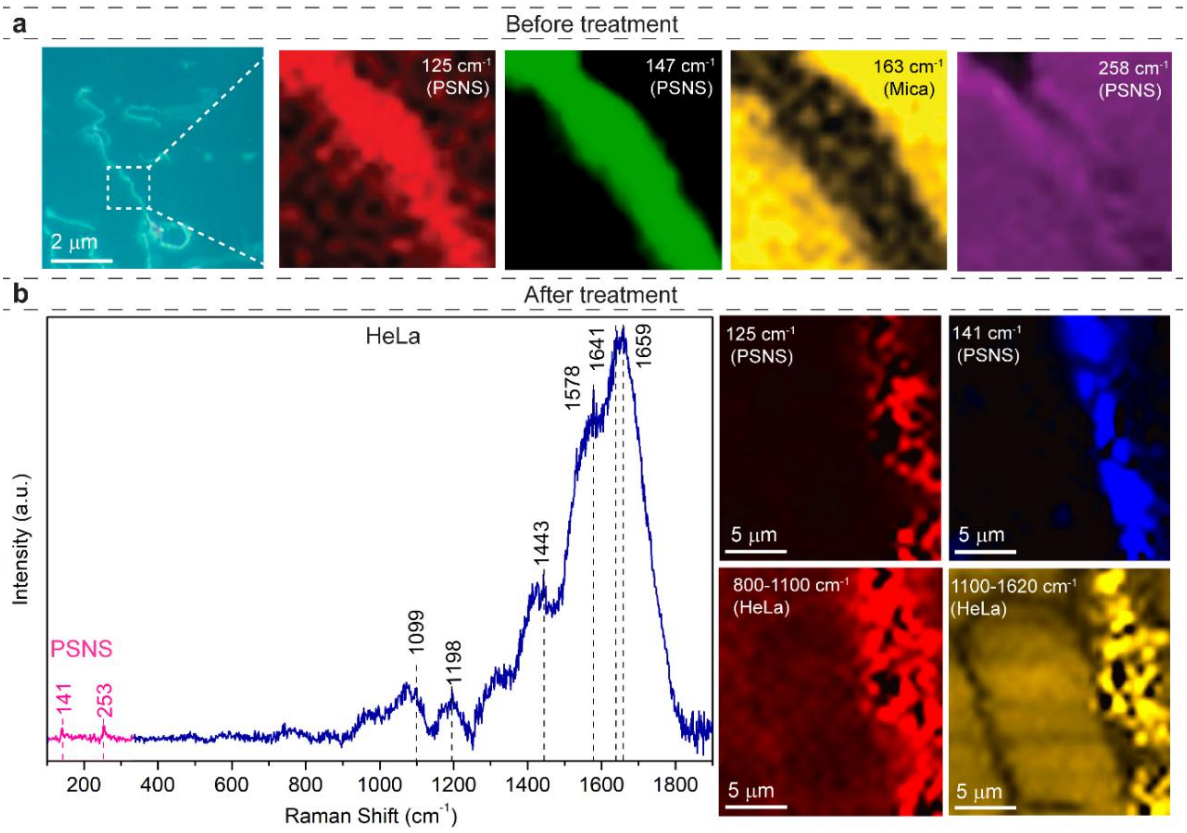

Figure 5.7. (a) Optical image of Raman mapping of PSNS region, and its corresponding Raman mapping before cell treatment. 125 cm^{-1}, 147 cm^{-1}, and 258 cm^{-1} mapping confirms the formation of PSNS. 163 cm^{-1} shows the mapping of mica substrate. (b) Raman spectra of HeLa cell on PSNS, and its corresponding mappings after treatment.

5.3.2. Apoptosis of HeLa Cell

The AFM mapping of HeLa cell, a HeLa cell trapped inside a PSNS and an apoptotic cell are shown in **Figure 5.8a, b** and **c** respectively. **Figure 5.8d** shows the FESEM image of apoptotic HeLa cell, where Pd NPS are present at the nucleus of the cell. To further confirm the presence of Pd NPs, we have verified the TEM image of PSNS. The TEM image (**Figure 5.8e**) also shows that the cell is attached to the PSNS and the encircled Pd NPs residing on the nucleus of the cell. The schematic of apoptosis of cell lead by PSNS is shown in **Figure 5.8f**, where Pd NPs from PSNS enter the cell and then attack the nucleus, leading to cell apoptosis.

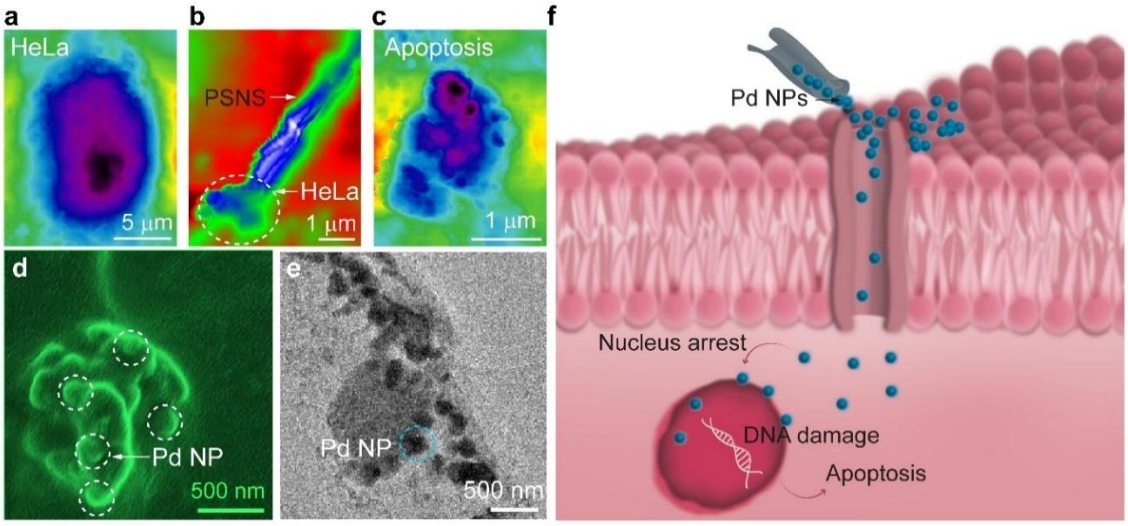

Figure 5.8. AFM mapping of (a) HeLa cell, (b) HeLa cell trapped inside a PSNS, (c) Apoptotic cell. (d) FESEM image of apoptotic cell, showing Pd NPs inside cell, (e) TEM image of cell, surrounded by Pd NPs. (f) schematic showing apoptosis of cell lead by PSNS through the insertion of Pd NPs into the cell.

5.3.3. Raman Spectra of A549 Cells after PSNS treatment

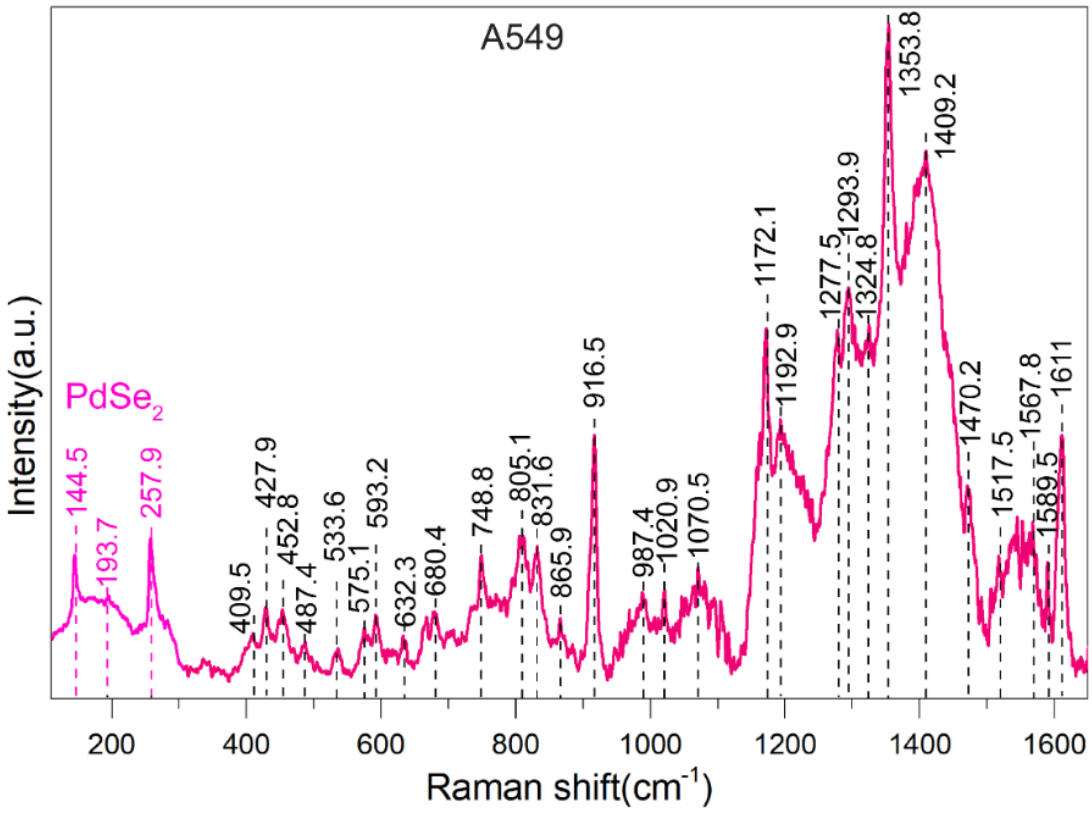

Figure 5.9. Raman spectra of A549 cell after treating with PSNS.

The Raman spectra of A549 cells have been shown in **Figure 5.9**, after treating with PSNS. 144.5 cm^{-1}, 193 cm^{-1}, 257.9 cm^{-1} modes confirm the presence of PSNS. However, strong Raman signals of A549 cells can be observed in PSNS. Cytochrome c, a key protein that is being increasingly recognized as an important factor, triggers various processes in cancer development.[38, 39] The Raman spectra of cytochrome c at 748 cm^{-1} and 1589 cm^{-1} of A549 cell are two sensitive indicators of cancer aggressiveness.

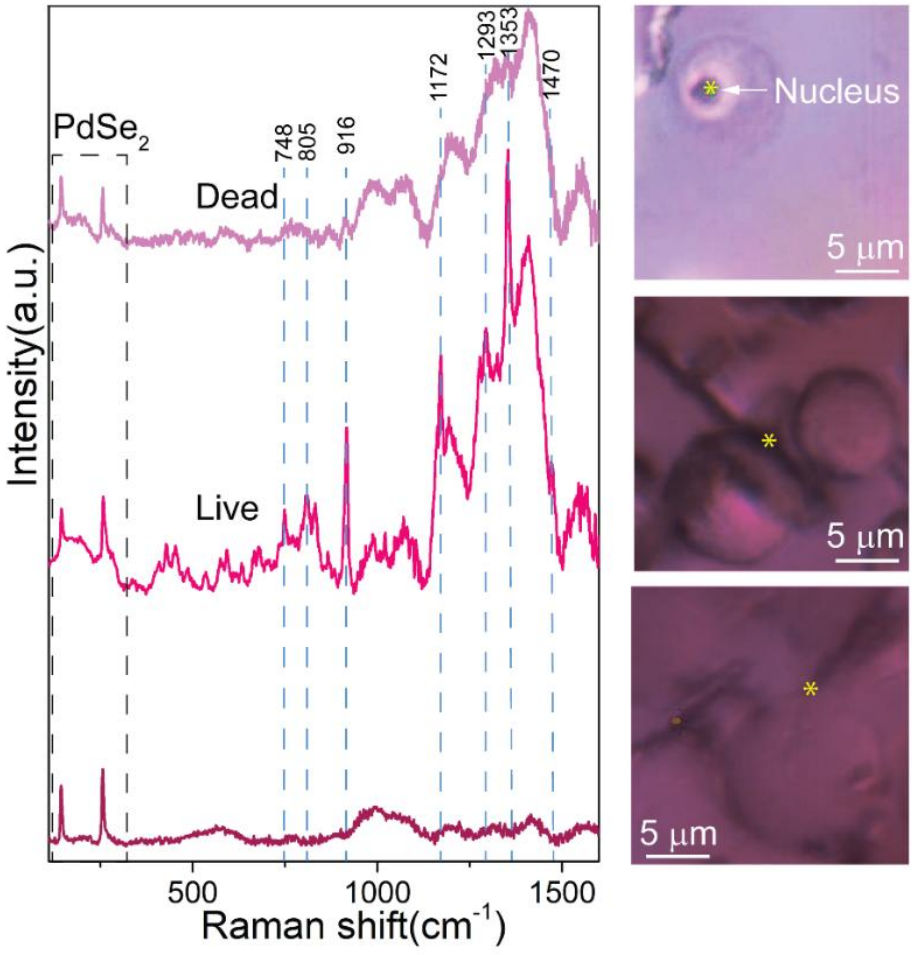

Figure 5.10. Raman spectra and the corresponding optical images of A549 cell at different time intervals after treating with PSNS.

Figure 5.10 provides the Raman spectra and the corresponding positions in the optical images of A549 cell attachment to the PSNS. SERS characteristic peak at 805 cm^{-1} assigned to RNA, decreased significantly from normal to the dead cells. Important differences associated with activated cell are also observed in the region 1100-1360 cm^{-1}. This region corresponds to vibrations

of adenine and guanine overlapped with vibrations corresponding to proteins and lipids. The peaks at 916 cm^{-1}, 1172 cm^{-1}, 1353 cm^{-1} decreased significantly in dead cells. The following peaks undergo a large decrease in the spectrum of dead cells compared to viable cells and can be used as markers of cell death: 748 cm^{-1}, 916 cm^{-1}, 1172 cm^{-1}, 1293 cm^{-1}, 1353 cm^{-1}, 1470 cm^{-1}. Raman spectrum of A549 cell from all its cellular components such as proteins, lipids, nucleic acids, and carbohydrates as provided in **Table 5.1**.

Table 5.1. Peak assignment for the Raman spectrum of A549 cells (ref[37])

Raman peak position (cm^{-1})	Tentative assignment of Raman peak position			
	DNA/RNA	Proteins	Lipids	Carbohydrates
632	–	C–C twist Phe	–	–
680	T, G	–	–	–
748	Cytochrome c	Ring br. Trp	–	–
805	O–P–O str. RNA		O–P–O	–
831	O–P–O asym. str.	Out of plane ring br. Tyr	–	–
865	–	Ring br. Tyr	–	–
916	BK, deoxyrib.	–	–	–
987	–	–	C–C head groups	–
1020	C–O deoxyrib.	–		–
1070	–	C–N str.	Chain C=C str.	–
1172	–	C–H in-plane bend Tyr	–	–
1277	T, A	Amide III	=CH bend	–
1293	–	Amide III ∝ helix	=CH defects	–
1324	G	CH defects	–	–
1353	A, G	CH defects	–	–
1409	–	COO^- stretch for Asp Glu.	–	–
1470	G, A	CH defects	CH defects	CH defects
1567	G, A	–	–	–
1589	–	C=N	–	–
1611	–	C=C Phe, Trp	–	–

5.3.4. Cell migration by filopodia and retraction process of Pd NPs

Filopodia have an important role in cell migration that function as tentacles for cells to probe their environment. Rich in filopodia is a characteristic of invasive cancer cells. Proliferation in A549 cancer cells is observed in **Figures 5.11a** and **5.11b**. Studying the mechanisms governing A549 cell proliferation provides insight into potential therapeutic strategies for treating lung cancer.

Figures 5.11c and **5.11d** demonstrate that filopodia are finger-like projections extending from the plasma membrane of A549 cells, composed of bundles of actin filaments. Cell body containing microvilli with numerous filopodia (**Figure 5.11c-h**), evidences their viability and potential for proliferation and migration. Here, filopodia are involved in the early steps of migration which is essential for cell movement and sensing the environment. They allow cells to detect gradient of extracellular signals that guide cancer cell movement towards the PSNS. The gradient of extracellular signals promotes both forward movement and mechanical stability required for migration of the cell.

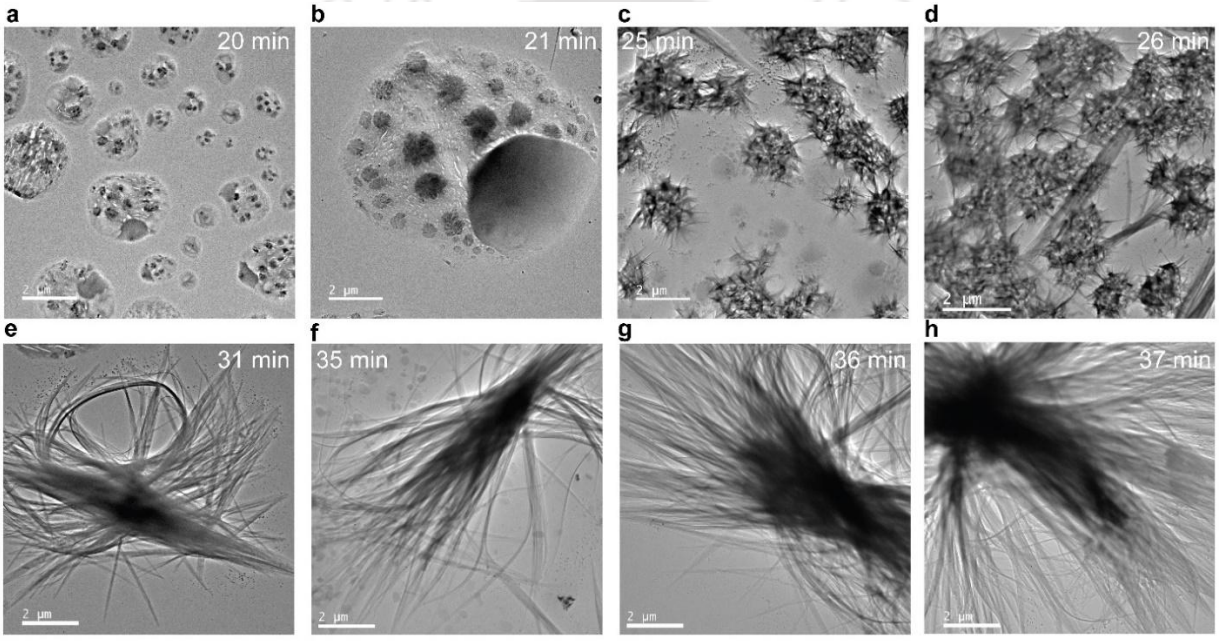

Figure 5.11. (a, b) Cell division of cancer cells. (c, d, e, f, g, h) Time-lapse images showing numerous filopodia growth. During this sequence of 37 minutes, filopodial elongation and movement can be seen.

The filopodia extensions of the cells can be seen adhering to the PSNS. **Figure 5.12a** shows the schematic of the retraction process of Pd NPs towards the cell. Pd NPs, their internalization and further consequences to the cells were determined using TEM. TEM examinations showed that both Pd NPs were internalized extensively. Several filopodia explore the Pd NPs encapsulated PSNS environment (**Figure 5.12b**). After finding a Pd NP, the filopodia bind to it and then retract towards the cell body (**Figure 5.12b, 5.12c**). Filopodia acts as cellular tentacles and after a few seconds binds to Pd NPs, then filopodia retract and pull the bound Pd NPs toward the cell.[40]

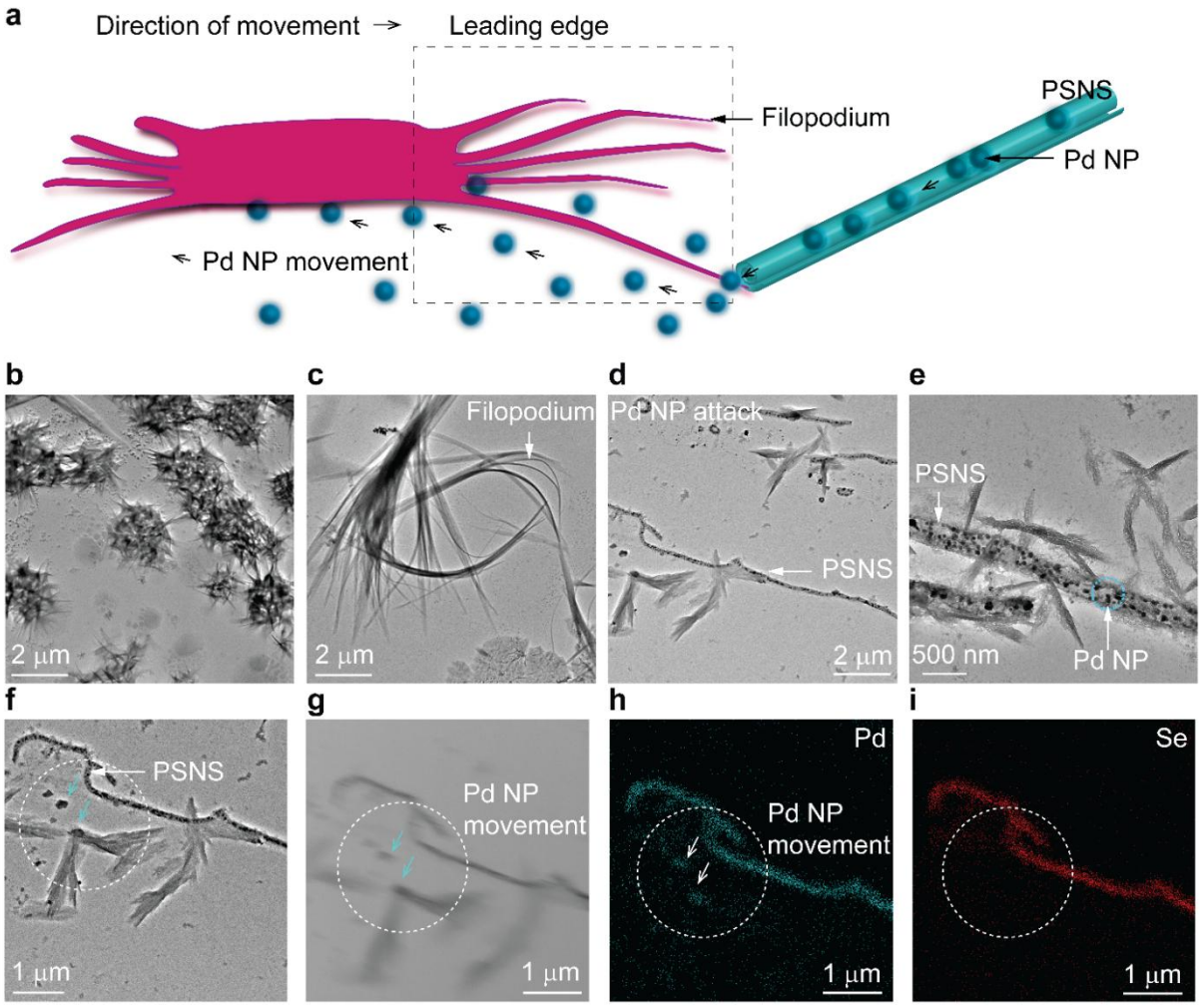

Figure 5.12. (a) Tracing of Pd NPs towards the cell. (b, c) Several filopodia explore the Pd NPs encapsulated PSNS environment. (d, e), (f, g) Pd NPs movement from the PSNS towards the cell, corresponding (h) Pd mapping shows the Pd NPs movement towards the nucleus, (i) Se mapping shows no Se movement towards the nucleus.

Cancer cells have increased negative charges on the glycocalyx, due to the presence of sialic acid residues making them more electronegative than normal cells. The negative charges move towards the non-bonded Pd of PSNS and Pd NPs efflux from the PSNS towards the cell surface induces n-doping on $PdSe_2$ surface (consistent with the observation of Raman peak shift from 147 to 144.5 cm^{-1}).[41] Surprisingly, a large number of Pd NPs continuously move towards the cell wall of cancer cell (**Figure 5.12e-h**). The physiochemical connections of Pd NPs with the nitrogen bases, phosphate groups of DNA and protein, the production of free radicals, results the disruption of the cell. [69] Upon binding with Pd NPs, filopodia would become inactive. Pd NPs penetrated the cells, induced breakage of filopodia in turn trigger cell death. Pd NPs movement started from the

PSNS towards the cancer cell. The Pd mapping confirms the migration of Pd NPs to the cancer cell (**Figure 5.12h**). The Se mapping in **Figure 5.12i** confirms that there is no movement of Se towards the cell.

5.3.5. Cell viability test

Monolayers cultures of HeLa cells were treated with varying concentration of Pd NPs and PSNS. The dose-dependent decrease in cell viability has been observed in **Figure 5.13**. Inhibitory Concentration (IC_{50}) has been determined from the sigmoidal dose-response curve generated using GraphPad prism software. IC_{50} for Pd NPs was found to be 72.38 µM. However, the concentration we used for studying cell viability for the PSNS thin film were not enough to achieve the IC_{50} value. The cell viability was measured by the following equation-

$$\textbf{\% of cell viability} = \frac{(A560-A600)Sample}{(A560-A600)Control} \times 100$$

From the viability calculations, it was found that PSNS are more cytotoxic than Pd NPs at lower concentrations. Surprisingly, Pd NPs are more cytotoxic than PSNS at higher concentrations.

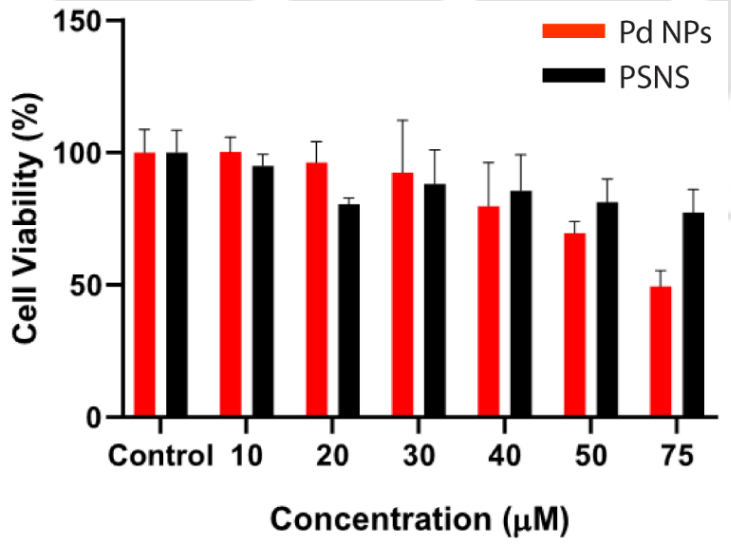

Figure 5.13 Assessment of viability of HeLa cells upon treatment with Pd NPs and PSNS.

5.4. Conclusion

In summary, we have demonstrated the synthesis technique of PSNS from the bilayer $PdSe_2$ sheet. The scrolling does not require multiple processing steps or any polymer coatings that could affect the physical properties of $PdSe_2$. We have created PSNS by providing $PdSe_2$ sheet with a normal force sufficient to overcome the interfacial adhesion in a H_2O environment. The PSNS are started to initiate from the edges of the bilayer $PdSe_2$ sheet. The conversion of $PdSe_2$ into PSNS via Pd NPs and unscrolling into sheet structures are fully controlled under H_2O environment. The PSNS is further treated with A549 and HeLa cancer cells. The Pd NPs from the PSNS moved towards the cancer cell to attack the nucleus. The cell viability test of PSNS suggests that PSNS is a potential candidate in the field of biomedical applications. We expect that our study will stimulate future experimental effort to create PSNS and such scrolled $PdSe_2$ may lead to novel properties that have yet to be explored. Our results suggest a much richer potential to fabricate nanoscrolls from $PdSe_2$ and other two-dimensional materials.

References

1. Li, H., Papadakis, R., Jafri, S. H. M., Thersleff, T., Michler, J., Ottosson, H., & Leifer, K. (2018). Superior adhesion of graphene nanoscrolls. Communications Physics, 1(1). https://doi.org/10.1038/s42005-018-0043-2.
2. Xie, X., Ju, L., Feng, X., Sun, Y., Zhou, R., Liu, K., Fan, S., Li, Q., & Jiang, K. (2009). Controlled Fabrication of High-Quality Carbon Nanoscrolls from Monolayer Graphene. Nano Letters, 9(7), 2565–2570 https://doi.org/10.1021/nl900677y
3. Zheng, J., Liu, H., Wu, B., Guo, Y., Wu, T., Yu, G., Liu, Y., & Zhu, D. (2011). Production of High-Quality Carbon Nanoscrolls with Microwave Spark Assistance in Liquid Nitrogen. Advanced Materials, 23(21), 2460–2463https://doi.org/10.1002/adma.201004759
4. Viculis, L. M., Mack, J. J., & Kaner, R. B. (2003). A Chemical Route to Carbon Nanoscrolls. Science, 299(5611), 1361https://doi.org/10.1126/science.1078842
5. Rurali, R., Coluci, V. R., & Galvão, D. S. (2006). Prediction of giant electroactuation for papyruslike carbon nanoscroll structures: First-principles calculations. Physical Review B, 74(8). https://doi.org/10.1103/physrevb.74.085414.
6. Sharifi, T., Gracia-Espino, E., Barzegar, H. R., Jia, X., Nitze, F., Hu, G., Nordblad, P., Tai, C., & Wågberg, T. (2013). Formation of nitrogen-doped graphene nanoscrolls by adsorption of magnetic γ-Fe2O3 nanoparticles. Nature Communications, 4(1). https://doi.org/10.1038/ncomms3319.
7. Aftab, S., Iqbal, M. Z., & Rim, Y. S. (2022). Recent Advances in Rolling 2D TMDs Nanosheets into 1D TMDs Nanotubes/Nanoscrolls. Small, 19(1). https://doi.org/10.1002/smll.202205418.
8. Qian, Q., Zu, R., Ji, Q., Jung, G. S., Zhang, K., Zhang, Y., Buehler, M. J., Kong, J., Gopalan, V., & Huang, S. (2020). Chirality-Dependent Second Harmonic Generation of MoS2 Nanoscroll with Enhanced Efficiency. ACS Nano, 14(10), 13333–13342. https://doi.org/10.1021/acsnano.0c05189.
9. Deng, W., You, C., Chen, X., Wang, Y., Li, Y., Feng, B., Shi, K., Chen, Y., Sun, L., & Zhang, Y. (2019). High-Performance Photodiode Based on Atomically Thin WSe2/MoS2 Nanoscroll Integration. Small, 15(30). https://doi.org/10.1002/smll.201901544.
10. Cui, X., Kong, Z., Gao, E., Huang, D., Hao, Y., Shen, H., Di, C., Xu, Z., Zheng, J., & Zhu, D. (2018). Rolling up transition metal dichalcogenide nanoscrolls via one drop of ethanol. Nature Communications, 9(1). https://doi.org/10.1038/s41467-018-03752-5.
11. Zhao, Y., You, H., Li, X., Pei, C., Huang, X., & Li, H. (2022). Solvent-Free Preparation of Closely Packed MoS2 Nanoscrolls for Improved Photosensitivity. ACS Applied Materials & Interfaces, 14(7), 9515–9524. https://doi.org/10.1021/acsami.1c24291.
12. Su, J., Li, X., Xu, M., Zhang, J., Liu, X., Zheng, X., Shi, Y., & Zhang, Q. (2023). Enhancing Photodetection Ability of MoS2 Nanoscrolls via Interface Engineering. ACS Applied Materials & Interfaces, 15(2), 3307–3316. https://doi.org/10.1021/acsami.2c18537.
13. Wang, R., Guo, S., Li, Z., Weller, D., Quan, S., Yu, J., Wu, M., Jiang, J., Wang, Y., & Liu, R. (2022). Strong Anisotropic Optical Properties by Rolling up MoS2 Nanoflake. The Journal of Physical Chemistry Letters, 13(36), 8409–8415. https://doi.org/10.1021/acs.jpclett.2c02072.
14. Meng, J., Wang, G., Li, X., Lu, X., Zhang, J., Yu, H., Chen, W., Du, L., Liao, M., Zhao, J., Chen, P., Zhu, J., Bai, X., Shi, D., & Zhang, G. (2016). Rolling Up a Monolayer MoS2Sheet. Small, 12(28), 3770–3774. https://doi.org/10.1002/smll.201601413.
15. Ghosh, R., Singh, M., Chang, L. W., Lin, H., Chen, Y. S., Muthu, J., Papnai, B., Kang, Y. S., Liao, Y., Bera, K. P., Guo, G., Hsieh, Y., Hofmann, M., & Chen, Y. (2022). Enhancing the Photoelectrochemical Hydrogen Evolution Reaction through Nanoscrolling of Two-Dimensional

Material Heterojunctions. ACS Nano, 16(4), 5743–5751. https://doi.org/10.1021/acsnano.1c10772.

16. Dhar, P., Gaur, S. S., Kumar, A., & Katiyar, V. (2018). Cellulose Nanocrystal Templated Graphene Nanoscrolls for High Performance Supercapacitors and Hydrogen Storage: An Experimental and Molecular Simulation Study. Scientific Reports, 8(1). https://doi.org/10.1038/s41598-018-22123-0.
17. Pallaoro, A., Hoonejani, M. R., Braun, G. B., Meinhart, C. D., & Moskovits, M. (2015). Rapid Identification by Surface-Enhanced Raman Spectroscopy of Cancer Cells at Low Concentrations Flowing in a Microfluidic Channel. ACS Nano, 9(4), 4328–4336. https://doi.org/10.1021/acsnano.5b00750.
18. Kennedy, L. C., Bickford, L. R., Lewinski, N. A., Coughlin, A. J., Hu, Y., Day, E. S., West, J. L., & Drezek, R. A. (2010). A New Era for Cancer Treatment: Gold-Nanoparticle-Mediated Thermal Therapies. Small, 7(2), 169–183. https://doi.org/10.1002/smll.201000134.
19. Xiao, J., Fan, S., Wang, F., Sun, L., Zheng, X., & Yan, C. (2014). Porous Pd nanoparticles with high photothermal conversion efficiency for efficient ablation of cancer cells. Nanoscale, 6(8), 4345–4351. https://doi.org/10.1039/c3nr06843a.
20. Nasrollahzadeh, M., Sajjadi, M., Shokouhimehr, M., & Varma, R. S. (2019). Recent developments in palladium (nano)catalysts supported on polymers for selective and sustainable oxidation processes. Coordination Chemistry Reviews, 397, 54–75. https://doi.org/10.1016/j.ccr.2019.06.010.
21. MubarakAli, D., Kim, H., Venkatesh, P. S., Kim, J., & Lee, S. (2022). A Systemic Review on the Synthesis, Characterization, and Applications of Palladium Nanoparticles in Biomedicine. Applied Biochemistry and Biotechnology, 195(6), 3699–3718. https://doi.org/10.1007/s12010-022-03840-9.
22. Bakuru, V. R., Velaga, B., Peela, N. R., & Kalidindi, S. B. (2018). Hybridization of Pd Nanoparticles with UiO-66(Hf) Metal-Organic Framework and the Effect of Nanostructure on the Catalytic Properties. Chemistry - a European Journal, 24(60), 15978–15982. https://doi.org/10.1002/chem.201803200.
23. Yaqoob, S. B., Adnan, R., Khan, R. M. R., & Rashid, M. (2020). Gold, Silver, and Palladium Nanoparticles: A Chemical Tool for Biomedical Applications. Frontiers in Chemistry, 8. https://doi.org/10.3389/fchem.2020.00376.
24. Al-Fakeh, M. S., Osman, S. O. M., Gassoumi, M., Rabhi, M., & Omer, M. (2021). Characterization, Antimicrobial and Anticancer Properties of Palladium Nanoparticles Biosynthesized Optimally Using Saudi Propolis. Nanomaterials, 11(10), 2666. https://doi.org/10.3390/nano11102666.
25. Zhao, R., Xiang, J., Wang, B., Chen, L., & Tan, S. (2022). Recent Advances in the Development of Noble Metal NPs for Cancer Therapy. Bioinorganic Chemistry and Applications, 2022(1). https://doi.org/10.1155/2022/2444516.
26. Kang, S., Shin, W., Kang, K., Choi, M., Kim, Y., Kim, Y., Min, D., & Jang, H. (2018). Revisiting of Pd Nanoparticles in Cancer Treatment: All-Round Excellence of Porous Pd Nanoplates in Gene-Thermo Combinational Therapy. ACS Applied Materials & Interfaces, 10(16), 13819–13828. https://doi.org/10.1021/acsami.8b01000.
27. Gurunathan, S., Kim, E., Han, J., Park, J., & Kim, J. (2015). Green Chemistry Approach for Synthesis of Effective Anticancer Palladium Nanoparticles. Molecules, 20(12), 22476–22498. https://doi.org/10.3390/molecules201219860.
28. Song, J., Xia, X., Chen, J., Xia, D., Xue, Q., Li, Q., & Dong, M. (2020). Folding 2D Graphene Nanoribbons into 3D Nanocages Induced by Platinum Nanoclusters. The Journal of Physical Chemistry C, 124(19), 10495–10501. https://doi.org/10.1021/acs.jpcc.0c00463.

29. Berman, D., Deshmukh, S. A., Sankaranarayanan, S. K. R. S., Erdemir, A., & Sumant, A. V. (2015). Macroscale superlubricity enabled by graphene nanoscroll formation. Science, 348(6239), 1118–1122. https://doi.org/10.1126/science.1262024.
30. Fu, M., Liang, L., Zou, Q., Nguyen, G. D., Xiao, K., Li, A., Kang, J., Wu, Z., & Gai, Z. (2019b). Defects in Highly Anisotropic Transition-Metal Dichalcogenide PdSe2. The Journal of Physical Chemistry Letters, 11(3), 740–746. https://doi.org/10.1021/acs.jpclett.9b03312.
31. Zeng, L., Wu, D., Lin, S., Xie, C., Yuan, H., Lu, W., Lau, S. P., Chai, Y., Luo, L., Li, Z., & Tsang, Y. H. (2018). Controlled Synthesis of 2D Palladium Diselenide for Sensitive Photodetector Applications. Advanced Functional Materials, 29(1). https://doi.org/10.1002/adfm.201806878.
32. Lin, J., Zuluaga, S., Yu, P., Liu, Z., Pantelides, S. T., & Suenaga, K. (2017b). Novel Pd2Se3 Two-Dimensional Phase Driven by Interlayer Fusion in Layered PdSe. Physical Review Letters, 119(1). https://doi.org/10.1103/physrevlett.119.016101.
33. Levchenko, S. M., & Qu, J. (2018). Biomolecular Component Analysis of Phospholipids Composition in Live HeLa Cells. Biosensors, 8(4), 123. https://doi.org/10.3390/bios8040123.
34. Qi, 齐. J., Liu, 刘. B., Li, 李. Y., Wu, 吴. D., & Tang, 唐. W. (2009). Raman spectroscopic study on Hela cells irradiated by X rays of different doses. Chinese Optics Letters, 7(8), 734–737. https://doi.org/10.3788/col20090708.0734.
35. De Gelder, J., De Gussem, K., Vandenabeele, P., & Moens, L. (2007). Reference database of Raman spectra of biological molecules. Journal of Raman Spectroscopy, 38(9), 1133–1147. https://doi.org/10.1002/jrs.1734.
36. Yamakoshi, H., Dodo, K., Okada, M., Ando, J., Palonpon, A., Fujita, K., Kawata, S., & Sodeoka, M. (2011). Imaging of EdU, an Alkyne-Tagged Cell Proliferation Probe, by Raman Microscopy. Journal of the American Chemical Society, 133(16), 6102–6105. https://doi.org/10.1021/ja108404p.
37. Arya, J. S., Joseph, M. M., Sherin, D. R., Nair, J. B., Manojkumar, T. K., & Maiti, K. K. (2019). Exploring Mitochondria-Mediated Intrinsic Apoptosis by New Phytochemical Entities: An Explicit Observation of Cytochrome c Dynamics on Lung and Melanoma Cancer Cells. Journal of Medicinal Chemistry, 62(17), 8311–8329. https://doi.org/10.1021/acs.jmedchem.9b01098.
38. Abramczyk, H., Brozek-Pluska, B., & Kopeć, M. (2022). Double face of cytochrome c in cancers by Raman imaging. Scientific Reports, 12(1). https://doi.org/10.1038/s41598-022-04803-0.
39. Wallace, D. C. (2012). Mitochondria and cancer. Nature Reviews. Cancer, 12(10), 685–698. https://doi.org/10.1038/nrc3365.
40. Mattila, P. K., & Lappalainen, P. (2008). Filopodia: molecular architecture and cellular functions. Nature Reviews Molecular Cell Biology, 9(6), 446–454. https://doi.org/10.1038/nrm2406.
41. Keisham, B., Cole, A., Nguyen, P., Mehta, A., & Berry, V. (2016). Cancer Cell Hyperactivity and Membrane Dipolarity Monitoring via Raman Mapping of Interfaced Graphene: Toward Non-Invasive Cancer Diagnostics. ACS Applied Materials & Interfaces, 8(48), 32717–32722. https://doi.org/10.1021/acsami.6b12307.

Chapter 6 - Layer-dependent Raman studies and strain-induced phase transition of bilayer $PdSe_2$ to Pd_2Se_3

Strain engineering plays a vital role in condensed matter physics and materials science because it can strongly modify the mechanical, electrical, and optical properties of a material and even induce a structural phase transition. Strain effects are fascinating in atomically thin two-dimensional (2D) layered materials. Most 2D layered materials, such as graphene and TMDs, whose layers interact with each other through van der Waal forces, don't change the phase while applying strain in the presence of defects. While in the case of defect rich $PdSe_2$, we show that strain engineering efficiently reduces the distance between layers, causing the melding of two layers into one, resulting in the formation of the new Pd_2Se_3 phase. Each phase has a separate and unique application as the band gap changes from indirect to quasi-direct. Here, we develop scotch tape and water-assisted transfer methods to transfer the as-grown $PdSe_2$ film from the growth substrate to a flexible substrate. The scotch tape assisted exfoliation doesn't directly affect the internal atomic structure of the defect rich $PdSe_2$ but it weakens the layer-to-layer interaction during the peeling process. When strain is applied to the scotch tape assisted exfoliated $PdSe_2$, strain can change the distance between the two $PdSe_2$ layers which cause local deformation that can push the layers closer. Strain causes the defect rich $PdSe_2$ layers to come into closer proximity, this may cause form strong interlayer interactions, leading to fusion of the layers. This can facilitate the merging of two $PdSe_2$ layers to Pd_2Se_3. We discover the phase evolution of the van der Waals $PdSe_2$ layer to Pd_2Se_3 under the uniaxial tensile strain of > 0.5 % in the case of water-assisted transfer and of > 0.2 % in the case of scotch tape transfer. The precise strain engineering can evolve the $PdSe_2$ layer into a Pd_2Se_3 probed by Raman fingerprints. This unique strain-induced phase modulation property enables the application of ultrathin $PdSe_2$ as a future strain sensor.

6.1. Introduction

Phase transitions of transition metal dichalcogenides (TMDs) have been achieved mostly by doping and alloying with the parent material.[1-5] Two-dimensional palladium diselenide $PdSe_2$, a star in the NTMD family has exceptional properties, which in the presence of defects, triggers the melding of two layers resulting in the formation of a new phase, Pd_2Se_3.[6] $PdSe_2$ exhibits layer dependent bandgap but the monolayer doesn't exist. The Se-loss thinning process of $PdSe_2$

driven by mechanical exfoliation and using the electron beam of a scanning transmission electron microscope, bring out a new phase; Pd_2Se_3.[6-11] Creating Se vacancies in $PdSe_2$ few layered films using in-situ controlled thermal annealing first leads to defective $PdSe_2$, then a phase change to a stable Se deficient form of $PdSe_{2-x}$, and finally to Pd metal.[10] On the other hand, while the chemical stoichiometry does not change with a reduction in layer numbers for most of the 2D layered materials, the multilayer Pd_2Se_3 changes its stoichiometry to $PdSe_2$ in the bilayer form under Se-rich growth conditions. Pd_2Se_3 is also an emerging 2D thermoelectric material that shows higher efficiency than other monolayer TMDs.[12] Pd_2Se_3 monolayer with a quasi-direct band gap (1.39 eV) [13], and carrier mobility of 178.02 $cm^2 V^{-1}s^{-1}$, is expected to show excellent anisotropic transport properties making it a promising material for optoelectronic devices and next-generation electronics due to their high electron mobility and excellent air stability.[14]

To date, strain engineering on ultrathin materials offers many unique properties. For example, applying uniaxial strain can evolve an indirect gap semiconductor to a direct band gap semiconductor. Recently, Luo et al. reported the anisotropic phonon behaviour of strained $PdSe_2$. [15] However, they did not observe the phase evolution, which could be attributed to the higher crystal quality of the ultrathin samples prepared via the exfoliation from bulk $PdSe_2$. The experimental investigations on the phonon response of strained $PdSe_2$ grown via the CVD method are still lacking, which is crucial for integrating few-layer $PdSe_2$ into flexible electronic devices and strain sensors.

6.2. Experimental section

6.2.1. Sample Preparation

Ultrathin $PdSe_2$ layers were first grown on mica via CVD following chapters 2. Bilayer $PdSe_2$ flakes were synthesized following a two-step CVD synthesis process, (i) Solution preparation, (ii) Low-temperature CVD growth. First, $PdCl_2$ powder (99.999%), Se powder purchased from Sigma Aldrich, and NaCl powder (> 99.0 %, Merck) were used for experiments without further purification. 7.6×10^{-3} mol L^{-1} $PdCl_2$ was first added into 20 mL distilled water. Na_2PdCl_4 solution was prepared by mixing and dissolving 3 mg of NaCl with the $PdCl_2$ solution, which undergoes vigorous stirring (180 r/min) for about 45 min at room temperature using a magnetic stirrer. After ultrasonic irradiation of the final 10.17×10^{-3} mol L^{-1} Na_2PdCl_4 solution for 3 hrs, the color of the

solution turned from initial pale yellow to dark brown. This observation indicates the reduction of Pd (II) ions to palladium Pd (0). Then, pre-patterning of Na_2PdCl_4 is done with the support of a quartz mask with circular openings. The quartz mask was placed on a freshly cleaved mica substrate. Then, under heating conditions, the as-prepared Na_2PdCl_4 solution was drop-cast in the circular opening area of the quartz mask. Na_2PdCl_4 solution on mica is heated at 50 °C on a hotplate for 45 mins. Then, the pre-patterned mica substrate is placed inside a quartz furnace for CVD. Before the growth, the quartz chamber was cleaned by purging Argon gas (300 sccm) via a rotary pump. In the CVD process, the temperature of the center zone is ramped up to 500 °C, and Se powder is kept at 1 cm away towards the upstream (temperature ~240 °C) to vaporize the Se and transport it to the growth substrate (~240 °C) with a carrier gas (Argon) flow (110 sccm) in a single-zone tube furnace with precise temperature control

6.2.2. Characterization technique

The as-grown phase and subsequent phase evolution under applied strain was studied using Micro-Raman spectroscopy (LabRam HR800, Jobin Yvon) with an excitation wavelength (λ_{ex}) of 532 nm (Ar ion laser). We used a 100X objective lens with a laser spot size of 1 μm for Raman measurements. The laser power was kept at minimal (1.5 mW) to avoid the possibility of laser-induced damage of the samples during the data curation. The Raman signals sent through a multimode fiber grating of 1800 grooves mm^{-1} were collected by a charge-coupled device which is integrated with the same system.

6.3. Results and discussion

6.3.1. Growth of bilayer $PdSe_2$

At first, $PdSe_2$ layers are grown via the CVD technique following our previous chapters.

(1) Na_2PdCl_4 solution patterning,

(2) pre-patterned substrate placed into the CVD furnace for the CVD growth of $PdSe_2$.

The study with multiple experiments reveals that initial concentration (C_i) ratio of $PdCl_2$: NaCl is strongly correlated with the thickness of the as-grown $PdSe_2$. The ratio of C_i of $PdCl_2$ to NaCl ($C_i=[PdCl_2]_i/[NaCl]_i$) is the primary factor in the formation of bilayer to multilayer growth of $PdSe_2$. Based on their C_i value, the growth can be categorized into two types:

(1) NaCl: $PdCl_2$→ 1:9 (4-armed growth), → Bilayer to multilayer $PdSe_2$

(2) NaCl: $PdCl_2$→ 1:14 (many armed growth). → Only bilayer $PdSe_2$

It has been observed that in 1:9 growth, the as-grown $PdSe_2$ started splitting from the edges after 3 months (**Figure 6.2a**), which is due to the significant presence of the NaCl in the as-grown $PdSe_2$, whereas 1:14 grown $PdSe_2$ doesn't degrade even after years (**Figure 6.2b**) confirming the high stability.

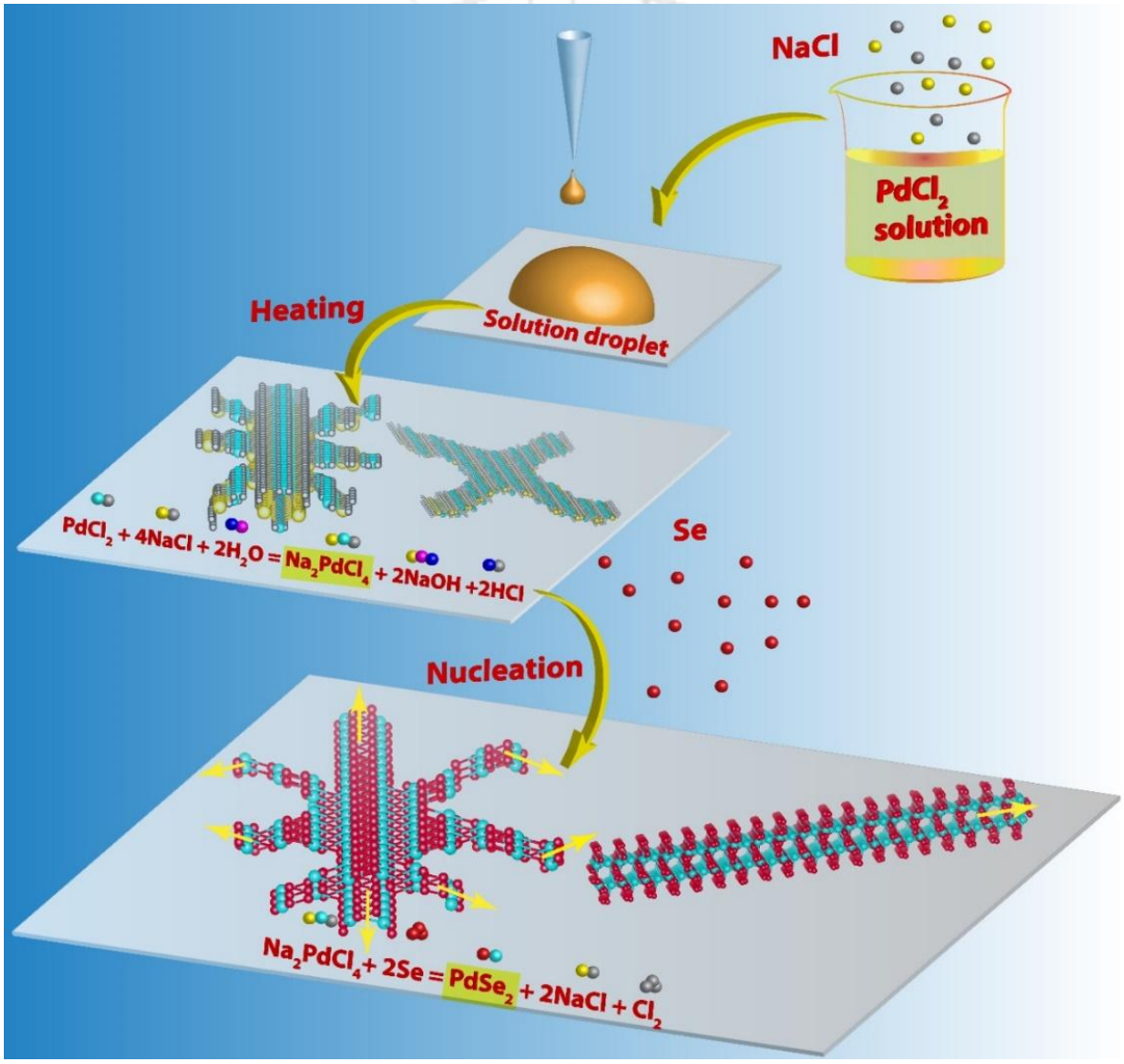

Figure 6.1. Schematic representation of solution assisted growth mechanism $PdSe_2$.

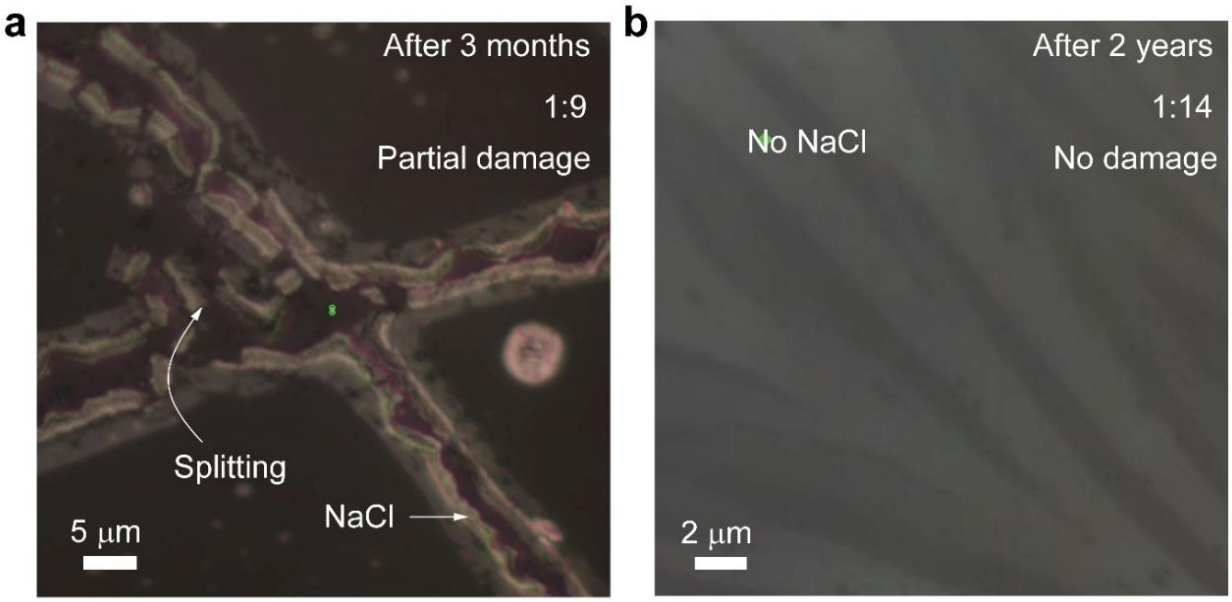

Figure 6.2. (a) Splitting of the edge of a three months aged 1:9 grown $PdSe_2$, (b) No splitting of edges in two years old 1:14 grown $PdSe_2$.

In 1:14 growth, the drop-casted solution on the mica substrate followed by heating on a hotplate in 4 different temperature windows (50 ℃, 60 ℃, 70 ℃, 80 ℃). As the quality of as-grown $PdSe_2$ depends on the $PdCl_2$ solution heating temperature, we have given a chart of optical images of $PdSe_2$ dendrites grown at different pre-heating temperatures. **Figure 6.3** reveals that pre-heating at 60 ℃ and 70 ℃ yields the best quality growth, whereas in the case of 50 ℃ and 80 ℃, we notice some inhomogeneous growth of $PdSe_2$. For the growth temperatures of 310 ℃ (inside CVD setup), we got dendritic pattern $PdSe_2$ having a maximum width of 2 μm. When the growth temperature is decreased to 290 ℃, we observe that the dendrites started approaching each other for joining of branches. When the growth temperature decreased further to 280 ℃, the dendritic branches joined and form a large area growth of $PdSe_2$. The large area flake size of the of $PdSe_2$ increased and was in the range 40-70μm. Thus, a lower temperature growth gives larger area 2D $PdSe_2$ film, while a larger temperature growth yields dendritic pattern of $PdSe_2$ growth.

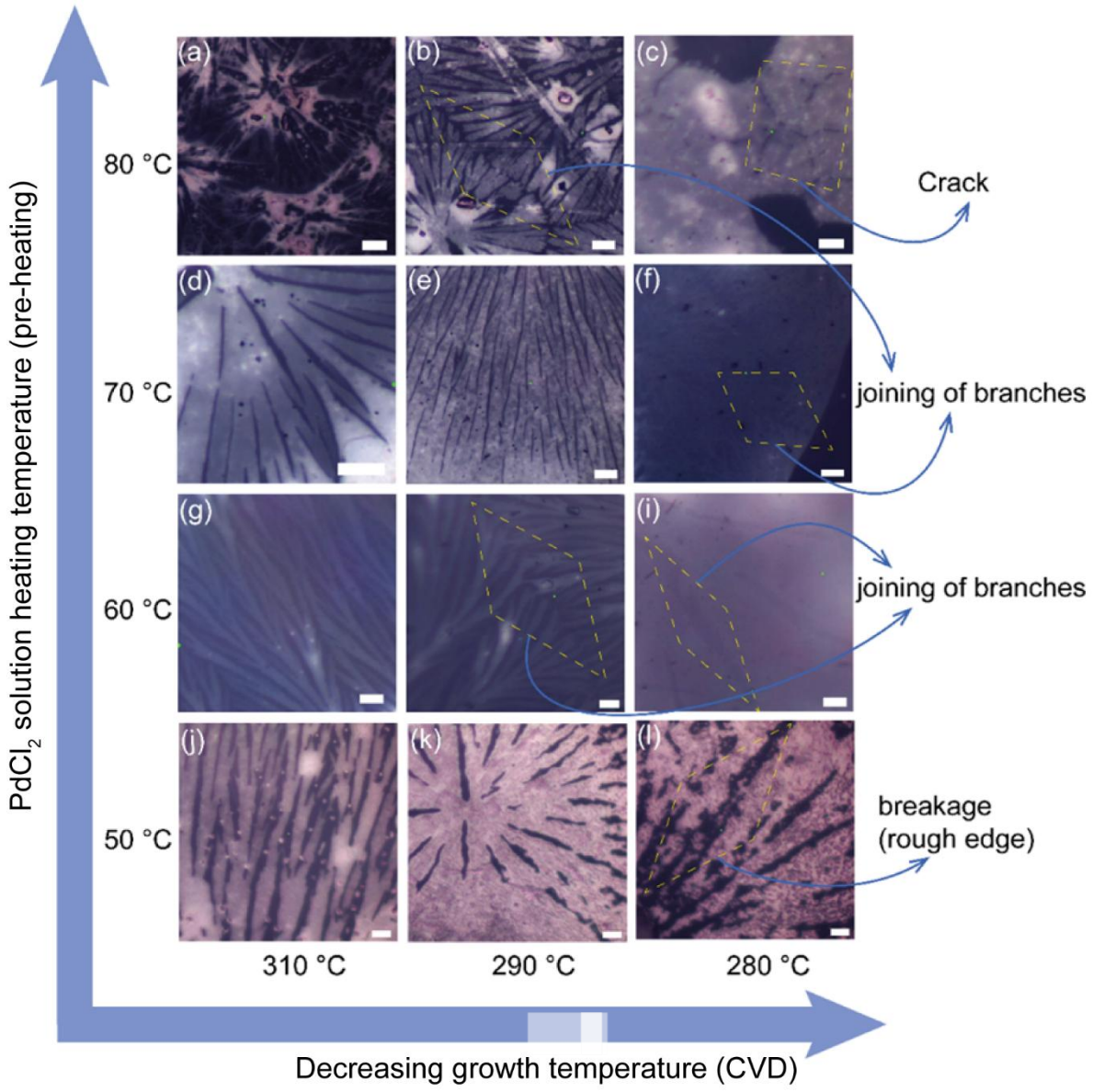

Figure 6.3. (a) Synergistic modulation of $PdSe_2$ morphology with growth temperatures and $PdCl_2$ heating temperature.

In the $PdCl_2$ film, the circular-shaped central region located in **Figure 6.4a** is the Pd source region, which act as a Pd source region during the CVD. **Figure 6.4b** shows the CVD grown region and the central bulk region. To further confirm the CVD grown layer of $PdSe_2$, we have carried out the AFM analysis. The **Figure 6.4c** elucidate that the thickness of $PdSe_2$ is about 1.2 nm (2L). **Figure 6.4d** illustrates the Raman mapping of A_g^3 mode of $PdSe_2$. The Raman mapping intensity decreases from the central region towards the edges, confirming the presence of bilayer. It is

further confirmed that the Pd source region acts as an initiation zone during CVD growth of $PdSe_2$. FESEM and optical micrograph images of only bilayer $PdSe_2$ is given in **Figure 6.4e, f**.

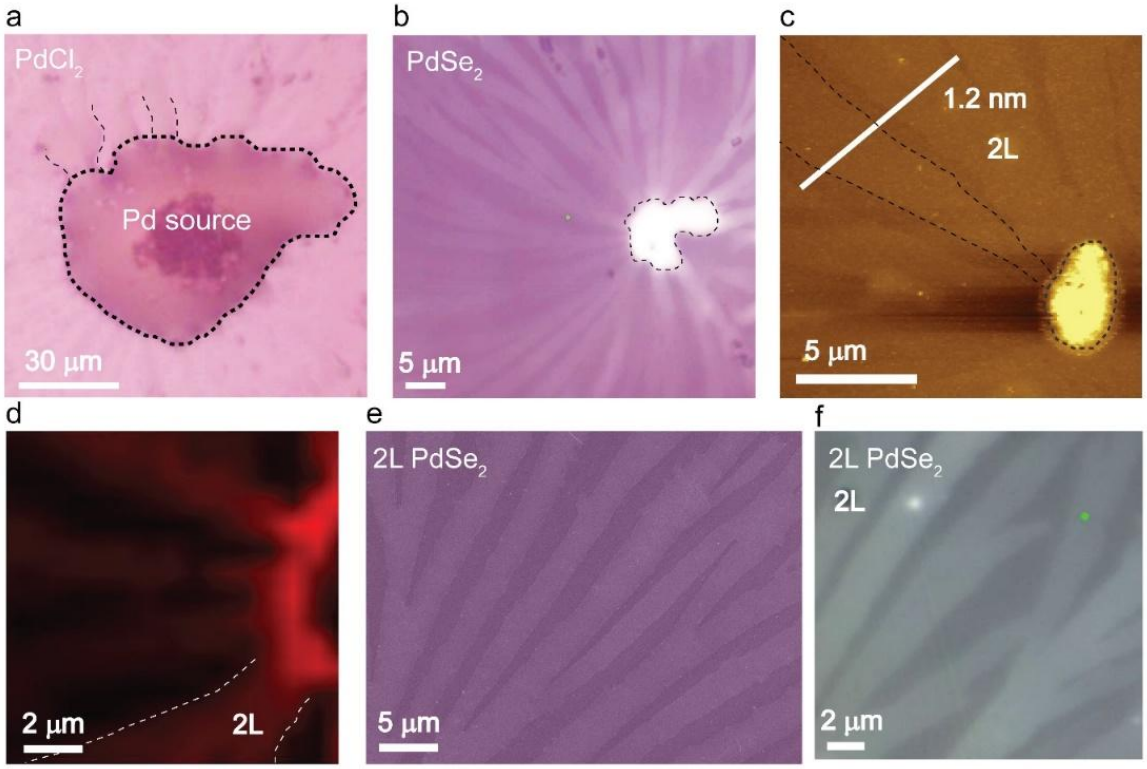

Figure 6.4. Optical micrograph of (a) $PdCl_2$ growth, (b) bilayer $PdSe_2$, (c) AFM image showing bilayer $PdSe_2$, (d) Raman mapping of A_g^3 mode of $PdSe_2$, (e,f) FESEM, and optical micrograph images of bilayer $PdSe_2$.

Historically, Raman mapping has been one of the potential tools for structural characterization of layered materials. From the image contrast, the Raman intensity, difference in wavenumber we can approximately identify the layer number. Raman mapping analyses on different positions demarcated as circle lead us a different pathway to confirm the layer number of as-grown $PdSe_2$. The position where the mappings was carried out is demarked by circles in **Figure 6.5**. There are eight Raman active modes, out of which A_g^1 and A_g^3 modes are highly intense modes as compared to other modes.

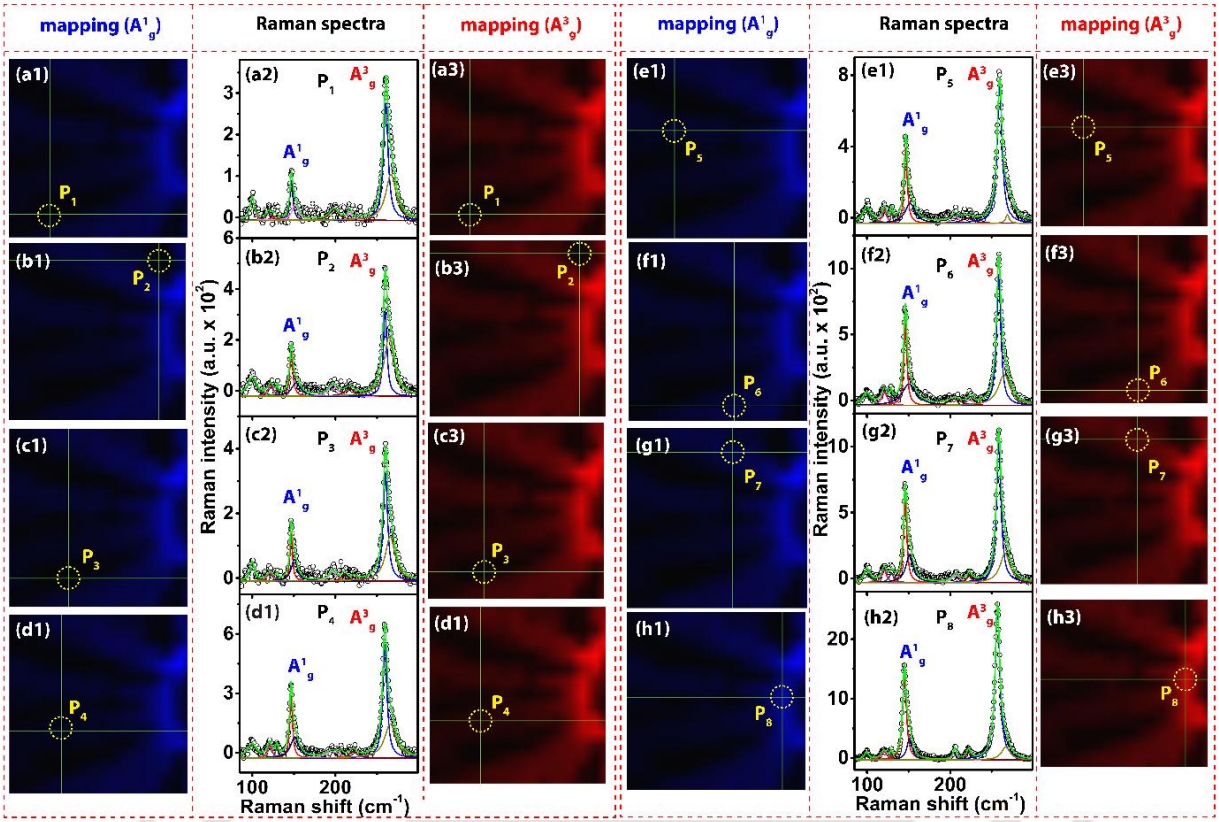

Figure 6.5. Raman mapping of A_g^1 and A_g^3 modes at different positions.

The corresponding Lorentzian fitting of different positions gives us a new pathway to validate the layer of $PdSe_2$ through Raman spectra (**Figure 6.6a**, **b**). The intensity ratio of A_g^1 and A_g^2 i.e. $I(A_g^1)/I(A_g^2)$ ratio can be taken as a fingerprint to identify the layer number of $PdSe_2$. We have plotted the $I(A_g^1)/I(A_g^2)$ intensity ratio as a function of layer number of $PdSe_2$(**Figure 6.6c**). $I(A_g^1)/I(A_g^2)$ intensity ratio almost linearly decreases with the increase in layer number. For a single layer $PdSe_2$ $I(A_g^1)/I(A_g^2)$ intensity ratio is ~1.3, whereas for 4 layer it is ~1. The corresponsing AFM images of monolayer (~0.6 nm), bi-layer (~1.4 nm), tri-layer (~2 nm), and 10L (~6 nm) is given in **Figure 6.7**.

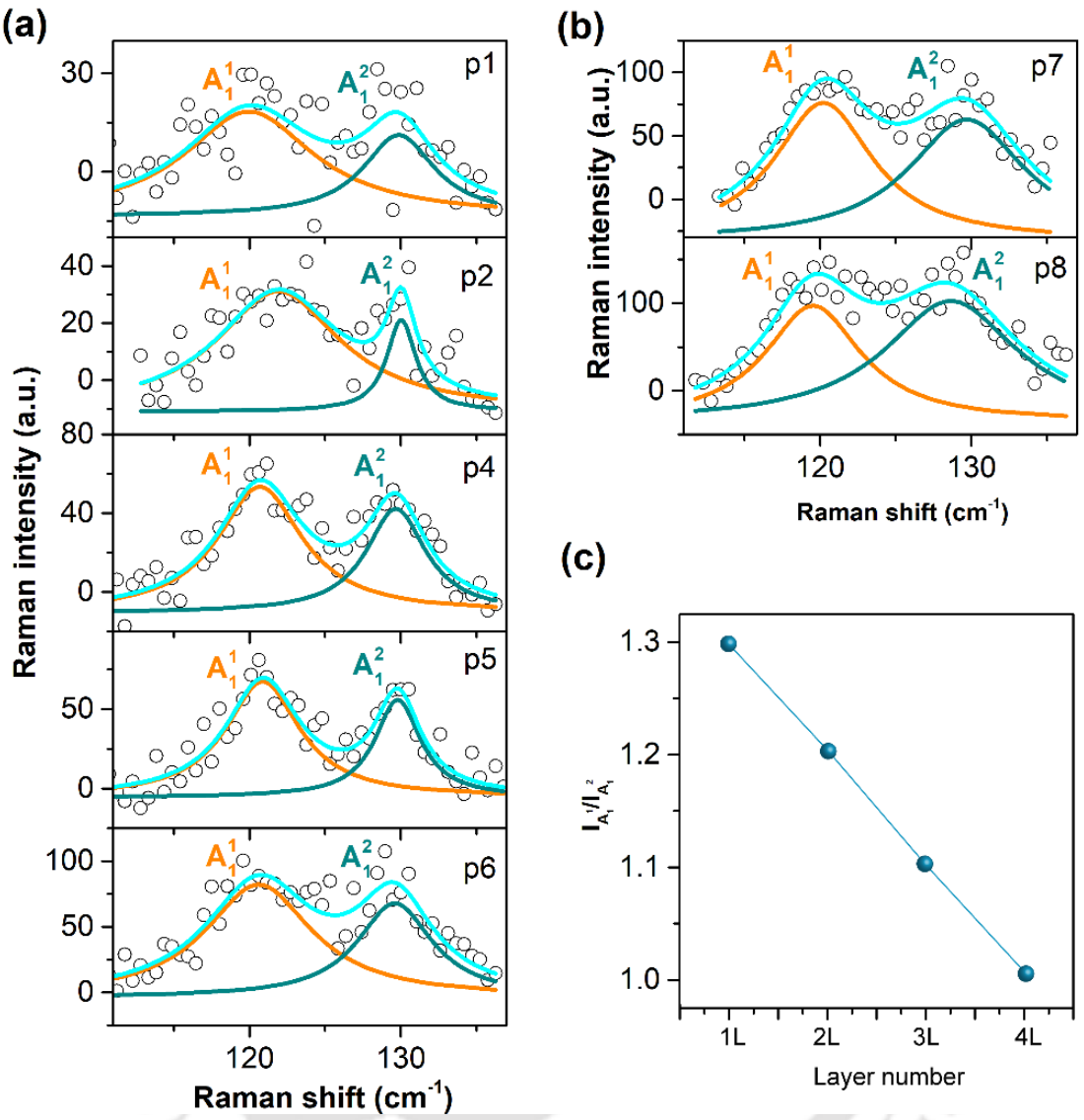

Figure 6.6. (a) Fitted Raman spectra of A_g^1 and A_g^2 modes of p1, p2, p4, p5, p6 positions and (b) p7, p8 of Figure 6.5, (c) I(A_g^1)/I(A_g^2) intensity ratio as a function of layer number of $PdSe_2$.

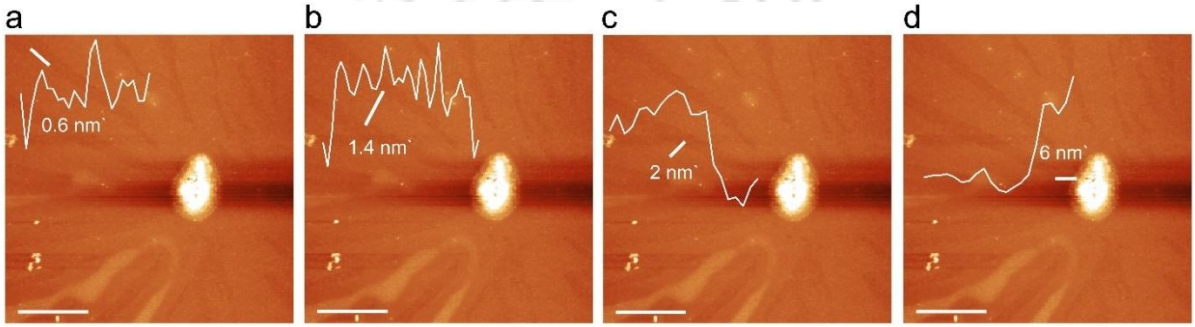

Figure 6.7. The position wise AFM image of (a) monolayer, (b) bilayer, (c) tri-layer (d) 10L.

6.3.2. Transfer of $PdSe_2$ for uniaxial tensile strain analyses

We transfer the CVD-grown bilayer $PdSe_2$ layer on a flexible substrate via three methods:

1. PMMA-assisted transfer process

It is a widely employed transfer technique for 2D layer transfer and commonly used for multilayer $PdSe_2$ transfer. In our case, we firstly used PMMA-assisted transfer process for the transfer of the $PdSe_2$ layer from growth substrate mica to flexible polyimide substrate. We followed our previous optimization (**chapter 2**) for this transfer technique. Briefly, a thin PMMA sacrificial layer is deposited over the $PdSe_2$/mica and then baked at 85 ℃. After that, PMMA/$PdSe_2$/mica is immersed into the 5% KOH solution for several hours to delaminate the PMMA/$PdSe_2$ membrane from the mica substrate. After that, PMMA/$PdSe_2$ is rinsed with DI water to remove KOH residue and fished on the polyimide substrate. PMMA/$PdSe_2$/polyimide was then dipped into the acetone, followed by isopropanol cleaning to remove PMMA and contamination from $PdSe_2$/polyimide. The $PdSe_2$/polyimide is dried adequately at 65 ℃ for 10 minutes. Nevertheless, the involvement of PMMA and KOH partially contaminates the $PdSe_2$ layer, which is not desirable. This delves our search for a more reliable contamination-free transfer of the $PdSe_2$ layer.

2. Water-assisted transfer process

We discovered a unique water-assisted transfer method, which is facile and different from the conventional one. A salt-assisted sacrificial layer is grown via the CVD technique for the implementation of this method. **Figure 6.8a** illustrates schematics of our transfer strategy. The salt layer below the $PdSe_2$ layer dissolves in water, which causes the spontaneous delamination of only $PdSe_2$ layer within a few seconds after the water droplet insertion. The delaminated $PdSe_2$ layer floated on the water surface is manually fished on the target substrate. The large area delamination of $PdSe_2$ layer is critical in such a way that when the mica touched the water surface, the adhesive force between the water and $PdSe_2$ layer should be higher than the electrostatic (van der Waal and non-van der Waal force) force between the $PdSe_2$ layer and mica. After delamination, the $PdSe_2$ layer floats on the water's surface due to buoyant force. Further, the floated $PdSe_2$ layer is fished on a flexible substrate and dried at 65 ℃ for 10 minutes. As can be seen from **Figure 6.8b**, the underneath NaCl layer is only present at the initiation zone, which is absent after the successful transfer. The schematic illustration in **Figure 6.8c** highlights the distribution of NaCl and $PdSe_2$ layers in the water-assisted transfer process.

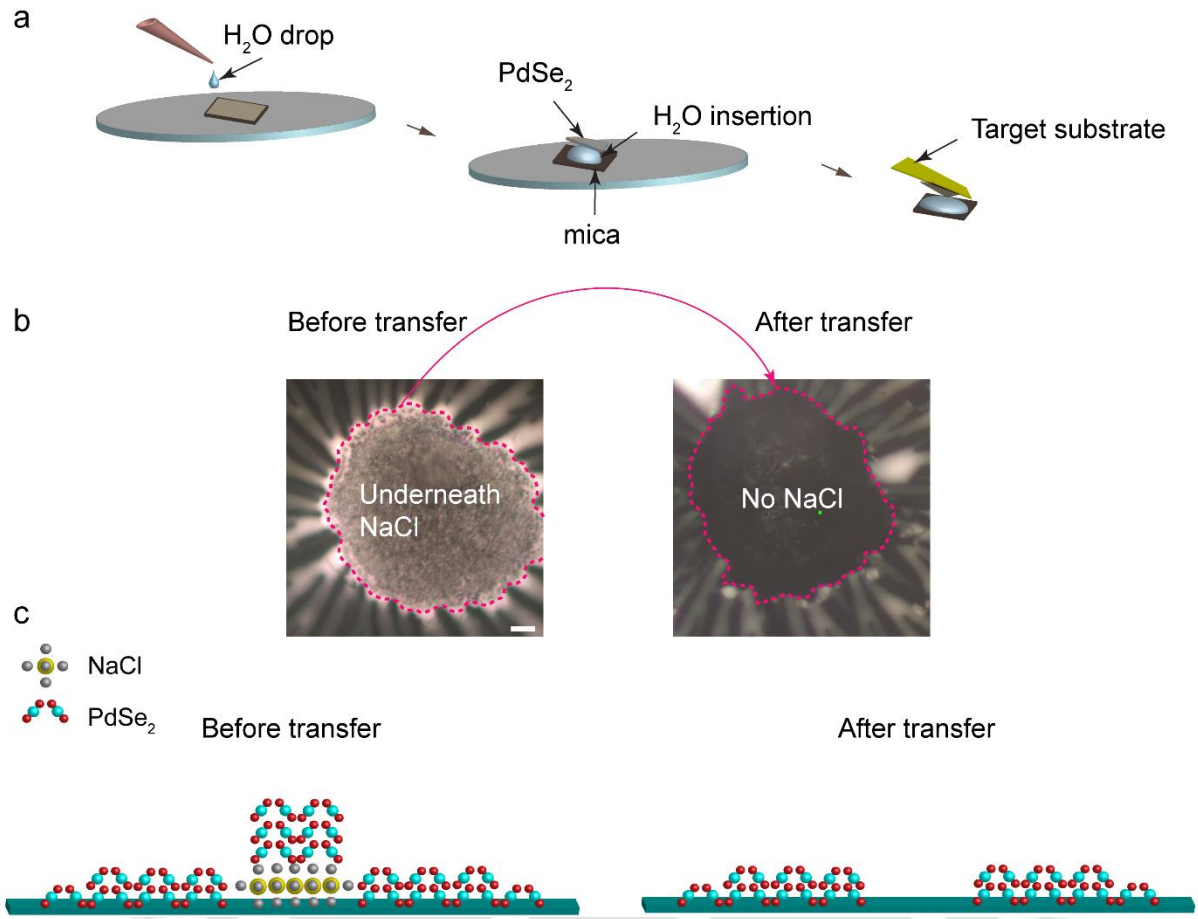

Figure 6.8. (a) Schematic illustration of stepwise processes for the water-assisted delamination and transfer of $PdSe_2$ layers on target substrate, (b) representative optical images to highlight the sustainability of underneath NaCl layer before the delamination process and absence of NaCl after transfer; (c). schematic illustration of $PdSe_2$ layer before and after successful transfer.

3. Scotch tape-assisted transfer

Further, we adopted a simple dry transfer technique which is found to be very advantageous to freely suspend $PdSe_2$ on any arbitrary substrate, as there is no capillary forces involved in the process. The scotch tape, which is a thermal release tape, was stamped on the as-grown film on mica surface, which is adhered to a glass slide to facilitate its handling. The bilayer $PdSe_2$ flake to be transferred are deposited onto the thermal release tape by mechanical exfoliation. The surface of the thermal release tape is inspected under the optical microscope to select the thinner flakes having a faint contrast under normal illumination. Raman spectroscopy can also be carried out on the surface of the thermal release tape to confirm the thickness of the flake. In order to transfer the

flake to the acceptor foreign substrate surface, the thermal release tape is pressed against the acceptor surface (here PET) and peeled off very slowly after heating it on the hotplate at 130°C for 15 minutes. The schematic illustration of scotch tape-assisted transfer of bilayer $PdSe_2$ flake on PET substrate is given in **Figure 6.9**.

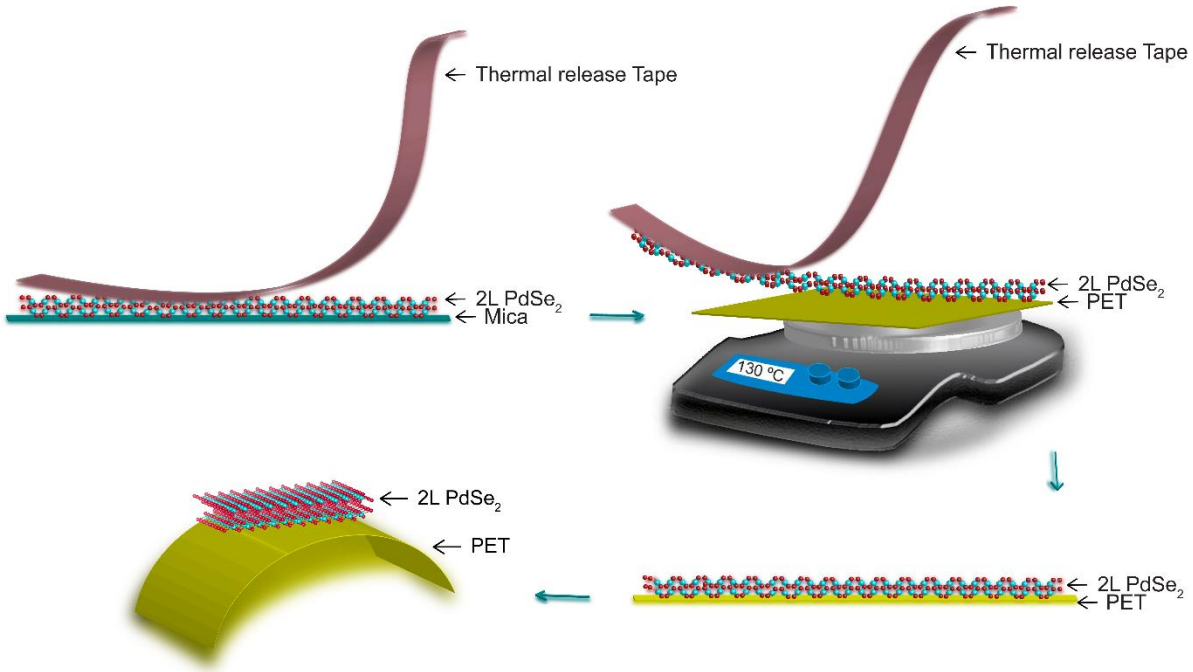

Figure 6.9. (a) Schematic illustration of stepwise processes for the thermal release tape assisted transfer of bilayer $PdSe_2$ flake on PET substrate.

While using PMMA-assisted transfer, the polymer layer is removed using solvents at the end of the transfer process, but significant amounts of polymer residue can still be found on the transferred films. This PMMA residue in turn, leads to non-ideal effects such as unintentional doping effects. As seen in the AFM image **Figure 6.10a**, PMMA-assisted transfer leaves residue which is more than 8 nm in thickness. Water assisted transfer method produce folds and wrinkles in the bilayer $PdSe_2$, due to the presence of trapped water blisters as confirmed from the AFM image (**Figure 6.10b**). However, the water assisted transfer method is one of the most versatile methods that allows one to transfer flakes without using any polymers. Transferring freely suspended structures can be done straightforwardly in case of scotch tape assisted transfer technique. AFM image (**Figure 6.10c)** confirms that the bilayer is free from contamination after transfer, as the layer

thickness is 1.2 nm. The AFM thickness profile of $PdSe_2$ layer is intact after the transfer. However, the edge of $PdSe_2$ is flipped due to local shear force at the edges.

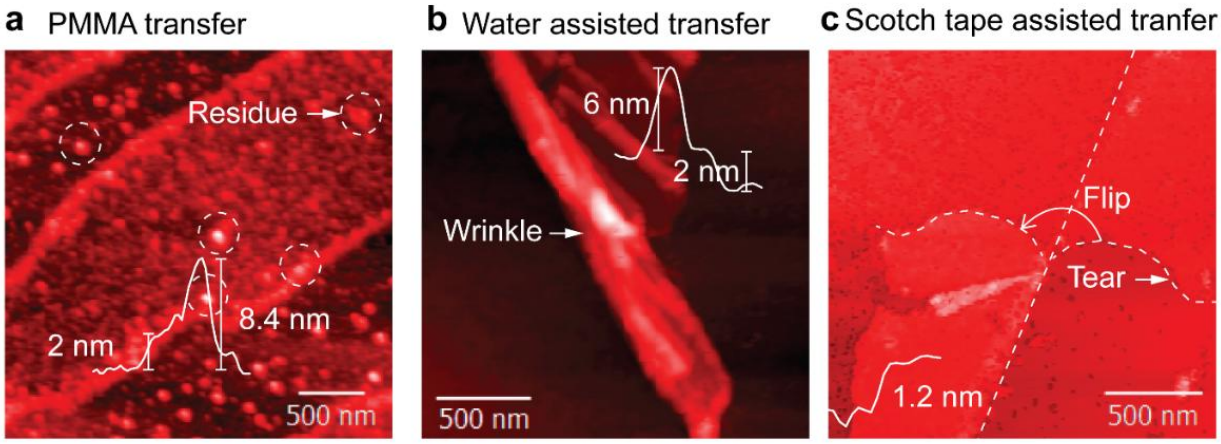

Figure 6.10. AFM images of $PdSe_2$ after (a)PMMA assisted transfer, (b) water assisted transfer, (c) scotch tape assisted transfer.

6.3.3. Phase evolution of $PdSe_2$ under uniaxial tensile strain

Further, the impact of uniaxial strain on the $PdSe_2$ layer transferred through different methods is investigated. After each transfer process, we have studied the effect of uniaxial tensile strain on the phonon spectra of the $PdSe_2$ layer. In the case of the water-assisted transfer process and scotch tape-assisted transfer method, we found the evolution of Pd_2Se_3 phase under applied uniaxial tensile strain. In the case of water-assisted transfer, water molecules can interact with the $PdSe_2$ surface, disrupting the weak van der Waals bonds between the two $PdSe_2$ layers. The interaction between water and the $PdSe_2$ surface can induce defects at the interfaces. In the scotch tape exfoliation method, the tape adheres to the surface of the $PdSe_2$ layer. When the tape is pulled off, it physically shears the $PdSe_2$ away from the mica substrate. The scotch tape assisted exfoliation doesn't directly affect the internal atomic structure of the defect rich $PdSe_2$. When strain is applied to the scotch tape assisted exfoliated $PdSe_2$, strain can change the distance between the two $PdSe_2$ layers which cause local deformation that can push the layers closer. Strain causes the defect rich $PdSe_2$ layers to come into closer proximity and this may cause strong interlayer interactions, leading to fusion of the layers. This can facilitate the merging of two $PdSe_2$ layers to Pd_2Se_3. In case of water-assisted transfer, 0.5 % of uniaxial tensile strain creates the equivalent energy to transform $PdSe_2$ to Pd_2Se_3. Note that, 0.17% strain is enough to produce a Pd_2Se_3 in the case of scotch tape transfer involving mechanical exfoliation. In contrast, we did not observe any phase

evolution in the case of PMMA-assisted transfer, which could be attributed to the contaminated interface of the $PdSe_2$ layer and substrate. The transfer methods and effect of uniaxial strain are explained in detail in the following section.

We used a two-point bending method to introduce the uniaxial tensile strain to the $PdSe_2$ layer. Assuming that the PET substrate with exfoliated $PdSe_2$ before bending are virtually strain-free, we can compute the radius of curvature R, [16] the induced strain; $\varepsilon = \tau/R$, where 2τ is the thickness of the substrate (**Figure 6.11a**). A slide caliper is probed to bend the $PdSe_2$ adhered PET substrate (photograph shown in **Figure 6.11b**), to monitor the effect of strain on the Raman spectra of $PdSe_2$. Raman spectra are collected using a 532 nm laser with 80 μW power and a spot size of ~1 μm

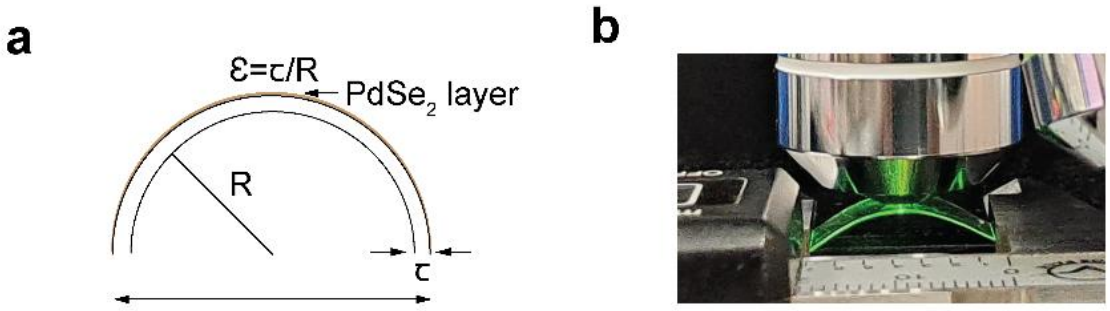

Figure 6.11. (a) Schematic of strain engineering. (b) Photograph of two point bending method at the time of Raman measurement.

Figure 6.12a shows the Raman spectra of the $PdSe_2$ layer (PMMA-transferred) under applied uniaxial tensile strain from 0 to 0.5%. The A_g^1 and A_g^3 phonon mode positions are redshifted with increasing strain till 0.5 % (**Figure 6.12a**). The rate of shifting in Raman mode for A_g^1 and A_g^3 is -0.51 ± 0.18 cm^{-1}/% strain and -1.16 ± 0.18 cm^{-1}/% strain, respectively.

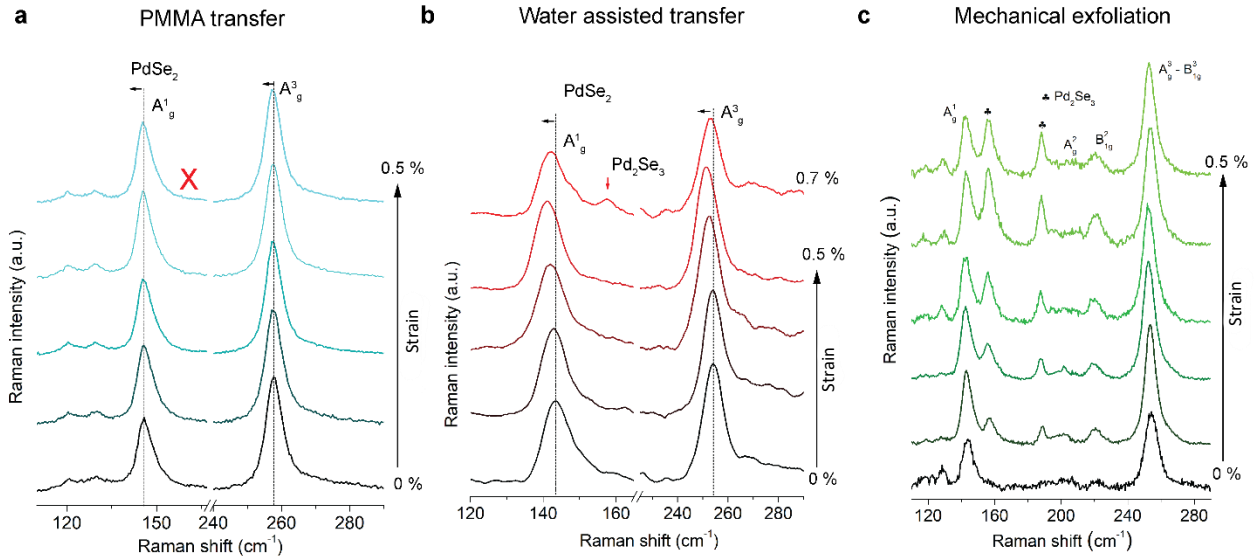

Figure 6.12. Raman spectra of CVD-grown $PdSe_2$ layer on the flexible substrate under applied uniaxial tensile strain for different transfer techniques. (a) PMMA assisted transferred sample. The cross symbol implies that even after 0.5 % applied strain, there is no evolution of the Pd_2Se_3 phase. (b) Water-assisted transferred sample. The arrow indicates the evolution of the Pd_2Se_3 phase at 0.7 % applied strain. (c) scotch tape assisted transferred sample. The symbol represents the evolution of the Pd_2Se_3 phase (the characteristic Raman peak at 156 cm^{-1}) at 0.17 % applied strain. The vertical dotted line visualizes the redshift of Raman modes' peak positions in each case.

The strain-induced Raman shift of the water-assisted transferred $PdSe_2$ sample is shown in **Figure 6.12b**, which indicates a redshift in the A_g^1 and A_g^3 modes with strain. However, the shift here is higher than that of the PMMA transfer case. The rate of shift of A_g^1 and A_g^3 are -3.91 ± 1.03 cm^{-1}/% strain and -3.87 ± 0.91 cm^{-1}/% strain, respectively. It indicates that better stress transfer happens in the water- assisted transferred $PdSe_2$ layer than PMMA transferred $PdSe_2$ layer from the substrate. The better stress transfer in the water-transferred sample can be attributed to the contamination-free clean interface between the $PdSe_2$ layer and the substrate. When 0.7 % tensile strain is applied, we observe that the A_g^1 and A_g^3 modes started shifting towards the initial value i.e., the peak shift is less than the 0.5 % strain along with an evolution of Pd_2Se_3 phase (marked with an arrow in **Figure 6.12b**). However, beyond 0.7 %, the redshift value becomes negligible with increasing strain. This indicates that the strain is relaxed due to decreasing stress transfer from the substrate due to slippage of the sample-substrate interface. The rate of shift of A_g^1 mode for scotch tape transferred $PdSe_2$ membrane is - 4.61 ± 1.13 cm^{-1}/% strain. The strain-dependent Raman spectra in scotch tape-assisted transferred sample reveals the evolution of the phase with the application of 0.17 % strain. A_g^1 mode of both $PdSe_2$ and Pd_2Se_3 are fitted at their individual

peak positions to get the maximum intensity. The intensity ratio of A_g^1 mode of $PdSe_2$ and Pd_2Se_3 decreases from 10 to 1 with increasing strain (**Figure 6.13a**).

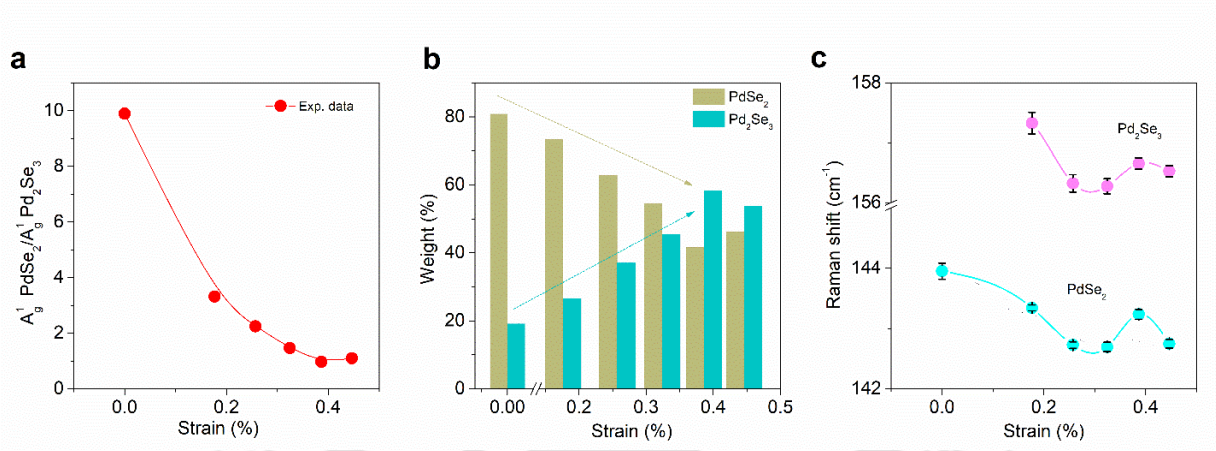

Figure 6.13. (a) The intensity ratio of A_g^1 Raman mode of two phases as a function of applied strain. (b) Weight percentage of A_g^1 Raman mode for $PdSe_2$ and Pd_2Se_3 as a function of strain which indicates that with increasing strain the contribution of Pd_2Se_3 phase increases. (c) A_g^1 peak positions of the two phases as a function of strain.

The weightage of the A_g^1 mode of Pd_2Se_3 increases from 19 % to 58 % and with strain while that of $PdSe_2$ decreases from 81 % to 42 %, with increasing strain from 0 to 0.4 % (**Figure 6.13b**). **Figure 6.13c** shows the trend in redshift of the A_g^1 mode of Pd_2Se_3 and $PdSe_2$. A significant redshift (1.2 cm^{-1} and 1 cm^{-1}) in the A_g^1 peak position of Pd_2Se_3 and $PdSe_2$ has been observed until 0.32 % strain. **Figure 6.13c** show that the characteristic Raman peak of Pd_2Se_3 at 156 cm^{-1} started arising at 0.17 % of uniaxial strain. As the strain increases from 0.17 to 0.45 %, the intensity of 156 cm^{-1} mode increases significantly. This indicates that the uniaxial tensile strain creates a compressive stress along the c-direction, which introduces the insertion of Pd atoms from two layers of $PdSe_2$ and finally form one layer of Pd_2Se_3. According to Xu et. al., strong interlayer interaction in $PdSe_2$ leads to Pd_2Se_3 stoichiometry, which is supporting our experimental observations.[17] To further investigate on Pd_2Se_3 phase evaluation, we have conducted rapid thermal annealing (RTA) at various temperatures.

6.3.4. Impact of RTA on the Raman modes

RTA was conducted on the sample to check the impact of temperature on the phase evolution. The Raman spectra of RTA at 300 ℃ treated sample show a new peak is at 198 cm^{-1}, which is assigned to one of the Pd_2Se_3 peaks. The EDX spectrum of RTA at 350 ℃ treated sample is shown in

Figure 6.14, which predominantly show two peaks from Pd and Se, with the large peaks from the substrate.

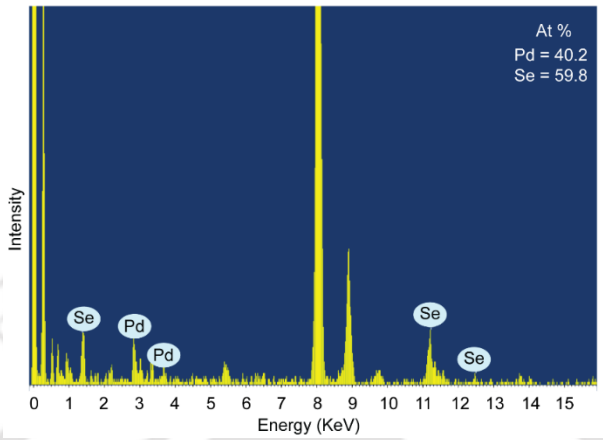

Figure 6.14. EDX spectrum of CVD grown $PdSe_2$ after annealing at 350 ℃.

Atomic percentages of the Pd and Se peaks can be used to confirm that a Se deficient condition arises in the annealed sample. The FWHM of A_g^1 and A_g^2 also significantly increase with increasing annealing temperature upto 300 ℃ (**Figure 6.15a**). This indicates that the crystallinity of the sample degrades at higher temperatures, which is attributed to the Se deficient condition in the parent material. As the concentration of Se vacancies increases, the interlayer distance decreases.[6, 10] According to Lin et. al., the interlayer distance between two $PdSe_2$ layers decreases from 0.45 nm to 0.28 nm while attaining the Pd_2Se_3 stoichiometry, which is almost the typical Pd-Se bond length predicted by DFT calculations. But it remains to be seen whether this is experimentally achievable by any of the top-down exfoliation method or bottom-up CVD method. Interestingly, after RTA at 350 ℃, we have noticed appearance of sharp peaks at 157 cm^{-1}, 189 cm^{-1}, 198 cm^{-1} and 212 cm^{-1}. These peaks are assigned to the Pd_2Se_3 modes,[14] which is formed due to the merging of bilayer $PdSe_2$ in presence of Se defects.

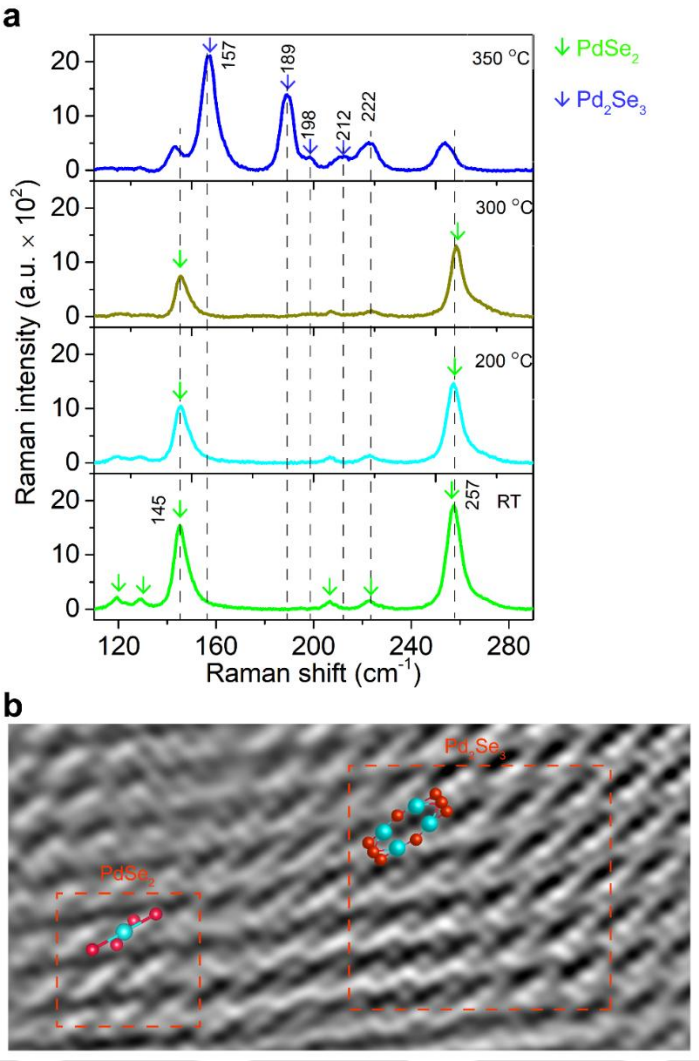

Figure 6.15.(a) Raman spectra of CVD grown $PdSe_2$ layer at room temperature (RT) and RTA temperatures at 200 ℃, 300 ℃ and 350 ℃. (b) HRTEM image of $PdSe_2$ after RTA at 350 ℃.

To further confirm the evaluation of new Pd_2Se_3 phase, we have carried out HRTEM imaging on the RTA treated samples. The HRTEM image (**Figure 6.15b**) confirms the existence of both the Pd_2Se_3 and $PdSe_2$ phases in the RTA at 350 ℃ sample. The inevitable presence of Se vacancies triggers the interlayer fusion providing the premise for the merging of the two $PdSe_2$ layers.

6.4. Conclusion

A scotch tape transfer method has been developed to transfer the as-grown $PdSe_2$ film from the growth substrate to a flexible substrate and study the phonon responses under uniaxial tensile strain. The phase evolution of the van der Waals $PdSe_2$ layer to Pd_2Se_3 under the uniaxial tensile

strain of > 0.2 % in the case of scotch tape transfer and of > 0.5 % in the case of water-assisted transfer. The precise strain engineering can evolve the $PdSe_2$ layer into a Pd_2Se_3 probed by Raman fingerprints. In summary, these results show that the external strain can lead to phase transition in layered $PdSe_2$ sheet, which can be used to discover and control new phases of other 2D materials. Therefore, expanding the portfolio of phase-change materials will open up new application spaces in the research area, and it play a crucial role in the development of new devices and technologies in the future.

References

1. Voiry, D., Mohite, A., & Chhowalla, M. (2015). Phase engineering of transition metal dichalcogenides. Chemical Society Reviews, 44(9), 2702–2712. https://doi.org/10.1039/C5CS00151J.
2. Duerloo, K. N., Li, Y., & Reed, E. J. (2014). Structural phase transitions in two-dimensional Mo- and W-dichalcogenide monolayers. Nature Communications, 5(1). https://doi.org/10.1038/ncomms5214.
3. Zhang, H., Liu, L., & Lau, W. (2013). Dimension-dependent phase transition and magnetic properties of VS2. Journal of Materials Chemistry A, 1(36), 10821. https://doi.org/10.1039/C3TA12098H.
4. Li, Y., Duerloo, K. N., Wauson, K., & Reed, E. J. (2016). Structural semiconductor-to-semimetal phase transition in two-dimensional materials induced by electrostatic gating. Nature Communications, 7(1) https://doi.org/10.1038/ncomms10671.
5. Wang, Y., Xiao, J., Zhu, H., Li, Y., Alsaid, Y., Fong, K. Y., Zhou, Y., Wang, S., Shi, W., Wang, Y., Zettl, A., Reed, E. J., & Zhang, X. (2017). Structural phase transition in monolayer MoTe2 driven by electrostatic doping. Nature, 550(7677), 487–491 https://doi.org/10.1038/nature24043.
6. Lin, J., Zuluaga, S., Yu, P., Liu, Z., Pantelides, S. T., & Suenaga, K. (2017). Novel Pd2Se3 Two-Dimensional Phase Driven by Interlayer Fusion in Layered PdSe. Physical Review Letters, 119(1). https://doi.org/10.1103/PhysRevLett.119.016101.
7. Zuluaga, S., Lin, J., Suenaga, K., & Pantelides, S. T. (2018b). Two-dimensional PdSe 2 -Pd 2 Se 3 junctions can serve as nanowires. 2D Materials, 5(3), 035025. https://doi.org/10.1088/2053-1583/aac34c.
8. Tai, K., Chen, J., Wen, Y., Park, H., Zhang, Q., Lu, Y., Chang, R., Tang, P., Allen, C. S., Wu, W., & Warner, J. H. (2020b). Phase Variations and Layer Epitaxy of 2D PdSe2 Grown on 2D Monolayers by Direct Selenization of Molecular Pd Precursors. ACS Nano, 14(9), 11677–11690. https://doi.org/10.1021/acsnano.0c04230 https://doi.org/10.1021/acsnano.0c04230.
9. Fu, M., Liang, L., Zou, Q., Nguyen, G. D., Xiao, K., Li, A., Kang, J., Wu, Z., & Gai, Z. (2019). Defects in Highly Anisotropic Transition-Metal Dichalcogenide PdSe2. The Journal of Physical Chemistry Letters, 11(3), 740–746. https://doi.org/10.1021/acs.jpclett.9b03312.
10. Ryu, G. H., Zhu, T., Chen, J., Sinha, S., Shautsova, V., Grossman, J. C., & Warner, J. H. (2019). Striated 2D Lattice with Sub-nm 1D Etch Channels by Controlled Thermally Induced Phase Transformations of PdSe2. Advanced Materials, 31(46). https://doi.org/10.1002/adma.201904251.
11. Chen, J., Ryu, G. H., Sinha, S., & Warner, J. H. (2019). Atomic Structure and Dynamics of Defects and Grain Boundaries in 2D Pd2Se3 Monolayers. ACS Nano, 13(7), 8256–8264. https://doi.org/10.1021/acsnano.9b03645.
12. Naghavi, S. S., He, J., Xia, Y., & Wolverton, C. (2018). Pd2Se3 Monolayer: A Promising Two-Dimensional Thermoelectric Material with Ultralow Lattice Thermal Conductivity and High Power Factor. Chemistry of Materials, 30(16), 5639–5647. https://doi.org/10.1021/acs.chemmater.8b01914.
13. Li, X., Zhang, S., Guo, Y., Wang, F. Q., & Wang, Q. (2018). Physical Properties and Photovoltaic Application of Semiconducting Pd2Se3 Monolayer. Nanomaterials, 8(10), 832. https://doi.org/10.3390/nano8100832.
14. Zhu, X., Li, F., Wang, Y., Qiao, M., & Li, Y. (2018). Pd2Se3monolayer: a novel two-dimensional material with excellent electronic, transport, and optical properties. Journal of Materials Chemistry C, 6(16), 4494–4500. https://doi.org/10.1039/C8TC00810H.

15. Luo, W., Oyedele, A. D., Gu, Y., Li, T., Wang, X., Haglund, A. V., Mandrus, D., Puretzky, A. A., Xiao, K., Liang, L., & Ling, X. (2020). Anisotropic Phonon Response of Few-Layer PdSe2 under Uniaxial Strain. Advanced Functional Materials, 30(35). https://doi.org/10.1002/adfm.202003215.
16. Chen, C., Rosenblatt, S., Bolotin, K. I., Kalb, W., Kim, P., Kymissis, I., Stormer, H. L., Heinz, T. F., & Hone, J. (2009). Performance of monolayer graphene nanomechanical resonators with electrical readout. Nature Nanotechnology, 4(12), 861–867. https://doi.org/10.1038/nnano.2009.267
17. Xu, X., Robertson, J., & Li, H. (2020). Semiconducting few-layer PdSe2 and Pd2Se3: native point defects and contacts with native metallic Pd17Se15. Physical Chemistry Chemical Physics, 22(14), 7365–7373. https://doi.org/10.1039/C9CP06654C.

Chapter 7 - Summary and Outlook

This thesis investigates the unique synthesis techniques, properties, transfer techniques and potential applications of CVD grown 2D $PdSe_2$, 2D $PdSe_2$ dendrites, $PdSe_2$ nanoscroll and their future scopes for fundamental studies and multifunctional applications.

7.1. Summary and Highlights of Thesis

This thesis explores systematic study on CVD synthesis of $PdSe_2$, PdS_2, $PdTe_2$, NaCl assisted CVD synthesis of $PdSe_2$, $PdSe_2$ dendrites, controlled bilayer $PdSe_2$ and $PdSe_2$ nanoscroll. The $PdSe_2$ growth is carried on varieties of substrate such as mica, Si, SiO_2, TiO_2, glass, sapphire, quartz to study the substrate effects on the dendritic $PdSe_2$. When subject to tensile strain, we show that bilayer $PdSe_2$ can undergo a phase transition into Pd_2Se_3 due to Se vacancies and interlayer fusion of two $PdSe_2$ layers. We develop a novel and facile growth strategy for dendritic growth. Utilizing the advantages of water solubility of NaCl, we have demonstrated a chemical etchant-free and large-area transfer of $PdSe_2$ dendrites, which fully overcomes the limitations of PMMA-assisted transfer technique. The conversion of $PdSe_2$ into $PdSe_2$ nanoscroll via Pd nanoparticles and unscrolling into sheet are fully controlled under H_2O environment. Encapsulation of $PdSe_2$ nanoscroll with live cancer cells demonstrated that the Pd nanoparticles attack the cancer cell leading to the nuclear arrest and death of cancer cells. Further, the bilayer $PdSe_2$ is exploited for the finding of thermal conductivity. The estimated thermal conductivity is ~36.8 W/m. K and ~10.1 W/m. K for bi-layer and few-layer (~5L) $PdSe_2$ respectively. Dendritic $PdSe_2$ detects Rhodamine B (RhB) with a significant SERS enhancement ($> 10^5$), whereas SERS spectrum of MB molecules at the $PdSe_2$-Pd_2Se_3 region decorated with Pd NPs shows the highest enhancement factor of 3×10^5. The significant contributions of the thesis are summarized as follows:

7.1.1. Salt-catalyzed directed growth of bilayer $PdSe_2$

We developed a salt solution-assisted catalytic growth of dendritic strictly bilayer $PdSe_2$ and other NTMDs on mica substrate. Besides the growth kinetics, we provided a clear vision of the $PdSe_2$-Pd_2Se_3 junction as a metallic wire using DFT calculations and experimental evidence of growing such junctions. The SERS spectrum of MB molecules at the $PdSe_2$-Pd_2Se_3 junction region decorated with Pd NPs shows significantly higher SERS enhancement. DFT calculation shows that the $PdSe_2$-Pd_2Se_3 junction has a metallic property accountable for the high SERS sensitivity. We

introduce a NaCl catalyzed CVD growth of 2L $PdSe_2$ dendrites and $PdSe_2$-Pd_2Se_3 junctions on the mica substrate through the salt solution pre-treatment. The pre-treated structure triggers the formation of molten Pd-O droplets, which undergo a phase evolution from Pd NPs to Pd_2Se_3 (in Se-poor condition) to $PdSe_2$ (in Se-rich condition). Pd NPs hotspots on $PdSe_2$-Pd_2Se_3 junctions enable significant SERS enhancement with an enhancement factor (EF$\sim 3\times10^5$), to detect methylene blue molecules due to multiple factors, such as charge transfer and electromagnetic field enhancement. This is confirmed by DFT calculations and Finite element method (FEM) simulation, along with Raman imaging. The FEM simulations revealed an electric field enhancement factor of 5.546×10^3 for Pd NPs decorated bilayer $PdSe_2$, and the remaining enhancement factor is expected to be contributed by charge transfer mechanisms. *This work has been published in "Chem.Mater. 36,5922−5934 (2024)".*

7.1.2. Temperature-dependent Raman study of CVD grown $PdSe_2$

We have grown ultrathin sheet-like bilayer and ribbon-like few-layer $PdSe_2$ on mica substrate with high chemical and structural uniformity via a low temperature CVD growth process. Temperature-dependent Raman studies have been carried out to understand the phonon-phonon interactions in the as-grown bilayer and few-layer (5-layer) $PdSe_2$. We found a wide variation of temperature co-efficient in CVD- grown $PdSe_2$. This work reveals that evaluating the temperature co-efficient is an alternative approach to find the anisotropic ratio in $PdSe_2$ using an unpolarized laser. We found an anisotropic ratio, 1.42 and 1.28 for bilayer and few-layer, respectively with using unpolarized laser source. We have estimated the thermal conductivity of few-layer $PdSe_2$, utilizing Raman spectroscopic measurement technique. At room temperature, the estimated thermal conductivity is ~36.8 W/m. K and ~10.1 W/m. K for bi-layer and few-layer (~5L) $PdSe_2$ respectively. *This work has been published in "J. Mater. Chem. C, 9, 16693–16708 (2021)".*

7.1.3. 2D $PdSe_2$ dendrites for plasmon-free SERS substrate

We addressed high vacancies of upper Se atoms, as we know surface Se atoms can escape more easily. From the TEM and AFM image analysis, a systematic study on various defects, edge geometry, and nanopore in dendritic $PdSe_2$ has been presented. Near-infrared (NIR) PL studies revealed a decrease in bandgap in monolayer and bilayer dendritic $PdSe_2$, which further supports the presence of Se vacancies. In addition, an additional peak in the XPS spectrum confirms the

presence of defects in $PdSe_2$. It is shown that defects, nanopores, and edge geometry in dendritic $PdSe_2$ act as trapping sites for foreign molecules. These active sites and vacancies play a crucial role in the enhanced Raman signal of Rhodamine B. SERS signal associated photoluminescence of RhB/$PdSe_2$ hybrid system confirms that the Se vacancy sites in defective dendritic $PdSe_2$ act as hotspots for SERS of RhB molecule. The density functional theory (DFT) calculations show that the inclusion of the Se-defect into the $PdSe_2$ system alters its electronic behavior from semiconductor to metallic. The topological line defect of Se_{TLU} (top layer upper Se atom) in $PdSe_2$ in presence of excess Pd behaves as quasi-one-dimensional metallic wire, which is responsible for the high SERS enhancement. *This work has been published in "npj 2D Materials and Applications (2023) 7:8 (2023)".*

7.1.4. Scrolling and unscrolling of bilayer $PdSe_2$ for selective killing of cancer cells

We have demonstrated the scrolling of bilayer $PdSe_2$ and its unscrolling using an external stimulus; heat. The nanoscrolls are formed from the edges of bilayer $PdSe_2$ sheet. The conversion of $PdSe_2$ into $PdSe_2$ nanoscroll via Pd nanoparticles and water- assisted unscrolling into sheet structures are fully controlled under H_2O environment. Unscrolling of the $PdSe_2$ nanoscroll is triggered by increasing the temperature to nearly 55 °C in H_2O environment. The structures are characterized using spectroscopy and microscopy. We have observed that the $PdSe_2$ nanoscroll tends to unscroll its free outer layer, which is useful for the delivery of cargo in a specific condition. We highlight its applicability by encapsulating live cancer cells, where Pd nanoparticles attack the cancer cell leading to the nuclear arrest and death of cancer cells.

7.1.5. Strain-induced phase transition of bilayer $PdSe_2$ to Pd_2Se_3

We investigated the uniaxial tensile strain mediated evolution of new Pd_2Se_3 phase from the high quality $PdSe_2$ bilayer. To obtain stable bilayer $PdSe_2$, we employ a two-step growth method. To perform strain engineering on $PdSe_2$, we have transferred it onto a flexible PET substrate after growth on mica substrate. As PMMA assisted transfer technique involves polymers, a scotch-tape assisted transfer technique is introduced to eliminate any unwanted effects by polymers. Using Raman spectroscopy, we show that bilayer $PdSe_2$ can undergo phase transition into Pd_2Se_3 due to Se vacancies and interlayer fusion of two $PdSe_2$ layers, when subject to tensile strain. This phase transition arose in the case of polymer free transfer methods like, water assisted and scotch tape

assisted transfer techniques; whereas the phase transition is unachievable in the case of polymer assisted transfer techniques. Here we particularly focus on the Raman intensity, in which the Raman intensity did not notably change under strain. Drastic change in the Raman intensities is observed in the process of applying uniaxial tensile strain. Under the uniaxial tensile strain of > 0.5 % in the case of water-assisted transfer and of > 0.2 % in the case of scotch tape transfer; bilayer $PdSe_2$ change its phase to Pd_2Se_3. Further RTA analyses confirmed the transition of $PdSe_2$ phase to Pd_2Se_3 with the generation of new Raman peaks at 157 cm^{-1}, 189 cm^{-1}, 198 cm^{-1} and 212 cm^{-1}.

7.2. Novel contributions to the $PdSe_2$ world

The primary contribution of this thesis is the development of a salt-solution-assisted, highly reproducible synthesis method for bilayer $PdSe_2$. This approach addresses key limitations in current $PdSe_2$ research, particularly the reliance on mechanical exfoliation and high-temperature CVD techniques, which are not easily scalable for industrial applications. Here are some novel contributions in the $PdSe_2$ field**:**

1. This thesis introduces a novel low temperature NaCl assisted CVD synthesis route for $PdSe_2$, PdS_2, $PdTe_2$, $PdSe_2$ dendrites, controlled bilayer $PdSe_2$.
2. We introduce a controlled H_2O assisted chemical etchant-free transfer technique of $PdSe_2$, which fully overcomes the limitations of PMMA-assisted transfer technique.
3. This work develops a $PdSe_2$-Pd_2Se_3 junction region experimentally decorated with Pd NPs demonstrating its applicability in higher SERS enhancement.
4. This work demonstrates that utilizing Raman spectroscopic measurement technique, the estimated thermal conductivity is ~36.8 W/m. K and ~10.1 W/m. K for bi-layer and few-layer (~5L) $PdSe_2$ respectively.
5. This thesis provides a systematic study on defects, nanopores, and edge geometries in bilayer dendritic $PdSe_2$, which act as trapping sites for foreign molecules. These defect sites induce a transition in the electronic behavior of $PdSe_2$ from semiconducting to metallic, playing a crucial role in the enhanced Raman signal of Rhodamine B.
6. This thesis presents the first report on synthesis of $PdSe_2$ nanoscrolls. We demonstrate the scrolling and unscrolling of bilayer $PdSe_2$ in response to external stimuli.

7. This thesis proposes on the first study on $PdSe_2$ nanoscrolls in the field of cancer research. Notably, the nanoscrolls exhibit a unique tendency to unscroll their free outer layer under specific conditions, making them promising vehicles for targeted cargo delivery. To demonstrate their biomedical potential, we encapsulate live cancer cells within the $PdSe_2$ nanoscrolls and introduce palladium nanoparticles (Pd NPs), which selectively interact with the cell, inducing nuclear arrest and ultimately leading to death of cancer cell.
8. This thesis investigates the uniaxial tensile strain mediated evolution of new Pd_2Se_3 phase from the $PdSe_2$ bilayer.

7.3. Scope for Future Work

While 2D $PdSe_2$ has shown immense promise across a wide range of applications in 2D field, several challenges remain. One of the main limitations identified in this thesis is the difficulty of producing bilayer $PdSe_2$, $PdSe_2$ dendrites, and $PdSe_2$ nanoscroll. Future research should focus on optimizing synthesis techniques, such as improving the consistency of chemical vapor deposition methods and exploring alternative routes for scalable production. Additionally, more efforts should be made to develop efficient techniques for integrating $PdSe_2$ and $PdSe_2$ nanoscroll into biomedical field. A few of the future scopes are listed below:

1. The future of $PdSe_2$ lies in the NaCl solution-assisted layer-controlled CVD technique, the large-scale synthesis and large-area chemical etchant-free transfer of bilayer $PdSe_2$, providing a novel and easy pathway for commercial device fabrication.
2. Nanopore sensing involves using tiny pores to detect the size, and other properties of foreign molecules as they pass through or interact with the nanopore. In the field of nanopore sensing applications, there exist two major limitations fundamental to conventional methods of fabricating nanopores: (i) high dependence on high-end instruments like STM, TEM to drill nanopores, (ii) only a single nanopore can be processed at a time. Therefore, there is a constant demand for a stable pore fabrication technique for the mass production of nanopores. Hence, there is intense research to achieve nanopores in stable 2D material. As a stable 2D NTMD, $PdSe_2$ with controlled nanopores can gain significant attention in the field of nanopore sensing due to its in-plane anisotropic properties.

3. The flexibility and mechanical properties of $PdSe_2$ open up exciting possibilities in flexible electronics and wearable devices. However, further research is needed to enhance its robustness, and to explore how it can be combined with other materials to improve performance and durability in flexible applications.
4. We anticipate that 2D $PdSe_2$ may replace the BP in the biomedical field due to its in-plane anisotropy with high stability in ambient conditions. In the field of Cancer biology, $PdSe_2$ nanoscroll can be loaded with chemotherapy drugs and targeted specifically to cancer cells.
5. The phase evolution of Pd_2Se_3 from bilayer $PdSe_2$ is a topic of great interest in material science due to the impact of these phases on its electronic, optical, and mechanical properties. These phases can be controlled by various external factors such as temperature, pressure, or chemical treatments. The transition between these phases is significant because each phase exhibits distinct characteristics that can be exploited in different applications.
6. Improving the quality of PdS_2 and $PdTe_2$ is essential for realizing their full potential in applications such as electronics, optoelectronics, catalysis, energy storage, and sensors.
7. As $PdSe_2$ nanoscroll can unscroll, functionalizing $PdSe_2$ nanoscroll with targeting ligands that bind to cancer cell receptors would enhance the specificity of drug delivery, minimizing side effects typically associated with chemotherapy.